



A multi-frequency inductive 5th generation EM system for geophysical exploration

Carlos A. Dias¹, Hédison K. Sato², Mitsuro Yamashita³, Abel Carrasquilla¹, Edson E.S. Sampaio², Olivar A.L. de Lima² and Luiz G.C.L.Loures¹

(1) Laboratório de Engenharia e Exploração de Petróleo – LENEP/UENF (dias@lenep.uenf.br); (2) Centro de Pesquisas em Geofísica e

Geologia – CPGG/UFBA (olivar@cpgg.ufba.br); (3) Phoenix Geophysics Limited, Toronto, Ontario-Canada (mits@phoenix.geophysics.co)

Abstract

The multi-frequency inductive electromagnetic systems had their origin in the work by Dias (1968; 1973) and five generations of these equipments appeared in the market since then. The system discussed here belongs to the last generation. It consists of a loop-loop minimum coupling system operating at 54 values of frequency in the interval 1.125 Hz to 10.473 KHz, with transmitter-receiver separation spreading up to 1 km on a terrain of 100 Ω m resistivity background. A scheme is also presented here for processing the field data and constructing 2D pseudo-sections for resistivity and polarization parameter. The area test for this experiment is situated on a gnaissic basement covered by intemperized basement rock and quaternary beach sediments on the Farm São João in Rio das Ostras/RJ. This system was capable to discriminate and map a zone of washed sand, probably more indicated for groundwater taking, and a zone where clay minerals are present.

Introduction

This topic requires a historical background recovering. Dias (1968, 1973) introduced the idea and demonstrated the viability for measuring inductively, in the field, the IP electrical property of the rocks (due to disseminated metallics and/or clay minerals in the matrix of the rocks). In theoretical terms, this innovation consists of two items: (a) to explore a larger portion of the frequency spectrum where IP occurs (10^{-4} Hz to 1 MHz; Dias, 2000) and (b) to measure inductively, i.e. without grounded electrodes, the electromagnetic field which provides the desired information. A new system and procedures were then needed.

A prototype system was designed and constructed for such a purpose by late McPhar Geophysics Limited, a Canadian company of geophysical instruments, in 1973, under request and supervision by Dias and financing by CNPq. This equipment consisted of: i) a horizontal loop transmitter, ii) a tripod mounted movable loop receiver measuring in-phase and quadrature components for both vertical and radial magnetic field components, iii) sweeping through 12 values of frequency in the range 21 Hz to 43.008 KHz ($f=21 \times 2^{n-1}$ Hz, $n=1,2,\dots,12$), iv) transmitter-receiver separation spreading up to 1 km, v) a phase reference cable linking transmitter to receiver. The experiment with this system, in the copper province of Curaçá Valley/BA, resulted in the MSc dissertation by Sato (1979) under Dias supervision.

Still in 1973, McPhar constructed a second system, similar to the first one, however measuring the ellipsis of polarization parameters (inclination and ellipticity) of the total magnetic field.

Collapsing McPhar, two new Canadian companies succeeded it. In 1975, Geoprobe Limited bought all the rights from McPhar on Dias prototype. In 1976, Geoprobe started to commercialize a 3rd generation system, essentially measuring the same items as Dias prototype, improving however the number of frequencies from 14 to 16 coarse values x 8 fine values (totalizing 128 values) in the range 1 Hz to 40 KHz and claiming to do measurements with transmitter-receiver separation up to 2 km. It also introduced precise stable crystal clocks for synchronous measurements then eliminating the need for a phase reference cable connecting transmitter to receiver. This equipment was not entirely reliable, but it stayed in the market until 1982. The second and succedaneous company to McPhar was Phoenix Geophysics Limited, which around 1979 started to commercialize a multi-frequency EM system for measuring spectral IP in the field, but going back measuring the electric field and using grounded electrodes. This equipment was the 4th generation in the line.

The new system, object of this paper, is then the 5th generation. It was constructed by Phoenix (Eng. Mitsuro Yamashita, who was a participant in the previous historical period), under Dias request and co-designing and financing by PADCT/CNPq. It is a further development of Dias prototype, incorporating new technological advances and new functions and characteristics, as follows:

i) it measures: the absolute in-phase and quadrature components, the amplitude and phase as well, of the magnetic (x,y,z) components simultaneously; it also measures the parameters of the ellipsis of polarization (tilt angle and ellipticity). It still measures the electric field three components if required; ii) it sweeps through 54 values of frequency in the interval 1.125 Hz to 10.473 KHz (approximately as $f=1.125 \times 1.18819^{n-1}$, $n=1,2,\dots,54$); iii) transmitter-receiver separation could spread up to 1 km on a ground resistivity of 100 Ω m background; iv) it uses no cable but high precision satellite regulated clocks (GPS) for phase reference and frequency scanning of both transmitter and receiver subsystems; v) it uses statistical procedures for improving the quality of the measurements (it does stacking a large number of times for each measurement and determines

Multi-frequency Inductive EM System

its standard deviation, selecting the bad ones for elimination); vi) it can do time-domain traditional EM and IP; vii) it is all computer controlled.

Still as part of a field test, this system was used for taking measurements looking for groundwater on the Farm São João, Rio das Ostras/RJ, from 15 to 22 March/2001, with the transmitter set at a given point and the receiver displaced along a line N150°E. The stations were spaced 50 m apart until 600m, and 100m since then until the 1000m station. Measurements were made using three kinds of receiver: a) a highly sensitive magnetic-core coil (normally used for audio-magnetotelluric measurements); b) an air-core coil with a pre-amplifier; c) the same air-core coil as in (b) without pre-amplifier.

Geological Features about the Area

The test area is roughly plane and corresponds to the crystalline basement gnaisses at small depths, covered by sediments resulting from the interperized basement and sands from marine origin. In the initial section of the profile going until the 500 m station the surface of the terrain is composed by washed sand, reworked and transported by eolian processes, almost 100% fine sand of quartz. From the 500 m station until 1000 m the terrain is increasingly clay-rich until it becomes a shallow meadow.

Field Procedures

This item will be subdivided as:

a) Calibration

(i) V6-TEM Unit: This is the receiver subsystem. It can be calibrated anywhere at the beginning of an experiment. It consists of determining the values of the internal parameters for each value of frequency, based on standard voltages and GPS signals; (ii) Receiving coils: They are calibrated by determining and recording the coefficients which relate the induced voltage to the value of the magnetic field at the coil, for each value of frequency. For this, the receiving coil should be placed at the center of a small size loop on a place where the ground effect could be neglected (a highly resistive ground), in order to consider as a reference the free-space value of the computed magnetic field at the central point of the small coil. In the present case, the three types of receiving coils (before indicated) were used; (iii) Transmitter Unit: This subsystem is powered by a 3.5 KVA motor generator and drives the transmitter loop, which spreads over the ground, contouring stakes. It is calibrated actually doing a true transmission in situ. It consists on measuring and recording the intensity of the current passing in the transmitter unit for each value of frequency and, at the same time, establishing a timing routine based on the GPS signals, same cadence and frequency scanning for both, transmitter and receiver. It should be done over again every time the size of the loop is changed.

b) Transmitting loop size

In our experiment we used squared shape loops. For assuring the condition of a point magnetic dipole we adopted: 12 m x 12 m loop size for measurements from 100 m until 200 m; 40 m x 40 m for measurements from 250 m until 600; and 100 m x 100 m for measurements from 700 m until 1000 m.

c) Measurement stations

Describing the highly sensitive magnetic-core loop, as **c**, the air-cored loop with pre-amplifier, as **p**, and the air-cored loop without pre-amplifier, as **a**, the measurements made in this experiment were as follows: (c, p, a) at stations 100 m up to 800m; (c, p) at station 900 m; and (c) at station 1000 m. The selection was done based on the noise level.

Data Treatment and Processing

This item can be described in the following three sub-items:

a) Conversion of the field data measurements to apparent resistivity and “polarization parameter”

This conversion is made using the scheme due to Dias (1968). It consists in writing the mutual impedance function for a pair of transmitter-receiver loops at minimum coupling on the surface of a homogeneous equivalent half-space allowed to assume complex conductivity, in terms of the in-phase and quadrature components for the radial magnetic field. As coordinates axis are taken the induction number, given as $\theta_A = (\mu_0 \omega |\sigma_A| / 2)^{1/2} r$, and the polarization parameter given as the imaginary part of the conductivity to its modulus, i.e. $\sigma_I / |\sigma_A|$, where $\mu_0 = 4\pi \times 10^{-7}$ (MKS) is the vacuum magnetic permeability, $\omega = 2\pi f$ rad/s (f is in Hz), σ_A is the complex apparent conductivity (σ_R, σ_I) in S/m and r is the transmitter-receiver separation in m.

The field data measurements here are expressed in terms of in-phase and quadrature components of the radial magnetic field normalized to the primary magnetic field, similarly as in Dias representation, composing a pair (X,Y). The pair (X,Y) is then converted to $(\theta_A, \sigma_I / |\sigma_A|)$. From θ_A the value of $|\sigma_A|$ or its inverse is obtained.

b) Association of $(|\rho_A|, \sigma_I / |\sigma_A|)$ to space points on the profile cross section

This scheme was developed by Sato and Dias, as described in Sato (1979). It consists in determining the point nearest to the receiver position, which stays on the geometric locus given by half the “skin depth of the radial magnetic component” generated by the magnetic dipole source set on the transmitter position. If the skin depth is indicated by δ_d for the magnetic dipole source, we have according to Sato (1979):

$$\frac{r}{\delta_d} = \theta - \frac{(\theta - \theta_1)(\theta - \theta_2)(\theta - \theta_3)}{\theta_1 \theta_2 \theta_3 - 1 + \exp(\alpha\theta) - \beta\theta} \quad (1)$$

Multi-frequency Inductive EM System

where r is the transmitter-receiver separation and $\theta_1=1.184$, $\theta_2=7.051$, $\theta_3=8.581$, $\alpha=0.540$ and $\beta=14.973$. It is interesting to note that $\theta=r/\delta_{pw}$ where $\delta_{pw}=(\mu_0\omega|\sigma_A|/2)^{-1/2}$ is the plane wave skin depth.

Taking the transmitter position as the origin, the coordinates for the lateral position (x) and depth (y) when given a pair (r , $(\delta_d/2)/r$) are $x = r/[1 + ((\delta_d/2)/r)^2]$, $y = (\delta_d/2)/[1 + ((\delta_d/2)/r)^2]$.

Pseudo-Sections of $|\rho_A|$ and $\sigma_I/|\sigma_A|$

Following the steps (a) and (b) described in the previous part, we constructed pseudo-sections for apparent resistivity and apparent polarization parameter versus (log) frequency and versus depth, for the three types of receiver, using a package developed by Sato (unreleased), as shown on Figures 1, 2, 3 and 4.

One can appreciate the striking difference between the two representations, taking the log of frequency or the depth, for the vertical coordinate. In the second case (Figs. 2 and 4), one can verify the presence of a shadow zone due to the dipole skin depth effect, which does not exist on Figs. 1 and 3.

It is observed that the high sensitive receiver provides a more complete and reliable set of field data; and that the representation of the functions versus depth looks more likely the ground structure expected from the geological information.

Interpretation

For this purpose, let us consider only the pseudo-sections supported on data provided by the high sensitive receiver versus depth.

From the resistivity pseudo-section Fig 2(a) one can associate the zone with $|\rho_A|$ in between 10 to 30 Ωm as the most probable to provide good ground water. The zone more conductive than that may well be associated to clay-rich zone and or more salted water, and the zone more resistive (between 30-100 Ωm) may be the altered basement rock sediment. As to the pseudo-section of $\sigma_I/|\sigma_A|$, one should be aware that (Dias, 1968): a) the effect due to the heterogeneity of the half-space can result either in negative values for $\sigma_I/|\sigma_A|$ or weak positive values (no greater than 0.15); b) the effect due to the presence of IP sources can considerably elevate the values of $\sigma_I/|\sigma_A|$ positively; c) consequently, the values of $\sigma_I/|\sigma_A|$ around zero means either lack of heterogeneity and polarization or a compensation of the two.

Observing the pseudo-section of $\sigma_I/|\sigma_A|$ given by Fig. 4(a), one can see at the first half portion of the profile a zone of small resistivity contrast showing small values of $\sigma_I/|\sigma_A|$, possibly associated to the most probable zone to be a ground water reservoir. It corresponds to the washed fine sand of quartz zone exposed on the surface. In the second half of the same profile, corresponding to 500 m until 1000 m stations, it shows large positive values of $\sigma_I/|\sigma_A|$ in good agreement with the

surface evidence for clay minerals presence. This could also be associated with more salted water at shallow depth as indicated by the more often presence of 3-10 Ωm conductive small zones as shown on Fig. 2 (a).

Conclusions

The present experiment evidenciates that:

- 1) This equipment and method provides reliable data at a high degree of resolution, adequate to measure in detail ground resistivity and inductive IP at depths down to 350 m on a background of 100 Ωm .
- 2) the data representation versus log of frequency in the vertical axis is inadequate. It is so due to the fact that the skin depth for a magnetic dipole source is not proportional to that same parameter for a plane wave. The best representation, when not through modelling, must be done based on the dipole source skin depth, like the one presented here;
- 3) the potential use for this equipment and method is of very large range of applications. In the present case, it was capable to separate through the parameter of polarization (subsidized by information on resistivity) a clay-poorer zone from the clay-rich one.

In more general terms, we can say that a new and resourceful equipment for multi-frequency inductive electromagnetic exploration is at hand, having in addition the capability to do the traditional EM and IP measurements. This system is entirely automatized and can give rise to an enormous amount of field data, good for theoretical work (442 pages of data, in this present experiment).

References

- Dias, C.A, 1968, A non-grounded method for measuring induced electrical polarization and conductivity. pp. 260. PhD. Dissertation, University of California, Berkeley, USA.
- Dias, C.A. & BNDE, 1973, Non-grounded method of geophysical exploration. Patent n° 920.660, Issued Feb. 6, 1973, Class 324-9 C.R.C.1, Filed May 31, 1971, Ottawa, Canada.
- Dias, C.A., 2000, Developments in a model to describe low-frequency electrical polarization of rocks, Geophysics, 65, 2, 437-451.
- Sato, H.K., 1979, *Método eletromagnético para interpretação de polarização induzida e resistividade usando o protótipo de um sistema a multi-freqüência*. MSc. Thesis, PPPG/UFBA.

Acknowledgments

We acknowledge the PADCT/CNPq/FINEP for providing the funds for acquisition of this equipment and CNPq/ANP for the funds which permitted to do this field test.

Multi-frequency Inductive EM System

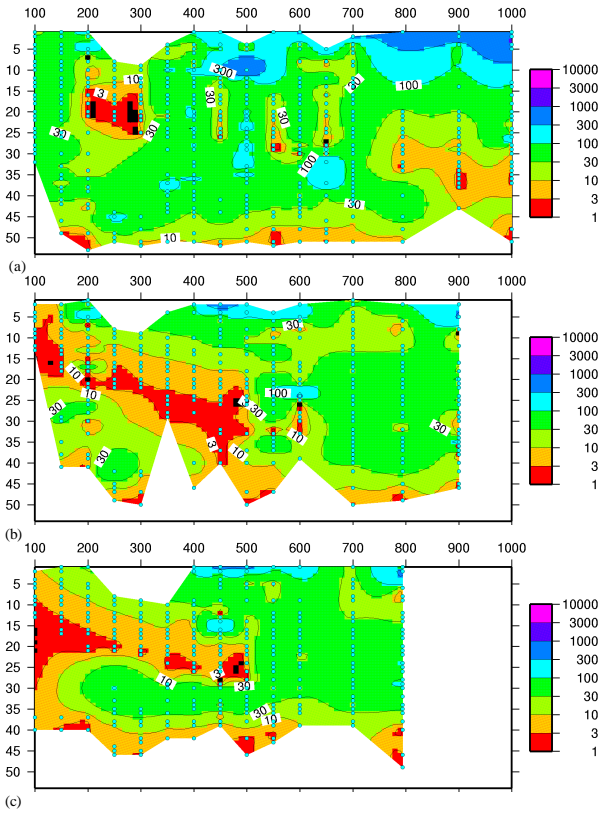


Fig. 1- Pseudo-sections of ρ_a versus log frequency: (a) highly sensitive magnetic-cored loop, (b) air-cored loop with pre-amplifier and (c) air-cored loop without pre-amplifier.

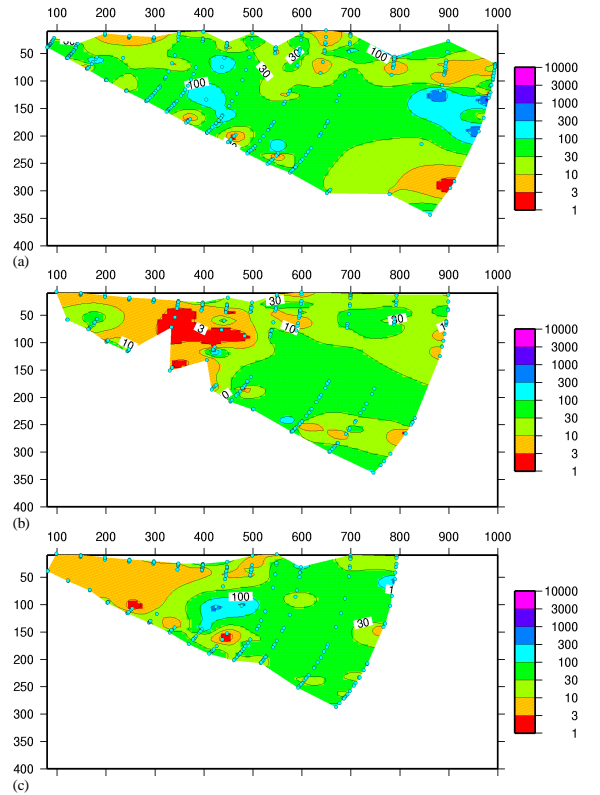


Fig. 2- Pseudo-sections of ρ_a versus depth (m): (a) highly sensitive magnetic-cored loop, (b) air-cored loop with pre-amplifier and (c) air-cored loop without pre-amplifier.

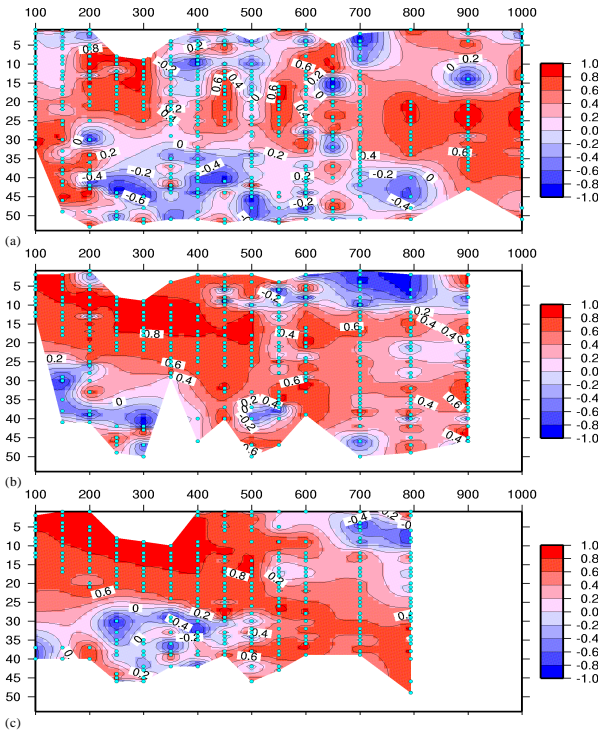


Fig. 3- Pseudo-sections of σ_r/σ_A versus log frequency: (a) highly sensitive magnetic-cored loop, (b) air-cored loop with pre-amplifier and (c) air-cored loop without pre-amplifier.

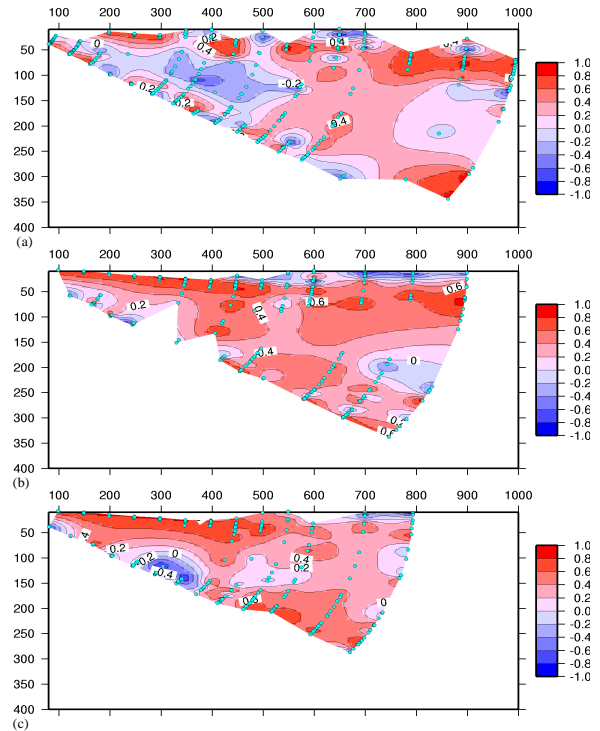


Fig. 4- Pseudo-sections of σ_r/σ_A versus depth(m): (a) highly sensitive magnetic-cored loop, (b) air-cored loop with pre-amplifier and (c) air-cored loop without pre-amplifier.



An Easy Windows Graphic Interface for 3-D Electrical Geophysics Modeling

Humberto Deodato M. Monteiro; Luiz Rijo; UNIVERSIDADE FEDERAL DO PARÁ, Brazil
humberto@cinbesa.com.br; rijo@amazon.com.br

Abstract

The finite element method is a very powerful tool for modeling complex problems in physical science, engineering and geophysics. However, for three dimensional analysis, the arduous pre-processing stage which consists of supplying the data for the mesh and the physical properties for each element is, certainly, a weakness of the method. In order to handle this disadvantage, we developed a simple Windows graphic interface for entering the information of the physical properties across the mesh at no great pains. We use the 3-D Resistivity and IP modeling problem to show how the proposed graphic interface facilitates the access of finite element data. Apparent resistivity and PFE pseudo-sections at 10 parallel survey lines, one dipole unit apart, are displayed graphically to exhibit the output graphic interface that was also developed for presentation of the modeling results.

Introduction

Since 1972, still as graduate student, one of us (LR) have been engaged in developing a package of computer programs for modeling and interpretation of electrical geophysics, Rijo, 1977. This effort has culminated in the electrical Geophysics suite 2000, eGs 2000 for short, a new version of the former EGSLIB (Electrical Geophysics Software Library) which has been used by many people here and abroad.

In the old days (seventies, eighties and half of nineties of the last century) the programs of the EGSLIB were developed for mainframes and workstations under Unix. At beginning, the input data for running the programs were submitted by punched cards, and afterward through coded commands at the prompt of a donkey monochrome monitor. Certainly this was a drawback for using programs that require quite large quantity of input data that had to be changed constantly at each running submission, as it is commonly done in geophysics. Indeed, the work of most geophysicists is to try several different models during the process of interpreting their geophysical data.

With the advent of modern powerful personal computers all this have been changed dramatically. As matter of fact, not only geophysics, but our whole life have been changed for better or worst by these marvelous machines. Now, we have at our disposal

powerful tools as Visual Basic, C++, Java and Delphi for development of nice, easy and friendly graphics interfaces that facilitate the communication between the geophysicist and the machine. This is precisely what we have been done lately. Using Delphi we have already converted a large number of old programs from the EGSLIB to the new eGs 2000 for Windows. The engine continues to be in Fortran, however most of the source programs have been rewritten in Fortran 90 and converted into DLL (dynamic-link library) components.

The purpose of this work is to present an example of a typical 3-D modeling program of the eGs 2000. For that, we chose the Resistivity and IP modeling problem to illustrate how easy is to read in the finite element data. A fantastic improvement in comparison with the old manner used in the obsolete EGSLIB.

3-D IP and Resistivity Modeling

The three dimensional finite element method consists in dividing the subsurface into a mesh of prismatic elements as shown in Figure 1. This expedient allows us to substitute the continuous boundary value problem governed by the IP and Resistivity theory into a discrete problem in form of a system of algebraic linear equations which can be handled easily by the compute, Stang and Fix, 1973, Pelton et al. 1978 and Rijo, 1984.

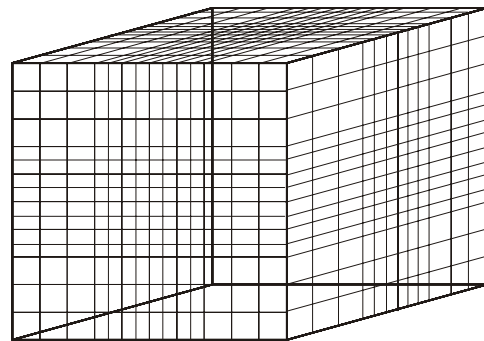


Figure 1. Three-dimensional Finite Element Mesh

The Input Graphic Interface

The finite element method is a very powerful tool for modeling complex problems in physical science, engineering and Geophysics. However, for three dimensional analysis, the arduous pre-processing stage which consists of supplying the mesh data and

An Easy Windows Graphic Interface for 3-D Electrical Geophysics Modeling

the physical properties for each element is, certainly, a weakness of the method. In order to handle this problem, we developed a simple Windows graphic interface for entering the information of the physical properties distribution within the mesh at no great pains.

We sliced the three-dimensional rectangular grid shown in Figure 1 into 2-D sections parallel to the XZ plane. The center of the grid has 100x10x9 uniform 0.25 dipole unit cubic elements. The total grid has 181x16x16 elements to accommodate the boundary conditions. The sliced sections, in the Y-direction, are given in groups according to the variation of the geometry and physical properties of the medium. The physical properties in each sliced section is introduced by coloring each cell according to the distribution of the resistivity and PFE (percent frequency effect) across X and Z mesh directions.

To illustrate how to use the interface, we chose the three-dimensional body shown in Figure 2, imbedded in 1000 ohm-m IP free host. The light-blue represent the host. The other four colors represent the resistivity and PFE values of each portion of the body as depicted in the Table 1.

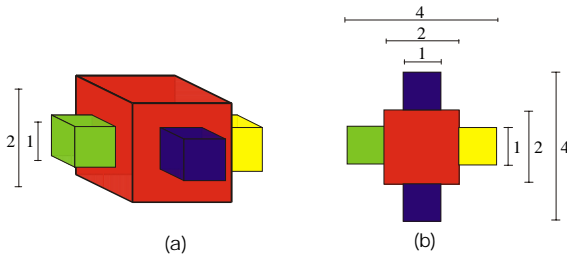







Figure 2. The geometry of the model. (a) three dimensional view. (b) horizontal plan view.

Table 1

	Resistivity ohm-m	Pfe %
	1000	0
	10	30
	50	10
	20	5
	100	20

Since the body is symmetric in Y-direction we need to slice only half of the body. Thus, the sixteen slices in Y-direction were divided in four groups of slices shown in Figure 3. Two slices of type (a), two of type (b), four of type (c) and eight of type (d).

In each of these sliced sections only 32 out of 100 elements in the horizontal direction are shown.

Likewise, only 11 elements out of the 16 are shown in the vertical direction.

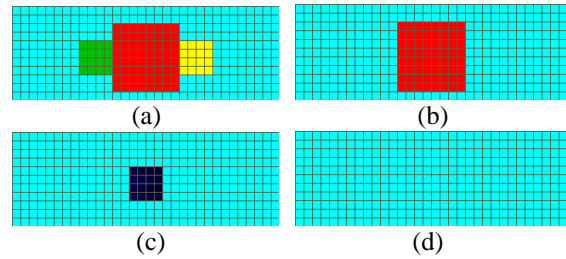


Figure 3. Grid slices parallel to XZ-plane.

The Output Graphic Interface

For each one of the 10 survey lines, separated by one dipole unit in y-direction, we calculated the apparent resistivity and PFE pseudo-sections. They are illustrated through Figures 4 to 13. The figures labeled (a) represent apparent resistivity and (b) represent the PFE. The pseudo-sections 1a and 1b are right on the center of the body. We observe that the value of the apparent resistivity increase from the center toward the border of the body. This is due to the influence of the resistive host. On the other hand, the values of PFE decrease because the polarization of the host is zero.

The small asymmetry of the resistivity and PFE of the body is barely noticed on the pseudo-sections.

Apparent resistivity and IP pseudo-sections are very blurry and thus we can not notice the details of the geometry of the three-dimensional body.

All pseudo-sections to be presented next were plotted within the eGS 2000 itself. For that, we developed a complete set of facilities in order to show the data results in more intuitive way.

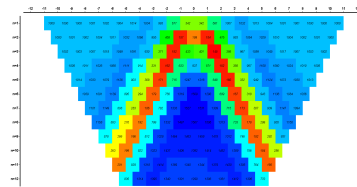


Figure 4a. App. resist. pseudo-section at $y = 0$.

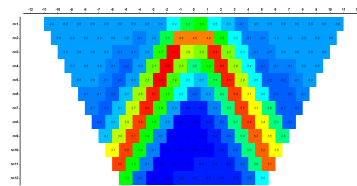


Figure 4b. PFE pseudo-section at $y = 0$.

An Easy Windows Graphic Interface for 3-D Electrical Geophysics Modeling

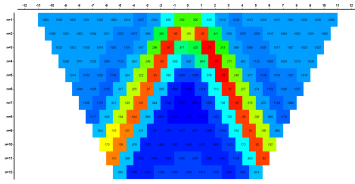


Figure 5a. App. resist. pseudo-section at $y = 1$.

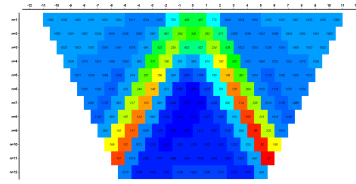


Figure 8a. App. resist. pseudo-section at $y = 4$.

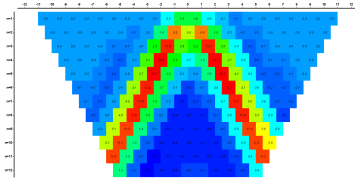


Figure 5b. PFE pseudo-section at $y = 1$. dipole unit.

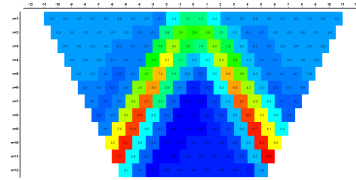


Figure 8b. PFE pseudo-section at $y = 4$ dipole units.

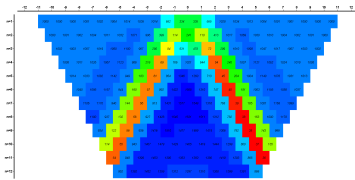


Figure 6a. App. resist. pseudo-section at $y = 2$.

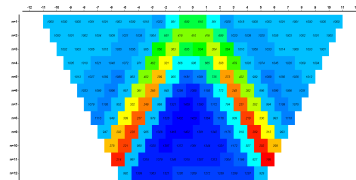


Figure 9a. App. resist. pseudo-section at $y = 5$.

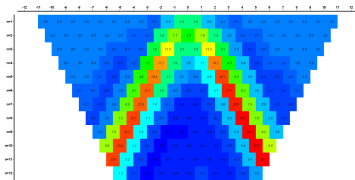


Figure 6b. PFE pseudo-section at $y = 2$ dipole units.

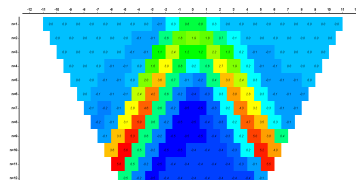


Figure 9b. PFE pseudo-section at $y = 5$ dipole units.

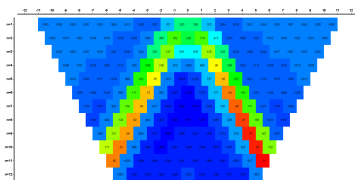


Figure 7a. App. resist. pseudo-section at $y = 3$.

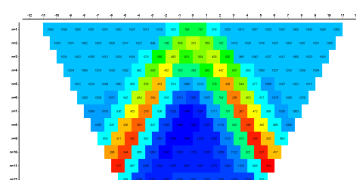


Figure 10a. App. resist. pseudo-section at $y = 6$.

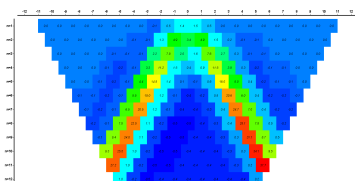


Figure 7b. PFE pseudo-section at $y = 3$ dipole units..

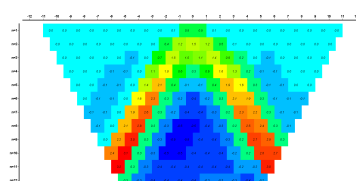


Figure 10b. PFE pseudo-section at $y = 6$ dipole units.

An Easy Windows Graphic Interface for 3-D Electrical Geophysics Modeling

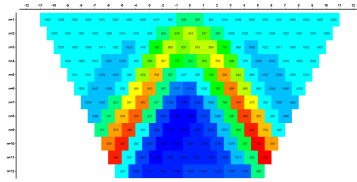


Figure 11a. App. resist. pseudo-section at $y = 7$.

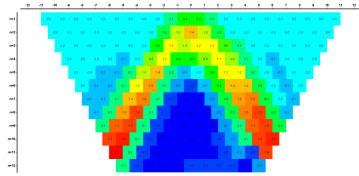


Figure 11b. PFE pseudo-section at $y = 7$ dipole units.

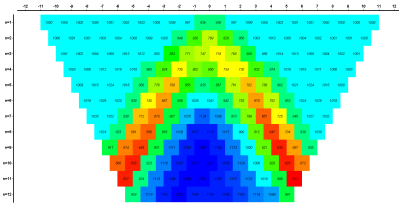


Figure 12a. App. resist. pseudo-section at $y = 8$.

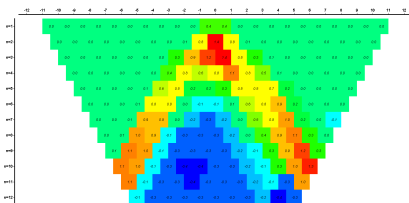


Figure 12b. PFE pseudo-section at $y = 8$ dipole units.

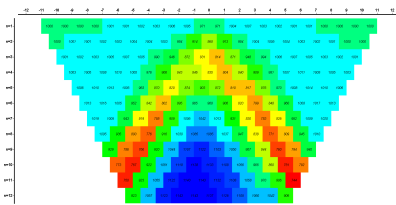


Figure 13a. App. resist. pseudo-section at $y = 9$.

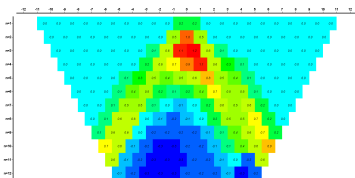


Figure 13b. PFE pseudo-section at $y = 9$ dipole units.

Conclusions

We developed a friendly input graphic interface that greatly facilitates the hard work of entering 3-D finite element data. In order to show how easy is to use the interface, we selected the 3-D Resistivity and IP modeling example. The apparent resistivity and PFE pseudo-sections are displayed by the output graphic interface. Both, the input and output interfaces belong to the eGs 2000. With them it is not necessary to use commercial software such as MATLAB, SURFER etc..., for displaying the final results. Thus, this capability makes our application independent of third part software packages.

Similar interfaces can be used in other Electrical Geophysics applications such as Magnetotelluric, Electromagnetic tomography, 3-D EM and so on.

References

Pelton W.H., Rijo L., Swift C.M., Jr., 1978, Inversion of two-dimensional resistivity and induced-polarization data: *Geophysics*, 43, 788-803.

Rijo, L. 1977. Modeling of Electrical and Electromagnetic Data. Ph.D. Thesis. University of Utah.

Rijo, L., 1984. Inversion of Three-Dimensional Resistivity and Induced Polarization Data. Expanded Abstracts. Fitty-Fourth Annual International Meeting, SEG, 113-117.

Stang G., and Fix, G. J., 1973, An analysis of the finite element method: Prentice-Hall, 306 p.

Acknowledgments

The development of the eGs 2000 has been partially funded by the projects PROINT 2000 and 2001 supported by University Federal do Pará. One of us (HM) thanks CAPES for supporting his graduate studies at the UFPA. Finally, we extend our acknowledgments to the Agência Nacional de Petróleo (ANP) for its financial support to our graduate course in Geophysics.

Analysis of Georadar Reflection Responses

Jacob Fokkema, Emile Fokkema, Sicco Beekman and Evert Slob. Delft University of Technology, The Netherlands

Abstract

Understanding the nature of the georadar reflection response in terms of the dielectric permittivity and conductivity contrast is important in the realm of interpretation. This motivates the present study, which has the aim to carry out an experiment in a controlled fashion such that the relation can be established between the measurement and the relevant physical parameters. In the present paper we present the results of such a measurement and an interpretation based upon a 1D model, which is realistic enough to accommodate sophisticated physical parameter models.

Introduction

The study of the reflection response in georadar data deserves our full attention if it is our aim not only to position the GPR reflection at its true depth position, but also to be able to identify the material contrast. Examples are found in Hagrey and Müller, 2000, and Lázaro-Mancilla and Gómez-Trevino, 2000. In the paper of Hagrey and Müller (2000), a research is presented reporting on a GPR study relating the pore-water content and the salinity in sand to the permittivity and conductivity contrast under controlled conditions. In the present research we have a similar goal. We buried a plastic pipe of 1m length with a diameter of 10cm in sand at a depth of 0.5m. The pipe was closed at both ends, but by means of a hose at both sides the pipe could be filled with any fluid desired without changing the in-situ conditions of the buried pipe (see Fig.1).

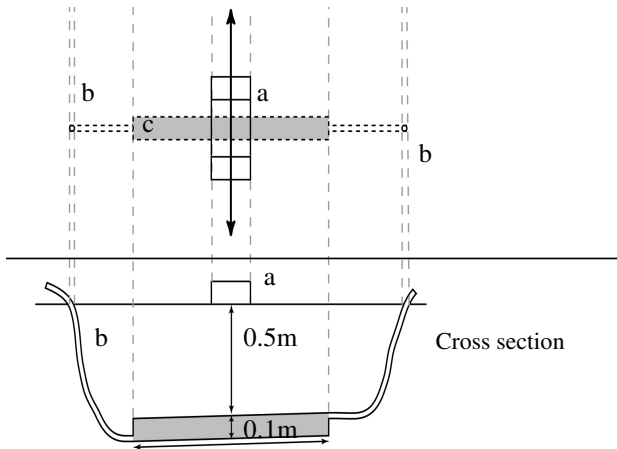


Figure 1. Georadar acquisition geometry. a: transmitting and receiving antennas; b: filling hose; c: testing pipe containing fluids.

The pipe is traversed with the pulseEKKO 1000, 450 and 900MHz georadar system in such a way that the pipe is perpendicular to measurement direction. In our measurements we considered the pipe filled with air, water, ethanol and glycerol to have a wide range of permittivity values. In Fig.2 we show the results for the 450MHz measurement when the pipe was filled with water. Clearly the internal multiples of the pipe are visible. In order to be able to translate the measurement to the permittivity values, we need a forward theoretical model to guide this operation. We decided to restrict ourselves to a 1D-analysis of the measurement carried out just above the buried pipe.

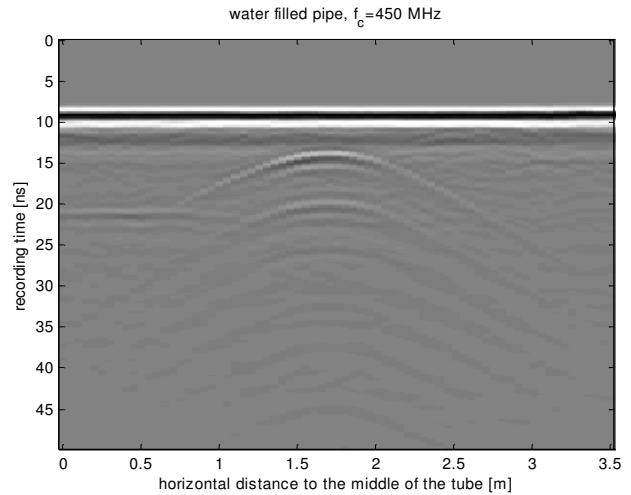


Figure 2. The pulseEKKO 1000 measurement

In the next section we discuss our 1D-model.

Theory

In our analysis we depart from the Maxwell equations in the frequency domain

$$\nabla \times \mathbf{H} - (\sigma + i\omega\epsilon) \mathbf{E} = \mathbf{J}^{\text{ex}} \quad (1)$$

and

$$\nabla \times \mathbf{E} + i\omega\mu \mathbf{H} = \mathbf{0}, \quad (2)$$

in which \mathbf{J}^{ex} accounts for the external source term that drives the electromagnetic wave propagation and represents our georadar system. In these equations a $\exp(i\omega t)$ dependence is assumed and $\omega = 2\pi f$. In the further analysis of the data we propose a 1D-treatment of the recorded GPR data. To that end we

GPR Reflection Response

assume a monostatic measurement where transmitter and receiver antenna coincide with the y-axis in the origin of the co-ordinate frame. Hence we have

$$J^{ex} = I(\omega)\delta(z)\delta(z) i_y, \quad (3)$$

where $I(\omega)$ represents the frequency spectrum of the transmitter antenna. Further we assume that we may neglect the x- and y-dependence of the parameters in the data, such that ∂_x and ∂_y operating on the field quantities have a vanishing contribution in Eqs. (1) and (2). The medium parameters and hence the field quantities only show z-dependence and their wave behaviour follows from the characteristic equation for E_y ,

$$\partial_z^2 E_y + \frac{\omega^2}{c^2} \bar{\epsilon}_r E_y = I(\omega)\delta(z), \quad (4)$$

with $c = \sqrt{1/(\epsilon_0\mu_0)}$, the electromagnetic velocity of light in vacuum and the complex relative permittivity parameter $\bar{\epsilon}_r(z, \omega) = \epsilon_r(z, \omega) - \frac{i\sigma(z)}{\omega\epsilon_0}$,

such that $\text{Im}\{\sqrt{\bar{\epsilon}_r}\} < 0$ for $\omega > 0$. There is no contrast in the magnetic permeability and consequently we take $\mu(z) = \mu_0$. The other characteristic equation for H_y is immaterial for our particular wave problem since it is decoupled and has no source stimulation. We consider the medium piece-wise homogeneous in the z-direction, such that these regions occupy the domains $(z_{n+1}-z_n)$ with $\bar{\epsilon}_r^{(n+1)}$ for $n=0,1,\dots$ and at $z=z_0=0$ we have the air-soil interface where the GPR antennas are located. In the light of these simplifications we have the following expression for $E_y(0, \omega)$ as solution of Eq.(4) at the air-soil interface, representing the measurement of the receiver GPR antenna

$$E_y(0, \omega) = G(\omega)S(\omega), \quad (5)$$

where the impulse response G is given by

$$G(\omega) = \frac{1 + R_1 W_1}{1 + r_0 W_1}, \quad (6)$$

and the global reflection coefficient follows from the recursion formula

$$R_n = \frac{r_n + R_{n+1} W_{n+1}}{1 + r_n R_{n+1} W_{n+1}} \quad n=1,2,\dots, \quad (7)$$

with the complex propagation factor

$$W_{n+1} = \exp\left[-4 \frac{i\omega}{c} (z_{n+1} - z_n) \sqrt{\bar{\epsilon}_r^{(n+1)}}\right], \quad (8)$$

and the local reflection coefficient, since there is no contrast in permeability, is given by

$$r_n = \frac{\sqrt{\bar{\epsilon}_r^{(n)}} - \sqrt{\bar{\epsilon}_r^{(n+1)}}}{\sqrt{\bar{\epsilon}_r^{(n)}} + \sqrt{\bar{\epsilon}_r^{(n+1)}}} \quad n=0,1,\dots, \quad (9)$$

such that $z_0 = 0$ and $\sqrt{\bar{\epsilon}_r^{(0)}} = 1$. The antenna GPR source signature S is represented as

$$S(\omega) = \frac{-\sqrt{\mu_0/\epsilon_0}}{\sqrt{\bar{\epsilon}_r^{(1)}} + 1} I(\omega). \quad (10)$$

Note that the soil medium directly under the transmitting antenna determines the source signature

through $\sqrt{\bar{\epsilon}_r^{(1)}}$. The term $\sqrt{\mu_0/\epsilon_0}$ is the wave impedance in vacuum.

In the next section we illustrate how the theoretical model aids the interpretation of the measurements.

Results

The measurements were carried out in a controlled environment consisting of a sandbox of 10x10x3 m, in which a plastic pipe was buried at 0.5m depth. The 450MHz-georadar measurement was carried out with a time sampling of 0.2ns and a total recording time of 50ns. The 900MHz measurement was performed with a time sampling of 0.1ns and a recording time of 30ns. The first step in the process is the signature deconvolution of the measurements with a desired signature, for which we took the third derivative of the Gaussian. In Fig. 3 this process is illustrated in the case of the air-filled pipe for both frequencies of operation. It appears that the operational centre frequency for the 450MHz system is 500MHz, while for the 900MHz system we observe that 650MHz is the actual centre frequency. We choose our desired signature such that in both cases its centre frequency was situated at 600MHz. Furthermore we restricted the recording time in both cases to 20ns. The actual signature deconvolution was carried out according to

$$E^{decon} = E^{measured} S^{desired} / S^{actual}, \quad (11)$$

GPR Reflection Response

where $S^{measured}$ is estimated from the actual measurement by selecting the first arriving signal. The latter is in fact representative for the expression of Eq.(10).

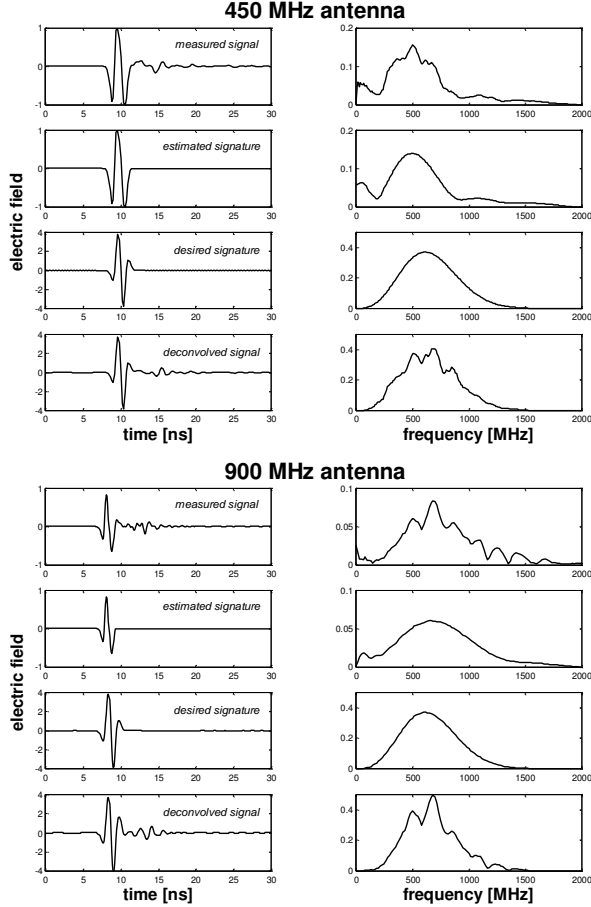


Figure 3. The process of deconvolution of the air-filled pipe for the 450 and 900MHz measurement.

Next we determine our theoretical result by computing the impulse response according to Eq. (6). The theoretical formulation supports internal multiples in the z -regions and this facilitates a realistic modelling result of the pipe embedded in the sand. In order to properly model the material parameters we considered the following expression for $\bar{\mathcal{E}}_r$,

$$\bar{\mathcal{E}}_r(\omega) = \varepsilon_r^\infty + \frac{\varepsilon_r^0 - \varepsilon_r^\infty}{1 + \frac{i\omega}{\omega_{rel}}} - \frac{i\sigma}{\omega\varepsilon_0}, \quad (12)$$

where we took into account for the relative permittivity $\varepsilon_r = \varepsilon_r(\omega)$ the frequency dependence according to the well-known Debye model. In the latter model

$\lim_{\omega \downarrow 0} \varepsilon_r(\omega) = \varepsilon_r^0$ and $\lim_{\omega \rightarrow \infty} \varepsilon_r(\omega) = \varepsilon_r^\infty$. These limits determine the starting and end values of the permittivities in the frequency band of interest, while the radial relaxation frequency ω_{rel} determines how rapid this transition goes.

In Fig.4 we show how the modelling results compare to the deconvolved measurements for the case that the pipe was filled with air, water, ethanol and glycerol. The best results were obtained for simultaneously 450 and 900MHz for the medium parameters shown in the table below.

Table I. Obtained parameters

medium	ε_r^0	ε_r^∞	f_{rel} (MHz)	σ (mS/m)
sand	3.2	2.9	200	7
air	1	1	-	0
water	80	60	143	0
ethanol	20	4	667	0
glycerol	40	8	1000	0

Conclusion

We conclude that our approach is successful in determining in a controlled way the medium parameters. We were able to come to one model that was able to explain both the 450 and 900 MHz results.

Acknowledgements

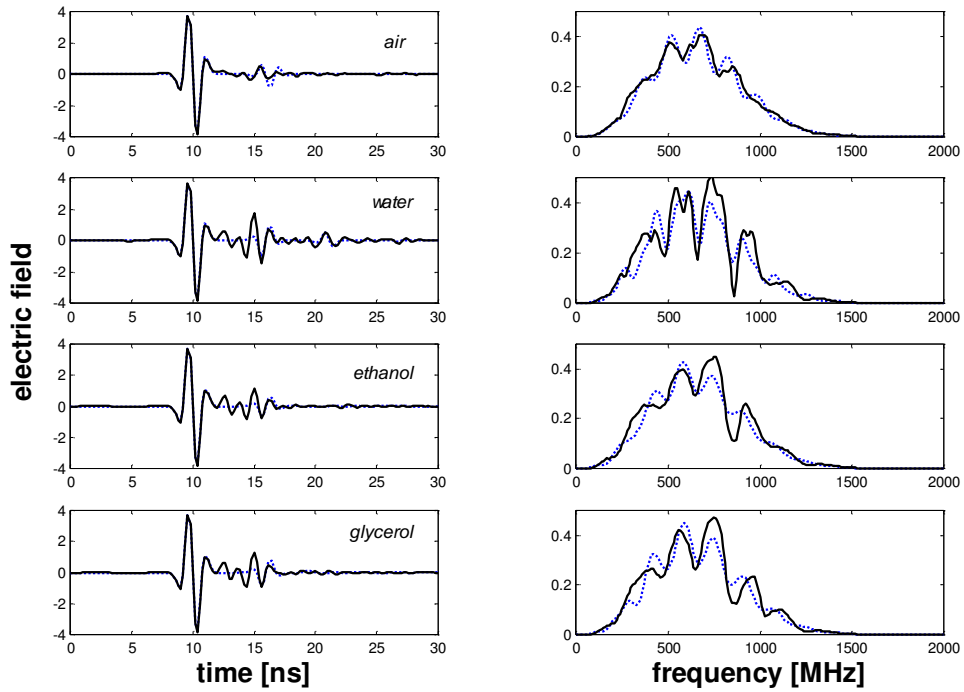
The first and fourth author carried out the research in the framework of the STW project DEL 4663, *Advanced relocatable multi-sensor system for buried landmine detection*. The authors are grateful for the financial support of this project. The second and third author performed the research in the framework of the so-called *free research project* of the Faculty of Applied Sciences. The faculty supported this publication.

References

- al Hagrey S.A., and Müller C., 2000, GPR study of pore water content and salinity in sand, *Geophysical Prospecting*, **48**, 63-85.
- Lázaro-Mancilla O., and Gómez-Trevino E., 2000, Ground penetrating radar inversion in 1-D: an approach for the estimation of electrical conductivity, dielectric permittivity and magnetic permeability, *Journal of Applied Geophysics*, **43**, 199-213.

GPR Reflection Response

450 MHz antenna



900 MHz Antenna

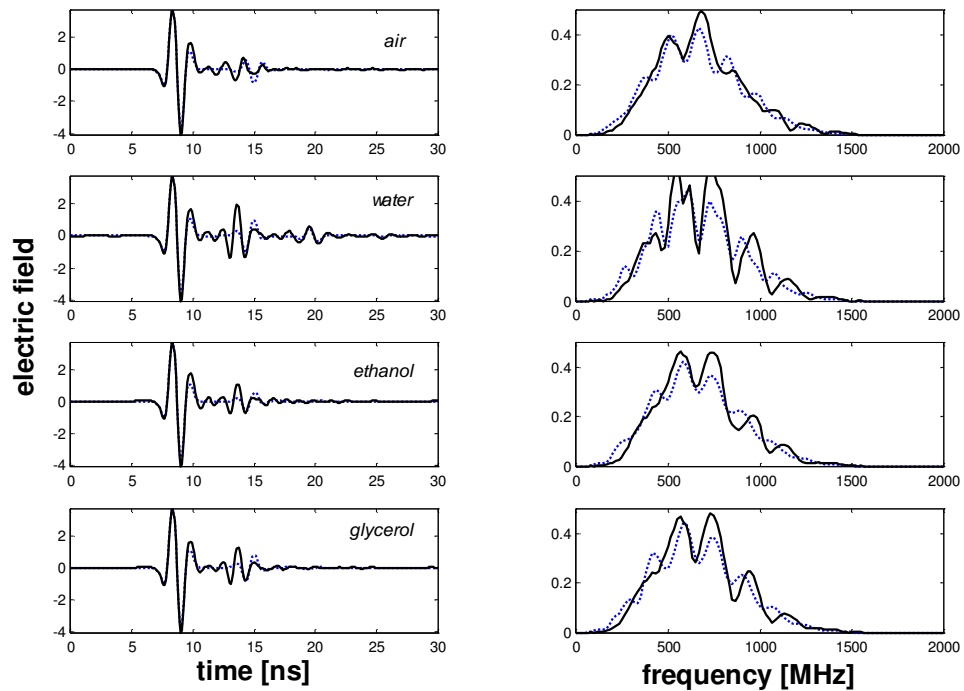


Figure 4. Comparison of deconvolved signals (solid) for 450MHz and 900MHz with the modelled result (dotted) for the cases where the pipe was filled with air, water, ethanol and glycerol.



Coast Effects on Magnetotelluric Data from the Brazilian Southeastern Region

Antonio L. Padilha, Ícaro Vitorello and Marcelo B. Pádua, INPE, Brazil

Abstract

The coast effect on magnetotelluric (MT) data acquired near the Brazilian SE coast in the state of São Paulo is investigated using two-dimensional (2D) modeling. The Atlantic ocean was modeled as a layer of constant resistivity (0.3 ohm.m) and thicknesses up to 2.0 km at 160 km from the coast, according to bathymetry. Offshore Santos Basin was also included in the model using parameters derived from boreholes and seismic lines. The continental resistivity model was constructed based on the electrical structure inferred from previous MT studies. The modeling exercise shows that the ocean-coast effects are very important for periods greater than some seconds at distances of tens of kilometers from the coast. Synthetic data from the model are compared with a MT sounding carried out in the Serra da Mantiqueira plateau. Splitting between TE and TM modes observed at a period of 30 s in the MT data can be explained as being generated by electric currents induced in the highly conductive Atlantic ocean (coast effect), about 90 km away.

Introduction

The Precambrian crystalline complex of southeastern Brazil is composed of lithologies of very distinct ages, composition, metamorphism and crustal level origin. They range in age from the Archean to the Neoproterozoic, in silica content from mafics to felsics, in metamorphic grade from greenschist to high grade granulite facies and have been transported from mid- and lower crust. Presently they are distributed along NE-SW tectonic structures related to a complex history of subduction and back-arc processes, orogeny and collapse from continental collision, and respective subsidence, uplift, denudation and magmatism.

To determine the electrical conductivity structure of the crust and mantle in this region, an information of prime importance to constrain the various tectonic evolutionary models already proposed, a number of magnetotelluric soundings have been carried out in recent years across some of the major geotectonic structures in the states of São Paulo, Rio de Janeiro and Minas Gerais (e.g., Figueiredo, 1997; Brito, 1998). However, in the interpretation of these data the authors have not taken into account the influence of remote conductivity contrasts, in this case represented by the adjacent Atlantic ocean.

The extension of the area influenced by a given conductivity anomaly (specially the sea-coast effect)

has been discussed by several workers (e.g., Ranganayaki and Madden, 1980; Menvielle and Tarits, 1994; Monteiro Santos et al., 2001). According to these workers, the electromagnetic field may be significantly distorted by these anomalies over large distances and the horizontal length scale used to quantify this distance is called the adjustment distance (AD). Ignoring such effects in the 2-D modeling of data acquired within the area affected by the coastal effect may introduce severe bias in the whole process of data interpretation.

In this paper, the effects of the ocean on MT data from SE Brazil were tested with the use of simple models and compared with experimental results from a station over the Serra da Mantiqueira plateau in the state of São Paulo.

Two-Dimensional Forward Modeling

A finite element code (Wannamaker et al., 1987) was used to calculate the 2D MT forward responses. The main features of the 2D model used in this discussion is shown in Figure 1, based on available information from geological and geophysical data. The landward conductivity structure is a simplified version of the geoelectrical model derived by Brito (1998) for a profile across the Taubaté Basin in the state of São Paulo. It comprises the following layers:

1. the upper and lower crust is represented by blocks of 10,000 ohm.m, as observed in the 2-D inversion of the above referred Brito's study;
2. a thin layer of 20 m and resistivity of 30 ohm.m (not shown in Figure 1) is included at the top of the upper crustal resistivity block to account for weathered overburden, as defined from AMT studies (Padilha and Vitorello, 1992);

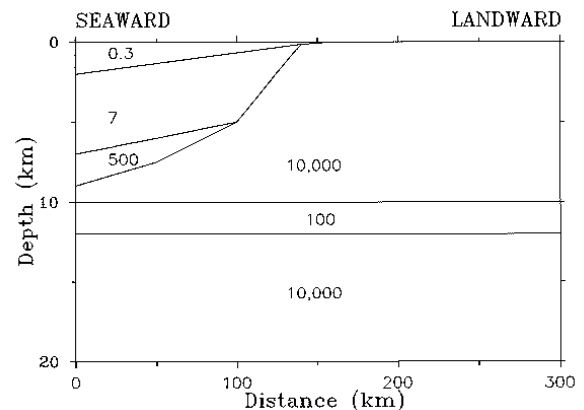


Figure 1 - Generalized 2D model used in this study. Resistivity values are given in ohm.m

Coast Effects on MT Data from SE Brazil

- an enhanced conductivity in the middle crust detected in the Brito's study is represented by a layer of 20 S (thickness of 2 km and resistivity of 100 ohm.m) at a depth of 10 km.

The geoelectrical structure for the oceanward part was derived from available bathymetry and geological/geophysical data for the Santos Basin published by PETROBRÁS's researchers (e.g., Macedo, 1989; Pereira and Feijó, 1994). It includes the following layers:

- the ocean is represented by a layer with resistivity of 0.3 ohm.m and thicknesses reaching 2 km at a distance of 160 km from the coast;
- the sediments in the Santos Basin are represented by a layer with a mean resistivity of 7 ohm.m and a maximum thickness of 5 km close to its depositor (information inferred from induction logs and seismic lines);
- a resistivity layer at the bottom of the sedimentary package, with resistivity of 500 ohm.m and maximum thickness of 2 km, represents salt provinces and volcanic rocks.

Different tests were performed using this basic model, checking the effects of including and excluding certain features. In particular, to test the effects of the ocean, two different models were run, both based

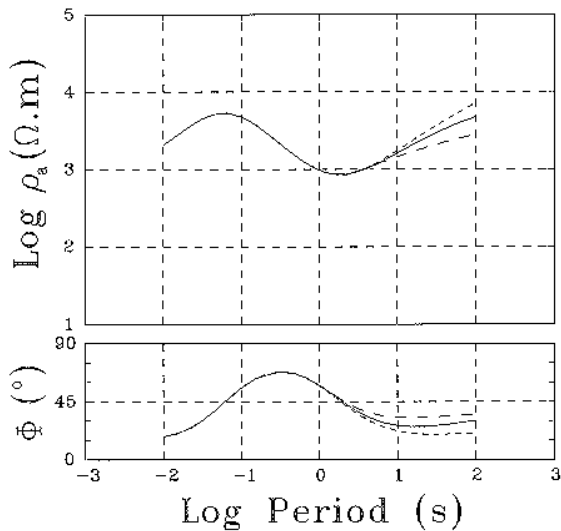


Figure 2 - Comparison of theoretical MT results generated by the 2D model of Figure 1 with and without the ocean at a site 50 km landward from the coast. Continuous line is the response without the ocean, long-dashed line is the TE-mode response with the ocean and short-dashed line is the TM-mode response with the ocean. Upper graph is apparent resistivity and lower graph is impedance phase.

on the model of Figure 1 but one having the ocean and another having no ocean. An example of the results is presented in Figure 2, considering a site at about 50 km landward from the coast. As can be seen in the picture, there is little difference in the response at short periods; beyond a given period (in this example, at about 10 s for apparent resistivity and 3 s for the phase), the curves for the models with and without an ocean differ significantly. In fact, the ocean splits the curves with the TM apparent resistivity curve rising and the TE apparent resistivity curve descending compared to the non-ocean response. The effect is reversed in the phase, which shows higher values for the TE-mode.

Similar calculations have been made considering stations theoretically located at different distances from the coast. The results of these tests are synthesized in Figure 3. It shows the periods at which the coast effects would be seen in apparent resistivity and phase in both modes of propagation of the electromagnetic waves. As already observed in Figure 2, it can be seen that for a given sounding the coast effect always appears at shorter periods in the phase than in the apparent resistivity. Also, the TM-mode is much more affected than the TE-mode in soundings carried out very close to the coast. The latter result can be explained by considering that the TM-mode has a much higher resolution than the TE-mode to sense the electrical charges concentrated parallel to the coast in the conductive sea. The highest resolution of the TM-mode disappears as we move away from the region where the lateral variation in conductivity occurs. In our case, the coast effect is seen at approximately the

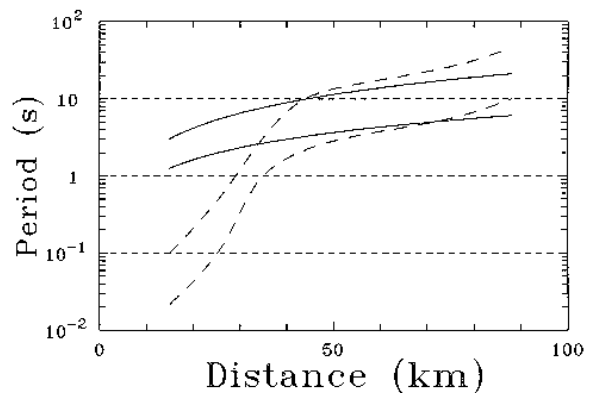


Figure 3 - Periods at which the sea-coast effect is theoretically sensed by the MT data as a function of the distance from the coast. Continuous lines are the TE-mode (upper curve is the effect on the apparent resistivity, lower curve is the effect on the phase) and dashed lines are the TM-mode (upper curve for apparent resistivity, lower curve for the phase).

Coast Effects on MT Data from SE Brazil

same periods in distances around 50 km from the coast.

Comparison with Experimental Data

Figure 4 shows apparent resistivity and phase data for a station located in the Serra da Mantiqueira plateau in the state of São Paulo, about 90 km away from the coast. The MT curves were obtained by using modern techniques for data processing and distortion correction but static shift was not evaluated (see Padua, 2000). The static shift on MT data corresponds to a shift of the apparent resistivities by a period independent multiplicative constant without affecting the phases and is normally generated by near-surface inhomogeneities. As a consequence, the apparent resistivity data shown in Figure 4 can not be used to verify the coast effect in this station.

On the other hand, the phases are not affected by this kind of local distortion. It can be seen that the split between both modes starts in phase at periods of approximately 20 to 30 s. This result and the format of the splitting between the curves is very similar to those foreseeing by the theoretical calculations presented in Figures 2 and 3. The main difference is that

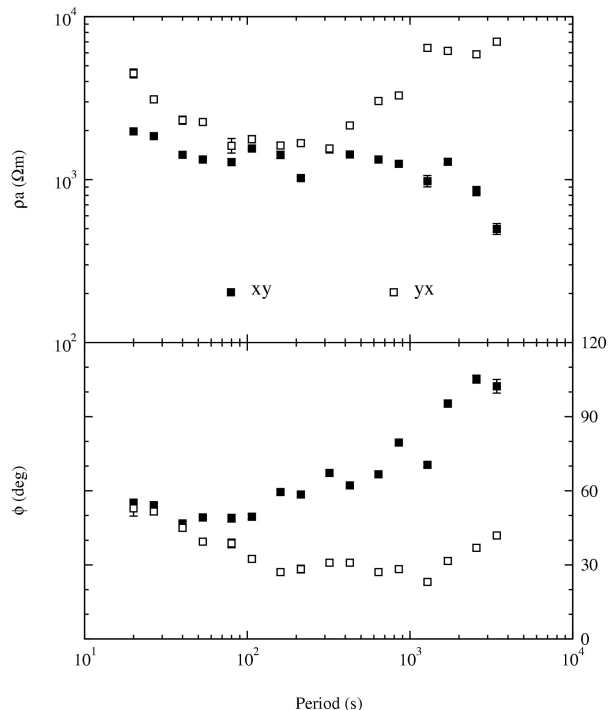


Figure 4 - Experimental apparent resistivities (upper graph) and impedance phases (lower graph) at a site over the Serra da Mantiqueira plateau. Closed symbols refer to TE-mode and open symbols to the TM-mode. Error bars are one standard deviation.

the period at which the effect starts is a little longer than expected (around 10 s). This difference can be explained by subsuperficial variations of conductivity in relation to the homogeneous model of Figure 1, generating a lower contrast of conductivities between the land and the ocean than assumed in the model.

Conclusions

This exercise shows that the sea-coast effect is extremely important on MT data acquired in the Southeastern region of Brazil. Due to the large contrast of conductivities between the sea and the highly resistive rocks of the local crust, the effects extend until very large distances from the coast, much more than reported by similar studies in other regions of the globe. Without correcting or taking into account this effect in the process of data interpretation, it is virtually impossible to study the geoelectrical features sampled by periods larger than tens of seconds (see limits in Figure 3). Probably in a region where the crust is less resistive (as in the case of the state of Rio de Janeiro; Figueiredo, 1997), the effect may be less critical but even so cannot be ignored.

Possible alternatives to minimize the coast effect include the numerical resolution of the problem (see Monteiro Santos et al., 2001) or the inclusion of the sea in the bidimensional modeling of the data. In both cases, however, we will face the difficulty of getting a reasonable model for the distribution of conductivities in the oceanic lithosphere, an information presently not available for this region of the South Atlantic.

References

- Brito, P.M.A., 1998, Sondagens magnetotélúricas transversais à Bacia de Taubaté, MSc Thesis, INPE, 106 p.
- Figueiredo, I., 1997, Investigação magnetotélúrica nas serras do sudeste brasileiro (RJ/MG): Uma proposta de modelo crustal, PhD Thesis, Observatório Nacional/CNPq, 163 p.
- Macedo, J.M., 1989, Evolução tectônica da Bacia de Santos e áreas continentais adjacentes, Boletim de Geociências da Petrobrás, 3, 159-173.
- Menvielle, M., and Tarits, P., 1994, Adjustment of the electromagnetic field distorted by 3-D heterogeneities, *Geophysical Journal International*, 116, 562-570.
- Monteiro Santos, F.A., Nolasco, M., Almeida, E.P., Pous, J., and Mendes-Victor, L.A., 2001, Coast effects on magnetic and magnetotelluric transfer functions and their correction: application to MT soundings carried out in SW Iberia, *Earth and Planetary Science Letters*, 186, 283-295.

Coast Effects on MT Data from SE Brazil

- Padua, M.B., 2000, Estudo experimental de distorções geradas por linhas férreas eletrificadas em sondagens magnetotélúricas, MSc Thesis, INPE, 76 p.
- Padilha, A.L., and Vitorello, Í., 1992, Investigações geoeletricas nas bacias de Taubaté, Volta Redonda e Resende, Expanded Abstracts of the 37th Congresso Brasileiro de Geologia, 2, 403-404.
- Pereira, M.J., and Feijó, F.J., 1994, Bacia de Santos, Boletim de Geociências da Petrobrás, 8, 219-234.
- Ranganayaki, R.P., and Madden, T.R., 1980, Generalized thin sheet analysis in magnetotellurics: an extension of Price's analysis, Geophysical Journal of the Royal Astronomical Society, 60, 445-457.
- Wannamaker, P.E., Stodt, J.A., and Rijo, L., 1987, A stable finite element solution for two-dimensional magnetotelluric modelling, Geophysical Journal of the Royal Astronomical Society, 88, 277-296.

Acknowledgments

This study was supported by research grants from FAPESP (00/00806-5) and fellowships from CNPq (350683/04-8 and 351398/94-5) and FAPESP (99/12381-0).



Crosswell electromagnetic tomography: some results using Born approximation

Licurgo Peixoto de Brito, Universidade Federal do Pará, licurgo@ufpa.br

José Felipe Souza de Almeida, Universidade Federal do Pará, jfelipealmeida@yahoo.com.br

Abstract

A method of crosswell electromagnetic imaging is presented and used to analyze the relevant parameters for electromagnetic tomography. The influence of a punctual inhomogeneity on the magnetic field is calculated through the Sensitivity function based on Born approximation. The analysis of the extremals of that function is applied to generate crosswell images. The method showed that the resolution is very good vertically and very poor horizontally. Images are not affected by increasing the number of receivers and their horizontal alignment with the scatter, but local maxima occur if transmitter and scatter are not horizontally aligned. Furthermore, vertical resolution is improved for increasing number of transmitters and the aperture. These results are in agreement with those well known in electromagnetic tomography literature.

Introduction

Electromagnetic tomography came after the X-ray tomography for diagnostic and seismic tomography. The success of these two imaging methods is partially due to the use of high frequencies for which the ray theory can be applied. For the lower frequencies used in electromagnetic tomography the wave equation is replaced by diffusion equation and the ray theory can not be applied anymore. So comes up the diffusion tomography as mentioned in Zhou et al. (1993). A good review of diffusion tomography can be found in Alumbaugh & Morrison (1995). These authors considered inhomogeneities with a cylindrical symmetry and used an interactive Born scheme to solve the forward problem and the least square technique for the inverse problem. Other possibilities for both forward and inverse problems can be found in Lee & Xie (1993) and Zhou et al. (1993). Because of tomography is computationally expensive it is important to find the relevant parameters and their influence in tomographic images. A simple method of doing so has been developed by Spies & Habashy (1995). They used Born approximation to find the Fréchet Derivatives (called Sensitivity Function) to evaluate the influence of a punctual inhomogeneity having low conductivity contrast with the homogeneous background. The main conclusions obtained by these authors are: 1-The region of the earth contributing to the crosswell electromagnetic response is a quasi-ellipsoidal volume encompassing both source and receiver; 2-The strongest response originates from the immediate vicinity of the source

and receiver; 3-The interwell contribution increases markedly with increasing frequency.

A method to obtain conductivity pseudo-sections from electromagnetic measurements has been presented by Brito (1994). This author defined a Detectability function (Δ) to calculate the influence of inhomogeneities on the electromagnetic field and, using a parametric representation of the geophysical model, analyzed the extremals of Δ . The values of the parameters associated to these extremals were used to build a section of Δ , giving a picture of the conductivity distribution.

In this paper we use the Sensitivity function as calculated by Spies & Habashy (1995) and the imaging method proposed by Brito (1994) to analyse the influence of model parameters on electromagnetic tomographic images.

Earth and electromagnetic system models

The earth is considered as an infinite homogeneous and isotropic background with an inside inhomogeneity. Background conductivity is σ_b and the inhomogeneity conductivity is $\sigma = \sigma_b + \sigma_s$, where σ_s is a perturbation due to the punctual scatter (Fig. 1). Two vertical boreholes are represented by straight dashed lines a distance L apart. Transmitter and receiver can move along these lines. Following Spies & Habashy (1995) the influence of the scatter on the magnetic field was calculated using Born approximation and is given by the Fréchet derivatives there called Sensitivity functions given by

$$F_{zz}(\mathbf{r}; \mathbf{r}_R, \mathbf{r}_T) = i\omega\mu_o I N_T A_T [(x - x_R)(x - x_T) + (y - y_R)(y - y_T)] \times S(\mathbf{r}, \mathbf{r}_R)S(\mathbf{r}, \mathbf{r}_T); \quad (1)$$

$$F_{xz}(\mathbf{r}; \mathbf{r}_R, \mathbf{r}_T) = -i\omega\mu_o I N_T A_T (z - z_R)(x - x_T)S(\mathbf{r}, \mathbf{r}_R)S(\mathbf{r}, \mathbf{r}_T);$$

$$F_{yz}(\mathbf{r}; \mathbf{r}_R, \mathbf{r}_T) = -i\omega\mu_o I N_T A_T (z - z_R)(y - y_T)S(\mathbf{r}, \mathbf{r}_R)S(\mathbf{r}, \mathbf{r}_T);$$

where

$$S(\mathbf{r}, \mathbf{r}') = \frac{e^{ik_b|\mathbf{r}-\mathbf{r}'|}}{4\pi|\mathbf{r}-\mathbf{r}'|^3} [1 - ik_b|\mathbf{r}-\mathbf{r}'|]$$

$$\text{and } |\mathbf{r}-\mathbf{r}'| = [(x-x')^2 + (y-y')^2 + (z-z')^2]^{\frac{1}{2}}.$$

The subscripts zz , xz and yz indicate the direction of the receiver and transmitter axes, respectively.

Because of electromagnetic coupling F_{zz} is the strongest component of the scattered field. Therefore, to outline the method we used, only this function will be considered in this work. Furthermore, we will keep the scatter on the xz plane where it gives the main contribution to the signal.

Crosswell Electromagnetics

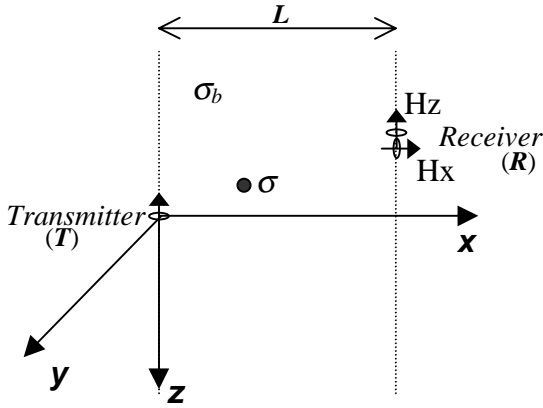


Fig 1 - Earth and electromagnetic model. Vertical dashed lines represent boreholes. The transmitter is a vertical magnetic dipole (z direction) and the receiver can measure both x and z components of the magnetic field. L is the distance between boreholes and σ_b and σ are the background and inhomogeneity conductivities respectively.

A plot of F_{zz} is given in Fig. 2 with an inhomogeneity at a distance $L/2$ from both transmitter and receiver. A parametric representation is made in order to keep the function independent on particular values of geometric and physical properties. The amplitude of F_{zz} is normalized by its maximum value and plotted as function of L/δ , where $\delta = (2/\omega\mu_0\sigma_b)^{1/2}$ is the skin depth of a plane wave in the background media. The parameter L/δ holds three important quantities: the distance between boreholes L , the electric current angular frequency $\omega = 2\pi f$ and the background conductivity σ_b . A number of combinations of these three properties can give the same value for L/δ , leading to the same sensitivity function value, independently of particular values of ω , σ_b and L . Remark that the scattered field vanishes for both low and high values of L/δ reaching the maximum near

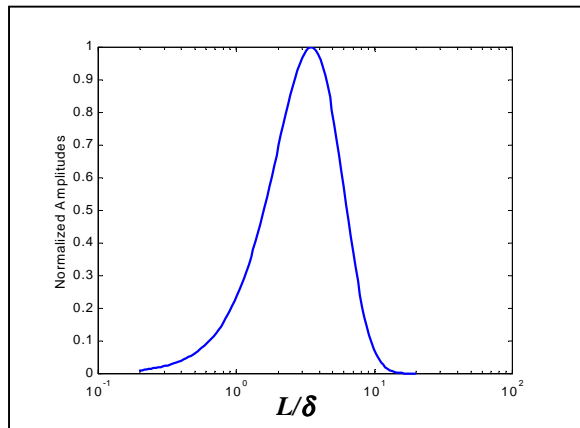


Fig. 2 - Sensitivity function F_{zz} . Normalized amplitude versus L/δ . The scatter is at a distance $L/2$ from both the transmitter and the receiver.

$L/\delta = 3.5$. This means that, for fixed values of L and σ , there is a frequency for which the inhomogeneity gives the maximum contribution to the signal and, for both very low and very high frequencies the scattered field is too small to be considered.

Model parameters

We use a polar coordinate system with the origin on the transmitter to localize both the scatter and the receiver (Fig. 3). Therefore four variables are needed to describe their position: (ρ_r, θ_r) for the receiver and (ρ_h, θ_h) for the heterogeneity. Besides, another variable L links the receiver positions to the distance between boreholes through $L = \rho_r \sin \theta_r$. This way we have five variables to geometrically describe the model.

Besides the geometrical variables two physical properties must be taken into account: the transmitter electric current frequency ω and the background conductivity σ_b .

So we have seven variables to deal with:

ρ_r , θ_r , ρ_h , θ_h , L , σ_b and ω .

It is wise to represent the

Sensitivity function in a parametric form, i.e., as function of dimensionless parameters. This way it will be independent of particular values of the seven variables. The parameters are a set of generalized coordinate defined as:

1 - $\theta = \theta_h/\theta_r \rightarrow$ indicating the angular distance from the inhomogeneity to the receiver.

2 - $\rho = \rho_h/\delta \rightarrow$ relating the frequency to the radial position of the inhomogeneity, for a given background conductivity.

3 - $L/\rho_r = \sin \theta_r \rightarrow$ this parameter is useful only as a constrain to L , ρ_r and θ_r , since they are all known model variables.

Therefore the seven variables are reduced to three dimensionless parameters and the first two are enough to relate the Sensitivity function to the inhomogeneity position.

Fig. 4 shows F_{zz} amplitude as function of θ and ρ for model variables indicated in the caption. Remark the maximum at $\rho_m = 1.7$ and $\theta_m = 1.0$. These values indicate that the inhomogeneity gives the maximum contribution to the signal if located at a distance $\rho_h = 1.7\delta$ from the transmitter and along the straight line from the transmitter to the receiver. Nevertheless, as these results are for a particular scatter position, we

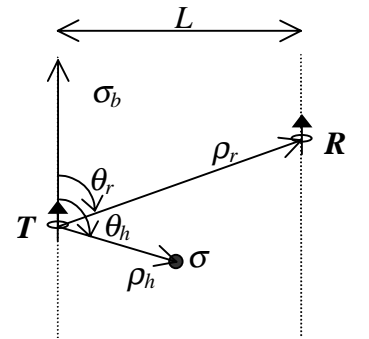


Fig. 3 - Polar coordinate system centered on the transmitter.

Crosswell Electromagnetics

will investigate how these maximum coordinates (ρ_m, θ_m) varies with inhomogeneity position.

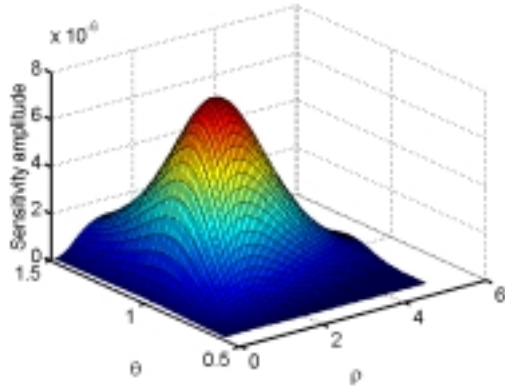


Fig. 4 – Normalized Sensitivity as function of ρ and θ . With $L = 100$ m, $\sigma_b = 0.1$ S/m, $\rho_h = 0.5L$ e $\theta_h = \pi/2$.

Analysis of the maximum of Sensitivity function

The scatter will be moved inside a region to verify how the coordinates of the maximum of F_{zz} will change. A trapezoidal region was taken to fit the polar coordinate system and model (Fig. 5). The vicinity of the wells are not included. They can be investigated by other methods (well logging for instance). The aperture $(1.8L/0.8L = 2.25)$ can be considered large if compared with usual values in electromagnetic tomography (Alumbaugh & Morrison, 1995). The values of ρ_m and θ_m obtained over the entire domain lie in the range $0.3 < \rho_m < 2.8$ and $0.53 < \theta_m < 1.41$ and its mean values are 1.6 and 0.97, respectively.

The mean values of ρ_m and θ_m will now be used to built Sensitivity sections.

Building Sensitivity sections

A single inhomogeneity is used in this work because Born approximation can not hold for 2 or more scatters. Additionally a single one is enough to establish the steps of building Sensitivity function sections.

We consider a small scatter in the region interwells. The background conductivity is assumed to be *a priori* known. A set of Sensitivity function (F_{zz})

values are obtained by varying the positions of transmitter (r_T) and receiver (r_R) and the frequency (ω). Each value of F_{zz} is then associated to a position (ρ_i, θ_i) , where

$$\rho_i = \rho_m \delta \text{ and } \theta_i = \theta_m \theta_r. \quad (2)$$

The coordinates ρ_i and θ_i replace ρ_h and θ_h , respectively, on the parameters ρ and θ . Furthermore ρ_m and θ_m are the values of ρ and θ corresponding to the maximum of F_{zz} . As seen in the previous section ρ_m and θ_m lie in a range, so associating F_{zz} to them through equations (2) means to define a region where the punctual heterogeneity must lie to give its maximum contribution to the signal. That region is called *main zone* (Brito, 1994). Using the mean values of ρ_m and θ_m in equations (2) is equivalent to set the inhomogeneity on the center of that zone. This center point is called *main zone center*.

The values of F_{zz} calculated from eq. (1) and associated to each corresponding position by eq. (2) can be plotted as seen in Fig. 6. Cartesian coordinates are now used for easy interpretation. The values of the model properties are given in the figure caption.

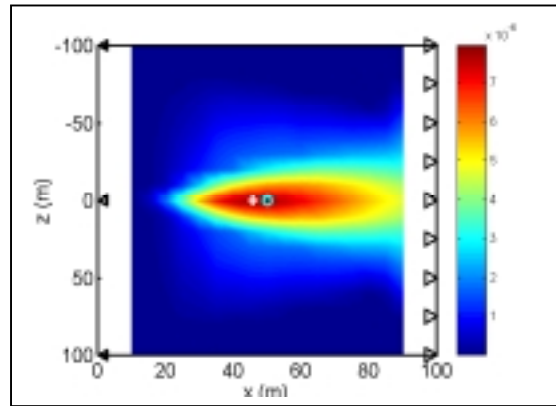


Fig. 6 – Sensitivity function mapping for the model represented in Fig. 1. With $L = 100$ m and $\sigma_b = 0.1$ S/m. The inhomogeneity position is showed by \odot and the maximum value of F_{zz} is indicated by +. The 3 transmitter and 9 receiver positions are marked on the left and right axes respectively.

Remark that F_{zz} vanishes as the distance from the inhomogeneity increases. On the other hand, the maximum Sensitivity value is close to the position of the inhomogeneity. It is for this reason that Sensitivity maps are similar to conductivity images. In this case there is no difference on the z coordinates of both scatter and maximum F_{zz} . Other models with different number of transmitter and receivers, and other heterogeneity positioning show small differences on these coordinates. This means that the

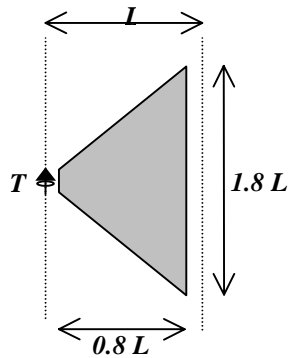


Fig. 5 – Trapezoidal domain for inhomogeneity positioning.

Crosswell Electromagnetics

vertical resolution of this imaging method is very good. On the x axis the difference is much greater than on z axis (see also Fig. 7). Hence the horizontal resolution is very poor. These results are similar to those found in electromagnetic tomography (Alumbaugh & Morrison, 1995, Zou et al., 1993). Even greatly increasing the number of transmitters the horizontal resolution can only be slightly improved (Almeida, 1999)

Data in Fig. 7 differs from those on Fig. 6 only by the number of receivers and the inhomogeneity position. As we can see, the vertical position of the maximum F_{zz} has no influence of the number of receivers. The same result appears in a number of other models not shown in this paper (Almeida, 1999). The difference between the inhomogeneity and F_{zz} maximum horizontal positions is not due to the increase number of receivers but only due to the poor horizontal resolution of the method.

The number and position of the transmitters have much greater influence on F_{zz} images than the receivers. Fig. 8 shows an example with two local maxima arising because there is no transmitter on the horizontal straight line passing over the scatter and a receiver. Nevertheless, vertical positioning of the F_{zz} maxima is still good.

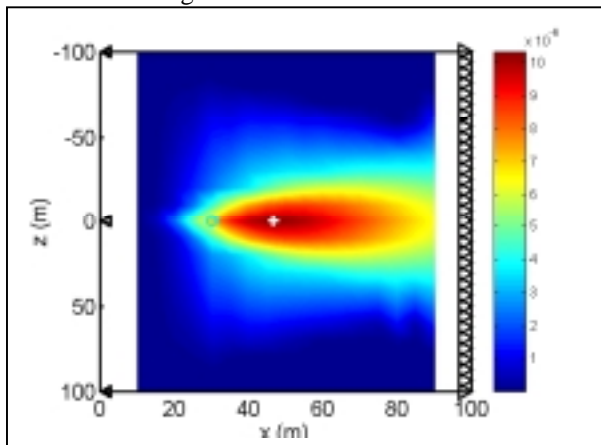


Fig. 7 – Same model as the one in Fig. 6 except by the inhomogeneity position and of using 33 instead of 9 receivers.

Conclusion

The imaging method showed in this paper indicates that the vertical resolution for detecting small conductive bodies by crosswell electromagnetics is very good, while the horizontal resolution is very poor. These results are similar to those obtained by the electromagnetic tomography as can be found in the cited literature. The number of receivers and their horizontal alignment with the scatter doesn't make any significant difference on the image quality or

resolutions. On the other hand, two or more maxima can occur if there is no transmitters horizontally aligned with the scatter. Finally, these results obtained in a quite simple way, can give some insight to constrain the parameters in a more expensive procedure such as inversion techniques.

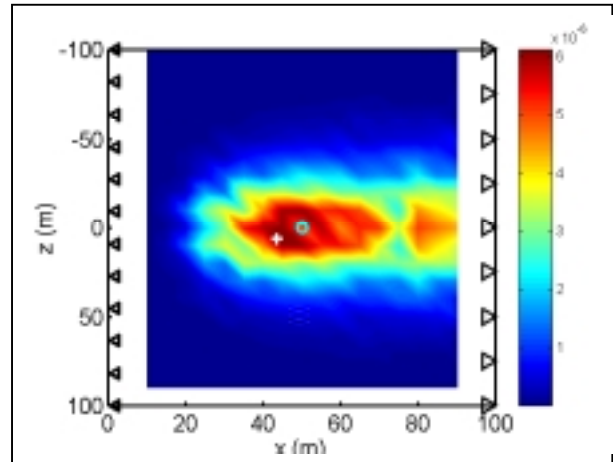


Fig. 8 – Same model as Fig. 6 now using 12 transmitters

Acknowledgement

The first author thanks to Departamento de Física da Universidade Federal do Pará (UFPA), by his partial time dedicated to the research. The second author thanks to CAPES by the financial support for his master thesis.

References

- Almeida, J. F. S., 1999. Aplicação da função Sensitividade na análise de medidas eletromagnéticas poço-a-poço. Belém: Dissertação de mestrado/UFPA. 1999. 34p.
- Alumbaugh, D. L., Morrison, H. F., 1995, Theoretical and practical considerations for crosswell electromagnetic tomography assuming a cylindrical geometry: *Geophysics*, 60, 3, 846-870.
- Brito, L. P., 1994, Região do espaço que mais influencia em medidas eletromagnéticas no domínio da frequência: caso de uma linha de corrente sobre um semi-espaço condutor. Belém: Tese de doutorado/UFPA. 1994. 128p.
- Lee, K. H., Xie, G., 1993, A New approach to imaging with low frequency electromagnetic field: *Geophysics*, 58, 6, 780-796.
- Spies, B. R., Habashy, T. M., 1995, Sensitivity analysis of crosswell electromagnetics: *Geophysics*, 60, 3, 834-845.
- Zhou, Q., Becker, A., Morrison, H. F., 1993, Audio-frequency electromagnetic tomography in 2-D: *Geophysics*, 58, 4, 482-495.



Desenvolvimento de um Sistema HLEM de Campo Magnético Induzido, no Domínio da Frequência, para Prospecção Mineral

Cristiano da Silva Marcolino¹, Francisco Yukio Hiodo¹, Carlos Alberto Mendonça¹

¹Instituto de Astronomia, Geofísica e Ciências Atmosféricas da USP - Email:marcolin@hotmail.com

Abstract

An electromagnetic system was developed using some parts of an old Slingram ABEM EM35/88 as transmitter and receiver coils and matching transformers. Modern circuits with low noise lock-in amplifiers and analog multiplier were used to detect signal from a high magnetic permeability receiver coil. In phase and quadrature voltage of lock-in amplifiers outputs were achieved using square waveform reference from the transmitter coil circuit. Comparison of these voltage by a precise analog multiplier give us the electrical apparent conductive of the overburden layer (conductor). One third lock-in circuit was used to adjust the spacing intercoil by nulling the total field component.

Introdução

Um sistema eletromagnético no domínio da frequência foi desenvolvido, usando-se componentes de um antigo sistema ABEM GUN 35/88. A reutilização de partes tais como a bobina transmissora e o transformador de acoplamento do estágio de potência do circuito de geração de sinal do módulo transmissor, e a bobina receptora, permitiu reduzir os custos do projeto, sendo que os componentes eletrônicos usados são comumente usados na área de eletrônica digital e analógica.

O sistema descrito funciona com duas frequências diferentes, de 880 e 3520 Hz.

Descrição do Método

O sistema eletromagnético EM35/88 baseia-se no princípio de que, quando um condutor elétrico é submetido a um campo magnético alternado, uma corrente secundária circula pelo mesmo. Por sua vez, esta corrente produz um campo magnético secundário que somado vetorialmente ao campo primário gera um campo total na bobina receptora, de amplitude e fase diferentes do campo primário aplicado. A composição dos dois campos gera uma elipse de polarização (Grant & West, 1965) característica, em cada ponto da superfície. A medida das componentes em fase e em quadratura do campo secundário permite caracterizar os parâmetros da elipse de polarização, que indica a presença de um condutor (soterrado) ou de uma descontinuidade lateral.

Segundo McNeill (1980), a razão entre os campos secundário e primário pode ser dada em função da condutividade elétrica aparente e de algumas constantes representadas abaixo:

$$\frac{H_s}{H_p} \approx \frac{i\omega\mu_0\sigma s^2}{4}$$

sendo:

H_s = campo secundário na bobina receptora

H_p = campo primário na bobina transmissora

$\omega=2\pi f$

f = frequência (Hz)

μ_0 = permeabilidade no vácuo

σ =condutividade aparente do solo

s = espaçamento entre bobinas (m)

$i= \sqrt{-1}$

Uma das vantagens do método eletromagnético, em relação a outros métodos geofísicos (eletroresistividade, p. ex.), é que as medidas de campo são mais rápidas, necessitando apenas de duas pessoas para operá-lo.

Medidas das Componentes Real e Imaginária

Para as medidas de intensidades relativas das componentes real e imaginária, deve-se ter 2 sinais de referência: um em fase e outro em quadratura, com o sinal transmitido. Na prática o transmissor está conectado ao receptor por um cabo coaxial que transporta o sinal de referência senoidal, sem interferência. As técnicas de detecção e tratamento do sinal usadas atualmente, decorreram do desenvolvimento do método proposto, por Sundberg (1936).

Descrição do Transmissor

O transmissor funciona do seguinte modo: um circuito gerador fornece um sinal quadrado simétrico, que é amplificado por um circuito amplificador classe B constituído de dois transformadores (entrada e saída), e então injetado na bobina transmissora. A sintonia do circuito LC paralelo é feita pelo ajuste de C. Para que o sinal de saída tenha amplitude máxima e o consumo de corrente seja o menor possível, o indutor (bobina

Projeto de um equipamento de campo magnético induzido para prospecção mineral

transmissora) deve estar em ressonância com o capacitor C. O diagrama de blocos do transmissor encontra-se na Fig 1.

Do equipamento transmissor original restaram apenas a bobina transmissora de núcleo de ferrite de alta permeabilidade magnética e o transformador 2 (TRAFO 2). O transformador 1 (TRAFO 1) com derivação central no secundário foi adquirido no comércio e é normalmente usado em circuitos de áudio.

Pelo fato de ter sido aproveitada a bobina transmissora do antigo equipamento decidiu-se usar também as frequências originais de 880 Hz e 3520Hz, pois a bobina foi projetada para esta faixa de frequência. A construção de uma nova com núcleo de ar seria conveniente do ponto de vista prático, pois poderia ser enrolada no formato “bambolê”, possibilitando outros arranjos além do horizontal coplanar.

O gerador de sinal é constituído por um oscilador de frequência ajustável, que fornece uma onda quadrada de frequência 14080 Hz, e de quatro divisores de frequência que dividem a frequência por dois, sequencialmente.

O sinal digital de saída é aplicado a dois amplificadores operacionais com ganho em malha aberta, que excitam o transformador 1 (TRAFO 1).

Para excitação da bobina transmissora no modo ressonante, foi construído um amplificador de potência push-pull classe B usando dois transistores NPN TIP31 alimentados com 12V. Além dos transistores também fazem parte do circuito o transformador de acoplamento com núcleo de alta permeabilidade do equipamento original TRAFO2, e o transformador 1 (TRAFO1). Esta configuração foi adotada devido à limitação de tensão (12 VDC) no campo.

Na saída do amplificador de potência é conectado um capacitor de poliéster C, em paralelo com a bobina transmissora L, para sintonia fina do circuito LC, na frequência de operação. Após ajuste, a tensão nos terminais da bobina atinge aproximadamente 250 volts.

Descrição do Receptor

A bobina receptora é constituída de um enrolamento de 4000 espiras de fio AWG 26 sobre um núcleo de permalloy de permeabilidade próxima de 20000. Envolvendo este conjunto, há uma folha de Cu aterrada com o terra dos circuitos analógicos de detecção, para atenuar o ruído originado dos esféricos e das ondas eletromagnéticas (radiofrequência).

A saída da bobina receptora é conectada ao primário do transformador cuja impedância de entrada é aproximadamente igual a do enrolamento da bobina. A saída deste transformador está acoplada a um amplificador diferencial de ganho 100 vezes, seguido de amplificador inversor de ganho ajustável, que perfazem um ganho máximo de 80 dB. Em seguida, o sinal é tratado por um filtro ativo rejeição (notch), tipo duplo T, centrado em 60 Hz, para atenuar o ruído de linha. Então, o sinal é derivado para 3 circuitos, fundamentados no detector sensível a fase DSF controlados pelos sinais em fase e em quadratura (defasado de $\pi/2$), com a tensão de referência proveniente do transmissor.

O primeiro DSF1 é chaveado pelo sinal proveniente do transformador conectado ao cabo coaxial de referência, que conduz o sinal de um solenóide (5 espiras) enrolado ao redor da bobina transmissora, até o receptor. Este transformador de acoplamento efetua o casamento de impedância, que permite a transferência máxima do sinal, reduzindo os efeitos do ruído, sem distorcer o sinal. Antes de ser aplicado aos DSF, o sinal senoidal é corrigido em fase por filtros ativos tipo all-pass de atraso ajustável de 0 a 2π , e então quadrado por circuitos comparadores de tensão. Estes circuitos são ajustados para fornecer os sinais em fase e em quadratura, para os 3 circuitos DSF.

O sinal de referência em fase é usado para demodulação síncrona DSF1 do sinal total resultante da composição vetorial dos campos primário e secundário. A tensão de saída é proporcional a amplitude do campo primário na bobina receptora.

Com o sinal em quadratura, o circuito DSF2 procede ao chaveamento do sinal decorrente do campo total, separando a componente secundária (imaginária) do campo total. O sinal de saída é proporcional a amplitude do campo secundário na bobina detectora. Como a amplitude do sinal de saída de DSF2 é cerca de 1000 vezes inferior ao de DSF1, ele deve ser amplificado de 60 dB, antes de ser tratado pelo estágio seguinte, que consiste de um multiplicador analógico.

As tensões nas saídas dos demoduladores síncronos DSF2 e DSF1 correspondentes às componentes em quadratura (campo secundário H_s) e em fase (campo primário H_p) são divididas no modo analógico pelo circuito multiplicador AD534, cujo sinal de saída é proporcional à condutividade elétrica aparente do alvo em subsuperfície.

Atualmente, o equipamento desenvolvido está sendo preparado para operações de campo, juntamente com o Geonics EM-34.

Projeto de um equipamento de campo magnético induzido para prospecção mineral

Bibliografia

Beck A. E., 1991. Physical Principles of Exploration Methods. Wuerz Publishing Ltd.

Fonseca, N.R.M., 1979. Equipamento Eletromagnético para Prospecção Geofísica e Modelamento Reduzido. Dissertação de Mestrado, UFPa-NCGG, pp 64.

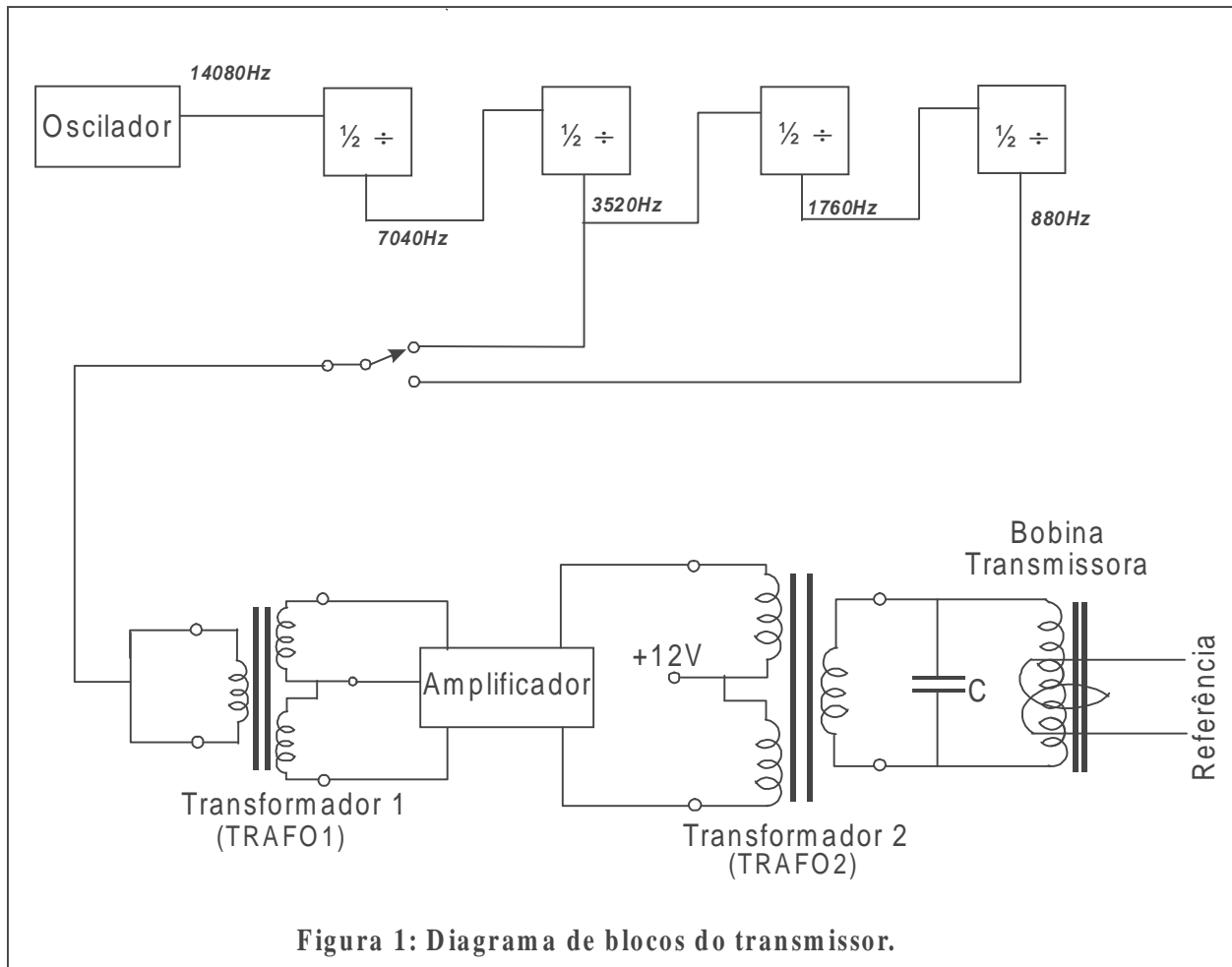
Grant, F. S. & West, G. F. 1965. Interpretation Theory in Applied Geophysics (McGraw-Hill)

MacNeil, J., 1980. Eletromagnetic Terrain Conductivity Measurement at Low Induction Numbers. Geonics Limited Technical Note TN-6.

Nabighian, M., 1988. Electromagnetic Methods in Applied Geophysics. Society of Exploration Geophysicists.

Silva, R.C.A & Verma, O.M., 1997- Anomalias Eletromagnéticas de Corpos Inclinados em Contacto com o Manto. 5º Congresso Internacional da SBGf, São Paulo.

Sundberg, K. 1936. Principles of the Swedish Geoletrical Methods. Reprinted from Ergänzungs-Hefte fur angewandte Geophysik, 199-361.



Projeto de um equipamento de campo magnético induzido para prospecção mineral

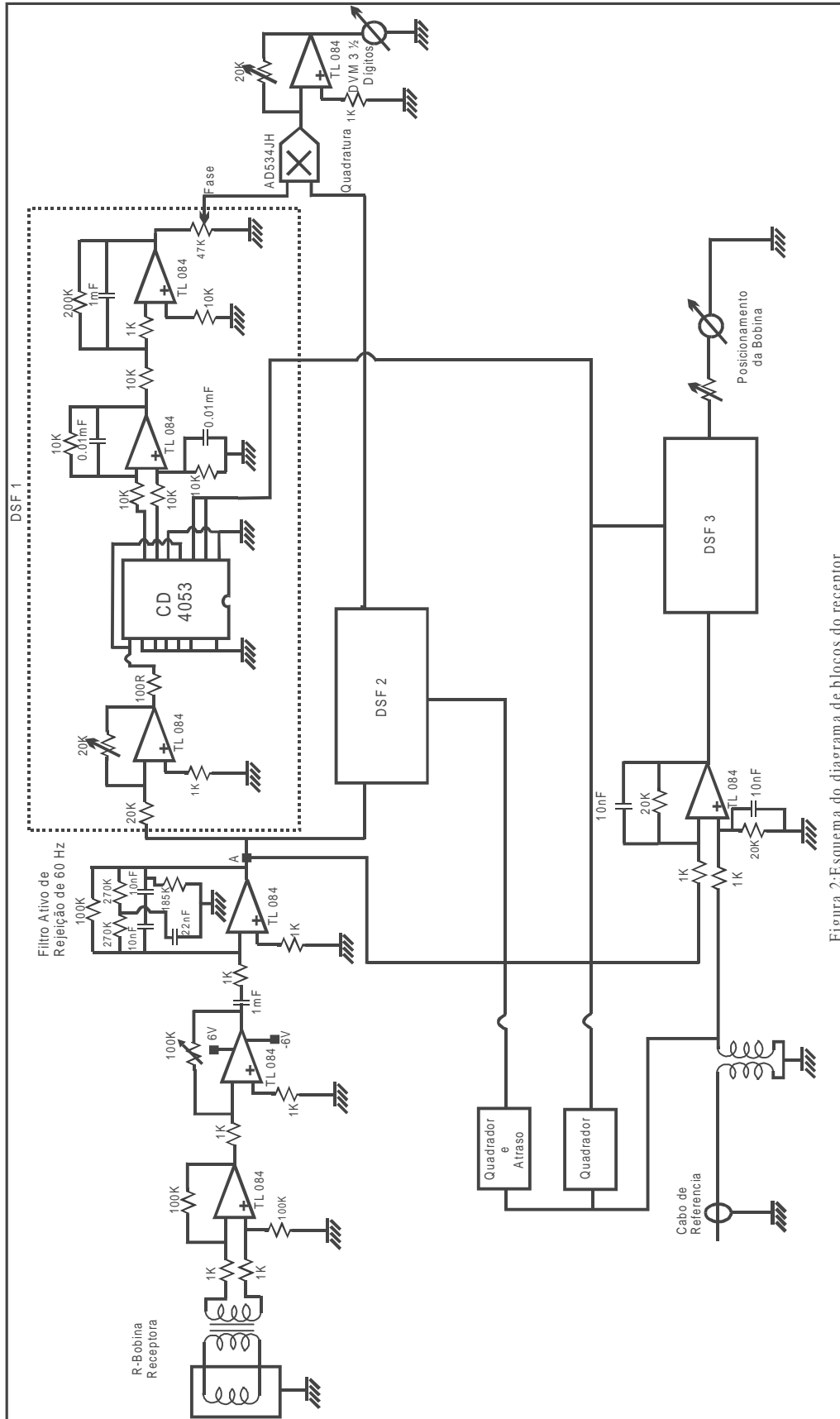


Figura 2: Esquema do diagrama de blocos do receptor



Dual-mode MT static shift correction using in-loop and single-loop TEM data

Max A. Meju*

* University of Leicester, Leicester LE1 7RH, United Kingdom. email:mxw@leicester.ac.uk

Abstract

Accurate removal of static shifts caused by near-surface heterogeneities in dual-mode magnetotelluric (MT) apparent resistivity sounding curves in complex geological terrains is an outstanding problem in MT data analysis. Using field examples, it is shown that the in-loop and single-loop TEM curves vary in the same manner as transverse electric and transverse magnetic mode MT apparent resistivity curves over 2D geological terrains. This suggests that dual-mode TEM data can be used to effectively remove static shift in MT sounding curves leaving only those signatures due to electromagnetic induction in larger local and regional structures that may then be reliably modelled using existing multi-dimensional interpretation schemes.

Introduction

The identification and accurate removal of static shifts caused by near-surface heterogeneities (e.g., Berdichevsky and Dmitriev, 1976) in dual-mode magnetotelluric (MT) apparent resistivity sounding curves in complex geological terrains are outstanding problems in MT data analysis and limit model resolution to a large extent. Partial remedies to the problem are provided by novel tensor decomposition and distortion tensor stripping techniques (e.g., Bahr, 1988; Groom and Bailey, 1989; Groom and Bahr, 1992), spatial filtering (e.g., Torres-Verdin and Bostick, 1992), statistical processing with regularized inversion (e.g., deGroot-Hedlin, 1991), three-dimensional modelling (e.g., Park, 1985) and apparent resistivity curve shifting using transient electromagnetic (TEM) constraints (e.g., Sternberg et al., 1988; Pellerin and Hohmann, 1990). Interestingly, joint processing of TEM and MT data is currently considered to be the most promising approach to MT static shift correction (Singer, 1992) and is based on the use of *a priori* constraints furnished by auxiliary magnetic field measurements (Larsen, 1977).

However, TEM-based studies of MT static shift correction (Sternberg et al., 1988; Pellerin and Hohmann, 1990; Meju, 1996) have so far focused on central-loop TEM soundings and the

prescribed remedies are mostly effective in simple layered earth media. Steep geological structures are common in many prospective terrains and there is no unequivocal method of correcting the usual dual-mode tensorial MT sounding curves. For example, Sternberg et al. (1988) noted that while the central-loop TEM apparent resistivity curves may serve for correcting overlapping statically shifted MT curves of similar shapes, the TEM curve may agree with the transverse electric (TE) MT polarization at one site but with the transverse magnetic (TM) polarization at another site and so did not find a very consistent pattern between the signatures of central-loop TEM and a given MT polarization. The method suggested by Pellerin and Hohmann (1990) for static shift affecting the responses of a deep-lying 3-D target embedded in a layered host could correct the locally longitudinal MT apparent resistivity curve but provides little information on the correct position of the latitudinal (orthogonal) apparent resistivity curve. It will be highly desirable in such cases to find an effective method for correcting the MT responses in both directions to their true positions without having to rely on the assumption that both curves will converge at some high frequency. Meju (1996) suggested that simultaneous 2D interpretation of dual-mode MT phase data with central-loop TEM constraints would solve the static shift problem in an area with a dominant structural strike providing that 1D conditions prevail above the anomalous structure and the TEM recordings are at sufficiently early times to ensure true 1D response. Unfortunately, in many complex terrains of current exploration interest (e.g., strongly deformed Archaean greenstone belts and overthrust carbonate environments) the outcropping crystalline basement rocks or thrust wedges may be steeply dipping so that the suggested central-loop based strategy will not always hold good.

The aim of this paper is to demonstrate that combined in-loop and single-loop TEM apparent resistivity data can be used to effectively remove static shifts in dual-mode MT soundings in

complex 2D environments. In the comparative graphical approach to be adopted here, it is necessary to present the TEM and MT field responses using an approximate common-scale (Meju, 1996) which relates MT wave period T (in seconds) and TEM transient decay time t (in seconds) in the form $T = 3.9t$. The TEM responses have been adjusted for transmitter turn-off effects and the all-time TEM apparent resistivity approximation (e.g., Bai and Meju, 2000) is adopted in this paper.

Example of correction of dual-mode MT field data

The Kenya Rift Valley (Figure 1) is part of the East African rift system, a continental-scale feature with major rift boundary faults at the margins yielding distinctive linear structures set within a complex of sutured Precambrian basement and younger intrusive components. Sections of it trend approximately north-south and have been the subject of recent TEM-MT studies (e.g., Simpson et al., 1997). It is an excellent natural laboratory for testing the hypothesis that dual-mode TEM data can be used

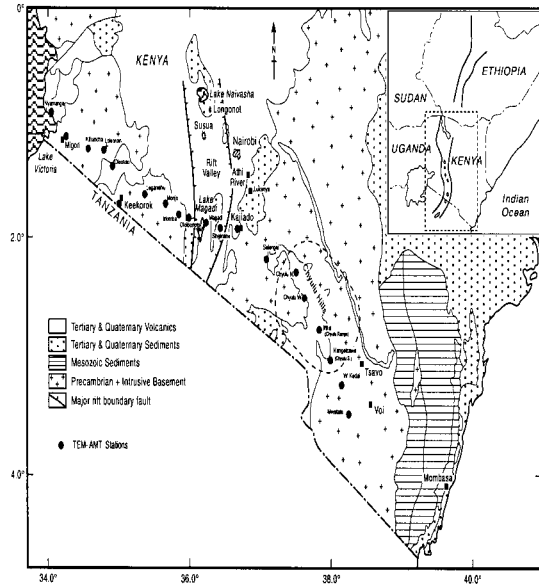


Figure 1. Geology and TEM-MT site location map for the Kenya rift valley survey.

for correcting static shift in orthogonal MT sounding curves in strongly deformed cratonic settings. Several dual-mode TEM and MT data were recorded in 1995 across the rift valley using 100 m telluric lines and 100 m-sided TEM loops. Sample sounding curves for sites located on the

various tectonic terrains along the survey line are shown in Figure 2. Since the main rift is approximately north-south in the survey locality and the declination of the geomagnetic field is about 1.5° east of geographic north, the MT north-south and east-west sounding curves serve as the TE and TM mode data. Notice that the central-loop curves resemble the MT TE polarization while the single-loop curves resemble the TM polarisation responses.

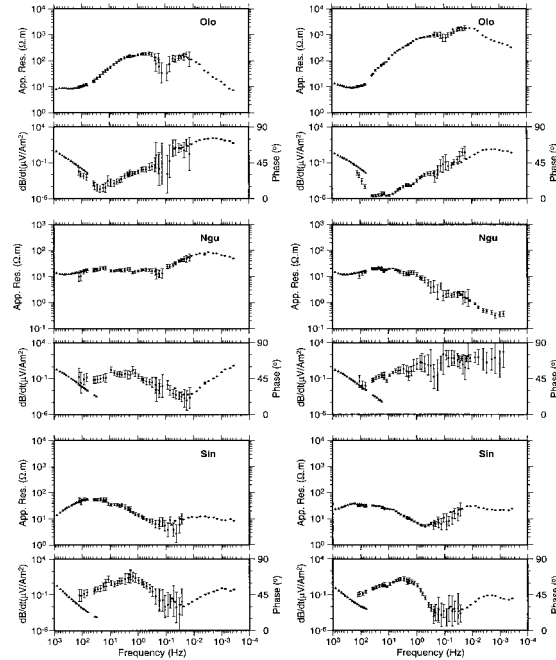


Figure 2. Comparison of dual-mode TEM and dual-mode MT data from representative stations across the Kenya Rift valley.

Note that there is abundant field evidence from several other geological terrains in support of this consistent response pattern. For example, a similar response pattern was seen in the data acquired in Parnaiba basin in northeast Brazil (see Meju et al., 1999, Figure 6). Numerous survey lines were recently recorded in the basin and transect major faults and grabens. The TEM single-loop data were found to be similar in shape to the TM mode MT curves while the central-loop data agreed with the TE mode curves.

Finally, an investigation of static shifts in AMT will not be complete without a treatment of the classic and highly powerful CSAMT method even though it typically yields single-mode data; a brief discussion of the implication of the proposed dual-mode procedure for static shift

correction in CSAMT soundings is given next using an example from an Archaean greenstone belt in Brazil, bearing in mind that such belts are important sources of gold.

CSAMT single-mode measurements across steep structures in Bahia state

Some state-of-the-art commercial CSAMT field systems often incorporate a narrow-bandwidth TEM unit for static correction. Since CSAMT data are typically acquired in the TM mode (across geological strike), it is important to determine the optimum or appropriate TEM field configuration for static correction in such cases. From the case studies presented above, it is obvious that the single-loop TEM method has the best potential for static corrections of TM mode data acquired over strongly linear structures. Hence, Meju and Fontes (1997)

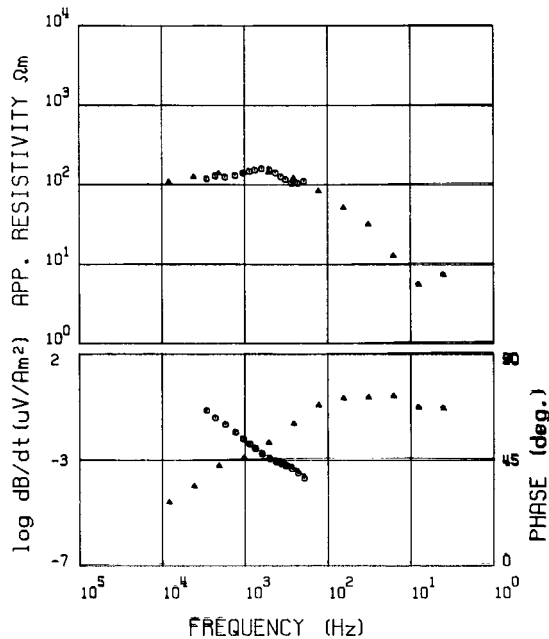


Figure 3. Comparison of single-loop TEM and TM mode MT data from Fazenda Brasileiro.

conducted only single-loop TEM soundings at CSAMT stations in the Archaean Itapicuru greenstone belt in Bahia State of Brazil where the local geology is dominated by steeply oriented geological structures with a dominant structural trend (see Palacky and Sena, 1979, fig. 1). Sample data are shown in Figure 3 for a station along one survey line. It was found that the single-loop TEM data matched the CSAMT measurements along the line surveyed in 1996. I therefore suggest that single-loop data are the

logical compliment to CSAMT (TM mode) data in surveys across such steep crystalline structures.

Conclusion

Accurate removal of static shifts caused by small-size surficial heterogeneous bodies in complex 2D geological structures is still an unresolved problem in magnetotelluric prospecting. It has been demonstrated that in-loop and single-loop TEM sounding curves vary in the same manner as the transverse electric and transverse magnetic MT apparent resistivity curves in 2D geological terrains. It is thus possible to use dual-mode TEM curves to correct for static shifts in dual-mode MT or CSMT data from coincident sounding locations.

References

- Bahr, K., 1988, Interpretation of the magnetotelluric impedance tensor Regional induction and local telluric distortion: *J. Geophys.*, **62**, 119-127.
- Bai, D., & Meju, M.A., 2000. All-time apparent resistivity for transient electromagnetic method, *Presented at IAGA 15th Workshop on Electromagnetic Induction in the Earth, Cabo Frio, Brazil*, Aug. 19-26, 2000. p.33.
- Berdichevsky, M. N. & Dmitriev, V. I., 1976. Distortion of magnetic and electric fields by near-surface lateral inhomogeneities, *Acta Geodaet. Geophys. et Montanist. Acad. Sci. Hung.*, **11**, 447-483.
- deGroot-Hedlin, C., 1991, Removal of static shift in two dimensions by regularized inversion: *Geophysics*, **56**, 2102-2106.
- Groom, R.W. and Bailey, R.C., 1989, Decomposition of magnetotelluric impedance tensor in the presence of local three-dimensional galvanic distortion: *J. Geophys. Res.*, **94**, 1913-1925.
- Groom, R.W. and Bahr, K., 1992, Corrections for near-surface effects: Decomposition of the magnetotelluric impedance tensor and scaling corrections for regional resistivities: A tutorial: *Surv. Geophys.*, **13**, 341-379.
- Larsen, J. C., 1977, Removal of local surface conductivity effects from low frequency mantle response curves: *Acta Geodaet. Geophys. et Montanist. Acad. Sci. Hung.*, **12**, 183-186.
- Meju, M.A., 1996, Joint inversion of TEM and distorted MT soundings: Some effective practical considerations: *Geophysics*, **61**, 56-65.
- Meju, M. A. and Fontes, S.L., 1997, Preliminary

- evaluation of combined TEM-CSAMT methods over the Pau-a-Pique sub-area of the Fazenda Brasileiro Mine, Brazil: Technical Report for CVRD/DOCEGEO, Salvador, Brazil. Feb. 1997.
- Meju, M. A., Fontes, S.L., Oliveira, M.F.B., Lima, J.P.R., Ulugergerli, E.U. & Carrasquilla, A. A., 1999. Regional aquifer mapping using combined VES-TEM-AMT/EMAP methods in the semi-arid eastern margin of Parnaiba Basin, Brazil, *Geophysics*, **64**, 337-356.
- Palacky, G.J. and Sena, F.O., 1979, Conductor identification in tropical terrains - Case histories from the Itapicuru greenstone belt, Bahia, Brazil: *Geophysics*, **44**, 1941-1962.
- Park, S. K., 1985, Distortion of magnetotelluric sounding curves by three-dimensional structures: *Geophysics*, **50**, 786-797.
- Pellerin, L. and Hohmann, G.W., 1990, Transient electromagnetic inversion: A remedy for MT static shifts: *Geophysics*, **55**, 1242-1250.
- Simpson, F.L., Haak, V., Khan, M.A., Sakkas, V., and Meju, M.A., 1997, The KRISP-94 MT survey of early 1995: first results: *Tectonophysics*, **278**, 261-272.
- Singer, M. Sh., 1992, Correction for distortions of MT fields: Limits of validity of the static approach: *Surv. Geophys.*, **13**, 309-340.
- Sternberg, B. K., Washburne, J. C. and Pellerin, L., 1988, Correction for the static shift in MT using transient electromagnetic soundings: *Geophysics*, **53**, 1459-1468.
- Torres-Verdin, C. and Bostick, F.X., 1992, Principles of spatial surface electric field filtering in magnetotellurics: Electromagnetic array profiling(EMAP): *Geophysics*, **57**, 603-622.

Electromagnetic Tomography with Absolute Constrains

Victor Cezar T. de Souza, Luiz Rijo, João J. Baptista, UNIVERSIDADE FEDERAL DO PARÁ, Brazil
 victocantins@globo.com, rijo@amazon.com.br

Abstract

An iterative inversion process is employed to analyze the incorporation of absolute constrains to obtain high resolution image of cross-well electromagnetic (EM) tomography. The image scheme assumes a cylindrical symmetry about vertical magnetic dipole sources and employs the finite element method to solve the scattered EM fields by anomalous conductivity imbedded in an homogeneous background. Images of illustrative models show that to obtain relevant results of inversion process, we have to incorporate absolute constrains for the first guess and also on the borders of model, to guarantee the convergence to experimental model. The resolution of method is examined through changing of frequency and conductivity contrast between the targets and the background. Reconstructed models show that, at low conductivity contrasts, the resolution improves with increasing frequency. On the other hand, for one given frequency, large contrasts make the resolution deteriorates. However when the frequency is decreased, the quality of image improves.

Introduction

With the advent of cross-hole seismic technology in the 1980's, a new generation of high resolution geophysical tools have become available for reservoir characterization. Recently the interest in cross-well methods has also extends to EM method for imaging inter-well electrical conductivity, due to improvements in field instrumentation, computing power and methods of interpretation. The principal goal of this method is to obtain high resolution images of subsurface electrical conductivity distribution, which is a vital information for deducing geological structure, rock porosity, fluid saturation and fracture orientation. However, the most promising area for using cross-well EM is to monitor processes which alter the physical properties of subsurface, like in enhanced oil recovery (EOR) projects. The image process usually implies making measurements of EM fields, in this case, at multiple receiver locations which are produced by sources at various other location. These measured fields are directly converted into a electrical conductivity spatial distribution using some type of tomographic reconstruction process or numerical inversion. We showed that to obtain reasonable image of conductivity distribution we have to add constrains to regular the process of inversion. Also we analyzed the influence of frequency, and of conductivity contrasts

between the background and the targets (anomalous bodies to the background) on reconstructed images.

The Geometry Model

Following the work of Alumbaugh and Morrison (1995). The geometry consists of a cylindrically symmetric region imbedded in an homogeneous background of electrical conductivity σ^P , as shown in Figure 1. The harmonic magnetic dipole sources are located in a borehole at $r=0$ and $z=z_{tx}$ on the axis of symmetry. If the anomalous conductivity $\sigma(r, z)$ is distributed symmetrically about this axis, then electric currents induced by the sources can exist only in the azimuthal direction, therefore exciting just TE mode. These currents in turn produce magnetic fields in the \hat{r} and \hat{z} directions which can be measured in a second borehole some distance away. This geometry has been employed here because it significantly simplifies the inversion process by reducing the full 3-D tensor equation to a 2-D scalar form. Thus, we get a slice of the 3-D model.

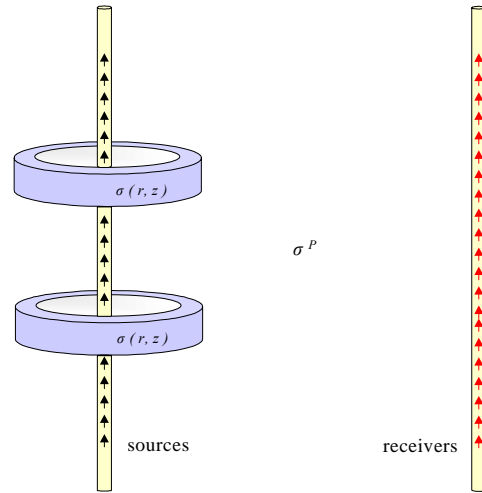


Figure 1 – Cylindrical 2-D geometry for the cross-well problem. The inhomogeneous bodies are cylindrically symmetric about the sources.

Forward Modeling

Considering the geometry illustrated in Figure 1. The governing diffusion equation for the electric field E_ϕ is

$$\frac{\partial^2 E_\phi}{\partial z^2} + \frac{\partial}{\partial r} \left[\frac{1}{r} \frac{\partial (r E_\phi)}{\partial r} \right] - i\omega\mu\sigma = i\omega\mu J_\phi, \quad (1)$$

EM Tomography with Absolute Constrains

where J_ϕ is the external source with current flowing in the azimuthal direction, r is the radius from the axis of symmetry, z is the vertical coordinate and a time dependence term $e^{i\omega t}$ is used, σ is the conductivity as a function of r and z , and μ is the magnetic permeability which is assumed to be equal to the free-space value.

We assume that an inhomogeneous annulus is embedded in a homogeneous whole-space with conductivity σ^p , as shown in Figure 1. The total field E_ϕ can be separated into its primary and secondary components. The primary field E_ϕ^p is generated by a vertical magnetic dipole in the homogeneous background medium. The electric field in a whole space can be expressed analytically (e.g., Ward and Hohmann, 1987) as

$$E_\phi^p = -\frac{i\omega\mu m_z}{4\pi R^3} (1 + ik_p R) e^{-ik_p R}, \quad (2)$$

where m_z is the magnetic moment, $k_p = \sqrt{-i\omega\mu\sigma^p}$ and $R = \sqrt{r^2 + z^2}$. The secondary field E_ϕ^s is due to inhomogeneities in the background medium and is given by

$$E_\phi^s = E_\phi - E_\phi^p, \quad (3)$$

The differential equation for the secondary electric field is

$$\frac{\partial^2 E_\phi^s}{\partial z^2} + \frac{\partial}{\partial r} \left[\frac{1}{r} \frac{\partial(rE_\phi^s)}{\partial r} \right] - i\omega\mu\sigma E_\phi^s - i\omega\mu(\sigma - \sigma^p)E_\phi^p = 0, \quad (4)$$

To solve (4) we apply the finite element formulation via Galerkin's method. The vertical component of the magnetic field is obtained by numerical differentiation of the relationship

$$H_z = -\frac{1}{i\omega\mu} \frac{1}{r} \frac{\partial(rE_\phi)}{\partial r}, \quad (5)$$

Inverse Modeling

The model used to produce the synthetic data, from now on denoted experimental model, follows the works by Zhou et al. (1993) and Alumbaugh (1995). The region inter-well was divided into 200 cells. Each cell represents a value of conductivity, and also one parameter in the inverse process. Two 20 x 20 m transversal sections of the anomalous bodies are located near the center of the model and are separated by 20 m. The conductivity of bodies is 0.02 S/m,

which is twice that of the background of the model (0.01 S/m). The 21 sources and receivers are spaced at 10 m intervals in the 200 m deep wells, as illustrated in Figure 2. In the scheme of inversion, the set of synthetic data is formed by total vertical magnetic fields measured at the receivers, which are corrupted with pseudo-random Gaussian noise with zero mean and standard deviation of 5%. Assuming that the noise floor of the system is constant, the noise-to-signal ratio will be smallest when the source and receiver are the same depth and the signal is strong. To get regularization in the inverse problem, we add absolute constrains, where the conductivities are known through the analysis of samples or well logging, for example. Following works of (Medeiros and Silva, 1996), the equation for updating the parameters is done by (Luiz, 1999).

$$\overline{\Delta P} = \left(\overline{J_0} \overline{J} + \mu \overline{A} \overline{A} + \lambda \overline{I} \right)^{-1} \left\{ \overline{J_0}^T \left[\overline{Y}_{obs} - \overline{f}(\overline{P_0}) \right] + \mu \overline{A}^T \left(\overline{\gamma} - \overline{A} \overline{P_0} \right) \right\}, \quad (6)$$

where $\overline{\Delta P}$ is the vector that represents the increments added on the parameters, $\overline{J_0}$ is the sensitivity matrix in relation to parameters, \overline{A} represents the matrix containing the information of absolute constrains, \overline{Y}_{obs} is the set of observations, $\overline{f}(\overline{P_0})$ is the vector containing the valuation in the iterative process, $\overline{\gamma}$ is the vector containing the values of absolute constrains, μ is the Lagrange's multiplier and λ is the damping parameter (Marquardt's parameter).

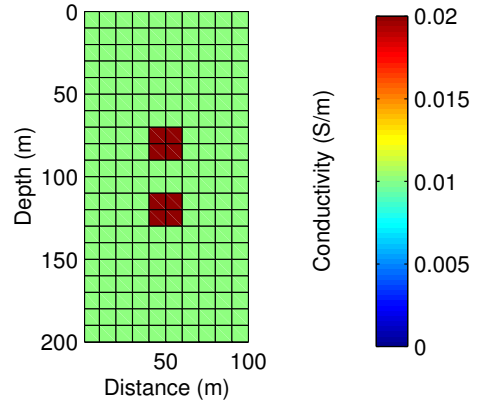


Figure 2 – Experimental model.

The first experiments were made to demonstrate that is impossible to obtain an image if we don't use constrains. As illustrated in Figure 3a, where the frequency utilized is the 100 kHz, and the first guess for host conductivity in the inverse process is 0.02 S/m, twice that of background of experimental model.

EM Tomography with Absolute Constrains

The image obtained diverge completely of model, as shown in Figure 3b.

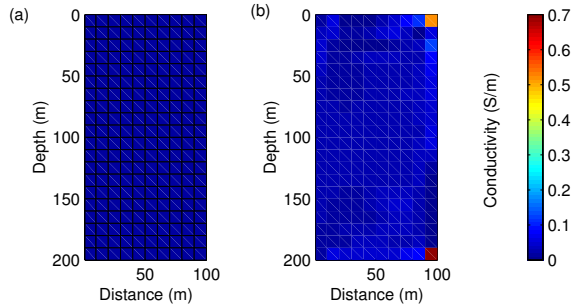


Figure 3 – Reconstructed images without constrains, (a) First guess, (b) Image.

Although absolute constrains (0.01 S/m) have been inserted in the cells on boundary of experimental model in the previous example, as shown Figure 4a, the image resulting continues diverging of the forward model. This is illustrated in Figure 4b.

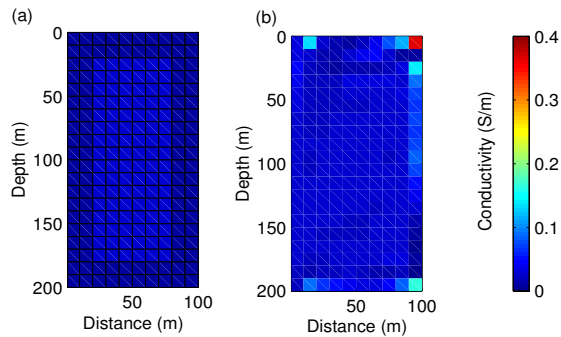


Figure 4 – Reconstructed images with constrains on the boundary, but with first guess far from background experimental model, (a) First guess, (b) Image.

Now we concluded from these two examples, that the choice for the first guess have to be close from the conductivity of the host of the experimental model

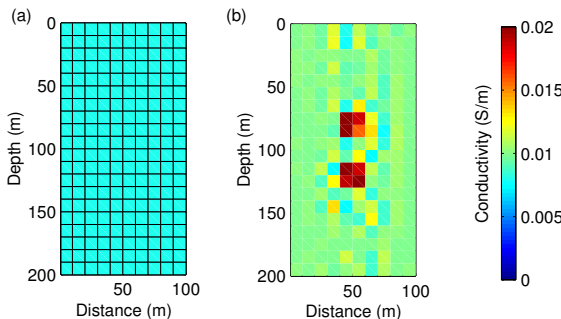


Figure 5 – Reconstructed images without constrains on the boundary, but with first model close from background forward model, (a) First guess, (b) Image.

We get acceptable images, when the value of conductivity for the first guess is close to the host of

the experimental model, even though absolute constrains have not been incorporated on boundary of the model as shown in Figure 5a. Where we set the first guess for the conductivity to 0.008 S/m, i.e., a variation of 20% of value background model. The image resulting matches with the experimental model, as demonstrated in Figure 5b.

We observed that using the same value (0.01 S/m) both to the absolute constrains on the cell around the borders and for the first guess (Figure 6a), the image obtained is much better than the image gotten without incorporating constrains on cells of boundary, as illustrated in Figure 6b as compared to Figure 5b.

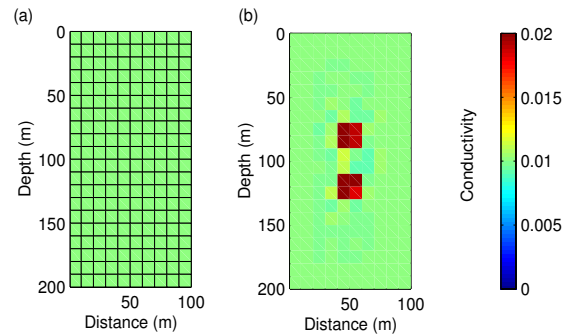


Figure 6 – Reconstructed images with the same value for the absolute constrains on the boundary, and for the first guess, (a) First guess, (b) Image.

Resolution of Method

The frequency is an important factor on the resolution of the image, as shown in figures 7b through 7d.

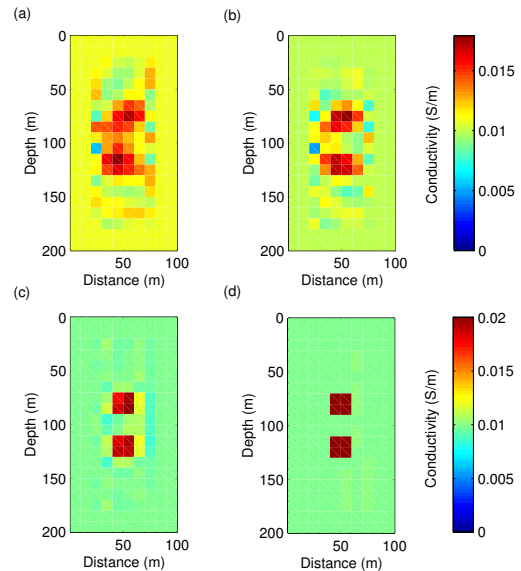


Figure 7 – Influence of frequency, (a) 5 kHz, (b) 10 kHz, (c) 50 kHz, (d) 1100 kHz.

We observed that, in low conductivity contrasts the image improves, when the frequency increases, on the other hand, for high frequencies, the measured

EM Tomography with Absolute Constrains

synthetic data are very small (order of 10^{-12}), which is not viable in practice.

To examine the effects of different conductivity contrasts on the image resolution, we used contrasts of 4, 6, 8 and 10 times, between the conductivities of target and of the host of the experimental model.

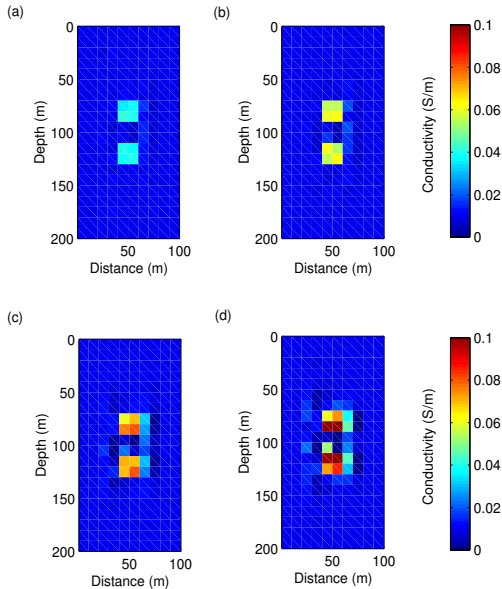


Figure 8 – Resolution at 30 kHz as a function of target conductivity $\sigma^p = 0.01$ S/m, (a) $\sigma = 0.04$ S/m, (b) $\sigma = 0.06$ S/m, (c) $\sigma = 0.08$ S/m, (d) $\sigma = 0.1$ S/m.

For a frequency of 30 kHz the images illustrated in Figures 8a through 8d show that when the conductivity of anomalous bodies, and thus the contrast between the targets and the background, is grown, the resolution of targets decreases.

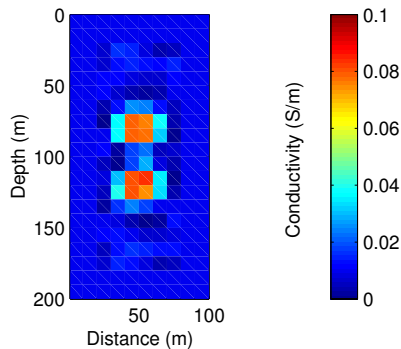


Figure 9 – Resolution at 5 kHz. The contrast of conductivity between target and the background is 10.

Thus, for one frequency given, the resolution of the images decreases, when the conductivity contrasts between the host and the inhomogeneous bodies becomes larger. However, when the frequency is decreased the resolution improves, as displayed in Figure 9.

Conclusions

We have discussed the incorporation of absolute constrains to obtain image from data cross-well EM. It has been illustrated that we have to incorporate two kinds of absolute constrains: one for the value of the first guess model, that should be in the range of approximately 80% of background's value, to guarantee the convergence of reconstructed model, and another kind of absolute constrain incorporated on the borders of the model that permits a gain of image's quality, these kind of constrains are considered weak constrains, since they not demand any information about the anomalous bodies, but only relating to the host. We examined the influence of frequency and of conductivity contrasts between the background and the target. At practicable applications we have shown that, in lower conductivity contrasts, the resolution of image becomes better, with increase of frequency. For high conductivity contrasts the resolution of image tends deteriorate, however if the frequency is decreased this effect is minimized.

References

- Alumbaugh, D. L., and Morrison, H. F., 1995, Theoretical and practical considerations for crosswell electromagnetic tomography assuming a cylindrical geometry: *Geophysics*, 60, 846-870.
- Luiz, J. G., 1999, Informação a priori na inversão de dados magnetotelúricos, PhD thesis, Universidade Federal do Pará – UFPA.
- Medeiros, W. E., and Silva, J. B. C., 1996, Geophysical Inversion using approximate equality constrains: *geophysics*, 61, 1678-1688.
- Rijo, L., 1996, Teoria dos métodos elétricos e eletromagnéticos – class notes – Department of Geophysics, Universidade Federal do Pará – UFPA.
- Ward, S. H., and Hohmann, G. W., 1988, Electromagnetic theory for geophysical applications, in Nabighian, M. N., Ed., *Electromagnetic method in applied geophysics theory*, Vol. 1: Soc. Explor. Geophys., 131-311.
- Zhou, Q., Becker, A., and Morrison, H.F., 1993, Audio-frequency electromagnetic tomography in 2-D: *Geophysics*, 58, 482- 495.

Acknowledgments

We would like to thank to Univesidade Federal do Pará for logistic support. This work was financed by Agência Nacional do Petróleo (ANP), Financiadora de Estudos e Projetos (FINEP) and CTPETRO/CNPq-46295/00-8.

Electromagnetic Tomography with Derivative Constraints

João J. Baptista; Luiz Rijo; Victor C. Souza, UNIVERSIDADE FEDERAL DO PARÁ, Brazil
 e-mail: jjunior@ufpa.br, rijo@amazon.com.br

Abstract

In this paper about electromagnetic tomography we test the use of smoothings constraints implemented by derivative operators of first, second and third order calculated by the regularization method proposed by Tikhonov. To get this, we use the same model published by Alumbaugh & Morrison (1995). During the inversion of the data we adopted the Marquardt algorithm. The finite elements method was used to calculate the forward model. The knowledge of the true conductivity of host is sufficient to guarantee the recuperation of the image at any frequency between 10 to 1000 kHz. In this case no other constraint is necessary. When the conductivity of the host is partially known, within 20%, the use of derivative constraints permits the achievement of good results in range of 50 and 500 kHz.

Introduction

Zhou et al. (1993) developed a technique to interpret data from electromagnetic crosswell tomography, applying the Born and Rytov approximations to the equation of the electromagnetic field. In their work, using the least square technique, was demonstrated that the electromagnetic imaging process reproduces the spatial distribution of the conductivity of the subsurface. In similar work, Alumbaugh (1993), Spies & Habashy (1995) analyzed the resolution of the crosswell electromagnetic tomography using the sensibility function or Frechet derivative function approximation, which relate small disturbances in the conductive structure to measures taken with a given source and receiver pair. The conclusion of these different studies indicate that two major properties of crosswell electromagnetic imaging can be determined from the sensitivity analyses and Zhou's wavenumber domain analyses: (1) image resolution improves with increasing frequency, and (2) the horizontal resolution depends on maximum vertical offset or aperture employed in the source and receiver.

Our goal in this paper is to test another constraining methodology of the electromagnetic tomography to retrieve the heterogeneity of the subsurface, by using of the Alumbaugh & Morrison (1995) model. A small modification will be done to the Marquardt algorithm that allows the introduction of complementary information about the parameters and to stabilize the problem. For this, the regularization method proposed by Tikhonov is

adopted to calculate the operators of several orders, that are the stabilizers employed in this work.

Model Geometry and forward problem

The Alumbaugh & Morrison (1995) model, consists of a cylindrical symmetric region of interest imbedded in an otherwise homogeneous background of electric conductivity σ . A source of magnetic dipole type with $e^{i\omega t}$ behavior is located at $r = 0$, $z = z_{tx}$ on the axis of symmetry. If the anomalous conductivity $\sigma(r,z)$ is distributed symmetrically about this axis, then electric currents induced by the source can exist in the azimuthal direction. These currents in turn produce magnetic fields in the \hat{r} and \hat{z} directions which can be measured either within the well transmitter borehole as is commonly done in electromagnetic well logging, or in a second borehole some distance away as is done for crosswell EM measurements. The Figure 1 shows the cross section of the mentioned model in which two bodies of conductivity $\sigma = 0.02 S/m$ are separated for 20 meters of distance and disposed in the mesh center. The imaging region is bounded in the semi-space between the wells and is divided in 10 elements at horizontal and 20 at the vertical directions, summing a total of 200 elements (Figure 1). For each frequency used in this work, which ranges from 10 kHz to 1 MHz, the magnetic field is measured in 21 receivers in the well i.e., there is a measure to each 10 meters that starts on the surface, making up 441 data and 882 observations (real and imaginary).

The forward problem was calculated by the finite elements method. The synthetic data to the inversion was generated using the model shown in the figure 1. It is assumed that a noise with gaussian distribution and 5 percent of the minimum value of electromagnetic field calculated was added to the synthetic data to simulate a real situation on the field.

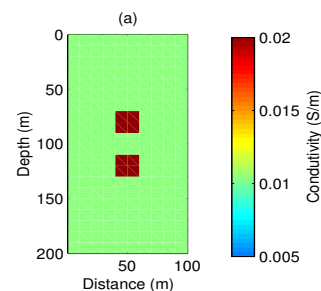


Figure 1 – Cross section of model applied in the studies

Electromagnetic Tomography with Derivative Constraints

The inverse problem

Initially, we assume that during the inversion process, only the host conductivity is known and set in 0.01 S/m. Actually, this value can be determined by well logging. The process initiate with a homogeneous model in which each element of mesh is set on 0.01 S/m (host conductivity)

The Figures 2 to 4 shows the results achieved to the frequencies from 50 kHz to 1 MHz. The analysis of these results shows that the image resolution increases with the frequency increment and, the knowledge of the host conductivity is of great importance to get good results in crosswell electromagnetic tomography.

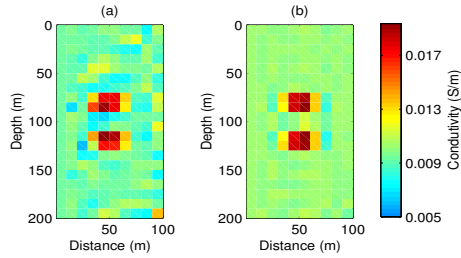


Figure 2-Image resolution at 10(a) and 50(b) kHz.

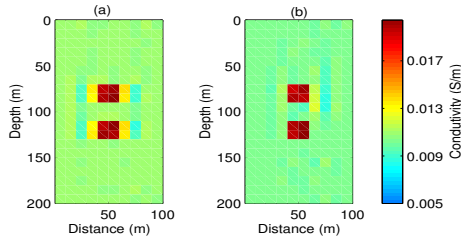


Figure 3-Image resolution at 100(a) and 250(b) kHz

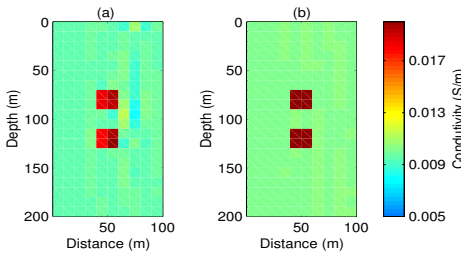


Figure 4-Image resolution at 500(a) and 1000(b) kHz

The results presented in Figures 2 to 4 were obtained assuming that the host conductivity is completely known. When this conductivity is partially known, is necessary the use of additional information that to allows to achieve good results. In the tentative to get good results on the case in which the

host conductivity is known with an error of 20 percent approximately, a small modification was applied to the Maquardt algorithm to allow the incorporation of complementary information and to stabile the tomography problem. Qualitative information is introduced as derivative operators calculated by Tihkonov regularization method. Following Medeiros & Silva (1996) and Luis (2000), the Marquardt algorithm becomes

$$\Delta p = [A^T A + \mu (H^T H + V^T V) + \lambda I]^{-1} [A^T \Delta y - \mu (H^T H + V^T V) p] \quad (1)$$

in which A is sensibility matrix, H and V are, respectively, the derivative operators matrixes, and Δy and p are, the residual and parameter vectors, and, μ and λ are respectively the Lagrange and Marquardt parameters.

The information represented by H and V matrixes varies from the bulk smoothness, which assumes equalness between the parameters (first order operator), until the information that tries to enhance the anomalous characteristics (second and third order operators).

Due to the bidimensional shape of model presented in this paper, the derivative operators will be applied about the parameters regarding their spatial distribution. Therefore, operators were built to be applied following the horizontal distribution (matrix H) and others to be applied following the vertical distribution (matrix V).

As in this work the derivative operators are the main stabilizer employed, we show the construction of the second order operator, regarding the parameters distribution shown in Figure 5.

P1	P2	P3	P4
P5	P6	P7	P8
P9	P10	P11	P12
P13	P14	P15	P16

Figure - 5 Parameters disposition in the bidimensional model

Considering that the number of parameters is equal to six (6), an operator applied in the horizontal direction will act sequentially on the 1 2 3 and 4 parameters and, on the other hand on 1 5 9 and 13 parameters when applied in the vertical direction. These operators are calculated using the binomial coefficient. For the parameters distribution shown above, a second order operator acting on the horizontal direction must have the following shape

Electromagnetic Tomography with Derivative Constraints

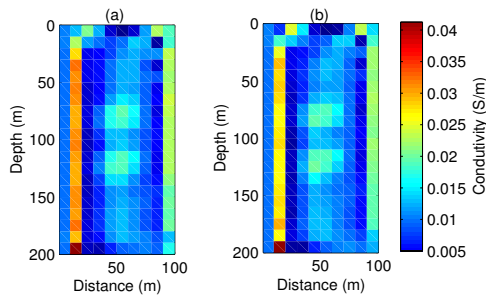
$$H = \begin{bmatrix} -1 & 2 & -1 & 0 & 0 & 0 & 0 & 0 & 0 & 0 & 0 & 0 & 0 & 0 & 0 & 0 & 0 & 0 & 0 & 0 & 0 \\ 0 & -1 & 2 & -1 & 0 & 0 & 0 & 0 & 0 & 0 & 0 & 0 & 0 & 0 & 0 & 0 & 0 & 0 & 0 & 0 & 0 \\ 0 & 0 & 0 & 0 & -1 & 2 & -1 & 0 & 0 & 0 & 0 & 0 & 0 & 0 & 0 & 0 & 0 & 0 & 0 & 0 \\ 0 & 0 & 0 & 0 & 0 & -1 & 2 & -1 & 0 & 0 & 0 & 0 & 0 & 0 & 0 & 0 & 0 & 0 & 0 & 0 \\ 0 & 0 & 0 & 0 & 0 & 0 & 0 & 0 & -1 & 2 & -1 & 0 & 0 & 0 & 0 & 0 & 0 & 0 & 0 & 0 \\ 0 & 0 & 0 & 0 & 0 & 0 & 0 & 0 & 0 & -1 & 2 & -1 & 0 & 0 & 0 & 0 & 0 & 0 & 0 & 0 \\ 0 & 0 & 0 & 0 & 0 & 0 & 0 & 0 & 0 & 0 & 0 & 0 & -1 & 2 & -1 & 0 & 0 & 0 & 0 & 0 \\ 0 & 0 & 0 & 0 & 0 & 0 & 0 & 0 & 0 & 0 & 0 & 0 & 0 & 0 & 0 & -1 & 2 & -1 & 0 & 0 \\ 0 & 0 & 0 & 0 & 0 & 0 & 0 & 0 & 0 & 0 & 0 & 0 & 0 & 0 & 0 & 0 & 0 & -1 & 2 & -1 \end{bmatrix}$$

On the other hand, an operator of the same order acting on the vertical direction presents the following pattern

$$V = \begin{bmatrix} -1 & 0 & 0 & 0 & 2 & 0 & 0 & 0 & -1 & 0 & 0 & 0 & 0 & 0 & 0 & 0 & 0 & 0 & 0 & 0 \\ 0 & 0 & 0 & 0 & -1 & 0 & 0 & 0 & 2 & 0 & 0 & 0 & -1 & 0 & 0 & 0 & 0 & 0 & 0 & 0 \\ 0 & -1 & 0 & 0 & 2 & 0 & 0 & 0 & -1 & 0 & 0 & 0 & 0 & 0 & 0 & 0 & 0 & 0 & 0 & 0 \\ 0 & 0 & 0 & 0 & 0 & -1 & 0 & 0 & 0 & 2 & 0 & 0 & 0 & -1 & 0 & 0 & 0 & 0 & 0 & 0 \\ 0 & 0 & -1 & 0 & 0 & 2 & 0 & 0 & 0 & -1 & 0 & 0 & 0 & 0 & 0 & 0 & 0 & 0 & 0 & 0 \\ 0 & 0 & 0 & 0 & 0 & -1 & 0 & 0 & 0 & 2 & 0 & 0 & 0 & -1 & 0 & 0 & 0 & 0 & 0 & 0 \\ 0 & 0 & 0 & -1 & 0 & 0 & 2 & 0 & 0 & 0 & -1 & 0 & 0 & 0 & 0 & 0 & 0 & 0 & 0 & 0 \\ 0 & 0 & 0 & 0 & 0 & 0 & -1 & 0 & 0 & 0 & 2 & 0 & 0 & 0 & -1 & 0 & 0 & 0 & 0 & 0 \\ 0 & 0 & 0 & 0 & 0 & 0 & 0 & -1 & 0 & 0 & 0 & 2 & 0 & 0 & 0 & -1 & 0 & 0 & 0 & 0 \end{bmatrix}$$

The information of the operators mentioned above is now used during the inversion process. Now, we assume a model in which the conductivity of each element (stimated parameter) is set on 0.008 S/m. The achieved results are presented in the Figures 6 - 10.

The analysis of these results shows that the use of the derivative operators is only efficient to frequencies between 100 and 500 kHz (Figure 7 - 9). For frequency values less 100 kHz the proposed method does not recuperate the image of the heterogeneity wherever derivative constraints are used or not, as illustrated in Figures 6a and 6b. On the other extreme, i.e. frequencies greater than 500 kHz, the image of the heterogeneity is not also well defined, mainly with the second and third derivative operators as shown in Figures 10b – 10d.



Figuras 6-Image obtained with non-constraint inversion (a) at 50 kHz. Image obtained with constraint inversion using the first order operator (b)

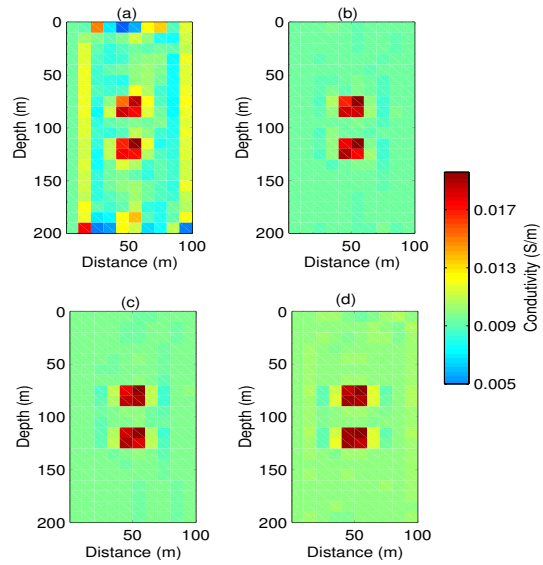


Figure 7 - Image obtained with a non-constraint inversion (a) at 100 kHz. Image obtained with a constraint inversion using the first(b), second(c) and third(d) order operators.

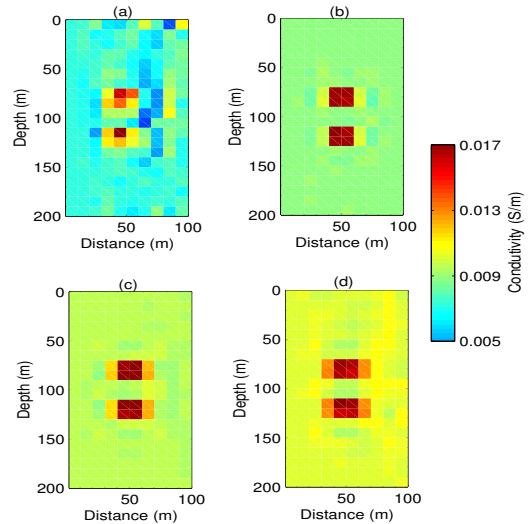


Figure 8 - Image obtained with a non-constraint inversion (a) at 250 kHz. Image obtained with a constraint inversion using the first(b), second(c) and third(d) order operators.

Electromagnetic Tomography with Derivative Constraints

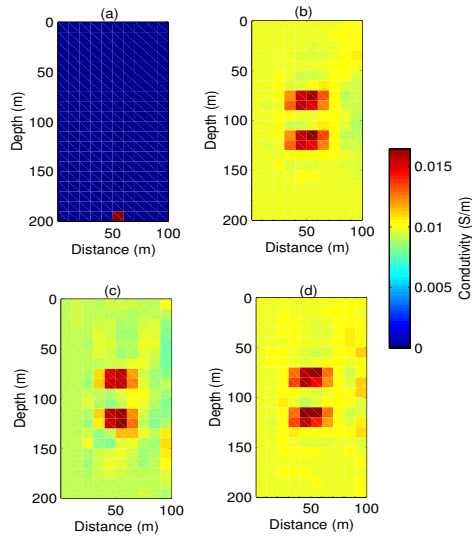


Figure 9 - Image obtained with a non-constraint inversion (a) at 500 kHz. Image obtained with a constraint inversion using the first(b), second(c) and third(d) order operators.

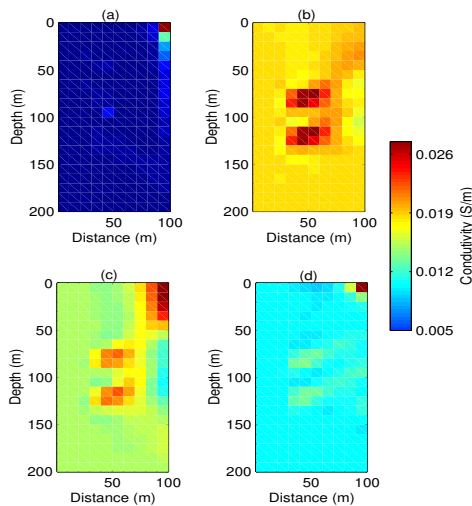


Figure 10 - Image obtained with a non-constraint inversion (a) at 1 MHz. Image obtained with a constraint inversion using the first(b), second(c) and third(d) order operators.

Conclusions

From the analysis of the results we conclude:

- The knowledge of the true conductivity of host is sufficient to guarantee the recuperation of the image at any frequency between 10 to 1000 kHz. In this case no other constraint is necessary. The true conductivity of the host can be easily obtained through well log measurements.
- When the conductivity of the host is partially known, within 20 percent the use of derivative constraints permits the achievement of good results in range of 50 e 500 kHz.
- For the cases studied, we observed that the first derivative operator performed better than the second and third ones.

References

- David L. Alumbaugh; H. Frank Morrison., 1995, Theoretical, and practical considerations for crosswell, electromagnetic tomography assuming a cylindrical geometry: *Geophysics*, 60, P. 846-870.
- José Gouvêia Luis.,2000, Informação a priori na inversão de dados MT: PhD Thesis, Curso de Pós-Graduação, em Geofísica Universidade Federal do Pará.
- M. L. Oristaglio; M. H. Worthington., 1995, Inversion of surface and borehole electromagnetic data for two- dimensional electrical conductivity models: *Geophysics*, 28, P. 663-657.
- Medeiros, W E., and J. B. C., 1996, Geophysical Inversion using approximate equality constraints: *geophysics*, 61, 1678-1688.
- L. Rijo., 1996, Teoria dos métodos elétricos e eletromagnéticos.: class notes.

Acknowledgments

We would like to thank to UFPa for logistic support. The basic research supports this work was found by de Agencia Nacional de Petroleo (ANP), Financiadora de Estudos e Projetos (FINEP) and CTPETRO/CNPq-46295/8. One up us (J.B) tanks CNPq for the doctorate scholarships.



Geoelectrostratigrafia Bi-dimensional da Parte Central da Bacia do São Francisco (MG)

Ana Lucia Rodrigues e Sergio Luiz Fontes
Observatório Nacional – MCT, Brasil, sergio@on.br

Resumo

No âmbito de um programa de exploração realizado no início da década de 90, o Observatório Nacional realizou 43 sondagens magnetotélúricas (MT), perfazendo um total de 7 perfis geoeletricos, ao longo de linhas sísmicas previamente levantadas, cobrindo uma área de 11.000 km², ao norte do estado de MG, na Bacia Proterozóica do São Francisco (ou Bacia do Bambuí). A variação de frequência utilizada foi de 0,001 a 400 Hz. A região localiza-se entre as latitudes 46° e 45° e longitudes 16° e 17°, próximo da zona de confluência dos rios S. Francisco e Paracatu, estendendo-se até as margens do Rio Urucuia (região transversal ao Rio S. Francisco). As cidades mais próximas são Santa Fé de Minas e São Romão. Os dados MT obtidos no levantamento geofísico foram interpretados anteriormente a partir de inversão 1D (Porsani e Fontes, 1992; Porsani, 1993), que supõe a variação da resistividade elétrica apenas com a profundidade, não se admitindo variação lateral ao longo dos perfis.

Tendo em vista o potencial para hidrocarbonetos da bacia, objetivou-se, neste trabalho, reinterpretar os perfis MT obtidos anteriormente, utilizando-se um algoritmo de inversão bi-dimensional (Mackie et al., 1997), que permite observar as mudanças laterais da resistividade elétrica, fornecendo informações que possibilitam a obtenção de interpretações mais precisas em sub-superfície.

Os resultados preliminares das inversões 2-D de quatro perfis MT apresentam estruturas de falhas não observadas nos estudos de inversão 1D.

Bacia Proterozóica do São Francisco

A Bacia do Bambuí, ou Bacia do São Francisco, abrange uma área de 216.800 Km². Cortada longitudinalmente pelo curso superior do Rio S. Francisco, engloba partes dos estados de Minas Gerais, Goiás e Bahia. A seqüência sedimentar pelítico-carbonática da bacia, pouco deformada e não metamorfizada, destaca-se por apresentar potencial exploratório. As emanações de gás em poços para água e as abundantes emanações naturais do Remanso do Fogo, já foram suficientes para a constatação da existência de gás termoquímico (Braun et al., 1990).

Estruturalmente, a bacia é afetada por grandes falhas longitudinais, ativas durante a sedimentação, que representam antigas linhas de fraqueza do embasamento (granítico-gnáissico), que foram reativadas no Ciclo Brasileiro (Alvarenga & Dardenne, 1978). Segundo o modelo de evolução geotectônica proposto por Thomaz Filho et al. (1998), os sedimentos teriam se depositado numa

bacia de antepaís, a partir do empilhamento tectônico resultante da compressão da Faixa de Dobramentos Brasília sobre o Cráton (750-500 Ma).

Geologia da Área

A geologia da área, apresentada na Fig. 1, é caracterizada principalmente por: *sedimentos detríticos Quaternários e Terciários*, que constituem *aluviões e coluviões* (areias, cascalhos, siltes, argila, areias silto-argilosas); *Formação Urucuia (Cretáceo Superior)*, caracterizada por arenitos, constituída na base por conglomerados e arenitos argilosos (Costa et al., 1976); *Grupo Aerado*, subdividido nas formações (da base para o topo): Abaeté - conglomerados e arenitos fluviais, Quiricó - Siltitos e argilitos e Formação Três Barras - Arenitos calcíferos e conglomeráticos, siltitos, argilitos e folhelhos (Hasui, 1969); *Grupo Santa Fé*, caracterizado por diamictitos, arenitos e pelitos (Dardenne et al., 1990), que repousam discordantemente sobre a *Formação Três Marias* (topo do Gr. Bambuí), recobrimdo em parte o Subgrupo Paraopeba (Branco & Costa, 1961), que é caracterizado por arenitos, siltitos e intercalações conglomeráticas (Branco & Costa, 1961; Braun, 1968; Grossi Sad & Quade, 1985).

Inversão 2-D

A inversão 2-D consiste em obter uma distribuição da condutividade elétrica que varia em profundidade e lateralmente, para os modos TE e TM, minimizando o erro entre as sondagens MT observadas (resistividade aparente e fase x frequência) e as curvas MT calculadas. Existem inúmeros algoritmos para realizar esta inversão 2-D. Neste trabalho foi utilizado o algoritmo proposto por Mackie et al. (1997), que utiliza a técnica do gradiente conjugado para a inversão 2-D não lineal.

Os resultados das inversões forneceram modelos da distribuição das resistividades elétricas das rochas em subsuperfície, relacionadas com os parâmetros físicos e estruturais.

Resultados e Interpretações Preliminares

Os resultados das inversões 2-D são apresentados na forma de seções da resistividade elétrica x profundidade para os quatro perfis estudados (Fig. 2).

Através das seções geoeletricas do perfil MT2, verifica-se boa correlação entre os valores observados e calculados de resistividade aparente e fase, nos modos TE e TM (Fig. 3).

Geoelectrostratigrafia da Bacia do São Francisco

Observam-se, em todos os perfis apresentados na Fig. 2, feições de resistividades muito baixas (menor que 10 $\Omega \cdot m$) a baixas (entre 10 e 60 $\Omega \cdot m$), nos primeiros 2 a 2,5 km de profundidade, aproximadamente, correspondentes às coberturas sedimentares (areias, cascalhos, siltes, argila). Algumas feições um pouco mais resistivas (em torno de 90 a 100 $\Omega \cdot m$) podem ser observadas próximas à superfície (aproximadamente nos primeiros 500m de profundidade), nos perfis MT1, MT2 e MT3, que possivelmente estão relacionadas às rochas carbonáticas do Grupo Bambuí. Abaixo de 2,5 km de profundidade, encontram-se os valores de resistividades mais elevados (superiores a 100 $\Omega \cdot m$), possivelmente associados ao embasamento

Observa-se ainda descontinuidade lateral de direção NE-SW, imediatamente abaixo da 5ª. estação do perfil MT2, a partir de 2 km de profundidade, aproximadamente. Esta possível estrutura de falha, que também pode ser visualizada no perfil paralelo MT4, não é observada em superfície, devendo ter sido originada antes do início da deposição dos sedimentos da bacia. Vale ressaltar que a feição estrutural observada nos perfis 2-D apresenta a mesma direção de outras estruturas mapeadas na superfície da bacia.

Conclusão

As baixas resistividades, encontradas principalmente próximas à superfície, apresentam boa correlação com a geologia conhecida da área, caracterizada por níveis sedimentares ricos em matéria orgânica.

Não foram encontradas resistividades muito altas para grandes profundidades, características de embasamento cristalino, possivelmente em função do embasamento (granítico-gnáissico) apresentar-se alterado.

Os resultados encontrados anteriormente para os perfis MT2 e MT4 (Porsani, 1993), obtidos com algoritmos de inversão 1D, apresentam resistividades superiores a 100 $\Omega \cdot m$, a partir de 2 km de profundidade aproximadamente, assim como na inversão 2-D. Porém, não haviam sido observadas descontinuidades laterais, que foram obtidas com a inversão 2-D.

A partir de interpretações conjugadas de todos os perfis MT realizados na área, além de sua correlação com a geologia e outras informações, poderão ser obtidos dados mais precisos sobre a estrutura e possivelmente, a partir dos novos resultados, propor novas áreas-alvo a serem investigadas com mais detalhe na bacia.

Referências Bibliográficas

ALVARENGA, C.J.S. & DARDENNE, M.A. Geologia dos Grupos Bambuí e Paranoá na Serra de São Domingos, MG. IN.: Cong.Bras.Geol, 30, 1978. Recife. Anais...Recife: SBG, 1978. V.2,

p.546-556;

BRAUN, O.P.G.; MELO, U. & DELLA PIAZZA, H., 1990. Bacias proterozóicas brasileiras com perspectivas exploratórias para hidrocarbonetos. In: Origem e evolução de bacias sedimentares. Petrobrás. Coord. Raja Gabaglia, G.P. & Milani, E.M., Editora Gávea. Rio de Janeiro, p.115-132;

DARDENNE, M.A. et al., 1990. Descoberta de pavimentos de origem glacial sobre arcóseos da Formação Três Marias na região de Santa Fé de Minas, MG. Ver. Escola de Minas, v.43, n.4, p. 65-66, 1990;

MACKIE, R.; RIEVEN, S.; RODI, W., 1997. User Manual and Software documentation Two-dimensional Inversion of Magnetotelluric data. MIT, Cambridge, USA.

PORSANI, J. L.; FONTES, S. L., 1992. Estudo magnetotelúrico na Bacia do São Francisco. CENPES/SUSEP/SEGEF. Relatório de Progresso.

PORSANI, J. L., 1993. Estudo Magnetotelúrico na Bacia do São Francisco. Petrobrás. Coord. Barbosa Silva, F. - Relatório Final;

THOMAZ-FILHO, A.; KAWASHITA, K.; CORDANI, U.G., 1998. A origem do Grupo Bambuí no contexto da Evolução Geotectônica e de Idades Radiométricas;

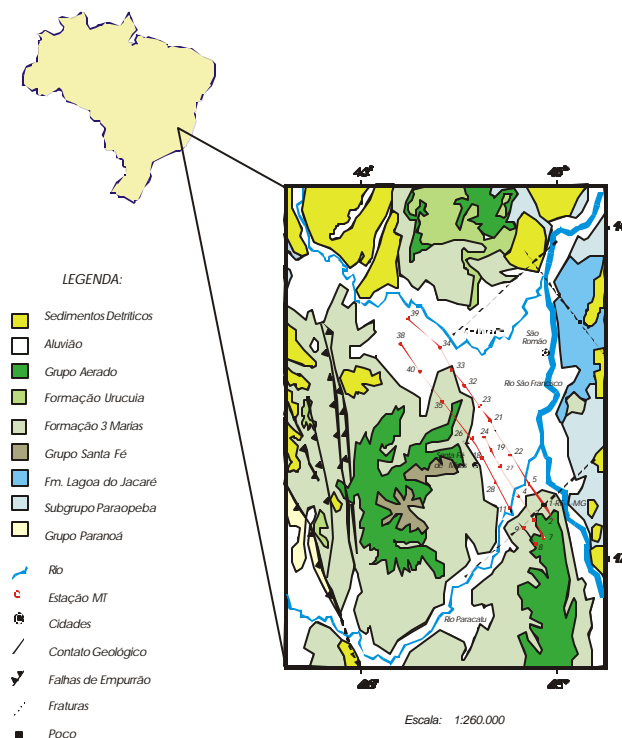


Fig.1- Mapa geológico de porção da bacia do São Francisco, mostrando a localização dos perfis MT

Geoeletoestratigrafia da Bacia do São Francisco

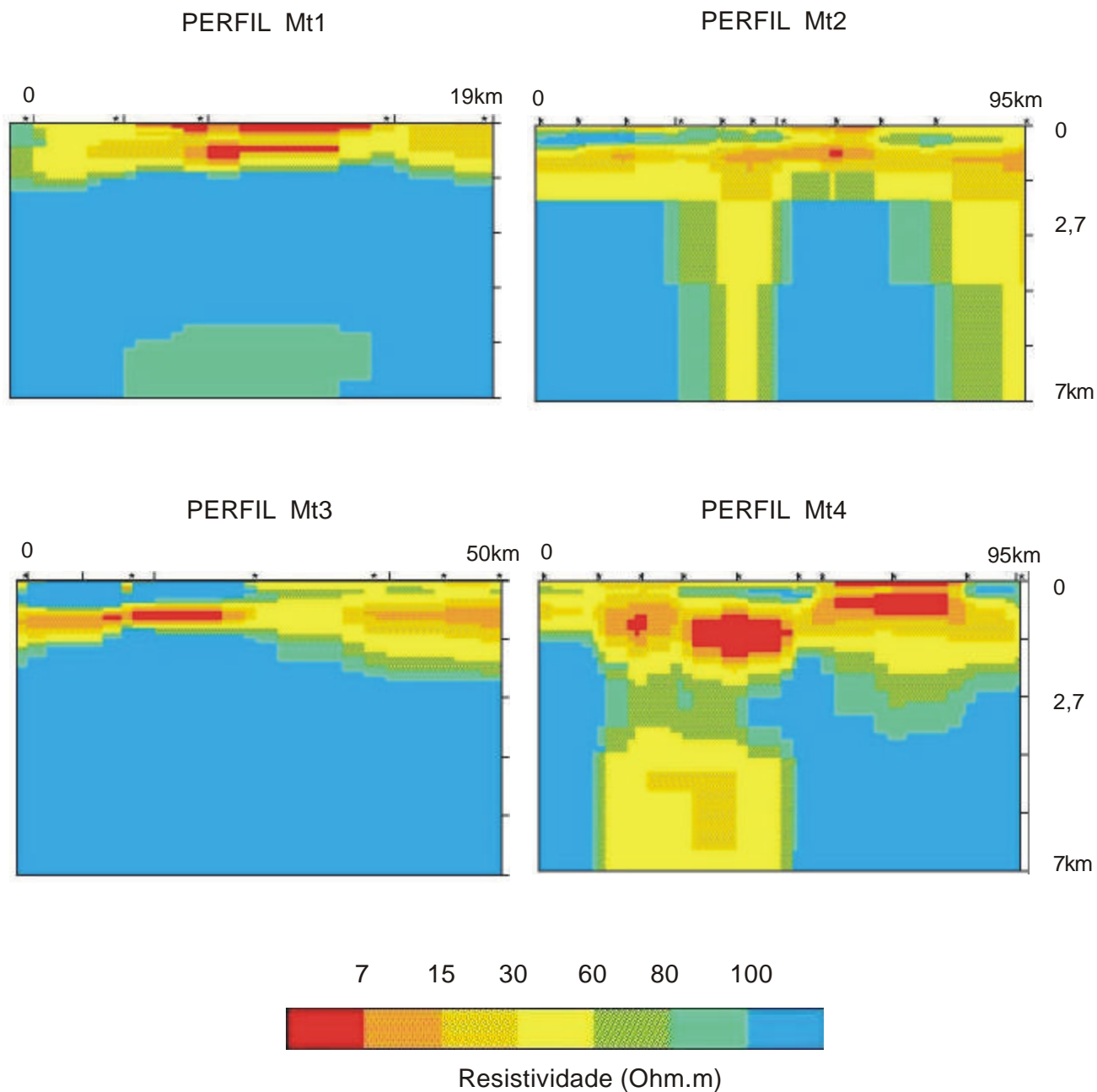


Fig. 2 Modelos geoeletricos 2-D resultantes da inversão 2-D para os perfis MT1, MT2, MT3 e MT4

Geoeletrorstratigrafia da Bacia do São Francisco

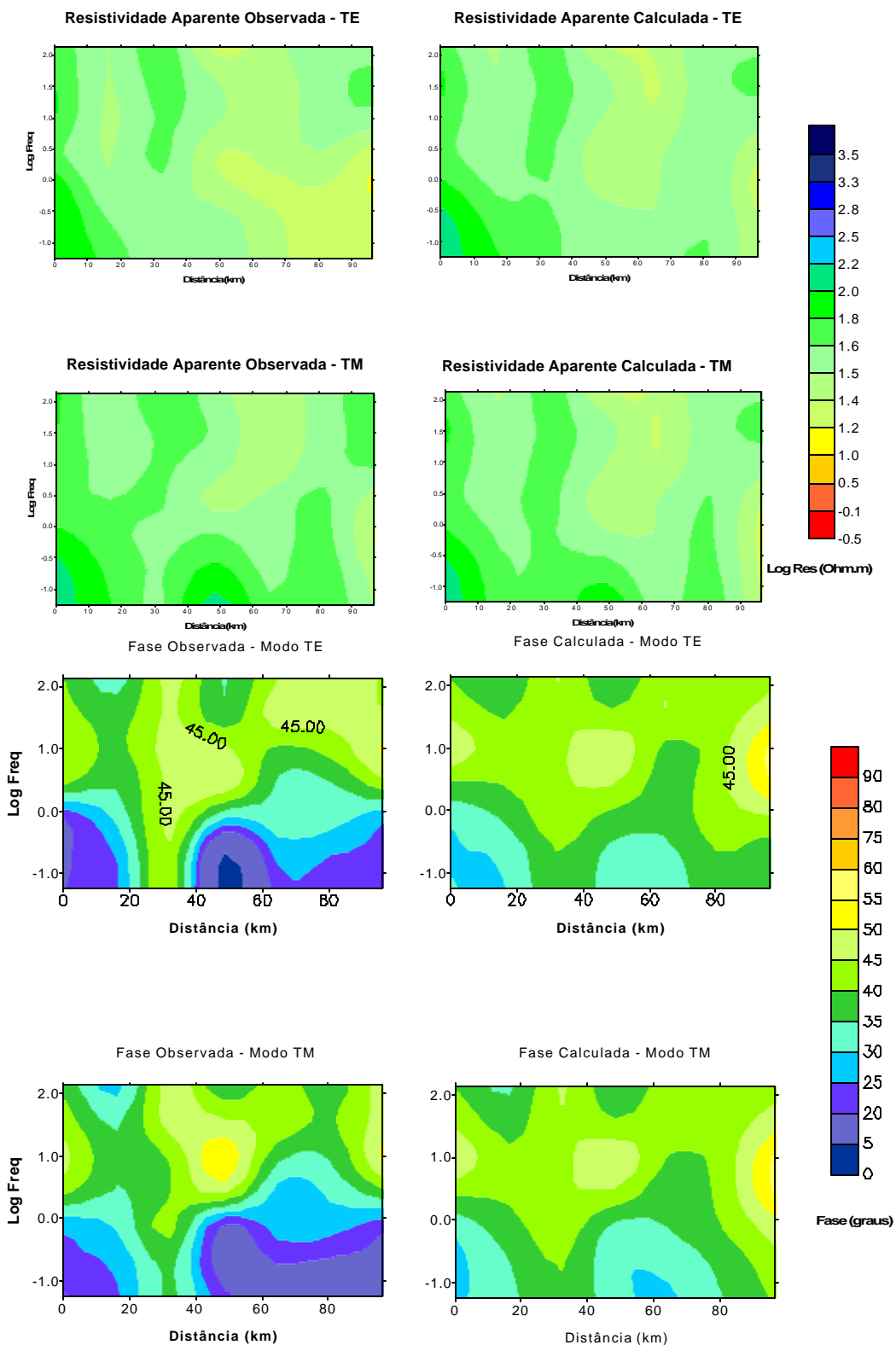


Fig. 3 Seções geolétricas observadas e calculadas - PERFIL MT2

Geração de Campo Magnético Direcional e Focalização por Combinações de Dipolos Magnéticos

Antonio V. C. Barbosa, UFPa, tonvini@bol.com.br, abarbosa@ufpa.br
Om P. Verma, UFPa, verma@ufpa.br

Abstract

An enhanced resolution is required in electromagnetic investigation of the “low Induction Number – LIN” targets. This could be obtained by creating a directional magnetic field flux and focusing it at a predetermine depth zone. This is achieved by combining the field of two magnetic dipoles in different configurations to obtain vertically and horizontally directed fields in the central portion of the dipole configuration. Focalization of the field in depth is controlled by the separation between the dipoles. Results in the forms of directional magnetic fields maps and the curves of the variations in the intensity of these magnetic field components with depth are presented. This study suggests an innovative way to create directional and focalized magnetic fields; consequently opens a new horizon in electromagnetic exploration methods.

Introdução

É necessário melhorar o poder de resolução dos métodos eletromagnéticos, particularmente quando são aplicados nas investigações de alvos com baixo número de indução “Low Induction Number – LIN”, como por exemplo em aplicações na engenharia civil (geotecnia), arqueologia e água subterrânea.

Este melhoramento pode ser obtido empregando campos magnéticos direcionais e focalizados. Campos com essas características podem ser gerados pelas combinações de dipolos transmissores em diferentes arranjos e variando o espaçamento entre eles.

Apresentamos um estudo teórico de geração de campos magnéticos direcionais e focalizados em profundidade, num semi-espaço homogêneo no domínio da frequência, pela combinação de diferentes pares de dipolos magnéticos transmissores – vertical (DMV) e horizontal (DMH) – e o espaçamento entre eles.

Metodologia

Os campos magnéticos gerados por diferentes arranjos de pares de dipolos foram calculados e mapeados num semi-espaço para vários espaçamentos entre transmissores, conforme demonstra a Figura 1.

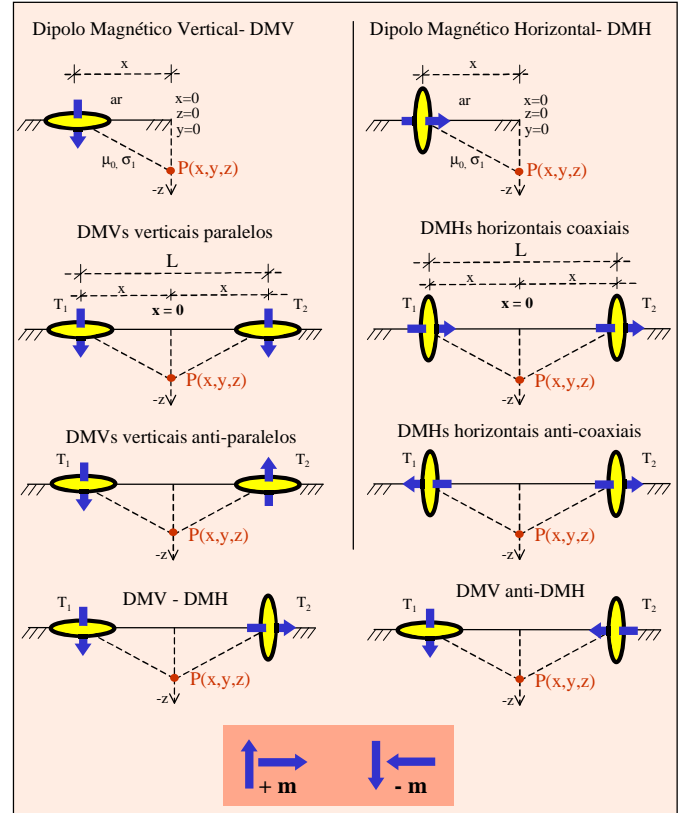


Figure 1 – Configurações dos dipolos magnéticos considerados nesse trabalho.

Rijo (1996) descreveu as equações das componentes dos campos magnéticos gerados por dipolos magnéticos verticais(DMV) e horizontais (DMH), num semi-espaço ($z \leq 0$) no plano $y=0$.

Para o dipolo magnético vertical (DMV), temos:

$$H_r = \frac{m}{2\pi} \int_0^{\infty} \frac{k_r^3 e^{-u_1 z}}{k_r + u_1} J_1(k_r r) dk_r \quad (1)$$

e

$$H_z = \frac{m}{2\pi} \int_0^{\infty} \frac{k_r^3 e^{-u_1 z}}{k_r + u_1} J_0(k_r r) dk_r \quad (2)$$

Campos Magnéticos Direcionais e Focalizados

Para o dipolo magnético horizontal na direção x (DMHx), temos:

$$H_x = \frac{-m}{2\pi} \left(\frac{1}{r} - \frac{2x^2}{r^3} \right) \int_0^\infty \frac{u_1 k_r e^{-u_1 z}}{k_r + u_1} J_1(k_r r) dk_r$$

$$- \frac{m}{2\pi} \left(\frac{x^2}{r^3} \right) \int_0^\infty \frac{u_1 k_r^2 e^{-u_1 z}}{k_r + u_1} J_0(k_r r) dk_r \quad (3)$$

e

$$H_z = \frac{-m}{2\pi} \left(\frac{x}{r} \right) \int_0^\infty \frac{k_r^3 e^{-u_1 z}}{k_r + u_1} J_1(k_r r) dk_r \quad (4)$$

em que $r = \sqrt{x^2 + y^2}$; $k_1 = -i\omega\mu_0\sigma_1$;

$u_1 = \sqrt{k_r^2 - k_1^2}$ e m é o momento do dipolo, $J_0(k_r r)$ e $J_1(k_r r)$ são as funções de Bessel de primeira espécie de ordem 0 e 1. A transformada de Henkel nas equações de 1 a 4 num semi-espaco homogêneo foram avaliados usando filtros lineares digitais (Guptasarma & Singh, 1997).

A frequência considerada é 10 kHz e a resistividade do semi-espaco 100 Ω .m. Assim, as correntes de deslocamentos foram desprezadas.

Resultados e discussão

Embora tenhamos calculado e mapeado o campo magnético no semi-espaco para todos os arranjos mostrados na Figura 1, apresentamos neste trabalho somente os resultados dos arranjos DMVs paralelos, DMHs anti-coaxiais, DMHs coaxiais e DMVs anti-paralelos; porque eles geraram: campos simétricos, e direcionais na parte central das configurações. Como os arranjos DMV – DMH e o DMV anti – DMH não apresentam essas propriedades não servem de objeto deste estudo.

Observamos que os campos magnéticos dos arranjos DMV's paralelos e DMHs anti-coaxiais, ilustrados nas Figuras 2 e 3, são fortemente direcionados na vertical na porção central do arranjo, na faixa de $-0.2 \leq x/L \leq 0.2$. Porém, no primeiro arranjo há mudança no sentido dos campos numa profundidade aproximada de $z/L = -0.36$. Entretanto, isto não ocorre no segundo arranjo.

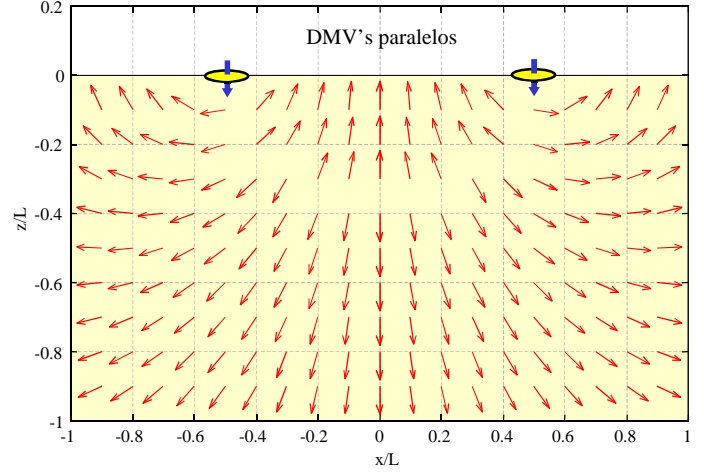


Figura 2 – Mapa de direção do campo magnético gerado por dois dipolos magnéticos verticais paralelos.

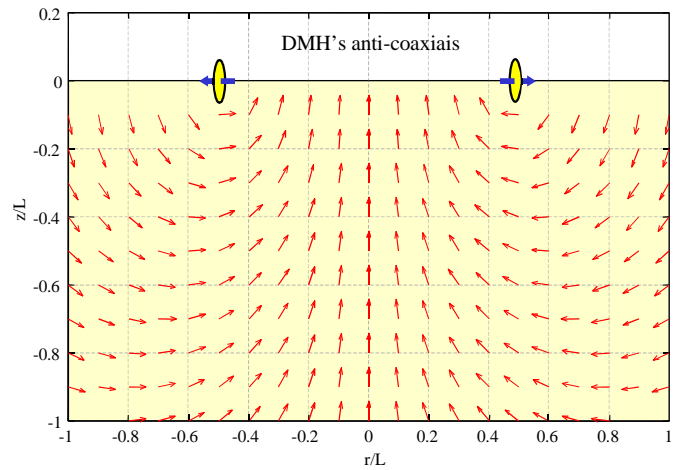


Figura 3 - Mapa de direção do campo magnético gerado por dois dipolos magnéticos horizontais anti-coaxiais.

As Figuras 4 e 5 ilustram a direção dos campos magnéticos gerados pelos arranjos DMHs coaxiais e DMVs anti-paralelos. Os campos desses arranjos estão fortemente direcionados horizontalmente na porção central, principalmente na faixa de $-0.2 \leq x/L \leq 0.2$. No arranjo DMHs coaxiais há mudança no sentido do campo na profundidade $z/L = -0.36$, contudo isso não ocorre no arranjo DMVs anti-paralelos.

Campos Magnéticos Direcionais e Focalizados

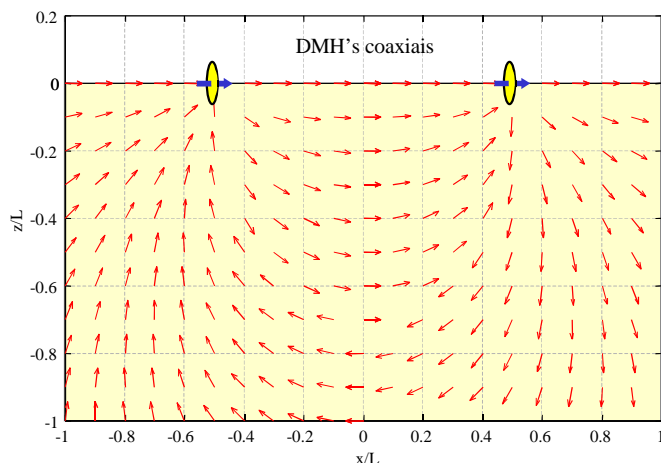


Figura 4 - Mapa de direção do campo magnético gerado por dois dipolos magnéticos horizontais coaxiais.

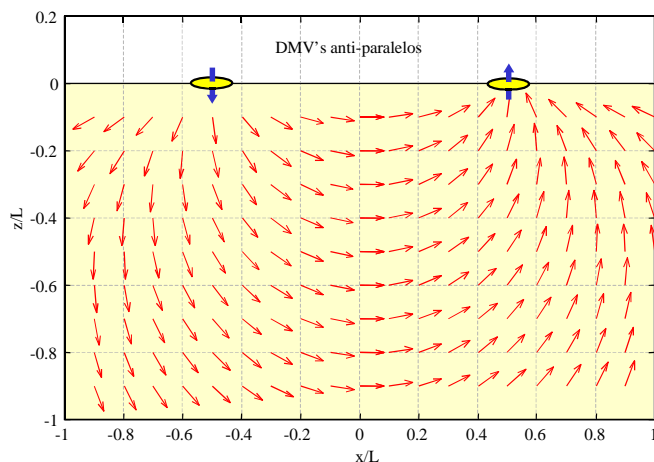


Figura 5 - Mapa de direção do campo magnético gerado por dois dipolos magnéticos verticais anti-paralelos.

As Figuras 6 e 7 ilustram variações em profundidade das componentes vertical (Hz) e horizontal (Hx) do campo magnético na linha central entre os dipolos transmissores ($x = 0$), para uma separação $L = 20$ m e frequência 10 kHz, num semi-espaço homogêneo de resistividade 100 Ω .m. Estas variações em profundidade das componentes Hz e Hx devido as quatro configurações de dipolos são comparados com os valores de um único dipolo.

Observamos que a componente vertical gerada pelo DMVs paralelos, na Figura 6, tem o maior valor na superfície seguido do DMV, contudo esse decai mais rapidamente em profundidade. Seu valor é superado pelo DMHs anti-coaxiais na profundidade $z/L = -0.15$. A componente vertical do dipolo DMHs anti-coaxiais alcançou seu máximo na profundidade $z/L = -0.25$ e a partir desse ponto o

campo decai em profundidade chegando a se igualar ao valor máximo do dipolo DMH na profundidade $z/L = -0.56$. Isto significa que o poder de investigação em profundidade do arranjo DMHs anti-coaxiais é maior que o dobro do dipolo (DMH), para as mesmas condições ambientais geolétricas e equipamentos. A componente vertical do arranjo DMHs anti-coaxiais, após a profundidade $z/L = -0.15$, é sempre maior do que os outros arranjos estudados até $z/L = -1.8$.

A componente horizontal, ilustrada na Figura 7, tem seu maior valor na superfície gerado pelo arranjo DMHs coaxiais, seguido pelo DMH; mas esses campos decaem acentuadamente com a profundidade. A componente Hx do arranjo DMVs anti-paralelo alcança seu valor máximo na profundidade $z/L = -0.23$ e a partir dessa profundidade seu valor decai, mas é sempre maior do que os outros arranjos até $z/L = -1.5$ quando se aproxima de zero. Nesse decaimento ele chega a se igualar ao valor máximo do dipolo DMH na profundidade $z/L = -0.56$, caracterizando que o poder de investigação deste arranjo é maior que o dobro de um único dipolo vertical.

Conclusão

O estudo realizado mostrou que é possível gerar campos direcionais (vertical ou horizontal) por combinações de dois dipolos transmissores, e focalizar os mesmos em diferentes profundidades variando o espaçamento entre eles. Também, mostra o poder de investigação em profundidade de uma seletiva combinação de dois dipolos é mais que o dobro de um dipolo empregado convencionalmente em situações similares.

Bibliografia

- Guptasarma, D. and Singh, B., 1997, New Digital Linear Filters for Hankel J_0 and J_1 transforms, *Geophysical Prospecting*, 45, 745 – 762.
- Rijo, L. R., 1996, Respostas Eletromagnéticas de dimensões $2 \frac{1}{2}$ e $3 \frac{1}{2}$, Dissertação Apresentada ao Concurso de Professor titular do Departamento de Geofísica do Centro de Geociências da Universidade Federal do Pará.

Agradecimentos

À CAPES pela bolsa de doutoramento concedida ao aluno Antônio Vinícius Barbosa. A João Augusto Pereira Neto pela colaboração na focalização dos campos magnéticos de dois dipolos.

Campos Magnéticos Direcionais e Focalizados

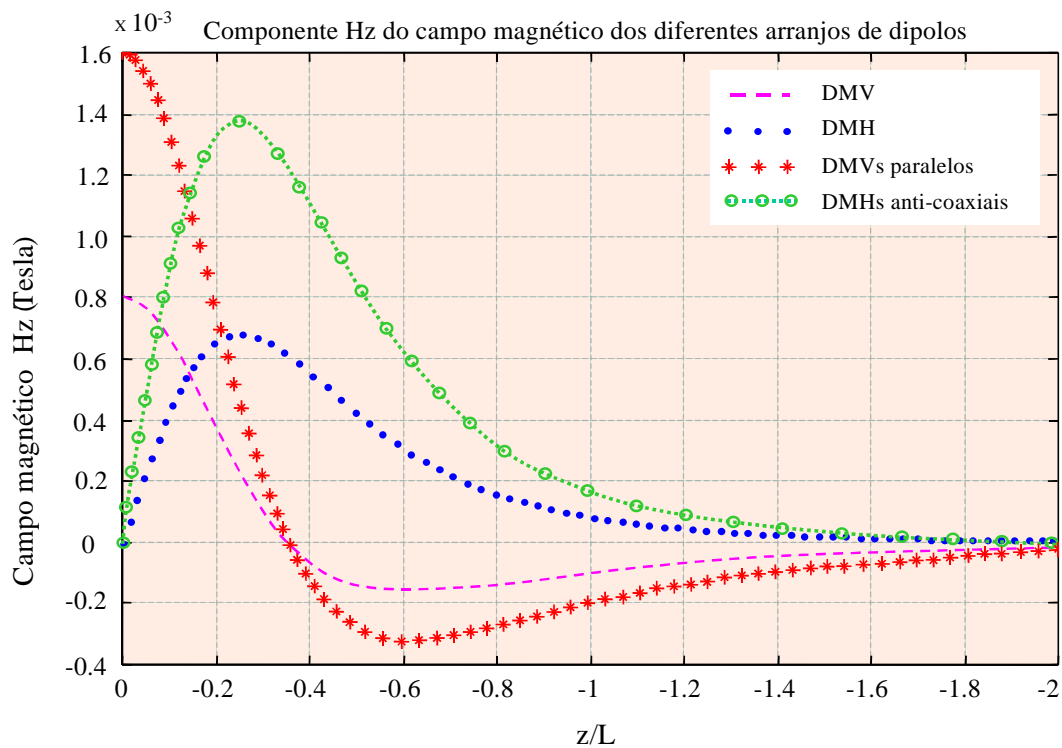


Figura 6 – Decaimento do campo Hz com a profundidade dos diferentes arranjos de dipolos.

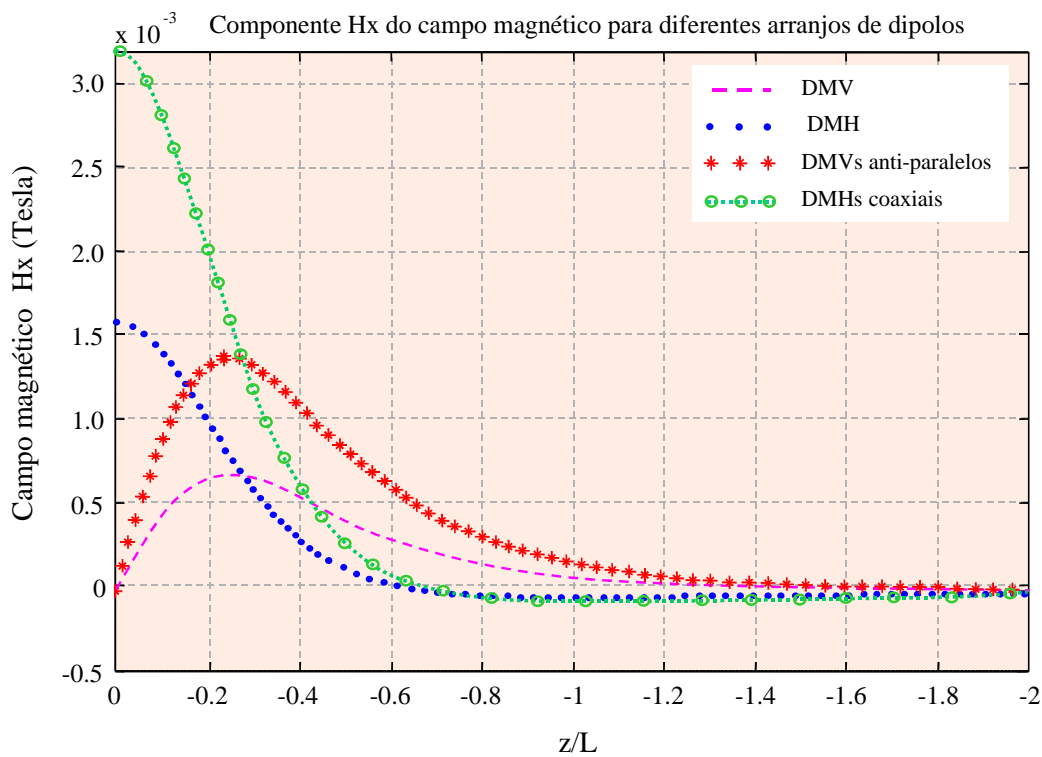


Figura 7 – Decaimento do campo Hx com a profundidade dos diferentes arranjos de dipolos.

Imageamento geoeétrico de colunas e secções de modelos 1-D utilizando técnicas geoestatísticas

José Márcio Lins Marinho, Universidade Federal do Ceará, Brasil

Sônia Maria Silva Vasconcelos, Universidade Federal do Ceará, Brasil

Resumo

O método do imageamento geoeétrico é uma importante ferramenta no mapeamento de estruturas 2-D, tendo sido propostas muitas técnicas de inversão com esta finalidade. No entanto, quando a estrutura em sub-superfície é próxima de camadas horizontais, a hipótese 1-D deve ser considerada como a mais efetiva para uma solução precisa. A combinação da técnica da sondagem elétrica convencional com técnicas geoestatísticas de imageamento, para investigação em áreas de geologia não complexa, foi aqui desenvolvida. As técnicas geoestatísticas, que incluem a krigagem associada a uma forte “anisotropia” horizontal, foram usadas primeiramente na elaboração de colunas geoeétricas de SEVs individualmente. Posteriormente, foram estendidas para o imageamento de secções geoeétricas. As secções imageadas em dois levantamentos são consistentes com as informações geológicas/hidrogeológicas disponíveis e com um levantamento anterior de eletrorresistividade realizado pela Universidade Federal do Ceará. A metodologia Geoestatística aqui estabelecida pode ser utilizada na representação de variáveis da perfilagem geofísica, assim como no imageamento bidimensional de propriedades físicas com distribuição em camadas horizontais.

Introdução

O método elétrico da resistividade é reconhecido como uma importante ferramenta na investigação de água subterrânea, e em estudos de geotécnica e de meio ambiente. O imageamento geoeétrico é uma técnica de levantamento muito utilizada em áreas de geologia complexa (Griffiths e Barker, 1993; Turberg e Barker, 1996). Ela envolve um sofisticado sistema de aquisição de dados ao longo de um perfil, onde as resistividades aparentes são plotadas em pseudo-secções, utilizando-se o conceito de profundidade de investigação. As pseudo-secções são interpretadas por modelamento (Lima et al., 1995) ou invertidas automaticamente usando-se algoritmos 2-D muito elaborados (p. exemplo, Loke e Barker, 1996; Abdul Nassir et al., 2000), sendo os resultados apresentados em pseudo-secções coloridas de resistividade verdadeira.

No entanto, em áreas de geologia não complexa, a hipótese do modelo 1-D é considerada mais adequada e está sendo sub-utilizada. Para tornar as interpretações 1-D mais úteis, propomos nesse trabalho, a partir do modelo geoeétrico multicamadas e de técnicas

geoestatísticas, o imageamento: a) da coluna geoeétrica de uma SEV (Sondagem Elétrica Vertical) isoladamente; b) de uma secção geoeétrica com várias SEVs.

Imageamento de coluna geoeétrica

Os resultados da interpretação de uma SEV são apresentados convencionalmente em forma de gráficos contendo os dados de campo, o modelo com os valores de resistividade impressos e a curva teórica correspondente ao modelo adotado. Atualmente, é crescente a utilização de modelo multicamadas na interpretação de SEVs (p. exemplo, Zohdy, 1989; Nowrozi et al., 1999).

Na Figura 1 apresentamos uma SEV Schlumberger, cujas medidas de campo foram invertidas usando-se um modelo multicamadas, onde o número camadas é igual ao número de pontos da curva de campo digitalizada (Zohdy e Birdorf, 1989).

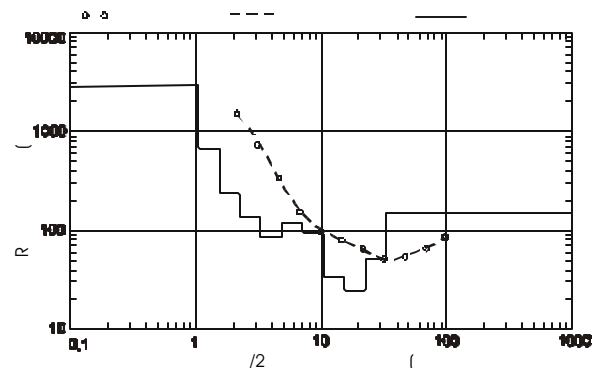


Figura 1 – Interpretação de uma sondagem elétrica através de modelo multicamadas.

O arquivo multicamadas obtido na inversão da SEV da Figura 1 foi repetido duas vezes em intervalos de 5m, obtendo-se um arquivo XYZ. Tendo este arquivo como entrada, obteve-se o imageamento da coluna geoeétrica dessa SEV (Figura 2), por krigagem ordinária, numa malha regular de 1m x 1m, para uma muito alta preferência (“anisotropia”) horizontal. O programa *Surfer versão 7.0*, produzido pela Golden Software, foi usado para se obter o imageamento da coluna geoeétrica.

O imageamento do modelo elétrico da SEV, com a descrição lito-hidrogeológica ao lado (Marinho e Vasconcelos, 2000b), nos parece tornar a interpretação de uma SEV mais comunicativa e informativa

Imageamento geolétrico

tanto para geofísicos quanto para os demais profissionais que se utilizam da técnica da sondagem elétrica.

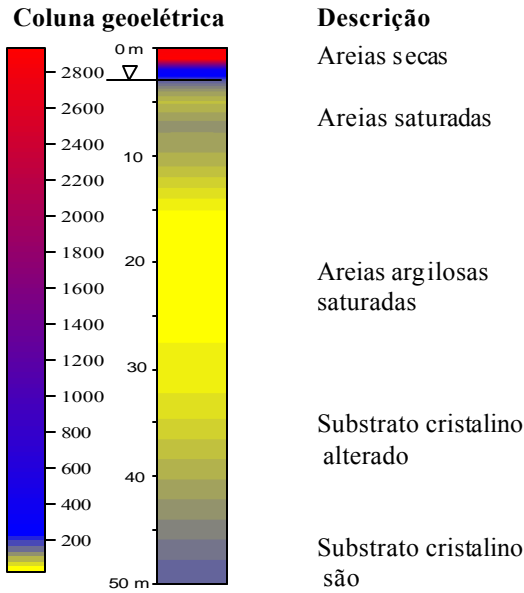


Figura 2 – Imageamento por krigagem da coluna geolétrica definida pelo modelo multicamadas da Figura 1.

Imageamento de secção geolétrica

Para estender a idéia de imageamento de uma coluna geolétrica (Figura 2) para o imageamento de uma secção 2-D, devemos aprofundar alguns conceitos. Primeiramente, em áreas de geologia não complexa, prevalecem os princípios geológicos da ordem geométrica: sobreposição horizontal e continuidade lateral. Também precisamos mostrar que a resistividade na secção se comporta como uma variável regionalizada, que é base da Geoestatística (Matheron, 1963). As duas ferramentas da Geoestatística são o variograma e a krigagem (Landim, 1998).

Duas secções foram estudadas utilizando-se a mesma metodologia. Para cada secção foi criado um arquivo onde constam o posicionamento das SEVs no perfil e os dados de profundidade e de resistividade de cada modelo geolétrico multicamadas interpretado. Foram obtidos os semi-variogramas para a variável resistividade apenas na direção vertical, pois não fez sentido considerar a direção horizontal, tendo em vista o número reduzido de SEVs nos perfis. Os semi-variogramas experimentais indicam o comportamento de variável regionalizada para a resistividade tanto no perfil 1 (Figura 3a) quanto no perfil 2 (Figura 3b), conforme a conceituação básica da Geoestatística. O semi-variograma é expresso por (Landim, 1998):

$$(h) = 1/2n \{x(i+h) - x(i)\}^2 \quad (1)$$

onde n é o número de pares comparados, h é a distância entre os pontos e $x(i)$ é a resistividade no ponto i .

Os semi-variogramas mostram um comportamento linear com um efeito pepita (*nugget effect*) pequeno.

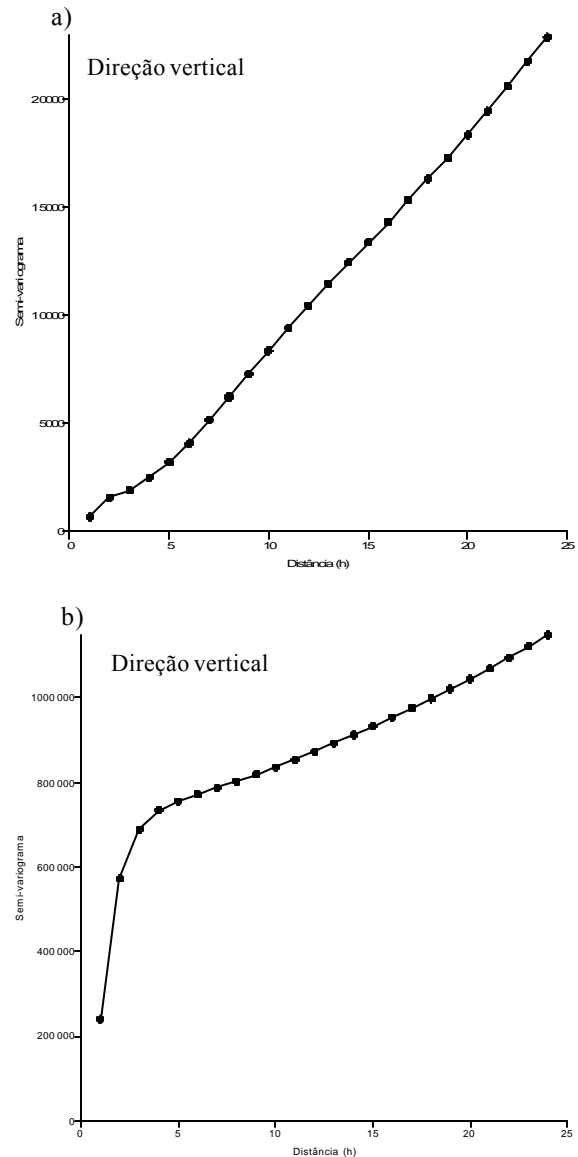


Figura 3 – Semi-variogramas para a resistividade: a) na secção 1; b) na secção 2.

Com base nesses semi-variogramas e nos princípios geológicos acima mencionados, fizemos o imageamento das duas secções por krigagem ordinária, usando a função linear de interpolação, num *grid* irregular de 1m (vertical) por 20m (horizontal), utili-

Imageamento geoeletrico

zando-se uma razão de anisotropia de 64. Este valor de anisotropia foi obtido após a simulação de uma secção com repetição de uma mesma SEV. Os resultados da krigagem através do *Surfer* se seguem.

Secção geoeletrica 1

A Secção 1 cruza a encosta de um afluente do Rio Cauípe, situada na zona costeira do Estado do Ceará, Brasil. Compreende uma cobertura de sedimentos arenosos inconsolidados e/ou manto de intemperismo sobre o embasamento gnáissico.

A secção imageada conforme a metodologia geoestatística adotada está na Figura 4. A tonalidade amarela nesse corte caracteriza a parte mais condutiva da secção, correspondendo também a parte saturada em água; a linha de contorno de 90 $\Omega\cdot m$, na parte superior da secção, corresponde aproximadamente ao nível estático, registrando-se acima deste uma cobertura resistiva, inconsolidada e não saturada. A linha de contorno de 400 $\Omega\cdot m$ corresponde à passagem em profundidade para a rocha sã. Entre esta e a linha inferior de 90 $\Omega\cdot m$ ocorre uma faixa que deve corresponder ao substrato cristalino alterado.

Nessa secção, sugere-se a captação de água subterrânea entre as SEVs 47 e 40, visto que nessa faixa a água é pouco condutiva e o mapa potenciométrico indica uma zona de convergência (Marinho e Vasconcelos, 2000a).

Secção geoeletrica 2

Esta secção está situada a cerca de 200m da linha de praia, na bacia do Rio Cauípe, Ceará. Compreende areias de dunas sobrepostas a sedimentos inconsolidados areno-argilosos depositados sobre o embasamento gnáissico regional. Próximo à secção ocorre uma cacimba com nível estático à 2m de profundidade, onde a água tem uma condutividade elétrica de 525 S/m (Marinho e Vasconcelos, 2000b).

O imageamento da resistividade verdadeira nessa secção, utilizando a técnica da krigagem, com altíssima preferência na direção horizontal, está mostrado na Figura 5. Observe a identificação nítida do nível freático superficial.

Sugere-se que a captação de água subterrânea seja feita preferencialmente entre as SEVs 50 e 51, onde encontra-se material arenoso até a cota aproximada de -35m. Abaixo dessa, inicia-se rochas do substrato cristalino com restrita possibilidade hidrogeológica.

Conclusões

A aplicação da técnica geoestatística da krigagem ao modelo multicamadas, decorrente da inversão 1-D de uma sondagem elétrica, resultou em uma imagem da coluna geoeletrica; esta mostrou-se muito expressiva da interpretação da SEV, tanto para geofísicos quanto para outros geocientistas.

Os semi-variogramas experimentais bidimensionais obtidos mostraram que a resistividade é uma variável regionalizada, abrindo espaço para a extensão do imageamento de colunas geoeletricas para o imageamento de secções geoeletricas por krigagem.

As duas secções geoeletricas imageadas nesse trabalho se mostraram consistentes com as informações geológicas/hidrogeológicas disponíveis, tendo sido evidenciadas as principais variações verticais e laterais de resistividade nas secções.

A combinação, aqui proposta, da inversão 1-D de dados de sondagem elétrica seguida do imageamento 2-D por Geoestatística, é de fácil aplicação em relação à análise 2-D da resistividade a partir de um complicado esquema de aquisição de dados de campo e das sofisticadas técnicas 2-D de inversão disponíveis.

Finalmente, a metodologia Geoestatística aqui desenvolvida pode ser aplicada no imageamento de variáveis da perfilagem geofísica, por exemplo, como também no imageamento 2-D de atributos que tenham estruturas grosseiramente horizontais.

Referências

- Abdul Nassir, S.S., Loke, C.Y., e Nawawi, M.N.M., 2000, Salt-water intrusion mapping by geoelectrical imaging surveys : Geophysical Prospecting 48,, 647-661.
- Griffiths, D.J. e Barker, R.D., 1993, Two-dimensional resistivity imaging and modelling in areas of complex geology : Journal of Applied Geophysics, 29, 211-226.
- Landim, P.M.B., 1998, Análise estatística de dados geológicos, UNESP, 226p.
- Lima, O.A.L., Sato, H.K. e Porsani, M.J, 1995, Imaging industrial contaminant plumes with resistivity techniques: Journal of Applied Geophysics 34, 93-108.
- Loke, M.H. e Barker, R.D., 1996, Rapid least-squares inversion of apparent resistivity pseudosection by a quasi-Newton method: Geophysical Prospecting, 44, 131-152.
- Marinho, J.M.L. e Vasconcelos, S.M.S., 2000a, Estudos hidrogeológicos e geofísicos da bacia hidrográfica do Rio Cauípe, Ceará : Relatório de Pes-

Imageamento geoeletrico

- quisa, CNPq/FUNCAP/UFC, Fortaleza, 52p.
- Marinho, J.M.L. e Vasconcelos, S.M.S., 2000b, Estudos geoeletricos/hidrogeologicos da zona costeira da bacia do Rio Caupe, Caucaia, Ceara, Brasil : I Cong. Mundial Integrado de Aguas Subterraneas, ABAS/ALHSUD/IAH, Fortaleza, CD-ROM, Paper 174 (19p.).
- Matheron, G., 1963, Principles of Geostatistics: Economic Geology, 58, 1246-1266.
- Nowroozi, A.A., Horrocks, S.B. e Henderson, P., 1999, Saltwater intrusion into the freshwater aquifer in the eastern shore of Virginia: a reconnaissance electrical resistivity survey: Journal of Applied Geophysics, 42, 1-22.
- Turberg, P. e Barker, R.D., 1996, Joint application of radio-magnetotelluric and electrical imaging surveys in complex subsurface environments: First Break, 14, 105-112.

- Zohdy, A.A.R. e Bisdorf, R.J., 1989, Programs for the automatic processing and interpretation of Schlumberger sounding curves in QuickBasic 4.0, U.S.G.S., Open-File Report, 89-137.
- Zohdy, A.A.R., 1989, A new method for the automatic interpretation of Schlumberger and Wenner sounding curves: Geophysics, 54, 245-253.

Agradecimentos

Gostaríamos de agradecer à Universidade Federal do Ceara e a FUNCAP (Fundo de Amparo à Pesquisa – Ceara) pelo apoio dado ao desenvolvimento desse trabalho.

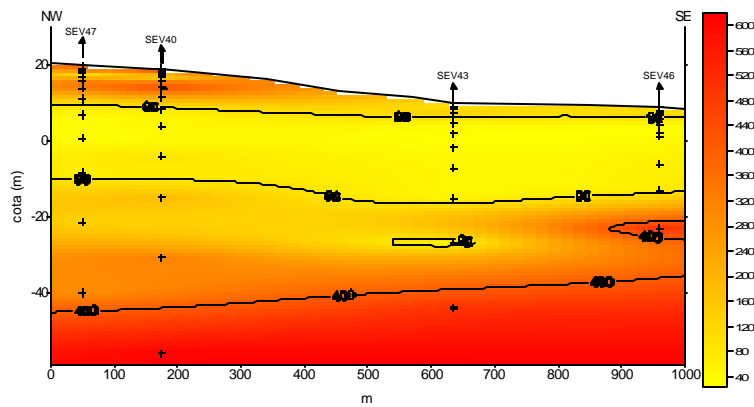


Figura 4 – Imageamento por krigagem da seção geoeletrica 1, a partir dos valores de resistividade (ohm.m) de modelos multicamadas. A tonalidade amarela corresponde ao aquífero freático superficial. O contorno superior de 90 ohm.m acompanha grosseiramente o nível estático.

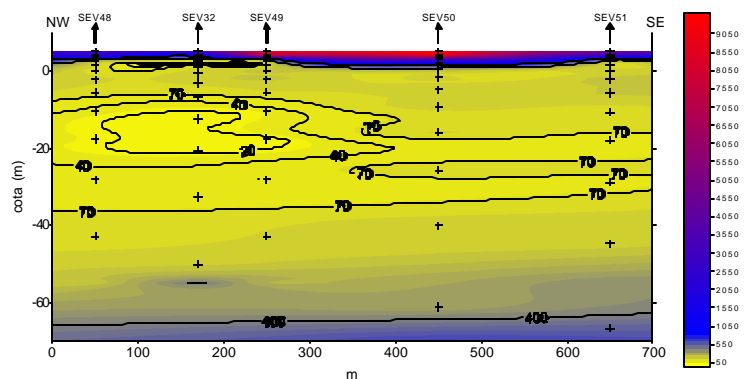


Figura 5 - Imageamento por krigagem da seção geoeletrica 2, a partir dos valores de resistividade (ohm.m) de modelos multicamadas. A tonalidade amarela define a zona saturada em água. A base da cor azul na parte superior da seção marca o nível freático. A cor azul na parte inferior mostra a passagem para o substrato cristalino impermeável.



Inversão bidimensional de sondagens elétricas verticais com algoritmos genéticos

Niraldo R. Ferreira, Milton J. Porsani e Olivar A.L. Lima

CPGG/UFBA

Abstract

This work investigates the two-dimensional (2D) resistivity inversion using genetic algorithm combined with Gauss-Newton method. In order to generate the 2D forward modeling the finite difference method was used. The 2D media parametrization consists of the partition of the media into homogeneous rectangles of fixed dimensions at fixed positions such that only their resistivities will be an unknown parameters. The schlumberger array was used in real data acquired over crystalline rocks. The test over real data produce promising results.

Introdução

O método da eletrorresistividade investiga a distribuição da resistividade elétrica do solo a partir de medidas efetuadas na superfície da Terra. Normalmente considera-se um modelo unidimensional (1D) do meio, estratificado em camadas planas e paralelas. A modelagem matemática é implementada com a teoria da filtragem linear e o processamento digital é feito rapidamente. Esta abordagem é apropriada para áreas sedimentares ou de aluvião. Porém, este procedimento não é adequado em áreas onde há considerável variação lateral de resistividade. Então métodos de interpretação bidimensional (2D) ou tridimensional (3D) devem ser empregados. Nestes casos, deve-se recorrer-se a técnicas numéricas, que neste trabalho foi o método das diferenças finitas 2D (Medeiros, 1987). O meio é dividido em blocos homogêneos e a resistividade destes blocos são os parâmetros de interesse. O ajuste ótimo entre dados e modelagem para obter os parâmetros do meio pode ser obtido de várias modos. Tradicionalmente são empregadas técnicas de inversão linearizada que fazem uma pesquisa local no espaço de modelos, no sentido dos mínimos quadrados. A técnica é eficiente, porém, a dependência de um bom modelo inicial pode produzir solução insatisfatória. Como alternativa, métodos de global têm sido investigados, por exemplo, os algoritmos genéticos (Ferreira, 1999). Estas técnicas são robustas, não dependem de um bom modelo inicial, porém são de custo computacional elevado. Neste trabalho utiliza-se um esquema um esquema híbrido, onde o algoritmo genético pesquisa a região de interesse e a inversão linearizada refina a solução.

Modelagem 2D

A resposta de uma Terra 2D a uma excitação superficial de corrente contínua puntiforme é descrita pela equação de Poisson:

$$-\nabla \cdot \{\sigma(x, z) \nabla \phi(x, y, z)\} = I \delta(x - x_f) \delta(y) \delta(z) \quad (1)$$

onde $\phi(x, y, z)$ é o potencial elétrico, I é a corrente elétrica contínua, $(x_f, 0, 0)$ é a posição da fonte na superfície e $\sigma(x, z)$ é a distribuição de condutividade. Condições de contorno de Neumann na superfície e mista nas laterais e fundo do modelo são também introduzidas (Medeiros, 1987). Embora a distribuição de condutividade seja 2D, o potencial é 3D. Contorna-se esta dificuldade tomando a transformada de Fourier de (1) na variável y obtendo:

$$-\nabla \cdot [\sigma(x, z) \nabla \tilde{\phi}(x, k, z)] + k^2 \sigma(x, z) \tilde{\phi}(x, k, z) = \frac{I}{2} \delta(x - x_f) \delta(z) \quad (2)$$

onde k é a variável da transformada de Fourier e $\tilde{\phi}$ é a transformada de Fourier do potencial e o operador ∇ agora opera apenas nas direções x e z por diferenças finitas produz um sistema linear que pode fornecer $\tilde{\phi}$ para um conjunto ótimo de valores de k . A transformada inversa de Fourier de $\tilde{\phi}$ e as resistividades aparentes ao obtidas de $K_g \Delta \phi$ e K_g' e o fator geométrico do arranjo de eletrodos $\Delta \phi$ ao diferenças de potencial escolhidas na superfície.

Inversão linearizada

Empregou-se o método de Gauss-Newton com amortecimento trabalhando no domínio do logaritmo dos parâmetros. A aplicação do processo mínimos quadrados produz a expressão (Sen et al, 1995)

$$\mathbf{m}_{k+1} = \mathbf{m}_k + (\mathbf{G}^T \mathbf{G} + \lambda \mathbf{I})^{-1} \mathbf{G}^T \Delta \mathbf{d} \quad (3)$$

onde n indica o número de iterações no processo recursivo \mathbf{m} é o vetor de parâmetros \mathbf{G} é a matriz sensibilidade λ é o parâmetro de amortecimento e $\Delta \mathbf{d}$ é a diferença entre observações e modelagem.

Algoritmos genéticos (AG)

São métodos não lineares de otimização global baseados nos mecanismos de seleção natural e da genética. Define-se o espaço de busca que estabelece para cada parâmetro um intervalo discretizado. A pesquisa de investigação deste espaço é feita com uma população de modelos. Os parâmetros são representados através de

uma codificação, geralmente binária, formando cadeias similares a cromossomos. Os AG consistem basicamente de três operadores: seleção, cruzamento e mutação (Goldberg, 1989). O processo começa com a escolha aleatória de uma população inicial de modelos no espaço de busca. Avalia-se o desempenho dos modelos com a expressão (Sen et al, 1995):

$$f = 1 - \frac{2 \sum |y_i - x_i|^2}{\sum |y_i + x_i|^2 + \sum |y_i - x_i|^2} \quad (4)$$

onde x_i representam as observações, y_i a modelagem e f é a função a ser maximizada. O operador de seleção é o primeiro a atuar sobre a população. Os modelos da geração corrente são selecionados segundo uma probabilidade P_s dependente de seus valores de desempenho. a ação do segundo operador, cruzamento começa com o acasalamento randômico dos modelos selecionados e o sorteio aleatório dos pontos de cruzamento na cadeia binária. Os bits à direita dos pontos de cruzamento, em cada par, são então permutados seguindo uma probabilidade de cruzamento P_x . Durante este processo os bits dos modelos podem sofrer mutação com uma probabilidade P_m , favorecendo a diversidade na população. Os modelos assim obtidos formam uma nova geração sobre a qual esta seqüência de procedimentos é repetida até a convergência entre os desempenhos médio e máximo da população. Utiliza-se também uma estratégia elitista denominada operador de renovação (Sen et al, 1995). Ele controla a influência dos indivíduos de uma geração na população seguinte, restando no processo uma parcela dos melhores indivíduos, visando melhorar o desempenho global do AG.

Neste trabalho propõe-se um algoritmo combinado de pesquisa local e global visando compartilhar o trabalho entre os dois métodos, para cada um agir na sua faixa de melhor desempenho. O AG atua procurando a região de interesse e a pesquisa local age definindo o mínimo global nesta região. Existem muitas possibilidades de hibridizar o AG (Chunduru et al, 1996), (Ferreira, 1999). Utilizou-se a formulação simples de permitir ao AG evoluir normalmente e o modelo de melhor desempenho ao final do AG serve de partida para a inversão linearizada (Ferreira, 1999).

Resultados Numéricos

O teste numérico apresentado foi realizado com dados reais obtidos no município de Conceição do Coité, Bahia, Brasil (Pinheiro Neto, 2000), região de terrenos cristalinos com alto grau de metamorfismo. O levantamento consistiu de 20 sondagens schlumberger alinhadas e não regularmente espaçadas como indica a Figura 1. As SEV têm AB/2 crescendo de 5 em 5 metros a partir de 7,5 metros. Na estação S5 existe um poço tubular. Existe uma falha geológica na altura da estação S6. Entre as estações S12 e S17 existe um trecho seco do açude Boa Vista com evidências de precipitação salina e na altura da estação S19 existe afloramento. O modelo consiste de um arranjo com 5

níveis de blocos retangulares, cada nível com 27 unidades, totalizando 135 blocos, cada um com 50 metros de largura e profundidades indicadas na Figura 1. A grade de diferenças finitas tem 302 nós na direção horizontal separados de 5 metros, exceto 5 nós em cada extremidade lateral destinados a compor as condições de contorno. Na vertical são 18 nós, sendo que os três mais profundos também são destinados às condições de contorno (Ferreira, 1999). A Figura 1 mostra o modelo inicial estimado a partir de inversões 1D e os gráficos de contorno dos modelos de bloco obtido com a inversão linearizada e com o algoritmo combinado. Na Figura 2 tem-se as pseudo-seções dos dados e das inversões linearizada e do método combinado. Para tratamento destes dados a inversão linearizada utilizou 10 iterações com fator de amortecimento $\lambda = 0,1$. O algoritmo combinado utilizou uma população de 250 modelos em 200 gerações, com probabilidades de 0,6 para cruzamento, 0,95 para renovação e 0,01 para mutação. Para refinar a solução genética foram utilizadas 10 iterações de inversão linearizada.

Conclusões

Apresentou-se um método para inversão simultânea de SEVs em meios com variação 2D de resistividade. A técnica combina inversão linearizada 2D com algoritmos genéticos. O método foi aplicado a dados reais obtidos em região com solo cristalino. Os resultados obtidos são promissores.

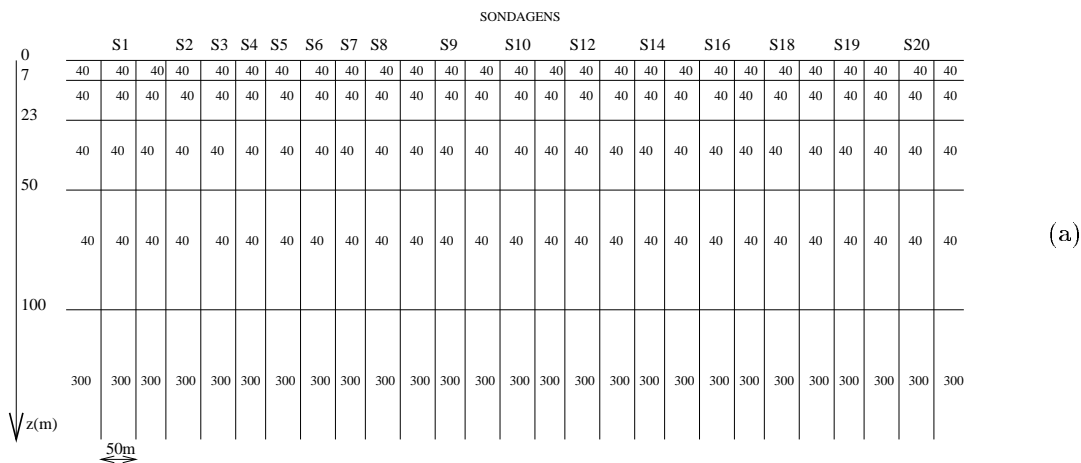
Agradecimentos

Os autores deste trabalho agradecem ao CPGG/UFBA, DEE/UFBA e CNPq, que possibilitaram a realização desta pesquisa.

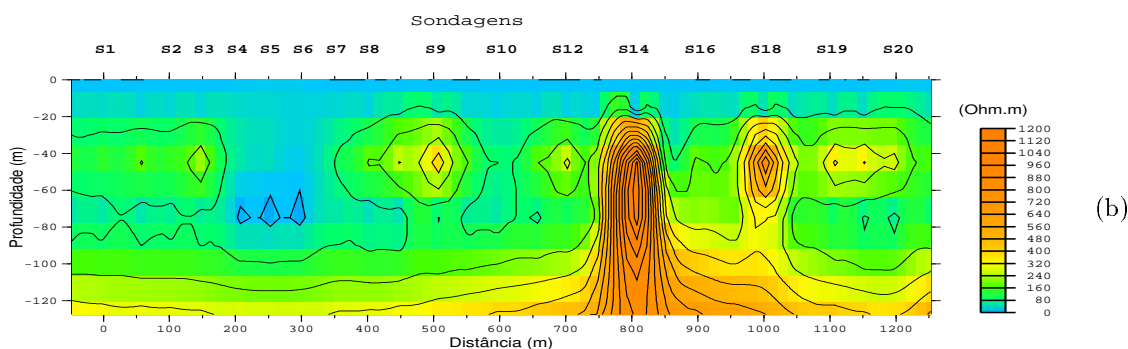
Referências

- Chunduru, R.K., Sen, M.K., and Stoffa, P.L., 1996, 2-D resistivity inversion using spline parameterization and simulated annealing: *Geophysics*, 61, 151-161.
- Ferreira, N.R., 1999, Inversão de dados de eletrorresistividade em meios bidimensionais, Tese de Doutorado, CPGG/UFBA, 90p.
- Goldberg, D.E., 1989, Genetic algorithms in search, optimization, and machine learning, Addison-Wesley Publ. Co., Inc., 412p.
- Medeiros, W.E., 1987, Eletro-resistividade aplicada à hidrogeologia do cristalino: Um problema de modelamento bidimensional, Dissert. de Mestrado, PPPG/UFBA, 149p.
- Pinheiro Neto, V., 1999, Modelagem petrofísica de rochas cristalinas fraturadas, Tese de doutorado (em andamento), CPGG/UFBA.
- Sen, M.K., Stoffa, P.L., 1995, Global optimization methods in geophysical inversion, Elsevier publications.

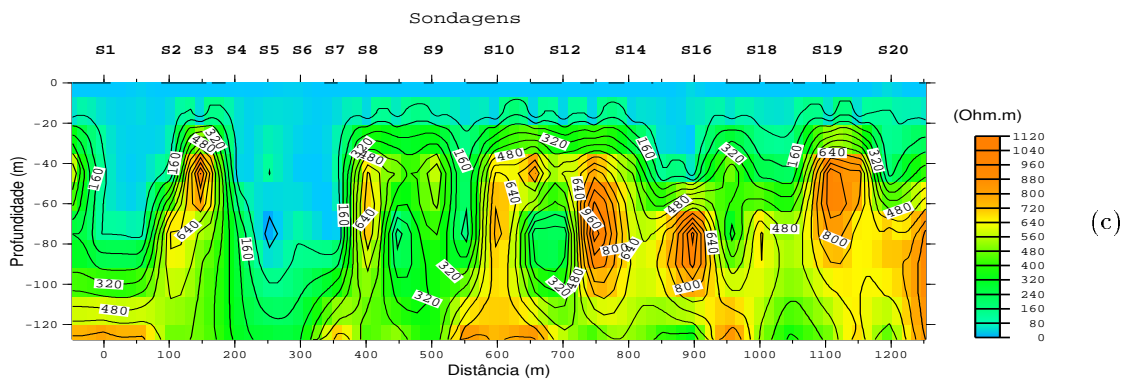
Inversão 2D de SEV com AG



(a)



(b)



(c)

Figura 1: Modelo de Blocos para o dado real: (a) Modelo inicial para a inversão linearizada; (b) Curvas de contorno do modelo obtido com com norma 1; (c) Curvas de contorno do modelo obtido com o algoritmo combinado.

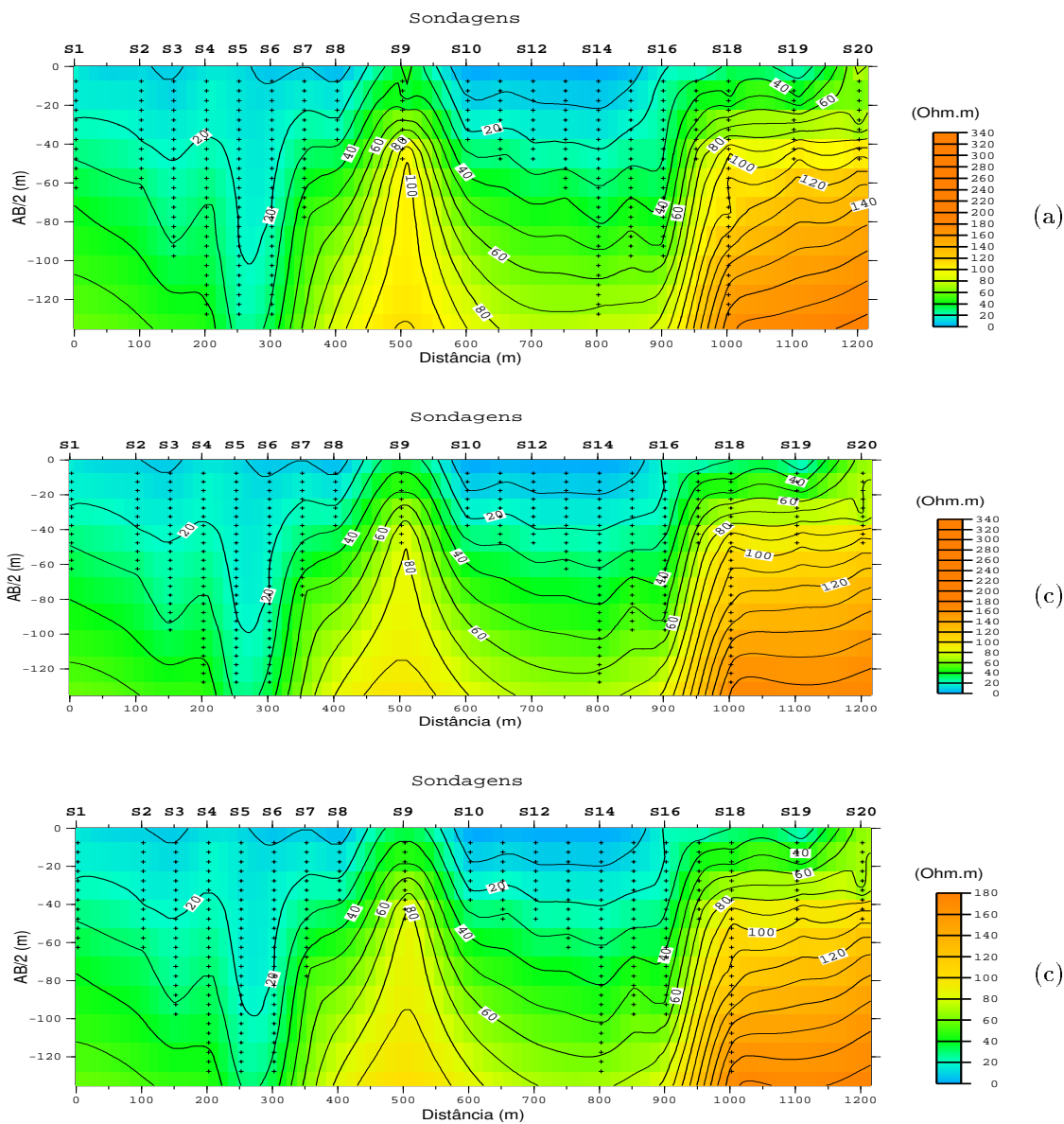


Figura 2: Pseudo-seção eletrorresistiva Schlumberger para: (a) Dado real; (b) Inversão linearizada norma 2; (c) Método combinado



Investigações eletromagnéticas (MT/TEM) na porção continental da bacia do Espírito Santo: primeiros resultados

Flaviana Almeida Costa, Sergio Luiz Fontes, Emanuele Francesco La Terra e Carlos Roberto Germano
Observatório Nacional – MCT, Brasil; flavia@dge1.on.br

Abstract

A 200 Km geophysical transect crossing both on shore terrains of the Espírito Santo basin and the contiguous crystalline region has recently been established. It includes magnetotellurics - MT, transient electromagnetics - TEM, potential field - magnetic and gravimetric measurements as part of a multi-institutional project involving UENF, UnB, Petrobras and Observatório Nacional aiming at the regional characterization of the basin. The objectives of the study comprehend better knowledge of the basement structure, continental crust - oceanic crust contact, crust- mantle contact, lateral variations of crustal structures, etc. This paper is concerned with the very first results obtained with the MT and TEM methods along the transect. Main results to date are the geoelectrical signatures of the on shore basin limits and the Colatina Vitória fault.

Introdução e objetivos

A abertura do setor petrolífero brasileiro estabeleceu um novo cenário para a atuação de empresas, organismos públicos e instituições de ensino e pesquisa. Tal fato determina a necessidade do conhecimento detalhado do potencial de cada área sedimentar e das reservas brasileiras.

A Bacia do Espírito Santo possui algumas peculiaridades que as tornam bastante interessante para um estudo tectônico. No Jurássico tardio, ao início da ruptura do Gondwana, ela se posicionava na zona limítrofe a sul da Grande Depressão Afro-Brasileira. Esse posicionamento também representa uma zona limite do grau de estiramento litosférico (grau mínimo) para a ocorrência de vulcanismo, já que as bacias a norte do Espírito Santo não apresentam sinais de tais eventos. Além desse interesse científico, a Bacia do Espírito Santo está relacionada dentre as bacias brasileiras que mais atraem interesse por parte das companhias de petróleo. Isso se deve à sua similaridade e conformação com a bacia de Campos e ao seu prematuro estágio atual de exploração de hidrocarbonetos.

Visando expandir os conhecimentos sobre a evolução termomecânica e o potencial em petróleo da Bacia do Espírito Santo, foi proposta pelo LENEP (envolvendo diversas instituições: ON, UnB e PETROBRÁS), a modelagem tectonofísica desta bacia. Levantamentos geofísicos incluindo os métodos eletromagnéticos e potenciais magnético e gravimétrico estão sendo conduzidos ao longo de um perfil de cerca de 200

Km, que atravessa sedimentos na porção continental da bacia e o cristalino.

Este trabalho apresenta a contribuição das sondagens eletromagnéticas para a modelagem tectônica da bacia do Espírito Santo, empregando os métodos magnetotelúrico - MT e eletromagnético transiente - TEM, com medidas espaçadas entre 5 e 10 Km ao longo do perfil referido. O primeiro modelo geolétrico delinea estruturas da bacia e do seu embasamento e a assinatura geolétrica da falha de Colatina, além de registrar a presença de condutor crustal regional já observado em outras áreas do sudeste brasileiro (FIGUEIREDO et al. 1997, FONTES et al. 2000).

Descrição Geológica-Geotectônica da área

A Bacia do Espírito Santo (Fig.1) localiza-se na margem continental leste do Brasil, entre os paralelos 18° e 20° de latitude sul, ocupando uma área aproximada de 50.000 km², os quais 5.000 km² são emersos. A porção emersa consiste em uma faixa alongada delimitada, a sul, pelo Alto de Vitória, a oeste, pelo embasamento cristalino pré-cambriano da Faixa Ribeira e, a norte, pelo Canyon de Mucuri. Este último é um limite arbitrário, assim como as extensões para o mar dos limites norte e sul.

As bacias da margem continental leste brasileira, entre as quais se situa a Bacia do Espírito Santo, estão geneticamente relacionadas à ruptura do Supercontinente Gondwana. O tectonismo extensional ocorreu principalmente no Neocomiano e praticamente cessou no final do Aptiano, quando os continentes já estavam separados e a crosta oceânica formava-se entre a América do Sul e a África.

Feições que se destacam na Bacia

Vulcanismo Terciário: além dos basaltos neocomianos da fase rift, comuns nas bacias de Santos e Campos (PONTE et al. 1978), existem ainda os derrames basálticos da Formação Abrolhos que ocorrem principalmente no Eoceno Médio. Essa ocorrência vulcânica criou condições geomórficas para o desenvolvimento de uma plataforma carbonática extensa (250 km de largura), que destaca-se no contexto da margem leste brasileira.

Paleocanyons de Regência e Fazenda Cedro: nas áreas de influência dos paleocanyons de Regência e Fazenda Cedro, as sequências sedimentares anteriores ao Cenomaniano foram total ou parcialmente removidas e substituídas por uma sedimentação de borda de talude, composta basicamente por folhelhos

Investigações eletromagnéticas (MT/TEM) na bacia do Espírito Santo: primeiros resultados

e intercalações de arenitos turbidíticos. Esses corpos arenosos são importantes reservatórios da bacia.

Estruturação da Bacia e áreas adjacentes

A bacia implantou-se em terrenos metamórficos de médio a alto grau, possivelmente arqueanos, total ou parcialmente retrabalhados nos ciclos Transamazônicos e Brasileiro. A estruturação desses terrenos, muito anterior à formação da bacia, foi um dos fatores que condicionaram todo o sistema de *rifts* desenvolvidos durante a ruptura continental (ASMUS & GUAZELLI 1981)

O embasamento da Bacia do Espírito Santo consiste em gnaisses, granulitos, migmatitos e granitóides, cuja estruturação possui direção geral N-NE (CORDANI et al. 1970).

CUNHA (1985), analisando imagens de radar, caracterizou quatro direções estruturais principais nos terrenos pré-cambrianos sem cobertura sedimentar: N20-30E, N60-80E, N10-25W e N45-60W.

As estruturas mapeadas na bacia são falhas normais, falhas listricas e domos de sal. São ainda descritas estruturas arqueadas associadas a pequenas falhas de empurrão, na parte norte da área emersa.

Aquisição, Processamento e inversão dos dados MT-TEM

A primeira etapa de campo (realizada em abril/2001) consistiu de 8 sondagens MT-TEM espaçadas entre 5 e 10 Km, com informação entre 5000 Hz e 200 Hz (dada pelo TEM) e 300 Hz e 0,001Hz com o método MT. Os dados dos campos elétricos e magnéticos foram medidos utilizando-se dois equipamentos EMI nas direções norte (XY) e leste magnético (YX), com os dipolos elétricos espaçados com cerca de 100m de comprimento. Os dados TEM foram obtidos com *loops* de 50 e 100m de lado, nas configurações *single-loop* e *in-loop*, utilizando-se o equipamento Sirotem MK3.

Numa segunda maior campanha de campo (programada para agosto/2001), estão previstas mais 30 sondagens MT-TEM ao longo do perfil, que vai de Povoação-ES, cruzando a linha de charneira da bacia, até Baixo Guandu-ES, já no embasamento que dista cerca de 100 km da borda oeste da bacia (Fig. 1).

Os dados MT foram processados utilizando técnicas convencionais no domínio da frequência. Além de fornecer uma estimativa da condutividade elétrica nas camadas mais rasas, os dados TEM também serão utilizados para a correção do efeito *static shift* observado em algumas sondagens MT.

Para a modelagem geoeétrica 2-D preliminar, foi utilizado o algoritmo de inversão não linear proposto por RODI & MACKIE, 2001.

Resultados

Foram observados valores acima de 3.000 Ω .m para a resistividade elétrica nas zonas cristalinas, enquanto a resistividade elétrica na região de borda da bacia está em torno de 100-700 Ω .m. Os dados são de boa qualidade em geral, tanto nas zonas cristalinas quanto próximo a zona sedimentar. Entretanto, nas proximidades de Colatina os dados apresentam-se mais ruidosos e com comportamento mais complexo, o que confirma a assinatura geoeétrica da zona de falhamento de Colatina. O modelo geoeétrico 2-D gerado a partir dos dados preliminares, está limitado a uma profundidade de 3km e evidencia a falha Colatina - Vitória, na porção NW do perfil (observado em laranja e amarelo na Fig. 2) e o limite da porção continental da bacia do Espírito Santo (zona menos resistiva à SE do perfil, Fig. 2). As pseudo-seções observadas e calculadas da fase (graus) x frequência, nos modos TE e TM, são apresentadas na Fig. 3. O modelo geoeétrico 2-D da Fig. 2 foi obtido com base apenas nos dados da fase, porque ainda não foi efetuada a correção estática. O ajuste deste modelo preliminar pode ser considerado razoável, em especial o modo TM, conforme observado na Fig. 3.

Conclusões

A variação da resistividade na porção SE do perfil, observado no modelo geoeétrico 2-D (Fig. 2), registra a presença de rochas alteradas possivelmente associadas a fraturamentos, marcando assim o limite continental à NW da Bacia, com profundidade em torno de 100 e 1000 m. Observa-se também a assinatura geoeétrica da falha Colatina - Vitória, expressa por uma zona vertical de resistividade inferior ao embasamento cristalino.

O modelo mostra ainda uma tendência menos resistiva a cerca de 2.600 m de profundidade. Isso nos induz a identificar a possível presença de um condutor crustal. Espera-se com os dados da segunda campanha de campo, atingir maiores profundidade e assim confirmar a presença deste condutor.

Agradecimentos

Este trabalho conta com financiamento do PADCT-CTPETRO, por intermédio de projeto coordenado por Fernando Moraes, do LENEP/UENF. A CAPES e o CNPq participam com bolsas de mestrado (F.A.C.) e de produtividade (S.L.F.), respectivamente.

Referências Bibliográficas

ASMUS, H. E.; GOMES, J. B.; PEREIRA, A. C. B. 1971. "Interpretação geológica regional da bacia

Investigações eletromagnéticas (MT/TEM) na bacia do Espírito Santo: primeiros resultados

- do Espírito Santo.” In: SBG, Congresso Brasileiro de Geologia, 25, São Paulo, Anais, 3: 235-252.
- ASMUS, H. E. & GUAZELLI, W. 1981. “Descrição sumária das estruturas da margem continental brasileira e das áreas oceânicas adjacentes: hipótese sobre o tectonismo causador e implicações para os prognósticos do potencial de recursos minerais.” In: ASMUS, H. E.; ed. Estruturas e tectonismo da margem continental brasileira e suas implicações nos processos sedimentares e na avaliação do potencial de recursos minerais. Rio de Janeiro, PETROBRÁS /CENPES /DINTEP. p. 187-269. (Série Projeto REMAC 9).
- CORDANI, U. G & BLAZEKOVIĆ, A. 1970. “Idades radiométricas das rochas vulcânicas de Abrolhos.” In: Congresso Brasileiro de Geologia, 24. Brasília, 1970. Anais Brasília, SBG V.1, 265-270.
- CUNHA, F. M. B. 1985. “Integração das bacias do litoral do sul da Bahia e do Espírito Santo com a faixa pré-cambriana adjacente.” Rio de Janeiro, PETROBRÁS/CENPES, 50p (Rel. Int.).
- EGBERT, G. D. 2000. “Processing and interpretation of Electromagnetic Induction Array Data: A Review”. In: XV Workshop on Electromagnetic Induction in the Earth, Cabo Frio; Invited Review Papers, 223 – 255.
- FIGUEIREDO, I., FONTES, S.L. and BRAGA, L.F.S., 1997. Electromagnetic Imaging of Mountain chains in southeast Brazil. Proceedings of the 5th International Congress of the Brazilian Geophysical Society., vol 2, 770-771.
- FONTES, S.L., FIGUEIREDO, I., BRITO, P.M.A., VITORELLO, I. and PADILHA, A.L., 2000. “Mid crustal conductivity of the Ribeira Fold Belt, SE Brazil”. 31st International Geologic Congress, Rio de Janeiro.
- PONTE, F. C. & ASMUS, H. E. 1978. “Geological framework of the Brazilian continental margin.” Geol. Rundschau, v.67, nº 1, p. 201-235.
- RODI, W. and MACKIE, R.L., 2001. Nonlinear conjugate gradients algorithms for 2-D magnetotelluric inversion. Geophysics, 66, 1, 174-187.

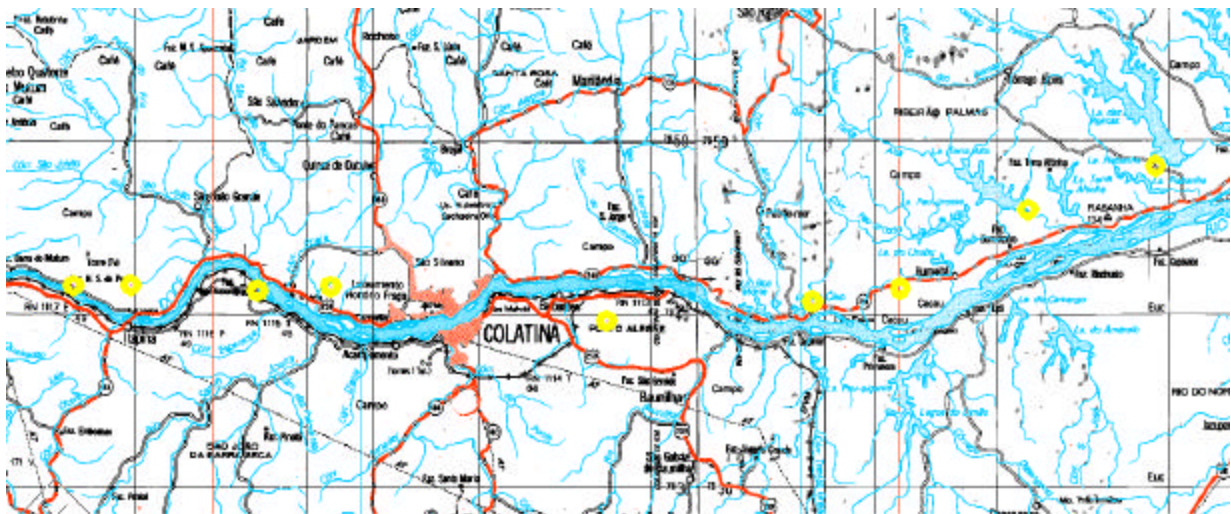


Fig.1. Mapa de localização das primeiras sondagens MT-TEM ao longo do perfil

Investigações eletromagnéticas (MT/TEM) na bacia do Espírito Santo: primeiros resultados

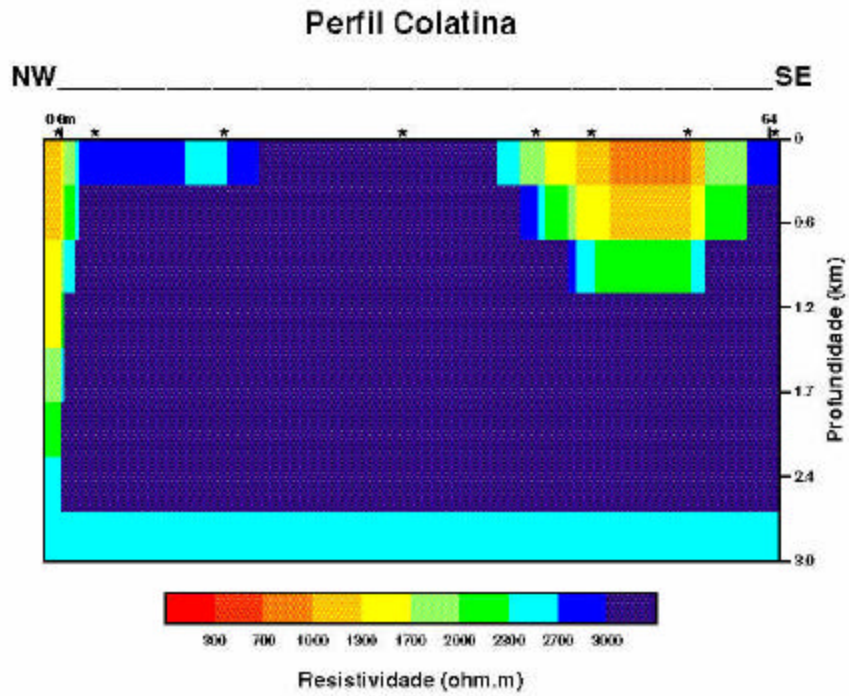


Fig. 2 Modelo geoeétrico 2-D do perfil Colatina

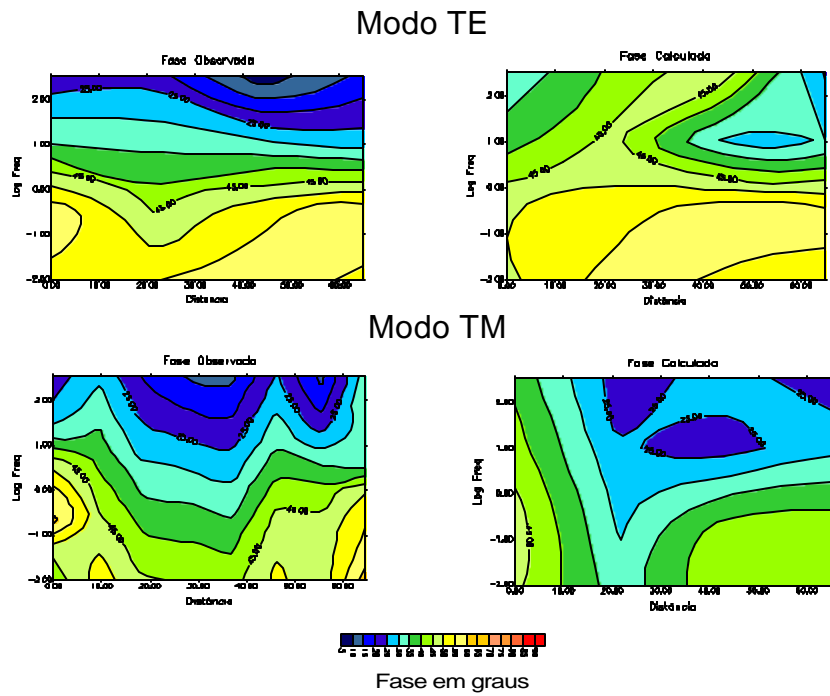


Fig. 3 Pseudoseções das fases observada e calculada (modos TE e TM) para o modelo da Fig. 2



Metamorphoses of Maxwell's Equations

Luiz Rijo; Universidade Federal do Pará, Brazil
 rijo@amazon.com.br

Abstract

Maxwell's equations are the starting-point of electrical geophysics. From Magnetotelluric method (low frequencies) to GPR (high frequencies) they are behind of every electric geophysics techniques.

Since their origin, more than one hundred years ago, Maxwell's equations have been redressed in many different manners. Maxwell started with a set of twenty equations. Heaviside purified them to four vector equations. With the contribution of Einstein's special theory of relativity the four vector equations are recast into two tensor equations. Now, with the aid of Clifford geometric algebra Cl_3 they have been reduced to just one single equation.

The saga of Maxwell's equations helps to clarify the physics of electromagnetism and simultaneously gives us more confidence to work with them

Introduction

Maxwell's equations are omnipresent throughout the electrical geophysics literature. Transient and Magnetotelluric soundings, Induction logging and GPR are few of many geophysical applications of Maxwell's equations. They are the starting-point of the theory and applications of all electric and electromagnetic geophysical methods [5], [9], [13]. In these references, as in many others in geophysics and electrical engineering, Maxwell's equations are quoted in the following *specialized* vector form (SI units):

$$\nabla \times \mathbf{E} + \partial \mathbf{B} / \partial t = 0, \quad (1)$$

$$\nabla \times \mathbf{H} - \partial \mathbf{D} / \partial t = \mathbf{J}, \quad (2)$$

$$\nabla \cdot \mathbf{B} = 0, \quad (3)$$

$$\nabla \cdot \mathbf{D} = \rho, \quad (4)$$

in which we have: \mathbf{E} *electric field*, \mathbf{D} *electric flux density*, \mathbf{H} *magnetic field* and \mathbf{B} *magnetic flux density*. ρ and \mathbf{J} are, respectively, the *free charge* and *free current densities*. Together, these quantities form the electromagnetic field.

A question commonly asked by my students is: what, in fact, is an electromagnetic field? What are the differences between \mathbf{E} and \mathbf{D} , \mathbf{B} and \mathbf{H} ? Is the sequential order of Maxwell's four vector equations relevant or not? Motivated by questions of this kind I decided to write this review paper. The aim is to present here an interesting account of Maxwell's

equations displayed in four different mathematical formalisms. Starting with the twenty original Maxwell's equations it will be seen that after successive reformulation they are reduced to four vector equations and then to two tensor equations and finally they come down to just one single equation. As reward of this journey, we will learn along the way that electric and magnetic fields are simply different aspect of a well-defined four-dimensional physical (geometrical) entity, the electromagnetic field. Also, we will see, accord to the physics of the electromagnetism, that the sequence of the four vector Maxwell's equations cannot be chosen arbitrary. Computationally, however, it does not matter which order the equations are displayed.

Maxwell's original equations

The set of four vector equations (1) - (4) popularly known as Maxwell's equations does not appear in Maxwell's writings. In fact, he introduced in his genial *Treatise on Electricity and Magnetism* [7] twenty differential equations in Cartesian coordinates, as a framework to explain in a unified theory all experimental observations on electricity, magnetism and optics known at his time. His ideas took many years to be comprehended by other scientists, essentially because of the intricate mathematical apparatus he used to construct the electromagnetic theory. As I said, this horrible sequence of formulas that constitutes the genuine Maxwell's equations is formed by twenty differential equations subdivided into eight groups:

$$a = dH / dy - dG / dz, \quad (1a)$$

$$b = dF / dz - dH / dx, \quad (2a)$$

$$c = dG / dx - dF / dy, \quad (3a)$$

$$da / dx + db / dy + dc / dz = 0, \quad (4b)$$

$$P = cdy / dt - bdz / dt - dF / dt - d\psi / dx, \quad (5c)$$

$$Q = ady / dt - cdz / dt - dG / dt - d\psi / dy, \quad (6c)$$

$$R = bdy / dt - adz / dt - dH / dt - d\psi / dz, \quad (7c)$$

$$4\pi u = d\gamma / dy - d\beta / dz, \quad (8d)$$

$$4\pi v = d\alpha / dz - d\gamma / dx, \quad (9d)$$

$$4\pi w = d\beta / dx - d\alpha / dy, \quad (10d)$$

$$u = CP + (K/4\pi)dP/dt, \quad (14f)$$

$$v = CQ + (K/4\pi)dQ/dt, \quad (15f)$$

$$w = CR + (K/4\pi)dR/dt, \quad (16f)$$

$$df/dx + dg/dy + dh/dz = 0, \quad (17g)$$

$$a = \mu\alpha, \quad (18h)$$

$$b = \mu\beta, \quad (19h)$$

$$c = \mu\gamma. \quad (20h)$$

The vector calculus had not been developed in Maxwell's time. That is why he employed such roundabout set of equations. In fact, Maxwell's work contributed significantly to the development of vector calculus.

Heaviside redresses Maxwell's equations

In 1885, twelve years after the publication of Maxwell's Treatise, Heaviside after a long and arduous research work published a completely revised set of Maxwell's equations translated in the language of vector calculus, created independently by Gibbs and himself [3], [4]. He condensed the potentials and fields components that appear in the long list of Maxwell's equations (1a – 20h) into a compact set of eight vector equations:

$$\mathbf{B} = \text{curl } \mathbf{A}, \quad (a)$$

$$\text{div} \mathbf{B} = 0, \quad (b)$$

$$\mathbf{E} = \nabla \mathbf{u} \mathbf{B} - \mathbf{A} - \text{grad } \psi, \quad (c)$$

$$\mathbf{C} = \text{curl } \mathbf{H} \quad (d)$$

$$\mathbf{D} = \varepsilon \mathbf{E}, \quad (e)$$

$$\mathbf{C} = (k + \varepsilon d/dt) \mathbf{E}, \quad (f)$$

$$\text{div} \mathbf{D} = \rho, \quad (g)$$

$$\mathbf{B} = \mu \mathbf{H}. \quad (h)$$

Here, Heaviside used the following identifications:

$$\mathbf{B} = (a, b, c), \mathbf{E} = (P, Q, R), \mathbf{C} = (4\pi u, 4\pi v, 4\pi w)$$

$$\mathbf{A} = (F, G, H), \mathbf{H} = (\alpha, \beta, \gamma) \text{ and } \mathbf{D} = (f, g, h).$$

Also, he used the symbol $\nabla \mathbf{u} \mathbf{B}$ for expressing the vector product $\mathbf{u} \times \mathbf{B}$.

Combining (g) and (e), (b) and (h), (c) and (a), and (d) and (f), Heaviside came out with the following four vector equations:

$$\text{div}(\varepsilon \mathbf{E}) = \rho, \quad (g \ \& \ e)$$

$$\text{div}(\mu \mathbf{H}) = 0, \quad (b \ \& \ h)$$

$$-\text{curl } \mathbf{E} = \mu \dot{\mathbf{H}}, \quad (c \ \& \ a)$$

$$\text{curl } \mathbf{H} = k\mathbf{E} + \varepsilon \dot{\mathbf{E}}. \quad (d \ \& \ f)$$

These are the four vector equations that gave rise all different versions of Maxwell's equations find today in all textbooks on electromagnetism.

Tensor Maxwell's equations

Electromagnetic theory conceived originally by Maxwell was essentially a mechanist subject. Forces, stresses, fluxes and even a material medium (*the ether*) capable to support electromagnetic disturbance were integral parts of the theory [7], [14]. At beginning, it took a great deal of effort by many specialists to understand the mechanism of Maxwell's electromagnetic theory [4]. Among them we distinguish Albert Einstein who in attempt to conciliate the classic Newtonian mechanics with Maxwellian electrodynamics had to reformulate the concepts of space and time resulting in his special theory of relativity. With this new conception, the ether had to be discarded and the three-dimensional electric and magnetic fields turn out to be simply different relativist aspects of a unique quantity, the four-dimensional electromagnetic field.

With the help of theory of relativity, Maxwell's equations gained a new insight and more concise formulation. Starting with the electrostatic Coulomb's law and making use of Lorentz invariance it is well known that Maxwell's equations can be cast as second-rank anti-symmetric tensors in the following manner, [11] (SI units),

$$F_{\alpha\beta,\beta} = (\varepsilon_0 c)^{-1} J^\alpha, \quad (I)$$

$$G_{\alpha\beta,\beta} = 0, \quad (II)$$

where the constant $c = 299792458$ m/s is the speed of light, $\varepsilon_0 = 10^7/(4\pi c^2)$, $J^\alpha = (c\rho, J_x, J_y, J_z)$ is the current 4-vector and $(x^0, x^1, x^2, x^3) = (ct, x, y, z)$. The tensor $F_{\alpha\beta}$ is given by

$$(F_{\alpha\beta}) = \begin{pmatrix} 0 & E_x & E_y & E_z \\ -E_x & 0 & cB_z & -cB_y \\ -E_y & -cB_z & 0 & cB_x \\ -E_z & cB_y & -cB_x & 0 \end{pmatrix}$$

and its dual $G_{\alpha\beta}$ by

$$(G_{\alpha\beta}) = \begin{pmatrix} 0 & -cB_x & -cB_y & -cB_z \\ cB_x & 0 & E_z & -E_y \\ cB_y & -E_z & 0 & E_x \\ cB_z & E_y & -E_x & 0 \end{pmatrix}$$

Automatic summation over each repeated index (Einstein notation) and the partial derivative notation: e.g. $\partial f / \partial x_\beta = f_{,\beta}$ are used in (I) and (II).

In addition to be very simple and elegant these two tensor Maxwell's equations are invariant under Lorentz group [8], [11].

Differential forms and Maxwell's equations

Equations (I) and (II) can be rewritten in the language of differential forms ([2], [8]) as following:

$$d^* \mathbf{F} = (\epsilon_0 c)^{-1} * \mathbf{J}, \quad (\text{A})$$

$$d\mathbf{F} = 0. \quad (\text{B})$$

In equation (B), the space-time 2-form \mathbf{F} is called **Faraday** and it is expressed by $\mathbf{E}d\tau + c\mathbf{B}$, where \mathbf{E} and \mathbf{B} are, respectively, the 3-dimensional 1-form $\mathbf{E} = E_x dx + E_y dy + E_z dz$ and the 3-dimensional 2-form $\mathbf{B} = B_x dydz + B_y dzdx + B_z dxdy$.

The constant c is the speed of light, and $d\tau = cdt$. In equation (A), $*\mathbf{F}$ is the Hodge dual of **Faraday** and $*\mathbf{J}$ represents the 3-form $*\mathbf{J} = c\rho dxdydz + J_x d\tau dydz + J_y d\tau dzdx + J_z d\tau dxdy$.

Equation (B) informs that the exterior derivative of **Faraday** is zero, that is, **Faraday** is a closed 2-form in space-time. On the other hand, the exterior derivative of the dual $*\mathbf{F}$ is not zero unless the space is empty, that is, with no charge and current sources.

These two equations (A) and (B) summarize the

entire content of Maxwell's equation in a simple geometric language.

This is a very elegant and revealing manner to write Maxwell's equation. Misner et al. emphasize this point in their book [8, p 105] when they say: "forms illuminate electromagnetism and electromagnetism illuminates forms".

Like equations (I) and (II), (A) and (B) are also covariant in the sense that their form is preserved under Lorentz transformation.

The Maxwell's equation

Equations (I) and (II) as well as (A) and (B) are simple and very beautiful but they are not yet the most concise formulation of Maxwell's equation. The most compact formulation is obtained via Clifford algebra Cl_3 , [1], a modern geometric language. In a sense, Clifford algebra generalizes the geometry of complex algebra for multidimensional.

With this new language, Maxwell's equations are represented by one single equation:

$$\bar{\partial}\mathbf{F} = (\epsilon_0 c)^{-1} \bar{j} \quad (\text{C})$$

where \mathbf{F} is the space-time bivector $\mathbf{E} + ic\mathbf{B}$, $\bar{\partial}$ means the Clifford conjugate of the paragradiant $\partial = (c^{-1}\partial_t - \nabla)$ and \bar{j} is the involution of the 4-current $j = \rho c + \mathbf{J}$.

Applying the operational rules of Clifford algebra one can show that, [2],

$$\begin{aligned} \bar{\partial}\mathbf{F} &= (c^{-1}\partial_t + \nabla)(\mathbf{E} + ic\mathbf{B}) \\ &= \nabla \cdot \mathbf{E} + (c^{-1}\partial_t \mathbf{E} - \nabla \times \mathbf{B}) + ic\nabla \cdot \mathbf{B} + i(c^{-1}\partial_t \mathbf{B} + \nabla \times \mathbf{E}) \\ &= (\epsilon_0 c)^{-1} (c\rho - \mathbf{J}). \end{aligned} \quad (\text{D})$$

The real scalar part of this equation gives the Coulomb's law, whereas the real vector part is the Maxwell-Ampere's law. The imaginary scalar part is Gauss' law, and the imaginary vector part is Faraday's law.

Wonderful! All electromagnetism packed in one single equation. This is an excellent opportunity to paraphrase Boltzmann's words with respect to Maxwell's equations: "Was it a God who wrote these lines...", [12, p 14].

Conclusions

Equations (I) and (II), (A) and (B) and equation (C) reveal concisely the physics of electromagnetism wrapped by different mathematical dialects. Accord

to them the electric and magnetic fields are hidden behind the four-dimensional electromagnetic field (**Faraday** for example).

We observe that equations (I), (A) and the real part of equation (C) can be rewritten explicitly in the vector form:

$$\nabla \cdot (\epsilon_0 \mathbf{E}) = \rho, \tag{A1}$$

$$\nabla \times (\mathbf{B}/\mu_0) - \partial(\epsilon_0 \mathbf{E})/\partial t = \mathbf{J}, \tag{A2}$$

Likewise, equations (II), (B) and the imaginary part of (C) can be recast as

$$\nabla \cdot \mathbf{B} = 0, \tag{B1}$$

$$\nabla \times \mathbf{E} + \partial \mathbf{B} / \partial t = 0. \tag{B2}$$

The pairs (A1, A2) and (B1, B2) form the famous four vector Maxwell's equations in their most general context. They are not limited to linear, isotropic media, but apply to non-linear, anisotropic and non-homogeneous media. The sources ρ and \mathbf{J} contain implicitly all the information about the electrical properties of the media.

For applications in electric geophysics is more convenient to rewrite the Maxwell's equations as

$$\nabla \cdot \mathbf{D} = \rho_f, \tag{Coulomb's law}$$

$$\nabla \times \mathbf{H} - \partial \mathbf{D} / \partial t = \mathbf{J}_f, \tag{Maxwell- Ampere's law}$$

$$\nabla \cdot \mathbf{B} = 0, \tag{Gauss' law}$$

$$\nabla \times \mathbf{E} + \partial \mathbf{B} / \partial t = 0, \tag{Faraday's law}$$

The electrical flux density \mathbf{D} and the magnetic field \mathbf{H} are generally related with \mathbf{E} and \mathbf{B} by the following constitutive relationship [6]

$$\begin{pmatrix} \mathbf{D} \\ \mathbf{B} \end{pmatrix} = \begin{pmatrix} \epsilon & \xi \\ \zeta & \mu \end{pmatrix} \begin{pmatrix} \mathbf{E} \\ \mathbf{H} \end{pmatrix}$$

In geophysics, ξ and ζ are null, thus $\mathbf{D} = \epsilon \mathbf{E}$ and $\mathbf{B} = \mu \mathbf{H}$. In addition, $\mathbf{J}_f = \sigma \mathbf{E} + \mathbf{J}_{Tx}$, [10].

References

[1] Baylis, W. E. *Electrodynamics: A Modern Geometric Approach*. Springer-Verlag, New York, 1999.
 [2] Flanders, H. *Differential Forms*. Dover Publications, Inc., New York, 1989

[3] Heaviside, O. *Electromagnetic Theory*, Vol. 1, 2, 3. Chelsea Publishing Comp., New York, 1971
 [4] Hunt, B. J. *The Maxwellians*. Cornell University Press, Ithaca, New York, 1991
 [5] Kaufmann A. A and Keller G. V., *Inductive Mining Prospecting. Part I: Methods in Geochemistry and Geophysics 14B*. Elsevier Scientific Publishing Comp. Amsterdam, 1985.
 [6] Kong, J. A. *Theory of Electromagnetic Waves*. John Wiley & Sons, Inc. New York, 1973.
 [7] Maxwell, J. C. *A Treatise on Electricity and Magnetism, Vol. 1 and 2*. Dover Publications, Inc. New York, 1954.
 [8] Misner C. M., Thorne K. R. and Wheeler J. A, *Gravitation*. W H. Freeman and Company, New York, 1975.
 [9] Patra H. P. and Mallick K. *Geosounding Principles, 2. Time-varying Geoelectric Soundings. Methods in Geochemistry and Geophysics 14B*. Elsevier Scientific Publishing Comp. Amsterdam, 1980.
 [10] Rijo, L. *Eletromagnetismo com Mathematica*. In preparation.
 [11] Schwartz, M. *Principle of Electrodynamics*. McGraw-Hill Book Company, New York, 1972
 [12] Sommerfeld A. *Electrodynamics*. Academic Press. New York, 1952.
 [13] Ward S. H. and Hohmann G. W. *Electromagnetic Theory for Geo-physical Applications in Electro-magnetic Methods in Applied Geo-physics – Theory Vol 1*. (Ed. Nabighian, M.), SEG, Tulsa, 1987.
 [14] Whittaker, E. *A History of the Theories of Eather & Electricity* Dover Publications, Inc. New York, 1989.

Acknowledgments

I wish to thank the Organizing Committee of the 7th International Congress of the Brazilian Geophysical Society for inviting me to present this review paper.



Modelagem bidimensional de resistividade por diferenças finitas para um caso de modelo primário heterogêneo

Frederico A. F. de Oliveira e Hédison K. Sato

CPGG/UFBA

Abstract

The choice of suitable boundary conditions plays an important role on two-dimensional resistivity modelling by finite differences. It is known that Dirichlet or Neumann conditions lead to inaccurate numerical evaluation of potential compared to an empirical mixed boundary condition, imposed by the potential related to a primary model, evaluated at the grid boundary. Results show that the mixed boundary conditions using the homogeneous primary model are quite good. This work studies the application effects of the electric potential, derived recently for the horizontally layered model, to impose the mixed boundary conditions on the bidimensional resistivity modelling solution by finite differences.

It presents appropriated expressions of electric potential and its normal derivatives and their numerical evaluations by digital integral filters.

Our preliminary results show that primary model does not rule the accuracy of numerical modelling for lateral extensions used in this work.

Introdução

A escolha das condições de contorno no infinito é fundamental para a modelagem de dados de resistividade aparente pelo método das diferenças finitas. Na solução analítica, supõe-se que o potencial elétrico é nulo no infinito, o que corresponde à condição de Dirichlet. No entanto, como o meio discretizado é finito, os resultados passam a depender da escolha adequada das condições de contorno. Segundo Coggon (1971), a condição de Dirichlet causa subestimativa dos potenciais elétricos nos nós da grade, enquanto a condição de Neumann, a sobrestimativa destes, se comparados com as soluções analíticas para os mesmos modelos.

Dey e Morrison (1979) mostram que o emprego de uma condição empírica do tipo mista é melhor que as anteriores pois tira proveito do comportamento assintótico do potencial elétrico e de suas derivadas normais, que passam a ser avaliadas considerando um modelo geoeletrico primário, usado como base para o cálculo dos potenciais nos nós sobre os limites laterais a grade bidimensio-

nal, não requerendo hipótese *a priori* sobre o comportamento daquela função. As heterogeneidades são, assim, vistas como perturbações sobre o modelo primário. Usando o semi-espaco homogêneo como modelo primário, esses autores comprovam sua assertiva comparando a modelagem analítica com a de diferenças finitas.

No entanto, algumas situações geológicas mais se aproximam de heterogeneidades no interior de um meio de camadas do que em um meio homogêneo, por exemplo plumas de contaminação em aquíferos sedimentares, como ocorre na formação São Sebastião, na Bacia do Recôncavo-BA, conforme de Lima (1993). Ademais, a relevância do modelo primário na modelagem é desconhecida. Assim, o objetivo deste trabalho é analisar a modelagem bidimensional de resistividade para o caso do modelo primário heterogêneo, especificamente o modelo de camadas horizontais.

Formulação do problema e solução por diferenças finitas

Esta solução segue Dey e Morrison (1979). Seja uma fonte pontual de corrente elétrica contínua na superfície de um meio com distribuição bidimensional de condutividade, $\sigma(x, z)$. Procuram-se os potenciais elétricos $\Phi_{i,j}$ que solucionam a equação de Poisson, onde $i = 1, 2, \dots, N$ são os índices dos nós na direção horizontal e $j = 1, 2, \dots, M$, os índices a direção vertical. O problema é formulado partindo-se da aplicação da conservação das cargas elétricas em um volume que envolve a fonte. Como o meio estende-se infinitamente na direção y é conveniente a aplicação de uma Transformada de Fourier nesta direção, o que diminui a dimensão do problema de três para duas. Assim, o problema é formulado no domínio (x, k_y, z) como

$$\nabla \cdot \left[\sigma(x, z) \nabla \tilde{\Phi}(x, k_y, z) \right] + k_y^2 \sigma(x, z) \tilde{\Phi}(x, k_y, z) = \frac{\partial \gamma}{\partial t} \delta(x_s) \delta(z_s). \quad (1)$$

As condições de contorno a serem obedecidas em cada interface de descontinuidade da condutividade são 1) continuidade do potencial $\tilde{\Phi}_{i,j}$, e 2)

continuidade do componente normal do vetor densidade de corrente \mathbf{J} . Na superfície terra-ar, a aproximação da condutividade do ar para a do vácuo resulta na condição de Neumann, dada por

$$\sigma_{i,j} \frac{\partial \tilde{\Phi}_{i,j}}{\partial n} = 0 \quad (2)$$

onde $i = 1, 2, \dots, N$, $j = 1$ e n denota a direção normal à superfície. As condições de contorno *no infinito*, aplicadas nos limites laterais e inferior da malha, são do tipo mista, qual seja,

$$\frac{\partial \tilde{\Phi}_{i,j}}{\partial n} + \alpha \tilde{\Phi}_{i,j} = 0 \quad (3)$$

onde $i = 1$ para $j = 1, 2, \dots, M$ (borda esquerda), $i = M$ para $j = 1, 2, \dots, N$ (borda inferior) e $i = M$ para $j = 1, 2, \dots, M$, correspondente à borda direita. A expressão do potencial no modelo primário presta-se ao cálculo dos potenciais, e derivadas, sobre a fronteira, quando da aplicação das condições de contorno. Entretanto, como o problema é resolvido no domínio da frequência na direção y , aplica-se a Transformada de Fourier à solução do problema de camadas apresentada por Sato (2000), que resulta em

$$\tilde{\Phi} = \frac{I}{\pi \sqrt{2\pi} \sigma_m} \times \int_0^\infty \nu(u, k_y) e^{-(u^2 + k_y^2)^{1/2} \Delta z} \cos(xu) du + \xi(k_y) K_0 \{k_y [(\Delta z)^2 + x^2]^{1/2}\}, \quad (4)$$

$$\frac{\partial \tilde{\Phi}}{\partial x} = \frac{I}{\pi \sqrt{2\pi} \sigma_m} \times \left\{ \int_0^\infty -u \nu(u, k_y) e^{-(u^2 + k_y^2)^{1/2} \Delta z} \operatorname{sen}(xu) du - \frac{x k_y \xi(k_y)}{[(\Delta z)^2 + x^2]^{1/2}} K_1 \left\{ k_y [(\Delta z)^2 + x^2]^{1/2} \right\} \right\}, \quad (5)$$

$$\frac{\partial \tilde{\Phi}}{\partial z} = \frac{I}{\pi \sqrt{2\pi} \sigma_m} \times \left\{ \int_0^\infty \frac{e^{-(u^2 + k_y^2)^{1/2} \Delta z}}{(u^2 + k_y^2)^{1/2}} \frac{\partial \xi}{\partial z} \cos(xu) du - \int_0^\infty \nu(u, k_y) (u^2 + k_y^2) e^{-(u^2 + k_y^2)^{1/2} (\Delta z)} \cos(xu) du - \frac{(\Delta z) k_y H(k_y)}{[(\Delta z)^2 + x^2]^{1/2}} K_1 \left\{ k_y [(\Delta z)^2 + x^2]^{1/2} \right\} \right\}, \quad (6)$$

onde σ_m é a condutividade da camada que contém a fonte, $\nu(u)$ é o termo recorrente da solução do problema de camadas e $u = \lambda^2 - k^2$, sendo λ a constante de separação usada na solução da equação de Laplace em coordenadas cilíndricas, conforme de Oliveira (2001). Essas expressões são convenientes à implementação computacional usando filtros digitais para transformadas integrais desenvolvidos por Anderson (1975).

A equação (1) é integrada em cada elemento de área $\Delta A_{i,j}$ e, com a aplicação do teorema de Green, obtém-se a seguinte solução discreta,

$$- \oint_{L_{i,j}} \sigma_{i,j} \frac{\partial \tilde{\Phi}_{i,j}}{\partial n} dl + \iint_{\Delta A_{i,j}} k_y^2 \sigma_{i,j} \tilde{\Phi}_{i,j} dA = \frac{I}{2} \delta(x_s) \delta(z_s). \quad (7)$$

As equações de diferenças correspondentes à equação (7) encontram-se em Dey e Morrison (1979) e de Oliveira (2001).

Os potenciais $\tilde{\Phi}_{i,j}$ são calculados para um número limitado de frequências k_y e a transformada inversa é feita numericamente ajustando-se uma função-envelope exponencial, cujos coeficientes são ajustados dois a dois, à qual é aplicada a transformada inversa, dada por

$$\int_{k_{y1}}^{k_{y2}} e^{-\alpha k_y} \cos(bk_y) dk_y = \frac{e^{-\alpha k_y}}{a^2 + b^2} \cdot [b \operatorname{sen}(bk_y) - a \cos(bk_y)] \Big|_{k_{y1}}^{k_{y2}}. \quad (8)$$

Implementação computacional

As frequências utilizadas neste trabalho são as mesmas obtidas empiricamente por Medeiros (1987) para o modelo primário do tipo homogêneo, a despeito da disparidade com a solução do potencial em meios horizontalmente estratificados. A avaliação numérica do integral contida na equação (6) encontrou problemas quanto a precisão numérica em todas as frequências, o que se repetiu com o integral da equação (5) nas quatro frequências maiores. O problema foi contornado lançando-se mão do uso do modelo homogêneo nas frequências problemáticas, o que significa que o emprego do modelo primário de camadas limitou-se às bordas laterais e para as seis frequências menores.

Resultados e discussão

Usando o modelo do contato vertical entre um quarto de espaço e uma seqüência de camadas horizontais, alternou-se as resistividades da primeira e última camada na seqüência para simular num mesmo modelo, características distintas de estratificação (figuras 1 e 3). Em cada caso, modelou-se a resistividade aparente Schlumberger, ora montando-se a condição mista de contorno com a solução do potencial para meios homogêneos, ora para meios acamados. O desvio entre as duas modelagens, quantificada por

$$\varepsilon_{i,j} = 100 \times \left(\frac{\rho_c}{\rho_h} - 1 \right) \quad (9)$$

onde ρ_c é a resistividade aparente obtida com o modelo de camadas aplicada a definição das condições de contorno, e ρ_h , com o modelo do semi-espaço homogêneo.

As pseudo-seções nas figuras 2 e 4 mostram que os desvios são praticamente idênticos, visto que varia na faixa de -0,01 a 0,01 %, irrelevante para fins de exploração geofísica. Ainda assim, cabem algumas considerações sobre a distribuição espacial dos desvios. Verifica-se em ambas as pseudo-seções, um incremento do módulo dos desvios com a proximidade da borda lateral direita, onde o caráter de estratificação é mais acentuado, ao contrário do lado esquerdo, onde o meio é indistintamente homogêneo, nos dois modelos.

É possível também relacionar, conjuntamente ao módulo, o sinal dos desvios com os contrastes de resistividade da seqüência de camadas do bloco direito. No modelo da figura 3 o desvio cresce positivamente para a direita e para baixo, chegando a atingir o valor máximo de 0,05 %. Uma explicação para isso pode estar na natureza física do problema. A lei de Ohm estabelece que o módulo do vetor densidade de corrente é diretamente proporcional ao campo elétrico, sendo a condutividade σ a constante de proporcionalidade. Assim, como no segundo modelo a primeira camada é a mais condutiva, concentram-se mais linhas de corrente entre os seus limites, de maneira que as correntes experimentadas pelo estratos inferiores são menores e, por isso, é natural que haja maior imprecisão nos seus cálculos.

A hipótese de que o modelo geoeletrico primário influi na distribuição espacial dos desvios não pode ser ainda descartada. Partindo da premissa de que uma seqüência de estratos horizontais é uma aproximação mais verossímil para o modelo na fronteira, principalmente consideran-

do a geometria retangular dos elementos da malha, os potenciais nos nós sobre a borda da grade são calculados mais corretamente, assim como os demais – calculados a partir destes – o que implica em maior precisão na modelagem das resistividades aparentes, em relação às mesmas para o modelo primário homogêneo. Entretanto, a investigação dessa hipótese depende do conhecimento do comportamento do potencial e suas derivadas normais no domínio da freqüência, o que não foi feito neste trabalho. Nessa direção, testes com modelos menores podem identificar um limite máximo na extensão lateral do modelo para o emprego do modelo primário de camadas horizontais homogêneas.

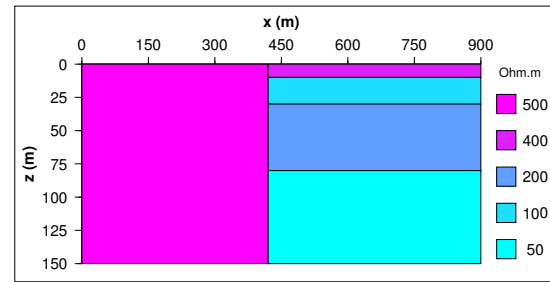


Figura 1: Modelo de resistividades de contato vertical entre um bloco homogêneo e uma seqüência de camadas horizontais.

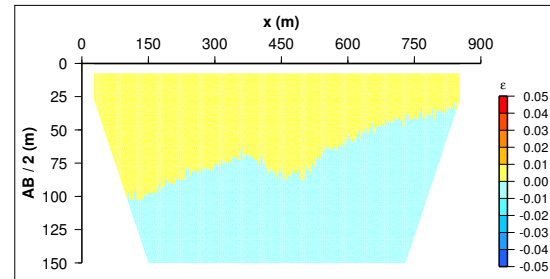


Figura 2: Pseudo-seção dos desvios entre as modelagens com as duas soluções na fronteira.

Conclusões

A implementação parcial de um modelo primário heterogêneo não traz qualquer melhora de significado prático à modelagem bidimensional de diferenças finitas. Ainda assim, o problema não está

Agradecimentos

Ao CPGG/UFBA pelo apoio técnico-financeiro a este trabalho.

Referências

Anderson, W. L. (1975) Improved digital filters for evaluating Fourier and Hankel transform integrals, *Rel. Téc.*, United States Geological Survey.

Coggon, J. H. (1971) Electromagnetic and electrical modeling by the finite element method, *Geophysics*, **36**(01):132–155.

Dey, A. e Morrison, H. F. (1979) Resistivity modeling for arbitrarily shaped two-dimensional structures, *Geophysical Prospecting*, **27**(01):106–136.

de Lima, O. A. L. (1993) Geophysical evaluation of sandstone aquifers in the reconcavo-tucano basin, bahia-brazil, *Geophysics*, **58**(11):1689–1702.

Medeiros, W. (1987) Eletro-resistividade Aplicada à Hidrogeologia do Cristalino: um Problema de Modelamento Bidimensional, Dissert. de Mestrado, Universidade Federal da Bahia, Salvador-Brasil.

de Oliveira, F. A. F. (2001) Modelo Primário de Camadas Horizontais na Modelagem Bidimensional de Resistividade por Diferenças Finitas, Trabalho de Graduação, Universidade Federal da Bahia, Salvador-Brasil.

Sato, H. K. (2000) Potential field from a dc current source arbitrarily located in a nonuniform layered medium, *Geophysics*, **65**(6):1726–1732.

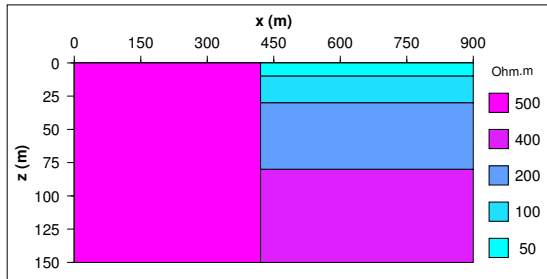


Figura 3: Modelo de resistividades de contato vertical entre um bloco homogêneo e uma seqüência de camadas horizontais.

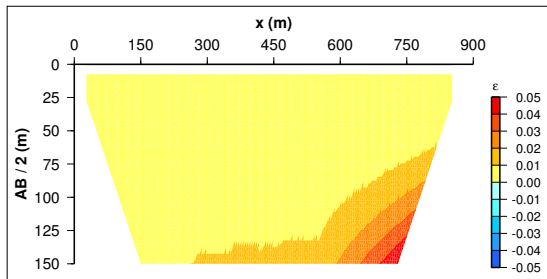


Figura 4: Pseudo-seção dos desvios entre as modelagens com as duas soluções na fronteira.

esgotado, pois resta saber se a causa está na física do problema ou se nas altas frequências. O crescimento sistemático dos desvios, quer positiva ou negativamente, com o aumento do caráter de estratificação do modelo na fronteira sugere que o modelo primário influi na precisão da modelagem.



Modelagem matemática e numérica da propagação de ondas eletromagnéticas acopladas a ondas elásticas, considerando-se o efeito sismomagnético

Ana Beatriz Quintal André, UENF – LENEP, beatrizquintal@bol.com.br

Viatcheslav Ivanovich Priimenko, UENF – LENEP, slava@lenep.uenf.br

Abstract

Interaction of electromagnetic fields with elastic bodies is the subject of many theoretical investigations in mechanics of continua for the last decades. Some variants of direct and inverse problems have been studied leading into the determination of some characteristics of medium. It is very interesting to study this phenomenon due to the possibility of applying this theory to geophysical prospecting and study of earthquake sources. Olsen [6] has represented some experimental results of interactions of power-line electromagnetic field with the Earth crust. He has showed that high harmonic fields are produced by basic harmonic field of frequency $\omega_0 = 60$ Hz. One possible explanation of this effect is a nonlinear interaction of electromagnetic field with seismic field. Our work is dedicated to the investigation of this interaction. We form the basic equations for the description of some variant of this coupling and consider a simple mathematical model of this process. It is possible to construct in linear approximation the solution of corresponding problem, showing that higher harmonic fields' generation process can be described for that model.

Introdução

O objetivo deste trabalho é a modelagem matemática e numérica da interação entre ondas eletromagnéticas e elásticas, considerando-se o efeito sismomagnético, a fim de analisar o comportamento e amplitudes relativas dos campos gerados dessa interação. O estudo desse fenômeno recebe especial atenção devido à possibilidade de aplicação dessa teoria à prospecção geofísica. Na literatura, são encontrados estudos de alguns problemas diretos e inversos que levam à determinação de algumas características do meio, como permeabilidade e permitividade elétricas, eletrocondutividade, as constantes de Lamé etc.

Olsen [6] representou alguns resultados experimentais das interações de campos eletromagnéticos, produzidos por uma linha de corrente, com a crosta. Em seus experimentos, foi possível mostrar que campos harmônicos de alta frequência são produzidos por campos harmônicos básicos de frequência $\omega_0 = 60$ Hz. Uma explicação para esse efeito seria uma interação não linear do campo eletromagnético com o campo sísmico. Este trabalho é dedicado à investigação dessa interação.

Basicamente, são definidos três diferentes tipos de interação entre campos eletromagnéticos e campos sísmicos: o efeito eletrocinético, o efeito piezoelétrico e o efeito sismomagnético. Considera-se o último efeito neste trabalho. As ondas sismomagnéticas podem ser definidas como variações geomagnéticas locais que se propagam simultaneamente à onda sísmica. Neste caso, a frequência e a velocidade dominantes de propagação dessas ondas sismomagnéticas induzidas são iguais à frequência e velocidade da onda sísmica. As ondas eletromagnéticas geradas por esse efeito são transversais à sua direção de propagação, como qualquer onda eletromagnética, mas propagam-se com a mesma velocidade das ondas sísmicas longitudinais que as geraram devido à existência de um estado quasi-estacionário. Essas ondas contêm informações sobre ambos os parâmetros eletromagnéticos e elásticos de um meio.

Modelagem matemática e numérica

O fenômeno de indução sismomagnética no campo magnético constante da Terra é descrito, matematicamente, pela solução dos sistemas de equações elásticas e eletromagnéticas acopladas, considerando-se a existência de um estado eletromagnético quasi-estacionário. No modelo matemático, a propagação de ondas eletromagnéticas e elásticas está sendo considerada do ponto de vista da elasticidade linear e da teoria eletromagnética linearizada. Essas equações estão acopladas devido a termos adicionais que descrevem os efeitos relativos à propagação de um campo eletromagnético em um meio elástico e condutivo.

Foram formuladas as equações básicas para a descrição de algumas formas desse acoplamento e considera-se uma modelagem matemática simples desse processo. Foi construída, em aproximação linear, a solução do problema correspondente mostrando-se que o processo de geração de campos harmônicos de alta frequência pode ser descrito nessa modelagem. Foram elaborados alguns algoritmos para a solução desse problema e conduzidos alguns experimentos numéricos, utilizando-se o MATLAB.

Especificamente, foram elaborados dois modelos matemáticos baseados no efeito sismomagnético, sendo que no primeiro modelo é considerada uma fonte magnética e no segundo, uma fonte sísmica.

Interação entre ondas eletromagnéticas e elásticas

Os dados iniciais usados na modelagem numérica são frequência angular da fonte (50 Hz); permeabilidade magnética do vácuo ($1,26 \times 10^{-6}$ H/m); condutividade elétrica do meio (1 S/m); velocidade da onda elástica (2 000 m/s); densidade do meio (2 650 Kg/m³); campo magnético inicial (40 A/m), comprimento de medida (10 m); velocidade adimensional (5). Os dados iniciais são os mesmos para dois modelos, sendo que no segundo modelo utiliza-se uma frequência da fonte sísmica de $\omega_s = 10$ Hz.

Modelo matemático 1 (fonte magnética)

O problema básico foi construído a partir de equações determinadas experimentalmente, onde os termos eletromagnéticos e elásticos estão acoplados, Dunkin [7]. Assim, considerando-se o processo 1D, supondo constantes os parâmetros eletromagnetoelásticos e considerando a existência de um estado quasi-estacionário, obteve-se o seguinte sistema adimensional:

$$\begin{cases} \frac{\partial h}{\partial t} = R^{-1} \frac{\partial^2 h}{\partial z^2} - \frac{\partial}{\partial z} \left(h \frac{\partial u}{\partial t} \right) - R^{-1} \frac{\partial}{\partial z} j(z, t) \\ \frac{\partial^2 u}{\partial t^2} = v^2 \frac{\partial^2 u}{\partial z^2} - Ph \frac{\partial h}{\partial z} \end{cases}$$

onde h é o campo magnético, u é o campo elástico, j é a densidade de corrente, z e t são as variáveis de espaço e tempo, v é a velocidade sísmica adimensional, $R = \sigma \mu_e L V_o$ é o número de Reynolds e $P = \mu_e H_o^2 \rho^{-1} V_o^{-2}$, sendo ρ a densidade do meio, μ_e a permeabilidade magnética, σ a condutividade elétrica, H_o o campo magnético da Terra, L o comprimento de medida e V_o a velocidade da onda sísmica.

É utilizada uma fonte harmônica eletromagnética de frequência $\omega = \omega_h$ localizada no ponto $z = 0$:

$$j(z, t) = \frac{1}{2\pi} e^{i\omega_h t} \delta(z)$$

O primeiro passo na solução do sistema não-linear é sua linearização. Assim, a solução é representada na forma $(u, h) = (0, h^0) + (u, g)$, onde $\|h^0\| \gg \|g\|$. A solução do problema é dada abaixo (fig. 1, 2 e 3):

$$\begin{cases} h^0(z, t) = h^0(z) e^{i\omega_h t} \\ g(z, t) = \sum_{n=0}^{\infty} g^{(n)}(z) e^{i(2n+3)\omega_h t} \\ u(z, t) = \sum_{n=0}^{\infty} u^{(n)}(z) e^{i2(n+1)\omega_h t}, \quad n = 0, 1, 2, \dots \end{cases}$$

Para determinação das funções $h^0(z)$, $g^{(n)}(z)$ e $u^{(n)}(z)$, $n=0, 1, 2, \dots$, tem-se o seguinte sistema:

$$\begin{cases} h^0(z) = \frac{1}{4\pi} \text{sign}(z) \cdot e^{i\alpha z|z|} \\ u^{(0)}(z) = \frac{P}{2v^2} (h^0(z))^2 * \frac{d}{dz} G_{s,o}(z) \\ g^{(0)}(z) = iR\lambda_{s,0} (h^0(z) \cdot u^{(0)}(z)) * \frac{d}{dz} G_{m,0}(z) \\ \vdots \\ u^{(n)}(z) = \frac{P}{v^2} (h^0(z) \cdot g^{(n-1)}(z)) * \frac{d}{dz} G_{s,o}(z) \\ g^{(n)}(z) = iR\lambda_{s,n} (h^0(z) \cdot u^{(n)}(z)) * \frac{d}{dz} G_{m,n}(z) \end{cases}$$

onde $\alpha = (1/2^{1/2})(i-1)$,

$$\lambda = R\omega_h, \quad \lambda_{m,n} = \sqrt{R(2n+3)\omega_h}, \quad \lambda_{s,n} = \frac{2(n+1)\omega_h}{v},$$

$$G_{m,n}(z) = \frac{1}{2\alpha\lambda_{m,n}i} e^{i\alpha\lambda_{m,n}|z|}, \quad \frac{dG_{m,n}(z)}{dz} = \frac{1}{2} e^{i\alpha\lambda_{m,n}|z|} \text{sign}(z),$$

$$G_{s,n}(z) = -\frac{1}{2\lambda_{s,n}i} e^{-i\lambda_{s,n}|z|}, \quad \frac{dG_{s,n}(z)}{dz} = \frac{1}{2} e^{-i\lambda_{s,n}|z|} \text{sign}(z).$$

Conclusões referentes ao modelo 1

Segundo o modelo do problema de eletromagnetoelasticidade, considerado em aproximação linear, é possível mostrar o efeito de geração de campos harmônicos, de elevada frequência, descrito experimentalmente por Olsen [6]. Foi demonstrado, matematicamente, que a fonte harmônica elétrica (de frequência $\omega_h = 60$ Hz) gera, em resultado da interação do campo eletromagnético com o elástico, oscilações eletromagnéticas com frequências $\omega_n = (2n+3)\omega_h$, $n=0, 1, 2, \dots$, e oscilações elásticas com frequências $\omega_n = 2(n+1)\omega_h$, $n=0, 1, 2, \dots$.

Numericamente, foi mostrado que as amplitudes de tais oscilações tendem a zero, rapidamente, à medida que n aumenta (fig. 4 e 5); e, aumentando-se o valor do campo magnético inicial (campo magnético da Terra), verificou-se significativo aumento das amplitudes $u^{(n)}$ e $g^{(n)}$.

Modelo matemático 2 (fonte sísmica)

Neste modelo, o problema básico foi construído a partir das mesmas equações experimentais que foram utilizadas para a formulação do modelo 1. E, além de feitas as mesmas simplificações iniciais, considera-se $P = 0$. Então, após adimensionalização, o problema básico torna-se:

$$\begin{cases} \frac{\partial h}{\partial t} - R^{-1} \frac{\partial^2 h}{\partial z^2} = -\frac{\partial}{\partial z} \left(h \frac{\partial u}{\partial t} \right) - H^o \frac{\partial^2 u}{\partial t \partial z} \\ \frac{\partial^2 u}{\partial t^2} - v^2 \frac{\partial^2 u}{\partial z^2} = -f^s \end{cases}$$

onde f^s é a fonte sísmica: $f^s = e^{i\omega_s t} \delta(z)$.

A solução para o problema é encontrada na forma (fig. 6):

$$\begin{cases} h(z,t) = \sum_{n=0}^{\infty} h_n(z) e^{i(n+1)\omega_s t} \\ u(z,t) = u_o(z) e^{i\omega_s t} \end{cases}$$

Para determinação de $H_n(z)$, $u_o(z)$, $n = 0, 1, 2, \dots$, recorre-se às seguintes equações:

$$\begin{cases} u_o(z) = \frac{i}{2\omega_s v} e^{-ik|z|}, \\ h_n(z) = i\omega_s (h_{n-1}(z)u_o(z)) * Gm^{(n)}(z), \end{cases}$$

onde $h_{-1}(z) \equiv H^o$,

$$Gm^{(n)}(z) = \frac{R}{2} e^{\alpha_n |z|} \text{sign}(z), \quad \alpha_n = (i-1) \sqrt{\frac{\omega_s (n+1)R}{2}}$$

Conclusões referentes ao modelo 2

Neste modelo, foi demonstrado, matematicamente, que a fonte sísmica (de frequência $\omega_s = 10 \text{ Hz}$) gera, como resultado da interação do campo eletromagnético com o elástico, as oscilações eletromagnéticas com frequência $\omega = (n+1)\omega_s$, $n=0, 1, 2, \dots$.

Numericamente, foi possível verificar que as amplitudes de tais oscilações tendem a zero, rapidamente, à medida que n aumenta (fig. 7). Sendo assim, pode-se desprezar valores de amplitude, calculados a partir de um determinado n , no cálculo do campo eletromagnético, $h(z,t)$, resultante da interação eletromagnetoelástica. Isso torna o processamento numérico mais suave.

Referências

1. PARIÁ G.: Magneto-elasticity and magneto-thermo-elasticity. Adv. Appl. Mech. 1967, 10, No.1.
2. ERINGEN A. C., MAUGEN G. A.: Electrodynamics of continua. Vol. I, II. Springer Verlag, Berlin, 1991.
3. KNOPOFF L.: The interaction between elastic waves motions and a magnetic field in electrical conductors. J. Geophys. Res. 1955, 60.
4. LAVRENTIEV M. M., PRIIMENKO V. I.: Simultaneous determination of elastic and electromagnetic medium parameters. In: Computerized Tomography. Proc. of the Fourth International Symposium, Novosibirsk, August 10-14, 1993. (Ed-in.Chief: Laurentiev M. M.) VSP, Utrecht, THE NETHERLANDS, 1995, pp. 302-309.
5. AVDEEV A. V., GORUYNOV E. V., PRIIMENKO V. I. and ZVJAGIN D. V.: Direct and Inverse Problems of Electromagnetoelasticity. In: 5th International Congress of the Brazilian Geophysical Society. Expanded Abstracts. São Paulo, Brazil, Vol. II, 1997, pp. 658-661.
6. OLSEN R. G.: Power-Transmission Electromagnetics. IEEE Antennas and Propagation Magazine, Vol. 36, No.6, December 1994.
7. DUNKIN, J. W. and Eringen, A. C., On the propagation of waves in an electromagnetic elastic solid, Inten. J. Eng. Sci., Vol.1., P.461-495, 1963.
8. LORENZI, A., Priimenko, V. I., Identification problems related to electro-magneto-elastic interactions, J. of Inverse and Ill-Posed Problems, Vol.4, N°2, P.115-146, 1996.
9. AVDEEV, A. V., Goruynov, E. V., Priimenko, V. I., An inverse problem of electromagnetoelasticity with unknown source of elastic oscillations, Preprint, N°1074, Computer Center of Siberian Branch of the Russia Academy of Sciences, 1996.

Figuras

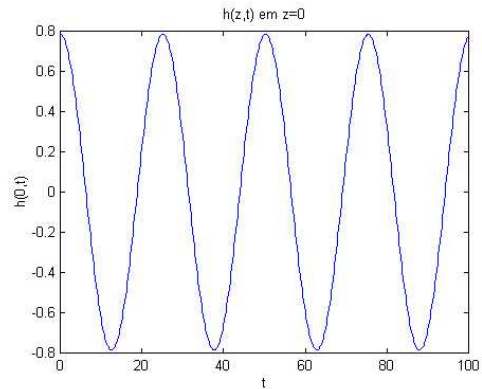


Figura 1. Campo $h^0(z,t)$, em $z = 0$.

Interação entre ondas eletromagnéticas e elásticas

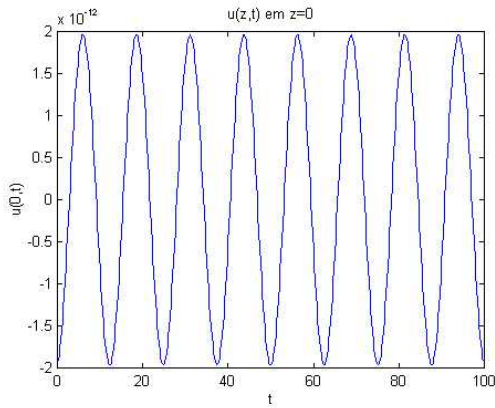


Figura 2. Campo $u(z,t)$, em $z = 0$.

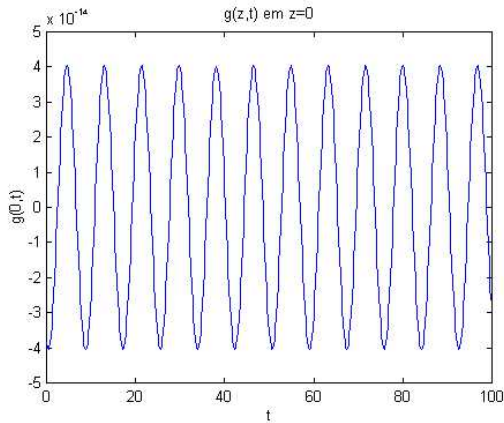


Figura 3. Campo $g(z,t)$, em $z = 0$.

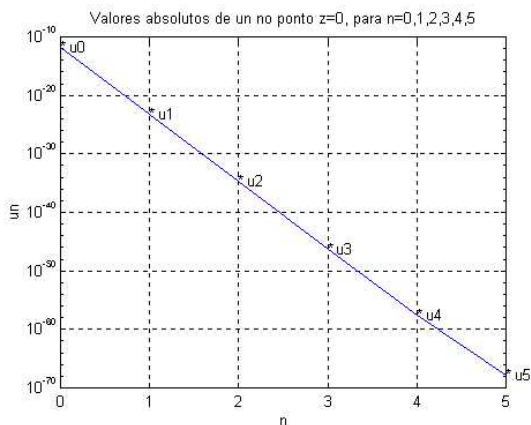


Figura 4. Decaimento, em $z = 0$, de u_n , com o aumento de n .

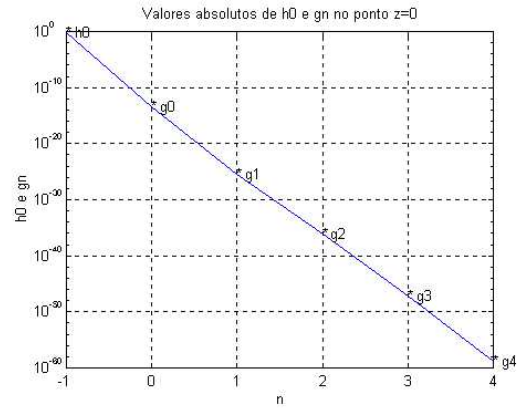


Figura 5. Decaimento, em $z = 0$, de g_n , com o aumento de n .

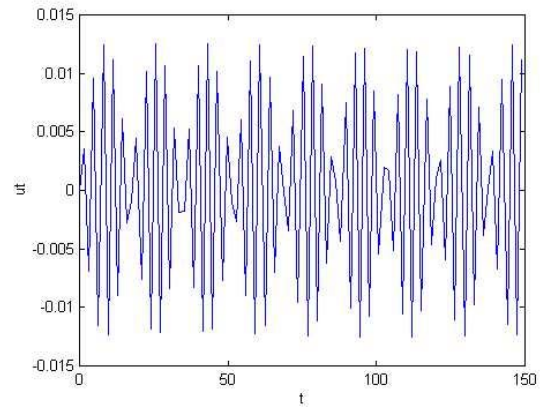


Figura 6. Campo $u(z,t)$ em $z = 0$

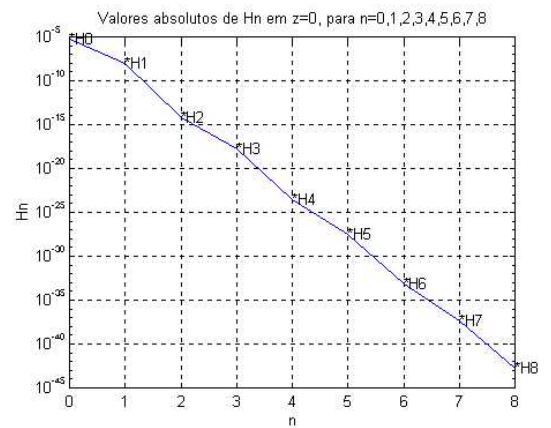


Figura 7. Decaimento, em $z = 0$, de $h_n(z)$, à medida que n aumenta.



Modeling of geomagnetic B field under the electrojet

Marcos W. C. Silva; Luiz Rijo – UNIVERSIDADE FEDERAL DO PARÁ, Brazil.
welbysilva@bol.com.br, rijo@amazon.com.br

Abstract

One of the traditional geophysical methods employed in the determination of conductivity distribution of subsurface in regional scale is the Magnetotelluric Method (MT). It uses both electric and magnetic fields at ground surface and is based on the hypothesis that these fields propagate as plane waves. In the equatorial region this hypothesis is not always valid for low frequencies in resistive terrain due to the presence of the equatorial electrojet.

Instead of using the electric and magnetic fields, as MT, here we employ the vertical component of the magnetic field normalized by the horizontal component to analyse the influence of a 2-D structure which is parallel to the electrojet upon the geomagnetic field scattered by a 2-D structure. The finite elements method was used for numerical modeling. The electrojet was modeled as infinite current line and as a planar gaussian distribution of current. The effects of the two electrojets on the response of the 2-D heterogeneity were compared against the plane waves results.

We concluded that at frequencies higher than 10^{-2} Hz there is no observable discrepancy between the plane wave and electrojet responses. Between 10^{-2} and 10^{-3} Hz the difference is very small. At these frequencies the lateral edges of the 2-D heterogeneity is easily detected. At 10^{-4} Hz the signature of the buried structure is no longer delineated, showing thus the influence of geometry of the equatorial electrojet source on the low frequency response.

Introduction

One of the traditional geophysical methods employed in the determination of conductivity distribution of subsurface in regional scale, is the Magnetotelluric Method (MT). Both the electric and the magnetic fields are measured at the surface to give the magnitude and phase of the impedance (Tikhonov, 1950 e Cagniard, 1953). The main hypothesis of this method is that the incident electromagnetic field is a plane wave emitted from the atmosphere. However, in the equatorial zone exist jets of ionospheric current, called the equatorial electrojet, which violated the hypothesis of plane wave at low frequencies in resistive terrain.

Using numerical modeling, several authors have simulated the MT response in the continental regions with the presence of the electrojet. Hermance & Peltier (1970) proposed an electrojet of type infinite

current line in E-W direction, localized at 110 km vertically above a stratified subsurface. Peltier & Hermance (1971) simulated an electrojet through an superficial current density according to one planar gaussian distribution, at 110 km of altitude and flowing in the E-W direction, and they concluded that the source effect increase both, when the media resistivity of subsurface and the period of waves became greater. On the other hand the effect decreases with the distance from the electrojet center. Hibbs & Jones (1973a) determined the electromagnetic response of 2-D heterogeneity and demonstrated in low frequencies ($< 10^{-1}$ Hz) that the source configuration influences the field values at subsurface. Indeed, Mota & Rijo (1991) concluded that the shallow lateral heterogeneity response due to plane wave is not affected by the presence of the current line or gaussian distribution but that the deepest 2-D structure response are affected by the medium host response.

Our aim in this work is to evaluate numerically the influence of the electrojet upon the geomagnetic response of 2-D structures parallel to electrojet E-W direction. We computed the ratio between the vertical and horizontal components of the magnetic field calculated at surface, modeling the electrojet as infinite current line and as a gaussian distribution of current density.

Methodology

The plane wave electromagnetic field induced by 2-D structure decouples itself in both TE and TM modes. In the presence of current lines parallel to strike, the induced field presents only the TE mode.

A current line located at 110 km of altitude in the E-W direction can be regarded as a good model of a concentrated electrojet (Hermance & Peltier, 1970). However, Hibbs & Jones (1973a) and Peltier & Hermance (1971) consider a planar gaussian current distribution with standard deviation of 240 km, located at 110 km of altitude, as a more adjusted model to the electrojet. In such a case, we obtain the total response by integration of all individuals responses of each current line, with the intensity changing in accord to gaussian distribution (Mota & Rijo, 1991).

In this work we use the finite element method to determine the TE mode electric field. Afterward, the magnetic field were calculated from the Maxwell equations. In order to improve the

Modeling of geomagnetic B field

numerical stability we separate the electromagnetic field in primary and secondary fields (Rijo, 1989).

The primary electrical field is given by the stratified media response (Ward & Hohmann, 1988). The integrals associated with the primary field components were calculated by the linear digital filter technique (Nissen & Enmark, 1986; Rijo, 1989).

The secondary field is governed by the equation, $\frac{\partial^2 E_y^s}{\partial x^2} + \frac{\partial^2 E_y^s}{\partial z^2} - i\omega\mu_0\sigma E_y^s = (\sigma - \sigma_p)E_y^p$, where σ_p and σ are, respectively, the homogeneous and heterogeneous medium conductivities. The right side of equation, $(\sigma - \sigma_p)E_y^p$, represents the source of secondary field, where E_y^p is the primary field calculated within the heterogeneity. The secondary magnetic field is obtained by numerical differentiation using the identities:

$$B_x^s = \frac{\mu_0}{\hat{z}} \frac{\partial E_y^s}{\partial z},$$

$$B_z^s = -\frac{\mu_0}{\hat{z}} \frac{\partial E_y^s}{\partial x}.$$

Finally, the total magnetic field components are computed summing up the primary and secondary components.

Model

Suggested by Arora (personal communication) we used the model shown in Figure 1 to investigate the effects of the electrojet on the magnetic fields response. The model is composed of two structures embedded in a 10 Ω-m host covered by a 50 Ω-m layer, with 2 km of thickness.

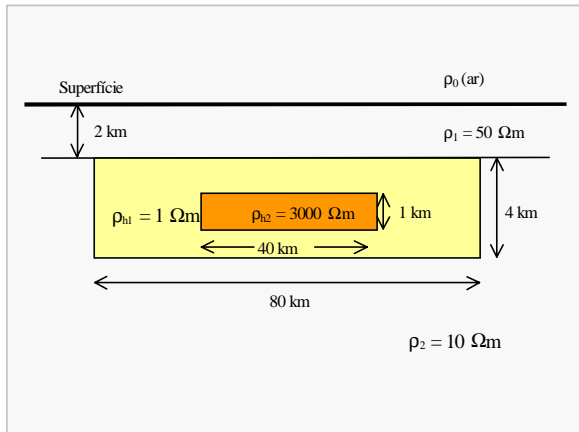


Figure 1 – Model of inhomogeneous semi-space.

The external structure has 80 km of width, 4 km of thickness, 1 Ω-m of resistivity and is located at 2km from the surface. The internal structure has 40

km of width, 1 km of thickness, 3000 Ω-m of resistivity and is located at 3,5 km from the surface.

Results

The experiments were realized with three kinds of sources: plane wave, infinite current line and planar gaussian distribution of current. The line and the center of the gaussian distribution are located at $x = 0$ km. The center of the 2-D heterogeneity is located at $x = 500$ km. We present the results in form of the ratio B_z/B_x computed at the surface for the frequencies 10^{-2} , 10^{-3} and 10^{-4} Hz. For frequencies higher than 10^{-2} Hz, the effects of the line and gaussian sources on the response are imperceptible.

To evaluate the effects of the electrojet sources let us visualize, first, the behavior of plane wave results. We observed in the Figure 2 (10^{-2} Hz) and 3 (10^{-3} Hz) that the external large peaks correspond to horizontal limit of the 80 km structure. Likewise, the smaller internal peaks correspond to horizontal limit of 40 km structure. In the Figure 4 (10^{-4} Hz) the information about the internal structure is no long clear because the higher skin depth. However, accentuated peaks are still present for external structure. In conclusion, with pane wave we can delineate clearly the structures from its geomagnetic response.

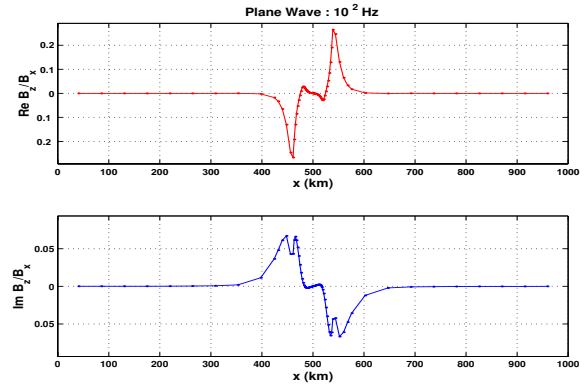


Figure 2 – Real and imaginary parts of the ratio B_z/B_x for plane waves. Frequency: 10^{-2} Hz.

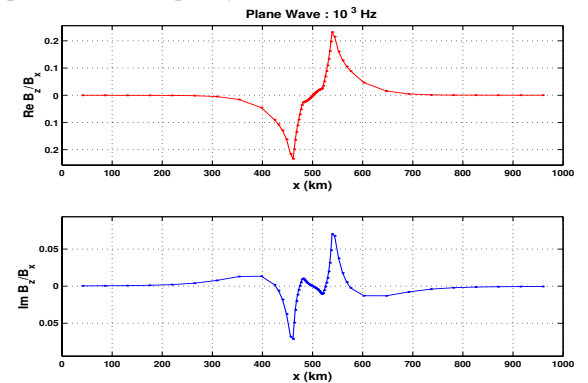


Figure 3 – Real and imaginary parts of the ratio B_z/B_x for plane waves. Frequency: 10^{-3} Hz.

Modeling of geomagnetic B field

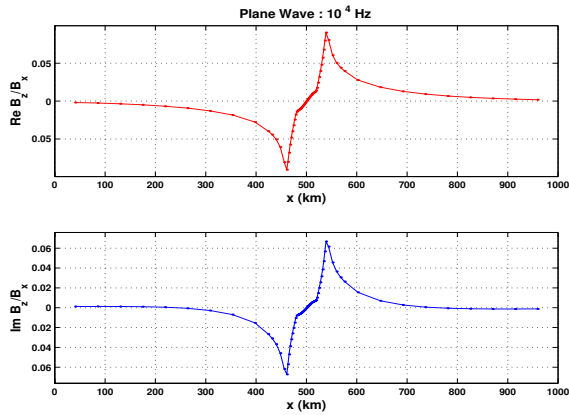


Figure 4 – Real and imaginary parts of the ratio B_z/B_x for plane waves. Frequency: 10^{-4} Hz.

Continuing our analysis let us now compare the results due to the infinite line source of current with these from plane wave previously discussed. The Figure 5 (10^{-2} Hz) is very similar to Figure 2. Thus, the effect of the line source at this frequency is extremely small. At frequency 10^{-3} Hz the response presents some influence of the source but we still can determine the limits of the two structures as illustrated in Figure 6.

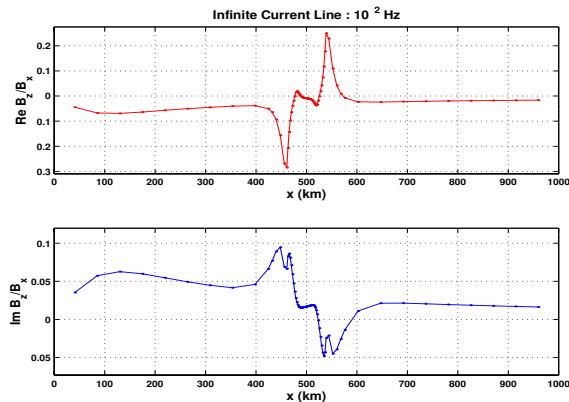


Figure 5 – Real and imaginary parts of the ratio B_z/B_x for infinite current line. Frequency: 10^{-2} Hz.

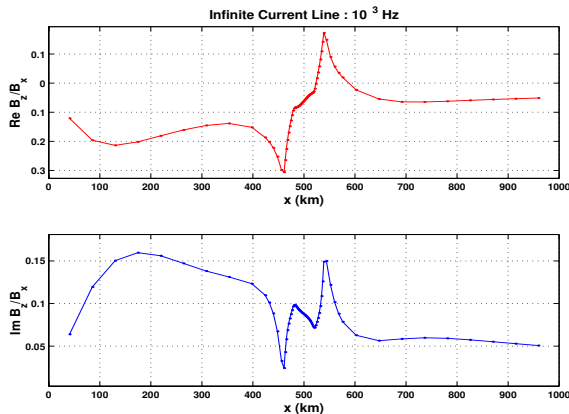


Figure 6 – Real and imaginary parts of the ratio B_z/B_x for infinite current line. Frequency: 10^{-3} Hz.

At frequency 10^{-4} Hz (Figure 7) the response is enough deformed such that the signature of the structures is barely seen.

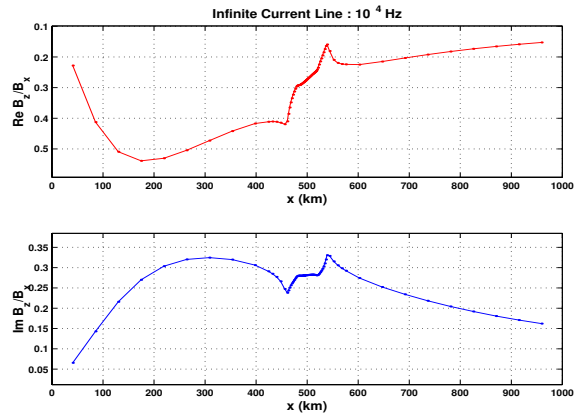


Figure 7 – Real and imaginary parts of the ratio B_z/B_x for infinite current line. Frequency: 10^{-4} Hz.

Finally the responses associated with the gaussian electrojet illustrated in Figures 8 (10^{-2} Hz), 9 (10^{-3} Hz) and 10 (10^{-3} Hz) show an intermediate behavior between plane waves and current line results.

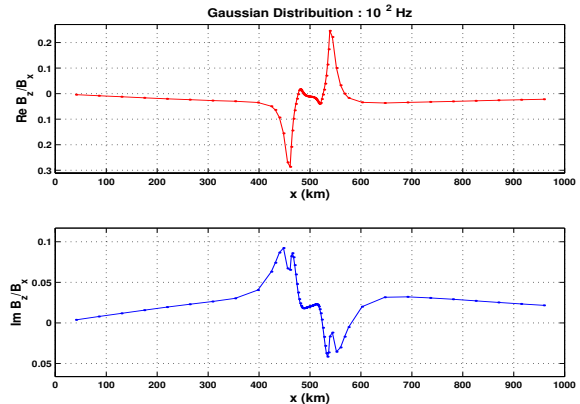


Figure 8 – Real and imaginary parts of the ratio B_z/B_x for gaussian distribution. Frequency: 10^{-2} Hz..

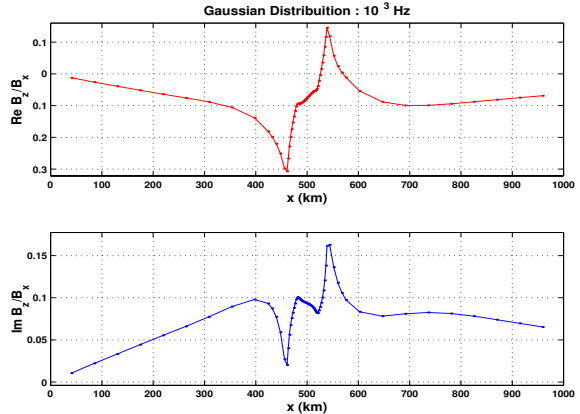


Figure 9 – Real and imaginary parts of the ratio B_z/B_x for gaussian distribution. Frequency: 10^{-3} Hz.

Modeling of geomagnetic B field

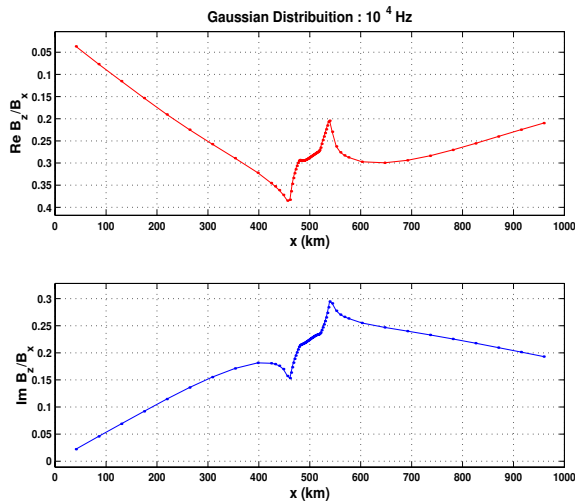


Figure 5 – Real and imaginary parts of the ratio B_z/B_x for gaussian distribution. Frequency: 10^{-4} Hz.

Conclusions

We investigated the effects on the B_z/B_x response of an E-W 2-D heterogeneity under the influence of the equatorial electrojet. Two models were used to simulate the electrojet: an infinite line of current located at 110 km above the ground and a gaussian distribution of current density with 240 km standard deviation. The effects of the two electrojets on the response of the 2-D heterogeneity were compared with the plane waves results. At frequencies higher than 10^{-2} Hz there is no observable discrepancy between the plane wave and electrojet responses. Between 10^{-2} and 10^{-3} Hz the difference is very small. At these frequencies the lateral edges of the 2-D heterogeneity is easily detected. At 10^{-4} Hz the signature of the buried structure is no longer delineated, showing thus the influence of geometry of the equatorial electrojet source on the low frequency response.

References

- Cagniard, L., 1953. Basic theory of the magnetotelluric method of geophysical prospecting. *Geophysics*, 18, 605-635.
- Hermance, J. F. & Peltier, W. R., 1970. Magnetotelluric fields of line current. *Journal of Geophysical Research*, 75, 3351-3356.
- Hibbs, R. D. & Jones, F. W., 1973a. Electromagnetic induction in the earth by a symmetric non-uniform source. *Journal of Geomagnetism and Geoelectricity*, 25, 75-86.
- Mota, J. P. & Rijo, L., 1991. Efeito devido ao eletrojato equatorial nos dados magnetotéluricos de estruturas 2D, paralelas e perpendiculares ao eletrojato. *Revista Brasileira de Geofísica*, 9,

161-177.

- Nissen & Enmark, 1986. An optimized digital filter for the Fourier transform. *Geophysical Prospecting*, 30, 501-514.
- Peltier, W. R. & Hermance, J. F., 1971. Magnetotelluric fields of a gaussian electrojet. *Canadian Journal of Earth Sciences*, 8, 338 – 346.
- Rijo, L., 1989. Teoria dos métodos elétricos e eletromagnéticos I e II. Notas de aula do curso de Pós-Graduação em Geofísica, CG/UFPA.
- Rijo, L., 1989. Um filtro digital ótimo para transformada cosseno. *Anais do 1^o Congresso Brasileiro de Geofísica*.
- Tikhonov, A. N., 1950. On determining electrical characteristics of the deep layers of the earth's crust. *Doklady*, 73, 295-297.
- Ward, S. H. and Hohmann, G. W., 1988, Electromagnetic theory for geophysical applications, in Nabighian, M. N., Ed., *Electromagnetic method in applied geophysics theory*, Vol. 1: Society of Exploration Geophysicists.

Acknowledgements

We would like to thank to Curso de Pós-Graduação em Geofísica - UFPA for logistic support and to Fundação Coordenação de Aperfeiçoamento de Pessoal de Nível Superior (CAPES), for financial support. Finally, we extend our acknowledgments to the Agência Nacional de Petróleo (ANP) for its financial support to our graduate course in Geophysics.



Multicomponent Induction Logging Response in a 3-D Borehole Environment

*Tsili Wang, Liming Yu, Otto Fanini, and Berthold Kriegshäuser
Baker Atlas, Houston, U.S.A.*

Summary

A multicomponent induction tool has the capability of resolving formation's resistivity anisotropy properties. However, the effects borehole fluid, tool eccentricity, invasion, and other borehole or formation related features on the tool response has not received a systematic study yet. In this paper, we applied a 3-D finite-difference modeling method to study multicomponent induction log response to (1) borehole fluid, (2) tool eccentricity, and (3) invasion (circular and noncircular).

We show that the coplanar-coil array (XX) configuration can be affected more by borehole fluid (resistive or conductive) than the conventional coaxial-coil array (ZZ) configuration. A decentralized tool will affect the XX and YY coil array responses differently, depending in which direction the tool is decentralized. This is much different from the case for the ZZ response where the effect is in general independent of the eccentricity direction. When the tool is decentralized in the X direction (to which the X transmitter dipole points), the YY response can be significantly distorted but the effect on the XX response will be minimal. The opposite is true when the tool is decentralized in the Y direction. In the presence of an elliptic invasion, both the XX- and ZZ-coil array responses are similar to those generated by a circular invasion with a radius given by the short axis of the elliptic invasion. The YY configuration response, however, is more accurately predicted by an average of the responses of two circular invasions whose radii are given by the long and short axes of the elliptic invasion, respectively.

INTRODUCTION

Induction logging measurements using mutually orthogonal source and receiver coils can be used to resolve the formation's resistivity anisotropy (Carvalho and Verma, 1998; Kriegshäuser et al., 2000). This is a big advantage over conventional, coaxial-coil induction tools that are not capable of detecting the resistivity anisotropy, especially in a vertical or near vertical well. In an ideal, but important, case where a formation exhibits the so-called transverse isotropy (Klein, 1993), multicomponent induction measurements suffice to resolve both the horizontal and vertical resistivities of the formation. Laminated sand shale sequences exhibit macroscopic electrical anisotropy. The petrophysical evaluation of thinly laminated and shale sequences utilizing the horizontal resistivity (i.e., parallel to the bedding) can either overlook hydrocarbons present in the laminar or underestimate their

productivity. The vertical resistivity utilization in the analysis results in a more accurate and reliable evaluation of the hydrocarbon producing potential of the laminar sands.

Interpretation of multicomponent induction logs can be complicated by various borehole and formation environments. Conventional coaxial-coil responses have been studied for years (Barber et al., 1995; Anderson et al., 1996; Anderson et al., 1997), but very limited knowledge has been acquired for non-coaxial coil configurations such as the coplanar source and receiver coils, which are part of the multicomponent induction tool. This study provides a systematic investigation of a multicomponent tool response in fundamentally important 3-D borehole environments. In reality, there are numerous factors that can affect the tool response. To limit the scope of our study, however, we have focused our efforts on the following issues: (1) borehole fluid, (2) tool eccentricity, and (3) invasion.

RESULTS

The multicomponent tool that we address in this paper was described in Kriegshäuser et al. (2000). At each depth position, the tool (3DEXTM) measures coplanar, cross-component as well as coaxial responses. The operating frequency is from tens of kilohertz to a few hundred kilohertz.

Borehole fluid effect

It is well known that borehole fluid (mud) has a minimum effect on conventional, coaxial induction logging tools unless the fluid is highly conductive. For a multicomponent tool, however, borehole fluid may exert significant influence on coplanar or mutually orthogonal sensors, regardless of the borehole fluid conductivity.

To illustrate the effect, we consider an 8.5-in diameter borehole in a uniform, 1 ohm-m isotropic formation. Figures 1 and 2 show the XX and ZZ responses for a 0.1 ohm-m mud and 1000 ohm-m mud, respectively. Here, the ZZ component is the conventional coaxial coil response and the XX component is the coplanar coil response. Because the formation bedding plane is normal to the borehole, the YY response will be the same as the XX response. As illustrated in Figure 1, the ZZ response is almost not affected by the 1000 ohm-m borehole mud, whereas the XX response is shifted up at all frequencies. Conversely, for a 0.1 ohm-m mud, the ZZ response is shifted down. The XX response is also shifted down by the conductive

Multicomponent Induction Log

borehole fluid at all frequencies. In this case, the shift is in the opposite direction to the case for a resistive mud.

Tool eccentricity effect

In field operations, a logging tool is often positioned off the borehole axis. This is especially the case in a highly deviated or horizontal well in which the tool string weight makes difficult to centralize a tool. As noted for the conventional coaxial tool that a decentralized tool can significantly increase the influence of borehole fluid on measurements. In such a case, the variable fluid annulus cross-section may result in high current density flowing through the thin fluid annulus section. The asymmetric current density distribution will introduce a large tool response, which may be erroneously interpreted to be a contribution from the formation response.

We will consider tool decentralization in either the X or Y direction in a plane perpendicular to the borehole axis, as shown in Figure 3. As expected, this decentralization makes no difference to the ZZ response, provided that the formation is azimuthally invariant. Figure 4 shows the real data from a field test. The mud resistivity R_m is around 1.5 ohm-m; the tool axis is decentralized 1.69 in from the borehole axis; and the frequency is 56 kHz. It is observed that the ZZ response remains essentially the same regardless of the tool position in the borehole. When the tool is decentralized in the X direction, the XX response is not much affected, but the YY response becomes substantially higher. Similarly, when the tool is decentralized in the Y direction, the YY response remains the same, but the XX response is increased.

To further study the tool eccentricity effect, we show in Figure 5 the differences in the YY-coil array responses between a decentralized (DEC) tool and a centralized (CEN) tool. The decentralization is in the X-direction. In all the cases, the tool axis is decentralized 1.5 in from the borehole axis. First, the effect is frequency dependent. Higher frequencies yield, in general, a higher tool eccentricity effect. Second, higher formation/mud resistivity contrasts produces larger eccentricity effects. Third, at low formation/mud resistivity contrasts, the eccentricity effect in a small borehole is smaller than that in a large borehole, and vice versa. Interestingly, at certain formation/mud resistivity contrasts (e.g., $R_t=20$ ohm-m and $R_m=1$ ohm-m), the eccentricity effects from different borehole sizes may be similar.

Invasion effect

A major use of the multicomponent induction tool is to resolve formation resistivity anisotropy. In thinly laminated sand shale sequences, the presence of an invasion zone, however, will change the formation anisotropy property. For instance, oil-based mud invasion into a sand/shale sequence tends to increase the formation anisotropy, whereas conductive, water-based mud may reduce the formation anisotropy because the invading fluid

brings the sand resistivity closer to that of shales. The impact of an invasion zone on the capability of a multicomponent induction tool in resolving formation anisotropy depends on the volume and shape of the invasion zone. A deep invasion zone may largely distort the estimation of the true formation anisotropy.

We consider an elliptic invasion zone, as shown in Figure 6. The long axis is in the X direction. Such invasion may result when formation permeability is anisotropic. When the long and short axes are equal, a circular invasion zone results. In the presence of non-circular invasion, the XX and YY component will respond differently even if the formation is homogeneous and isotropic. This provides a possibility to distinguish non-circular invasion from circular invasion with a multiple component induction tool.

In Figure 7, we show the XX, YY, and ZZ component responses to an elliptic invasion as a function of the long/short axis ratio. The cross-sectional area of the invasion is kept the same as that of a 20-in thick circular invasion. The uninvaded formation has $R_h=4$ ohm-m and $R_v=20$ ohm-m. The borehole fluid is 0.1 ohm-m; the invasion zone resistivity is assumed to be 1 ohm-m. First, note that the ZZ response has little dependence on the long/short axis ratio. The XX response, however, decreases (in magnitude) substantially as the invasion zone elongates. The YY response behaves oppositely.

It is interesting to compare the elliptic invasion response to that of a circular invasion. The radius of the circular invasion is made equal to either the long or the short axis of the elliptic invasion zone. Figure 8 shows that both the XX and ZZ responses to an elliptic invasion are similar to those of a circular invasion of the short axis. The YY response to an elliptic invasion zone can be approximated by an arithmetic average of the responses to circular invasion zones whose radii are given by the long and short axes of the elliptic invasion, respectively. These observations suggest that the response (XX, YY or ZZ) to an elliptic invasion can be approximated to the first order accuracy by that of one or two circular invasion zones. Worth noting is that Anderson et al. (1996) pointed out that the coaxial coil array induction tool response to a moderately deep, noncircular (e.g., elliptic) invasion can be replaced with that of a circular invasion with an equivalent radius. Here we suggest a similar relationship for coplanar coil array configurations.

CONCLUSIONS

- (1) The coplanar-coil (XX) configuration can be affected more by borehole fluid (resistive or conductive) than the conventional coaxial-coil (ZZ) configuration.
- (2) A decentralized tool will affect the XX and YY responses differently, depending in which direction the tool is decentralized. When the tool is decentralized in the X direction, the YY response can be significantly distorted

Multicomponent Induction Log

but the effect on the XX response will be minimal. The opposite is true when the tool is decentralized in the Y direction.

In the presence of an elliptic invasion with the long axis in the X-direction, both the XX and ZZ responses are similar with a radius given by the short axis of the elliptic invasion. The YY configuration response, however, is approximately the average of the responses of two circular invasions whose radii are given by the long and short axes of the elliptic invasion, respectively.

ACKNOWLEDGMENTS

Permission by Baker Atlas for publishing this work is acknowledged.

REFERENCES

Anderson, B., et al., 1997, New dimensions in modeling resistivity: *Oilfield Review*, **9**, 40-56.

Anderson, B., Barber, T., Druskin, V., Lee, P., Dussan, E., Knizhnerman, L., and Davydycheva, S., 1996, The response of multiarray induction tool in highly dipping formations with invasion and in arbitrary 3D geometries: Paper A, *in* 37th Ann. Log. Symp. Trans., Soc. Prof. Well Log Analysts.

Barber, T., Orban, A., Hazen, G., Long, T., Schlein, R., Alderman, S., Tabanou, J., and Seydoux, J., 1995, A multiarray induction tool optimized for efficient wellsite operation, SPE-30583, *in* Proc. SPE Ann. Tech. Conf., Soc. Petroleum Engineers, 549-561.

Beard, D.R., van der Horst, M., Strack, K.-M., and Tabarovsky, L.A., 1998, Electrical logging of a laminated formation: International Patent WO 98/00733.

Carvalho, P.R., and Verma, O.P., 1998, Induction tool with a coplanar coil system: *The Log Analyst*, **39**, 48-53.

Gupta, P., Kriegshäuser, B., Jericevic, Z., and Fanini, O., 1998, Method for inversion processing of transverse electromagnetic induction well logging measurements: United States Patent 5,854,991.

Klein, J.D., 1993, Induction log anisotropy corrections: *Petrophysics*, **34**, 18-27.

Kriegshäuser, B., Fanini, O., Forgang, S., Mollison, R., Yu, L., Gupta, P., Koelman, J.M.V., and van Popta, J., 2000, Increased Oil-In-Place in low resistivity reservoirs from multi-component induction log data: Paper A, Trans. of the SPWLA 41st Annual Logging Symposium.

Wang, T., and Fang, S., 2001, 3D anisotropy electromagnetic modeling using finite differences: *Geophysics*, accepted for publication.

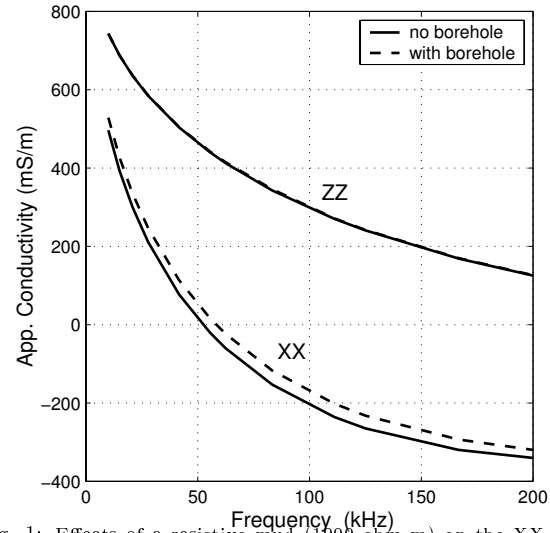


Fig. 1: Effects of a resistive mud (1000 ohm-m) on the XX and ZZ apparent conductivities. The borehole diameter is 8.5 in.

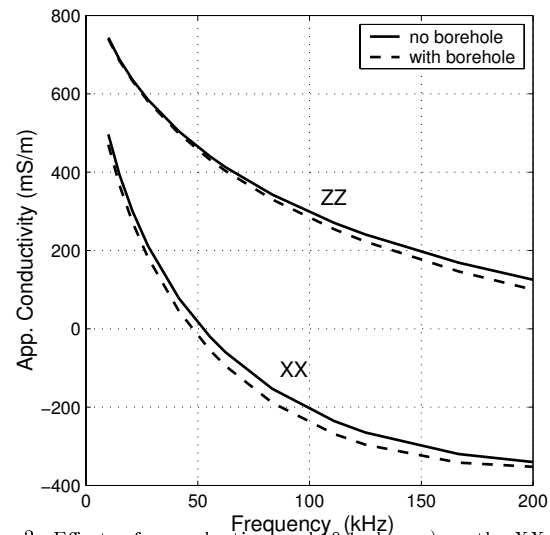


Fig. 2: Effects of a conductive mud (0.1 ohm-m) on the XX and ZZ apparent conductivities. The borehole diameter is 8.5 in.

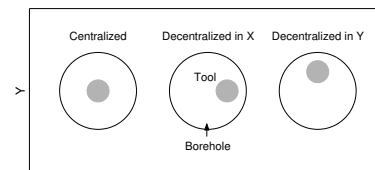


Fig. 3: A diagram showing a tool to be centralized or decentralized in either the X or Y direction.

Multicomponent Induction Log

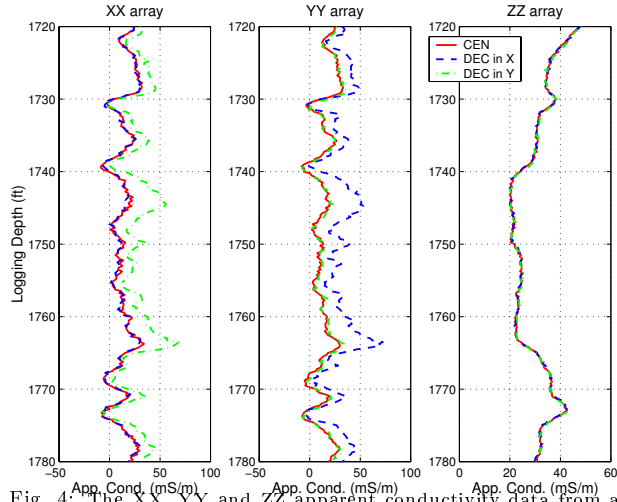


Fig. 4: The XX, YY and ZZ apparent conductivity data from a field test on the tool eccentricity effect. The symbols CEN and DEC stand for the responses of a centralized tool and a decentralized tool, respectively.

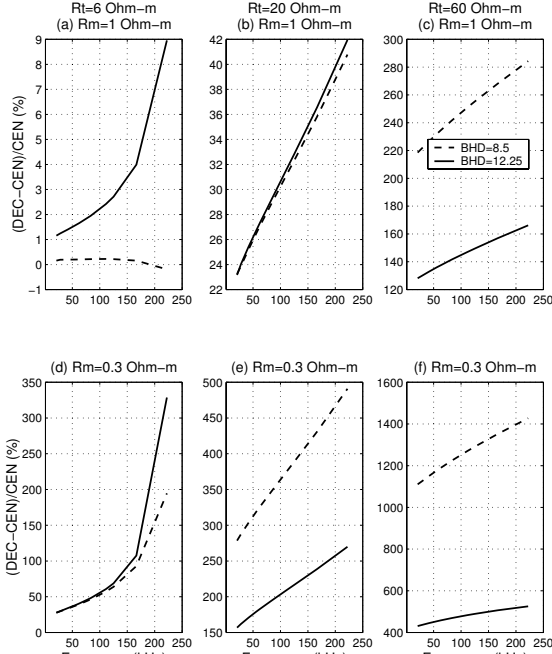


Fig. 5: Differences in YY-coil array responses between a centralized and a decentralized (in the X-direction) tool for various formation (R_t) and mud (R_m) resistivities. CEN and DEC denote centralized and decentralized apparent conductivities, respectively.

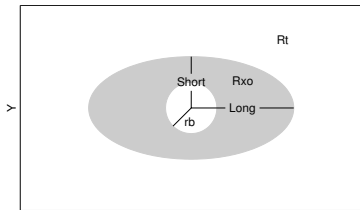


Fig. 6: The geometry of an elliptic invasion. The borehole diameter is 8.5 in. The mud resistivity is 0.1 ohm-m.

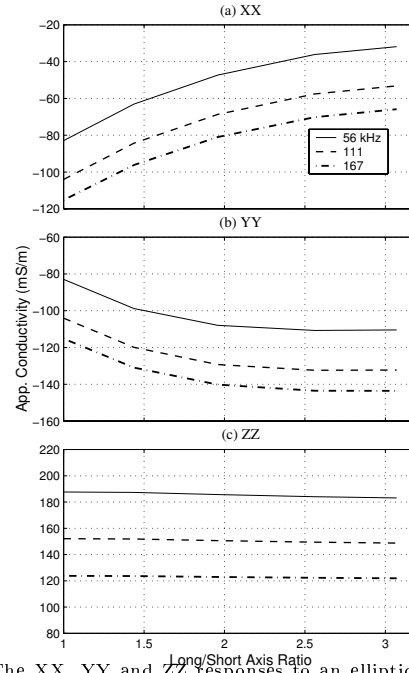


Fig. 7: The XX, YY and ZZ responses to an elliptic invasion in a homogeneous, anisotropic formation. The formation R_h and R_v values are 4 ohm-m and 20 ohm-m, respectively. The invasion zone resistivity is 1 ohm-m and isotropic. The total cross-sectional area of the elliptic invasion zone is kept the same as that of a 20-in thick circular invasion.

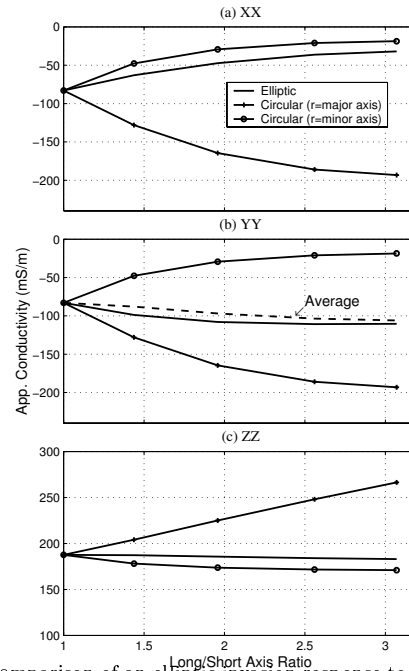


Fig. 8: Comparison of an elliptic invasion response to those of circular invasion zones whose radii are equal to the major and minor axes of the elliptic invasion zone, respectively. The frequency is 56 kHz.



Processing and Inversion Techniques for Multicomponent Induction Log Data

Berthold F. Kriegshäuser, Baker Atlas, Brazil, Otto N. Fanini, L. Yu, Baker Atlas, U.S.A.

Abstract

In this paper we present advanced processing and inversion techniques to derive horizontal and vertical formation resistivities from multicomponent induction log data. This newly developed induction logging tool (3DEXSM) is designed to identify and to delineate productive low-resistivity reservoirs frequently encountered in hydrocarbon exploration. An example of such a reservoir is a finely laminated sand/shale sequence of which the sand laminae can contain hydrocarbons found in deep water environments. These reservoirs exhibit electrical anisotropy, i.e., the resistivities parallel and perpendicular to bedding are different and cannot be accurately delineated by conventional induction instruments with their transmitter and receiver orientation parallel to the borehole axis. However, the new multicomponent transmitter-receiver configuration provides direct measurements to derive both horizontal and vertical resistivity that allows evaluation of the hydrocarbon bearing sand laminae. The tool is comprised of three mutually orthogonal induction transmitter-receiver configurations yielding all necessary data to derive the horizontal and vertical resistivities of the formation.

In this paper, we introduce various processing and inversion techniques such as real-time data processing, shoulder bed and borehole correction schemes, an automatic 'thin-layer' inversion scheme, and an efficient 'pseudo 2-D' inversion algorithm. We demonstrate the performance of these interpretation techniques on synthetic and field data sets.

Introduction

Petrophysical analysis in thinly laminated sand/shale sequences is challenging because conventional resistivity data are not sensitive enough to the resistivity of the thin sand laminae (Mollison et al., 1999; Schön et al., 1999). If the thickness of the individual laminae is below the resolution of the wireline instrument, then the sand/shale sequence can exhibit electrical anisotropy. Baker Atlas and Shell International E&P jointly developed a new multicomponent induction logging tool, 3DEX (Beard et al., 1998; Kriegshäuser et al., 2000) that measures the electrical anisotropy of these sequences. The instrument comprises three mutually orthogonal transmitter-receiver configurations that provide all necessary data to compute

horizontal and vertical resistivities of the formation. The tool measures all 9 magnetic field components*, for a number of frequencies ranging between 20 and 200 kHz. Processing of the multicomponent induction log data is more difficult because of the more complex response characteristics of the H_{xx} and H_{yy} data (see companion paper). Therefore, we developed a number of processing and inversion schemes to derive horizontal and vertical resistivity (R_h, R_v) of the formation. We first introduce a real-time processing scheme that provides estimates of R_h and R_v during logging. Then, we discuss data processing methods that effectively reduce shoulder bed effects in the data.

Real-time data processing, R0D

We developed a fast and yet robust inversion scheme that matches the field data at each logging point with synthetic responses of an anisotropic, whole-space model. A regularized Marquardt-Levenberg optimization (e.g., Lines and Treitel, 1984) is used to derive the optimum formation parameters. In this procedure we first calculate the synthetic tool responses in an isotropic 1 Ohm-m whole-space model, i.e., without boundaries in both horizontal and vertical direction. Then, we compare the synthetic whole-space responses with the measured field data at each logging depth and adjust iteratively the horizontal and vertical resistivities (R_h and R_v) to match the synthetic responses with the measured field responses in a least-square sense. This inversion process is extremely fast because it only involves analytical solutions for the anisotropic whole-space response and is executed in real-time during logging.

Figure 1 compares the real-time processing results (3DEX, R0D) with more rigorous 1-D inversion results based on 3DEX data and 2-D inversion results using HDIL data. The R0D results are not as detailed as the 1-D inversion result, and only provide a fast-look interpretation of the formation resistivities. However, since these results are displayed during data acquisition, they contain important information about data quality. In addition, they give a first impression about formation anisotropy in media without large resistivity contrasts.

* The nine magnetic field components are H_{xx}, H_{xy}, H_{xz}, H_{yx}, H_{yy}, H_{yz}, H_{zx}, H_{zy}, and H_{zz}. The first index indicates the transmitter direction and the second index corresponds to the receiver direction.

Processing of Multicomponent Induction Log Data

The resistivities derived from whole-space inversion and selected bed boundaries can then be integrated to construct a layered 1-D initial earth model. To further improve the whole-space inversion results, we developed an efficient shoulder bed correction scheme to correct the field data for shoulder bed effects (Kriegshäuser et al., 2000b).

Shoulder Bed Corrections

Data from the multicomponent induction tool can exhibit strong shoulder bed effects. In particular, the horizontal magnetic field components show more shoulder bed effects than the conventional vertical magnetic field data. To improve interpretation of the data, we developed an efficient shoulder bed correction scheme that removes shoulder effects from the measured data (Gupta et al., 1998). These corrected data are then used in the previously described whole-space processing (Kriegshäuser et al., 2000b).

From the initial model, constructed with whole-space inversion resistivities and bed boundaries, we calculate shoulder bed corrections and remove these from the field data. To do the shoulder bed corrections, we first calculate the 1-D layered host formation synthetic response, D_{1Dver} . Then, we calculate the corresponding whole-space responses at each layer using the horizontal and vertical resistivities of this layer, D_{WS} . The difference between the 1-D layered host response and the whole-space responses is the shoulder bed effect ΔD_{SB} ,

$$D_{1Dver} - D_{WS} = \Delta D_{SB} \quad \dots\dots\dots (1)$$

We then apply these corrections to the field data in order to reduce the shoulder bed effects,

$$H_{meas} - \Delta D_{SB} = H_{meas}^{corr,SB} \quad \dots\dots\dots (2)$$

These shoulder bed corrected data are subsequently used in the whole-space inversion scheme. The newly derived resistivities in both horizontal and vertical directions are then used to refine both, the 1-D layered earth model and the shoulder bed corrections. The process comprising whole-space response matching and refining shoulder bed corrections is repeated until convergence is achieved. Figure 2 illustrates the shoulder bed correction scheme on field data. After several iterations, the tool responses are almost squared and the shoulder bed effects are significantly reduced.

Dual frequency data transformation

The horizontal multicomponent magnetic components H_{xx} and H_{yy} are also affected more severely by borehole and near-zone effects compared to the standard induction tool responses, H_{zz} . This is caused by the different current pattern of the horizontal transmitter coils. The induced electric field component normal to the borehole wall is discontinuous, resulting in a charge build-up that can distort the induced current pattern and therefore, the measured signal. However, Tabarovsky and Epov (1979) introduced a very effective transformation of the single frequency responses that removes borehole and near-zone effects in the data. This so-called dual frequency transformation combines two single frequency data in the following manner:

$$H(f_1, f_2) = H(f_1) - \frac{f_1}{f_2} H(f_2) \quad \dots\dots\dots (3)$$

$H(f_1)$ and $H(f_2)$ are the magnetic field single frequency responses, respectively. This transformation is most effective at lower frequencies and performs very well for H_{xx} and H_{yy} . However, the signal-to-noise ratio (S/N) of the dual frequency response is significantly lower than the S/N of the single frequency data.

Thin layer inversion scheme

The ‘thin layer’ inversion scheme developed by Yu et al. (2001) combines single frequency H_{zz} data with dual frequency H_{xx} and H_{yy} data to compute horizontal and vertical resistivity of the formation.

The key elements of this inversion scheme are

- Discretizing the formation into equally thick layers;
- Utilizing a 1-D forward modeling solution of a horizontally layered formation to account for shoulder bed effects;
- Updating the horizontal and vertical resistivities based on the difference between the synthetic data and the measured data without calculation of a sensitivity matrix;
- Sequentially using H_{zz} data and the sum of H_{xx} and H_{yy} data, constrained by Moran and Gianzero’s equation (1979), to de-couple R_h and R_v in deviated wells;
- Utilizing the dual frequency data to stabilize the inverse process.

This scheme is extremely fast and provides very good estimates of horizontal and vertical formation resistivities because shoulder bed effects are accounted for in the forward modeling solution of the inverse process. Using dual frequency data allows reducing the borehole effect in the data. It takes about 5 minutes to process 1000 ft of data on a SUN® ULTRA5 workstation. Figure 3 compares inverted horizontal and vertical resistivities versus true values using synthetic

Processing of Multicomponent Induction Log Data

data. There is an excellent recovery of the formation parameters.

Pseudo 2-D inversion algorithm

An innovative and efficient pseudo 2-D inversion scheme can further improve the interpretation based on traditional 1-D inversion algorithms. The applicability of this scheme is important in cases where borehole and near-zone effects do not allow an interpretation based on 1-D inversion. This can be the case if either dual frequency data are not available due to low signal level or dual frequency data still contain borehole and near-zone effects. A rigorous 2-D inversion scheme, however, is too time-consuming and therefore, we developed a 'pseudo 2-D' inversion scheme (P2D). This hybrid scheme combines an accurate 2-D forward solution to compute the data mismatch with an approximate 1-D Jacobian calculation to update the formation parameters. The main features of the scheme are

- Construction of an initial synthetic 2-D model using a priori information;
- Full 2-D forward solution of the synthetic model to match field data;
- Approximation of the 2-D sensitivity matrix with a sensitivity matrix of the corresponding 1-D horizontally layered formation model;
- Formation parameter updating based on a fast Jacobian matrix calculation of the corresponding 1-D layered background model;
- Inversion slower than 1-D inversion but significantly faster than full 2-D inversion;
- Accuracy comparable to full 2-D inversion;

These features allow a significant and an essential improvement to the accuracy of conventional 1-D inversion results in cases where borehole and near-zone effects corrupt the multicomponent induction log data with an acceptable compromise in speed and performance (Kriegshäuser et al., 2001). The increase in speed compared to a full 2-D inversion scheme is proportional to the number of parameters used in the inversion. As an example, we compare in Figure 4 the P2D inversion results and 1-D inversion results against the true model. The improvement over the 1-D case is significant, and the resistivities derived with P2D are in excellent agreement with the true model. We also applied this scheme to real field data and found very good agreement of the P2D inversion results with full 2-D inversion results.

Conclusions

The new multicomponent induction logging tool acquires all data necessary to derive horizontal and

vertical resistivity of the formation in vertical, deviated and horizontal wells. The induction response of the coplanar coils is complex and sometimes not intuitive. Borehole and eccentricity effects can distort the coplanar responses more than conventional coaxial induction coil responses. However, state-of-the-art processing and inversion techniques are available to either remove these effects or to include them in the interpretation process of 3DEX induction log data.

References

- Beard, D. R., van der Horst, M., Strack, K.-M., and Tabarovsky, L. A., 1998, Electrical logging of a laminated formation: International Patent WO 98/00733.
- Gupta, P., Kriegshäuser, B., Jericevic, Z., and Fanini, O., 1998, Method for inversion processing of transverse electromagnetic induction well logging measurements, United States Patent 5,854,991.
- Kriegshäuser, B., Fanini, O., Forgang, S., Itskovich, G., Rabinovich, M., Tabarovsky, L., Yu, L., Epov, M., and v. d. Horst, J., 2000, A new multicomponent induction logging tool to resolve anisotropic formations, paper D in SPWLA 40th Annual Logging Symposium Transactions: Society of Professional Well Log Analysts.
- Kriegshäuser, B., Fanini, O., Gupta, P., Yu, L., and van der Horst, J., 2000, Wellsite interpretation of multicomponent induction log data: SPE 62906, Transactions of ACTE 2000.
- Kriegshäuser, B., McWilliams, S., Fanini, O., Yu, L., 2001, An efficient and accurate pseudo 2-D inversion scheme for multicomponent induction log data, *submitted to 71st Annual SEG meeting*.
- Mollison, R., Schön, J., Fanini, O., Kriegshäuser, B., Meyer, H., and Gupta, P., 1999, A model for hydrocarbon saturation estimation from an orthogonal tensor relationship in thinly laminated anisotropic reservoirs: Trans. of the SPWLA 40th Ann. Logging Symposium, paper OO.
- Moran, J. H., and Gianzero, S., 1979, Effects of formation anisotropy on resistivity-logging measurements, *Geophysics*, **44**, No. 7, 1266-1286.
- Schön, J. H., Mollison, R. A., and Georgi, D. T., 1999, Macroscopic electrical anisotropy of laminated reservoirs: A tensor resistivity tensor model: paper 56509, Trans. SPE ATCE.
- Tabarovsky, L.A., and Epov, M.I., 1979, Geometric and frequency focusing for investigation of anisotropic layers, *in* Electromagnetic well logging, Nauka, Siberian Division, Acad. Sci. USSR, Novosibirsk.
- Yu, L., Kriegshäuser, B., Fanini, O., and Xiao, J., 2001, A fast inversion method for multicomponent

Processing of Multicomponent Induction Log Data

induction log data, submitted to 71st Annual SEG meeting.

Acknowledgments

Baker Atlas and Shell Technology EP jointly developed the multicomponent induction logging tool. The authors are indebted to Shell for permission to use their data for this paper. The authors would like to thank B. Corley, M. Epov, A. Hördt, P. Gupta, G. Itskovich, S. McWilliams, R. Mollison, and L. Tabarovsky for valuable contributions during the development of the 3DEX processing and inversion schemes.

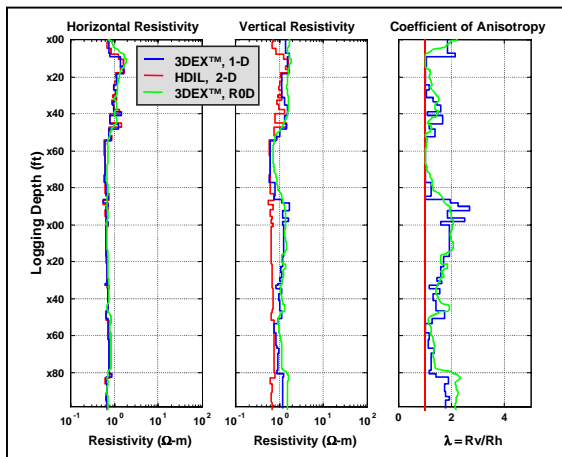


Figure 1: Real-time processing results versus more rigorous 1-D inversion data.

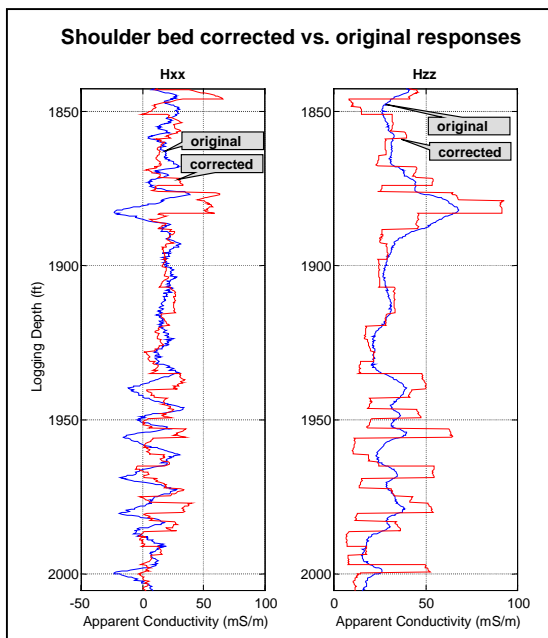


Figure 2: Shoulder bed corrected versus original field data for Hxx and Hzz, respectively. Removal of the shoulder bed effect 'squares' the measured curves.

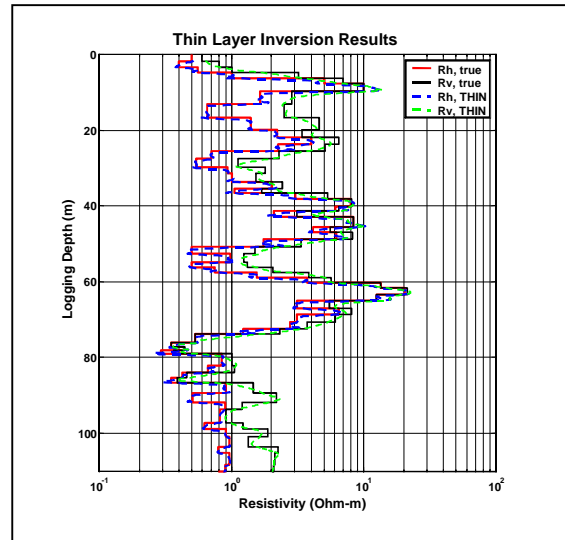


Figure 3: Thin layer inversion results applied to synthetic data. The algorithm successfully recovers the true formation resistivities.

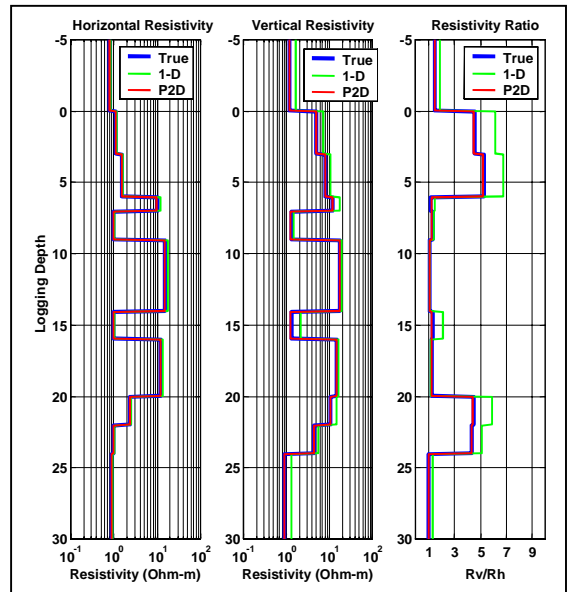


Figure 4: Inversion results using a 1-D and the new pseudo 2-D (P2D) scheme versus the true 2-D model. The main improvement of P2D over 1-D is in deriving Rv. The pseudo 2-D results compare very well with the true model resistivities.



Projeto de um sistema semi-automatizado de medidas de potencial elétrico natural ou induzido do solo para aplicações geoeletricas.

Francisco Y.Hiodo¹, Nilton Silva¹, Vagner R. Elis¹, Luis Galhardo F^o¹, Jorge E. da Silva¹

¹ Instituto de Astronomia, Geofísica e Ciências Atmosféricas da Universidade de São Paulo

Email: francisc@iag.usp.br

A s r a

The devices were developed to realize spontaneous and induce voltage measurement on the ground. In both case we used a multiwire cable with multiple voltage inputs along the length that becomes possible to connect it in six stainless electrodes fixed in the ground at same time. An automatic sequence digital system controlled by pushbutton touch allows to couple electrodes sequentially to a electronic DC voltmeter with autozeroing circuit based in PID servocontrol circuit. A 60 Hz notch filter and a roll-off low pass filter with time constant of 1s are used to minimize line and spheric noises. Electronic control system becomes too possible to couple cable with receiver datalogger of SYSCAL R-2 in dipole- dipole sounding array.

In r

Atualmente, as sondagens geoeletricas usando corrente chaveada são intensivamente empregadas na localização de descontinuidades laterais e no delineamento de camadas em subsuperfície. Elas competem com os métodos eletromagnéticos, que permitem levantamento mais rápido, mas não trazem informações do teor de argila no solo. Os caminhamentos clássicos nos arranjos polo- dipolo, dipolo- dipolo, operam com tensões elevadas e necessitam de vários cabos de conexão, que podem induzir a erros de posicionamento de eletrodos, durante uma prospecção mineral. Com o intuito de minimizar o número de operações, i.é, reduzir o risco de erros, foram desenvolvidos e montados um cabo flexível com múltiplas entradas ao longo de seu comprimento e, um circuito de comutação sequencial digital comandado por interruptor de pressão para medida de potencial dos vários eletrodos, não polarizáveis ou de aço inox. A saída deste circuito pode ser acoplada a um milivoltímetro de 3 ½ dígitos dotado de circuito de realimentação negativa e filtros ativos para medida de potencial espontâneo ou então, a um receptor (datalogger) de um eletrorresistivímetro (p. ex. Syscal R-2) de corrente chaveada, para medidas de potencial induzido no solo.

Me a- Ins r en a

Nos trabalhos de caminhamento elétrico dipolo-dipolo, os eletrodos de potencial (ou de corrente) são conectados alternadamente ao longo de uma linha,

necessitando, portanto, do apoio contínuo de um operador. Portanto torna-se um trabalho tedioso, sujeito a eventuais erros.

Uma alternativa seria a confecção de um cabo com múltiplas entradas que permitiria conexão com os eletrodos numa única etapa. Portanto com o recurso do cabo, o intercâmbio dos eletrodos deixaria de ser manual, para ser feita através de comutadores eletromecânicos (relés ou chaves analógicas). Para evitar possíveis erros de combinação de eletrodos, foi adotado um circuito de comutação sequencial comandado por lógica digital. Na primeira etapa do projeto, foi desenvolvido um cabo com 6 vias, para investigação em 6 níveis de profundidade no arranjo dipolo-dipolo ou então efetuar medidas sequenciais de potencial em 6 pontos escolhidos.

O cabo múltiplo de 10 mm de diâmetro, possui entradas a cada 10 metros, de cobre coberto com uma película de níquel que proporciona maior dureza e proteção contra oxidação. A cobertura de Ni confere uma boa dureza, que permite o uso de conectores jacaré para conexão com os eletrodos de aço inox cravados no solo.

No caso de investigação com tensão DC, foi desenvolvido um circuito de leitura de 3 ½ dígitos, com resolução de 100 nV, dotado de circuito de servocontrole PID (proporcional- integral-derivativo), que permite o autozeramento do potencial de contacto eletrodo- solo, por simples toque num interruptor de pressão. Como o circuito está dotado de filtro rejeição de 60 Hz, e filtros passa- baixo ativos de frequência de corte mínimo de 0,15 Hz, a constante de tempo destes filtros é da ordem de 1,5 s. Para ter-se o valor correto de tensão, o tempo de medida deve ser da ordem de 5 vezes o valor desta constante. No modo manual, o zeramento torna-se extremamente moroso devido ao valor desta constante de tempo. Com o recurso do circuito de servo-realimentação, o tempo de cancelamento do potencial eletroquímico (contacto eletrodo-solo) é da ordem de 5 s para uma deriva de 1 mV, em 15 minutos. Para facilidade de projeto, usou-se somente circuitos analógicos, no circuito de amostragem e retenção (sample and hold). Para ter-se esta estabilidade temporal foi necessário usar-se anel de guarda na entrada do integrador (memória analógica) para reduzir os efeitos de corrente de fuga.

Des r s r s

Para o comando sequencial dos eletrodos foi desenvolvido um circuito digital descrito a seguir.

O circuito de chaveamento dos eletrodos fixados no solo (Fig. 1) é formado de um multivibrador monostável usando 2 portas NOR (CD4001) que evita possíveis repiques da chave mecânica PULSO. A saída deste pulsador é aplicada na entrada CLK do circuito Johnson ou contador em anel (CD 4017), responsável pelo modo sequencial dos eletrodos de medida de potencial elétrico. As saídas sequenciais são aplicadas nos transistores NPN, que excitam os relés, responsáveis pela comutação, através do acionamento da chave SP/DP (modo potencial espontâneo ou dipolo-dipolo).

As medidas de potencial no modo DC são feitas por um milivoltímetro desenvolvido no IAG, onde foram usados capacitores de policarbonato de baixa fuga, amplificadores operacionais BIFET quádruplos de alto desempenho, baixo ruído e baixo consumo. Para usar-se uma única fonte de 9 V foi montado um circuito que proporciona uma alimentação simétrica $\pm 4,5V$, suficiente para polarizar os circuitos amplificadores e filtros ativos, que consomem 10 mA no total.

Na Fig. 2, um resistor R de 500 Ω é inserido em série com as resistências do solo (entre os 2 eletrodos de medida) e do amplificador diferencial de entrada. Nos extremos deste resistor estão conectados as saídas de 2 circuitos seguidores de tensão, responsáveis pela tensão de cancelamento do potencial eletroquímico eletrodo- solo. Esta tensão de cancelamento poderia ser aplicada diretamente no resistor de realimentação do amplificador diferencial, que produziria o mesmo efeito. Contudo esta configuração não foi adotada para não interferir na razão de rejeição em modo comum CMRR deste amplificador, que poderia afetar o ruído de entrada do circuito.

Na saída do amplificador diferencial de ganho unitário e impedância de entrada de 4 M Ω , estão conectados em sequência (cascata): um filtro rejeição centrado em 60 Hz, um filtro passa baixo de frequência de corte de 1,5 Hz e um filtro passa baixo roll-off com frequência de corte de 0,15 Hz, para redução do efeito dos esféricos (micropulsões, correntes telúricas, etc)

A seguir, existe um circuito de ação derivativa e proporcional para linearizar a função de transferência total do elo de feedback, e introduzir um amortecimento crítico no estágio de autozeramento. Este circuito de cancelamento é introduzido momentaneamente no elo de realimentação através de interruptor S, que deve ser pressionado por 5 segundos, até a convergência para zero, da tensão de saída do filtro roll-off. Uma vez zerado, a chave S é liberada, estando o circuito pronto para medidas de

tensão dos eletrodos de potencial, através de um milivoltímetro DVM de 3 ½ dígitos.

O e r a n a

Primeiramente são cravados os 2 eletrodos de corrente e os eletrodos de medida de potencial, cujo número depende da profundidade de investigação. Este arranjo retilíneo de eletrodos equidistantes é orientado, de modo a cruzar transversalmente a descontinuidade geológica de interesse. A seguir conecta-se os eletrodos de corrente (aço inox) à fonte e estende-se o cabo de múltiplas entradas ao longo da linha de eletrodos (aço inox) de medida do potencial elétrico. Então estas entradas são conectadas aos eletrodos de medida através de garras jacaré. Como estas comutações são feitas sequencialmente por um pequeno toque na chave S, a possibilidade de erro é minimizada. Após o término deste grupo de medidas, o cabo é facilmente arrastado de 10 metros, para uma nova sequência. Isto reduz o tempo total de um levantamento geoeletrico, e diminui a possibilidade de erros, nesta sequência tediosa e cansativa de medidas no campo.

Para medidas de potencial espontâneo usando eletrodos não polarizáveis de CuSO₄, onde não é injetado corrente no solo, o procedimento é idêntico, bastando o acionamento da chave seletora DP/SP, do circuito comutador (Fig.1).

C e n r s

O sistema desenvolvido foi utilizado num trabalho de delimitação do poluente churume num lixão já desativado em Ribeirão Preto, com sucesso. O seu uso reduziu apreciavelmente o tempo de trabalho de campo.

Nesta fase do projeto evitou-se o uso de microcontroladores da família do 82C51 ou PIC, para facilitar sua execução e solucionar um problema urgente. Futuramente estes microcircuitos com memórias RAM, EEPROM e Flash programados em linguagem C serão empregados para controle do circuito contador em anel CD4017, e de um conversor AD de 12 bits para conexão com um notebook, através de saída paralela da impressora.

B r a a

Bastianon, D., 1996. Desenvolvimento de um sistema de medida de resistividade elétrica complexa para aplicações geofísicas. Dissertação de Mestrado, IAG-USP, pp 80.

Figini, G., 1982. Eletrônica Industrial: Servomecanismos. Editora Hemus, pp 202.

Projeto de um sistema semi-automatizado de medidas de potencial elétrico natural ou induzido do solo para aplicações geolétricas

Frohr, F. & Orttenger, F., 1990. Técnicas de Controle Eletrônico: Controle Automático para Acionamentos Reguláveis de Corrente Contínua. Manual Siemens, pp 320.

Hiodo, F.Y.; Ribeiro, F.B. & Roque, A., 1993. Desenvolvimento de sistema de controle de

gamaespectrômetro de NaI (Tl). 3º Congr. Inter. da SBGf, Rio de Janeiro-RJ, 2: 865-870.
Telford, W.M., Geldart, L.P., Sheriff, R.E. & Keys, D.A., 1986. Applied Geophysics. pp860.

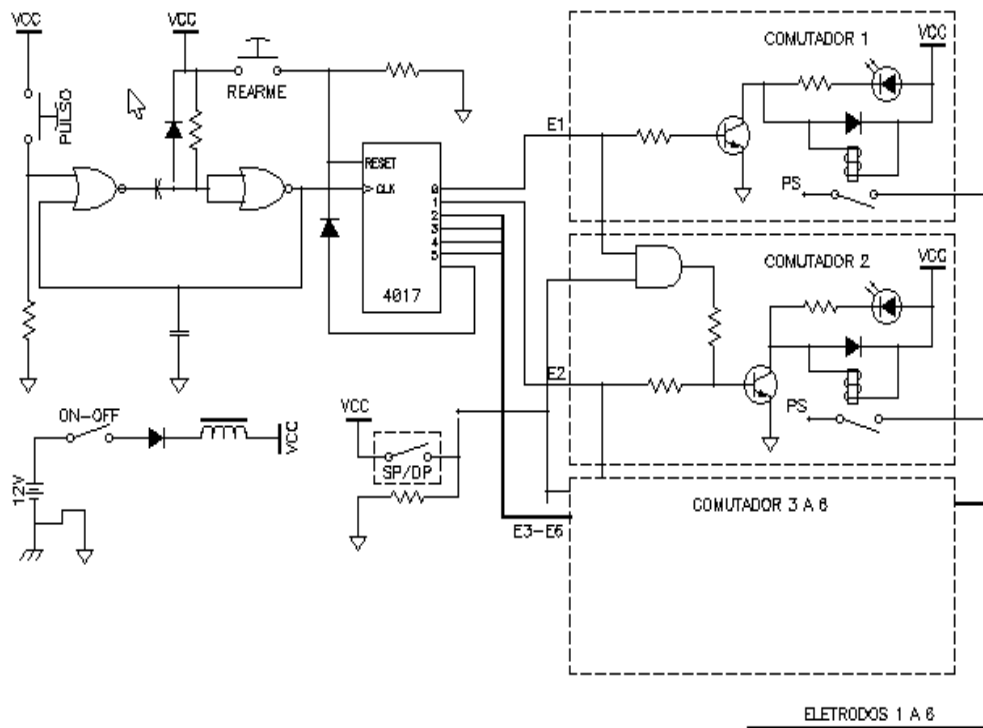


Fig.1 Diagrama esquemático do circuito de comando sequencial dos eletrodos de potencial elétrico do solo.

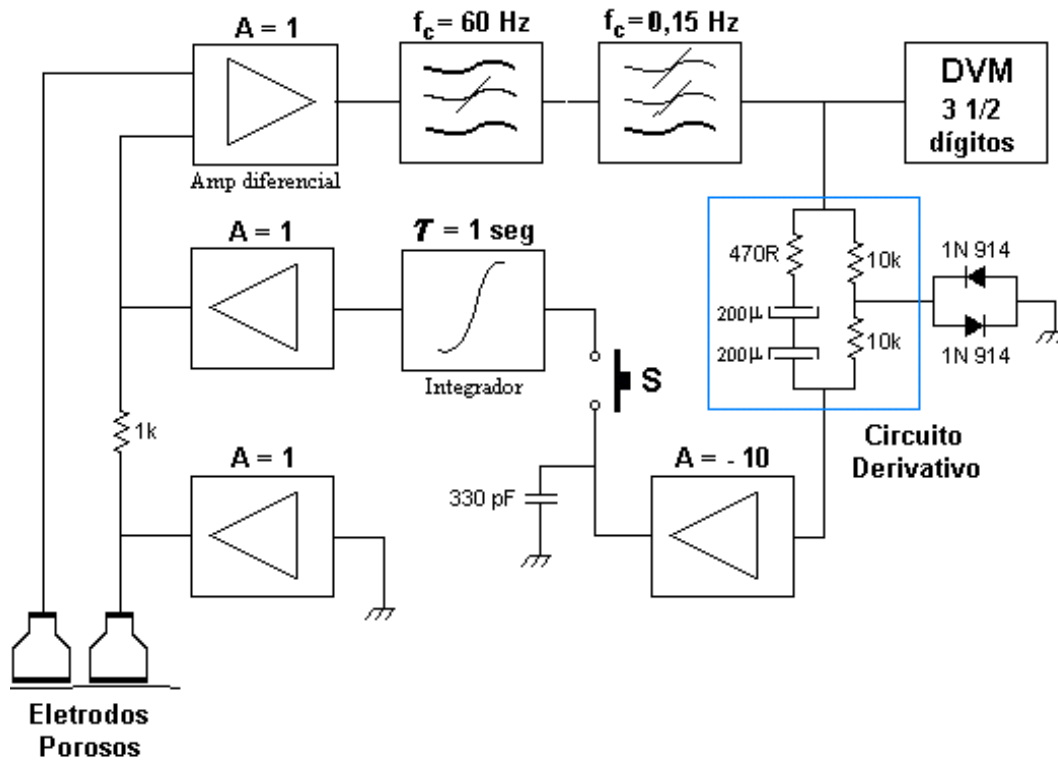


Fig. 2 Circuito de zeramento usando servocontrole PID e memória analógica, para medida de potencial DC do solo.



Recording Electro seismic signals in boreholes distant to the source

Paul Baggaley, Keele University, UK

Abstract

Electro seismic signals are recorded by antennas in boreholes at distance from the seismic source generating them. This is done in two different settings with two different antenna types. This allows us to see common factors between the two data sets such as polarity reversals, consistency of waveforms during experiments and amplitude variations with resistivity.

Introduction

Electro seismic phenomena (also called electrokinetic and seismoelectric) have been the subject of a large number of papers since their discovery over sixty years ago (Thompson 1936, Ivanov 1939). In a saturated porous medium an electric double layer forms at the interface between solid and fluid. Seismic waves cause a relative motion of the charges in the double layer creating an electro seismic signal. At a boundary between formations with different properties there is a non-equilibrium between the free charges and the seismic wave generates an electromagnetic wave (Zhu et al 1999).

The theory behind electro seismic signals has been advanced over recent years by Pride and Haartsen (1996) and Haartsen and Pride (1997), who have shown that these signals can be modelled numerically. There have also been papers showing the detection of electro seismic signals from subsurface interfaces in the field (Mikhailov et al (1997), Thompson and Gist (1993), Butler et al (1996)). These field trials all relied on applying a seismic source at the surface and detecting the resulting electro seismic signal with dipole antennas also at the surface.

More recently work has been carried out on detecting electro seismic signals in boreholes. Mikhailov (2000) studied electro seismic signals in boreholes to locate and characterise fractured permeable zones. This method involved hitting the borehole collar with a sledgehammer, to act as a source at the surface of the borehole being studied, and using downhole electrodes as the receiving antennas. Hunt and Worthington (2000) also studied electro seismic signals in a borehole but using a borehole hammer as a source which moved down the borehole between shots with an electrode pair a fixed distance below it so that there was a constant source/receiver spacing. None of these

studies tried to record electro seismic signals in adjacent boreholes or tried to determine if some signals in their data were from surrounding boreholes.

In a similar way to these Mikhailov et al (2000) and Hunt and Worthington (2000) our experiments will use a Stoneley borehole wave to generate a flow of pore fluid in a permeable formation around a borehole. This movement of pore fluid will be detected as an electro seismic signal by antennas in an adjacent borehole. We will present data from two sites with different geologies using slightly different methodologies. The first setting is a sandstone series with matrix dominated permeability and some fracturing due to bedding planes. Here we will use a downhole hammer the same as Hunt and Worthington (2000). The second setting is in marine metasediments formation where the permeability is controlled by the fracturing where we will use a sledgehammer at the surface the same as Mikhailov et al.

Method

The experiments were carried out with slightly different instrumentation and set-ups. This was because of difficulties in finding sites with uncased boreholes close enough together for our experiments, so we used the best equipment available to us at the time. The sites were all in the UK, at Mansfield in Nottingham and Reskajeage in Cornwall.

Mansfield

This site is on industrial land to the north east of a disused coking plant, where until 1980 organic solvents such as Phenyl and Ammonia were used to clean the coal. Forty uncased boreholes were drilled on this site to study the pollution plume from the coking plant, which has now been treated leaving the boreholes unused. The geology of this site is a coarse grained Bunter sandstone with some gravel beds. Although there is some fracturing due to the bedding planes the hydrogeology of the site is dominated by the permeability of the sandstone. Detailed geological and geophysical logs were taken some of which are shown here in figure 1. These logs are from borehole into which we would place the antenna.

In this experiment a Stoneley wave was generated by using a downhole hammer in the same way as Hunt and Worthington (2000). The downhole hammer is a 75cm steel cylinder with a central steel shaft attached to a nylon block. The shaft can slide

Recording Electro seismic signals

freely through the steel tube and is operated by a pull rope at the surface. The pressure pulse is generated by the nylon block as it moves upwards to strike the body of the tool. This generated a pulse with a centre frequency of 100 Hz. Throughout the experiment the downhole hammer was suspended in the borehole fluid (water).

The vertical electrical field induced by the Stoneley wave was detected by a string of electrode pair antennas suspended in the borehole fluid in an adjacent borehole 15.13m away from the borehole containing the downhole hammer. The electrodes

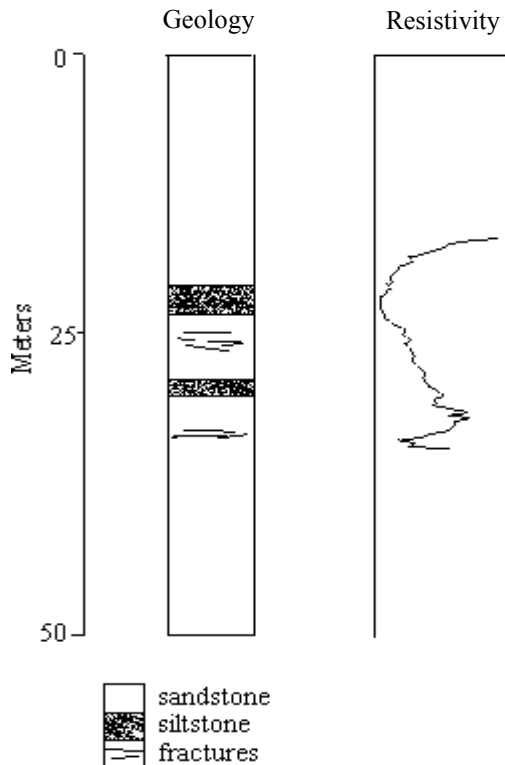


Figure 1 Geological and geophysical logs from Mansfield.

were made of lead and approximately 6 cm long with a 1 m spacing between electrodes in a pair. The sampling frequency was 8 kHz and shots were stacked sixty times with a one meter spacing between shot points while the electrodes were left in the same position throughout the whole experiment.

Reskajeage

Reskajeage quarry in Cornwall was one of the test sites also used by Hunt and Worthington (2000). It was developed over twenty years ago for the study of fluid flow in a fracture dominated environment and a total of twenty four boreholes were drilled

over an area of approximately 600m² with geological and geophysical logs taken to characterise the site. The geology is marine metasediments of Devonian age locally known as the Mylor Slates, which have angular fracture sets as well as bed planar jointing. Figure 4 shows the geological and resistivity logs for the borehole into which we would put the antenna. These show that although the hydrogeology may be dominated by the fractures the resistivity of the formation is controlled by the metasandstones while the conductivity of the fluid remains almost constant throughout the borehole.

In this experiment a Stoneley wave was generated by using a sledgehammer to strike the ground next to the collar of the borehole similar to that done by

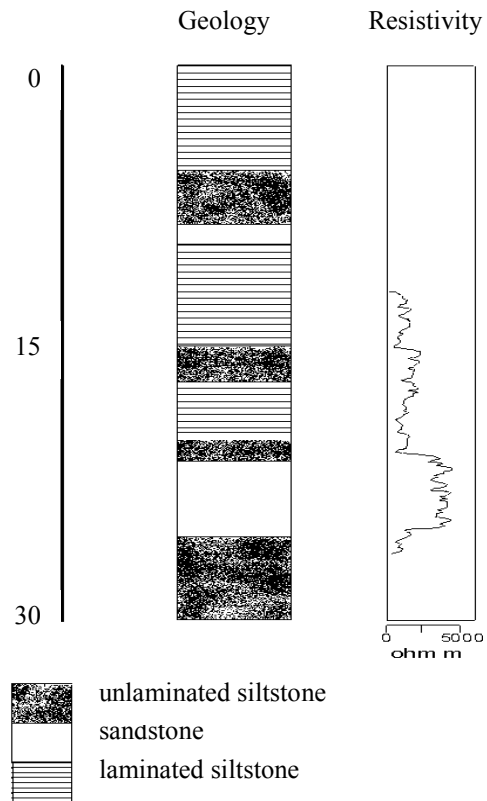


Figure 2 Geological and geophysical logs from Reskajeage.

Mikhailov et al (2000). This generated a pulse with a centre frequency of 240 Hz. The vertical electrical field induced by the Stoneley wave was detected by a single electrode dipole antenna suspended in the borehole fluid. The electrodes were made of copper and 3 m long with a 10 cm spacing between them. The sampling frequency was 32 kHz and shots were stacked ten times with the electrode pair moved one meter further down the borehole between stacks. After the survey was

Recording Electro seismic signals

completed the shot point was then moved to the top of an adjacent borehole 5 m away and the same survey process repeated with the electrodes occupying the same positions as before.

Noise Reduction

As in all electro seismic field experiments the data was dominated by electrical mains noise from remote power lines. This noise was at 50 Hz and removed using the sinusoid subtraction method (Butler and Russell, 1993). In the raw data the electrical noise had amplitudes of up to 2 mV/m whereas the electrical field induced by the seismic energy had amplitudes as low as 200 μ V/m.

Results

The electro seismic data from Mansfield (fig 3) shows three distinct peaks in the full waveform data. All these peaks have the same arrival time at all receivers and so have moved at electromagnetic wave velocities rather than seismic wave velocities. The waveforms varied only slightly with shot position. The three main arrivals all always arrived at the same times and the relative amplitudes all remained the same.

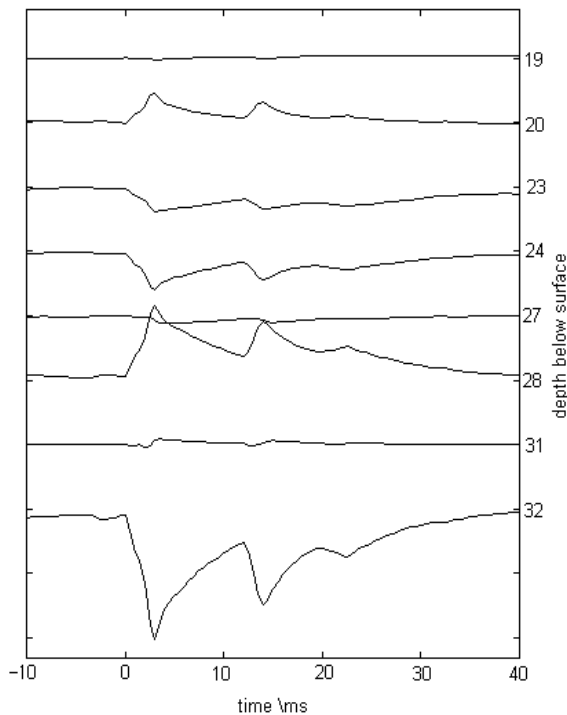


Figure 3 Electro seismic data from Mansfield.

The first peak starts to rise as soon as the hammer is struck but this is definitely not crosstalk from the

trigger cable. An accelerometer on the downhole hammer acted as a trigger and its output was recorded on a separate channel on the seismograph. It showed different characteristics to the electro seismic waveforms.

The second peak starts to arrive 12 ms later which is the time it takes for the S waves to travel between the borehole containing the source to the borehole containing the receivers. There is a third peak that starts to arrive 10 ms later still which could possibly correspond to a number of interfaces.

The results from Reskajeage with the source at the top of the borehole containing the receivers (figure 4) show two distinct types of arrivals marked by the lines a – a' and b – b'. The amplitude of the signals increases with resistivity and so is largest on the bottom trace where the resistivity of the formation suddenly increases with the change in lithology from siltstone to sandstone.

The second signal is much smaller than the first and arrives at 2.5 ms on traces at 16, 17, 18 and 19 m, and also on traces 13 m and 14 m. These are electro seismic signals that have travelled at electromagnetic velocities but have been rapidly attenuated.

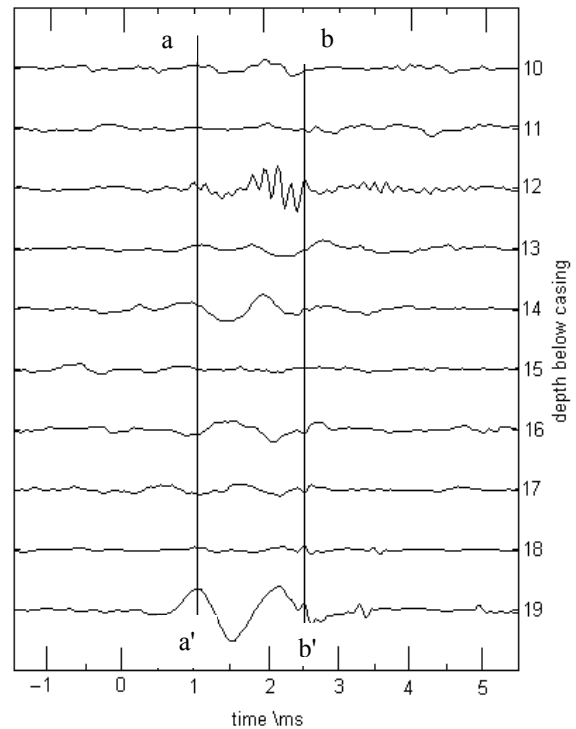


Figure 4 Electro seismic data from Reskajeage.

Recording Electro seismic signals

Discussion

The data from Mansfield and Reskajeage do not initially appear to be very similar but they do share three major characteristics. Firstly although the recorded waveforms differ between the two sites they are consistent throughout the respective data sets. The difference between them is probably due to the difference in the size of antenna used and differences in geology. Secondly the signal has undergone a 180° phase change on some traces as can be seen in figure 3 at depths of 20 m and 28 m for example. The reason for this is still unclear but it is a repeatable and real effect, which seems dependent on receiver position and is not affected by the location of the seismic source. Thirdly the amplitude of the electro seismic signals recorded also varies with the position of the receiving antenna. Comparing the peak amplitudes with the resistivity logs shows that there is a correlation between zones of high resistivity and high electro seismic amplitude. This is to be expected as these regions have fewest ions so when they are disturbed by the seismic energy the ions that are present can generate relatively large voltages.

Conclusion

This work from both sites shows that fractures can generate electro seismic signals which can be recorded in boreholes away from where the seismic energy is located. These signals travel at very high velocities and the waveform recorded depends on the characteristics of the antenna as much as upon the geology of the situation. The fact that the highest amplitude signals are recorded in zones of high resistivity allows us to selectively position the antennas in future experiments to get the best signal to noise ratio possible. This work was carried out as a prelude to establishing a combined electro seismic and micro seismic monitoring network around collapsing cavities. Using the information from this work now allows us to choose the most suitable type of antenna and best position for that antenna.

Acknowledgements

This research was funded by a Natural Environment Research Council (NERC) grant. Assistance with fieldwork from Prof. Peter Styles, Dr George Tuckwell, Duncan Bate and Alison Jagger is gratefully acknowledged.

References

- Butler, K. E. and Russell, R. D., 1993, Subtraction of powerline harmonics from geophysical records: *Geophysics*, **58**, 898-903
- Butler, K.E., Russell, R.D., Kestic, A. and Maxwell, M., 1996, Measurement of the seismoelectric response from a shallow boundary: *Geophysics* **61**, 1769-1778
- Haartsen, M.W. and Pride, S.R., 1997, Electro seismic waves from point sources in layered media: *J. Geophys. Res.*, **102**, 24745-24769
- Hunt, C. W. and Worthington, M. H., 2000, Borehole electrokinetic responses in fracture dominated hydraulically conductive zones: *Geophysical Research Letters* **27**, 1315-1318
- Ivanov, A.G. 1939, Effects of electrization of earth layers by elastic waves passing through them (in Russian): *Doklady Akademii Nauk. SSSR*, **24**, 42-45
- Mikhailov, O., Haartsen, M. W. and Toksoz, M. N., 1997, Electro seismic investigation of the shallow subsurface: Field measurements and numerical modelling: *Geophysics* **62**, 97-105
- Mikhailov, O., Queen, J. and Toksoz, M. N., 2000, Using borehole electro seismic measurements to detect and characterise fractured (permeable) zones: *Geophysics* **65**, 1098-1112
- Pride, S.R. and Haartsen, M.W., 1996, Electro seismic wave properties: *J. Acous. Soc. Am.*, **100**, 1301-1315
- Thompson, R.R., 1936, The seismic electric effect: *Geophysics*, **1**, 327-339
- Thompson, A.H. and Gist, G.A, 1993, Geophysical applications of electrokinetic conversion: *Leading Edge*, **12**, 1169-1173
- Zhu, Z., Haartsen, M. W. and Toksoz, M. N., 1999, Experimental studies of electrokinetic conversions in fluid-saturated borehole models: *Geophysics* **64**, 1349-1356
- Zhu, Z., Haartsen, M. W. and Toksoz, M. N., 2000, Experimental studies of seismoelectric conversions in fluid-saturated porous media: *J. Geophys. Res.*, **105**, 28055-28064



Resistivity imaging from MT and Seismic data in the Tucuman Plain, Argentina.

Favetto A, Pomposiello M.C. and Rossello E.
UBA-INGEIS-CONICET, Argentina

Abstract

MT data along two traverses in the Tucumán Plain were analyzed and it was found that basin sediments are formed mainly by two layers. Then, seismic reflection data coincident to the traverses have been used to constrain the geometry between the basement and the sedimentary rocks. The models obtained from data inversion show a sharp resistivity contrast at the interfaces.

Introduction

In 1990, a project to study sedimentary basins in the Pampean Ranges (PR) was started in order to determine their structure and thickness. The first stage was performed in the Tucumán Plain (TP), (at approximately 27.5° S), within a geothermal region bounded by the very high Aconquija Range to the west and the much lower Guasayán Range to the east, both of which are part of the Pampean Range (PR) (Pomposiello, et al., 1991, 1994; Osella, et al., 1993). From mid-October to early November, 1998, 18 wideband magnetotelluric (MT) sites were collected along two east-west (E-W) traverses primarily in Tucumán Province, but extending eastward into Santiago del Estero Province (Fig. 1). The northern traverse, called the 100 line, is 165 km long and coincides with a series of industry seismic reflection profiles re-processed to image structure to a depth of almost 40 km (Cristallini, 2000). The west end of the MT traverse is close to the base of the Aconquija Range and extends east across the Guasayán-Rosario (G-R) Fault system. The southern traverse, called the 300 line, extends 80 km across a widespread,

economically important, low-temperature (<60°C) geothermal reservoir.

A previous analysis of this MT data was performed in order to describe the sedimentary basin and to define the permeable horizons hosting aquifers. Due to the presence of a very conductive shallow structure, the electromagnetic fields are very distorted (Pomposiello et al., 2000).

In this paper we present a new interpretation using seismic reflection data coincident to the profile (Fig.1). The 2-D model was obtained using as constrain the geometry of the interface between Precambrian basement and sedimentary rocks. The model shows at this interface a sharp resistivity contrast.

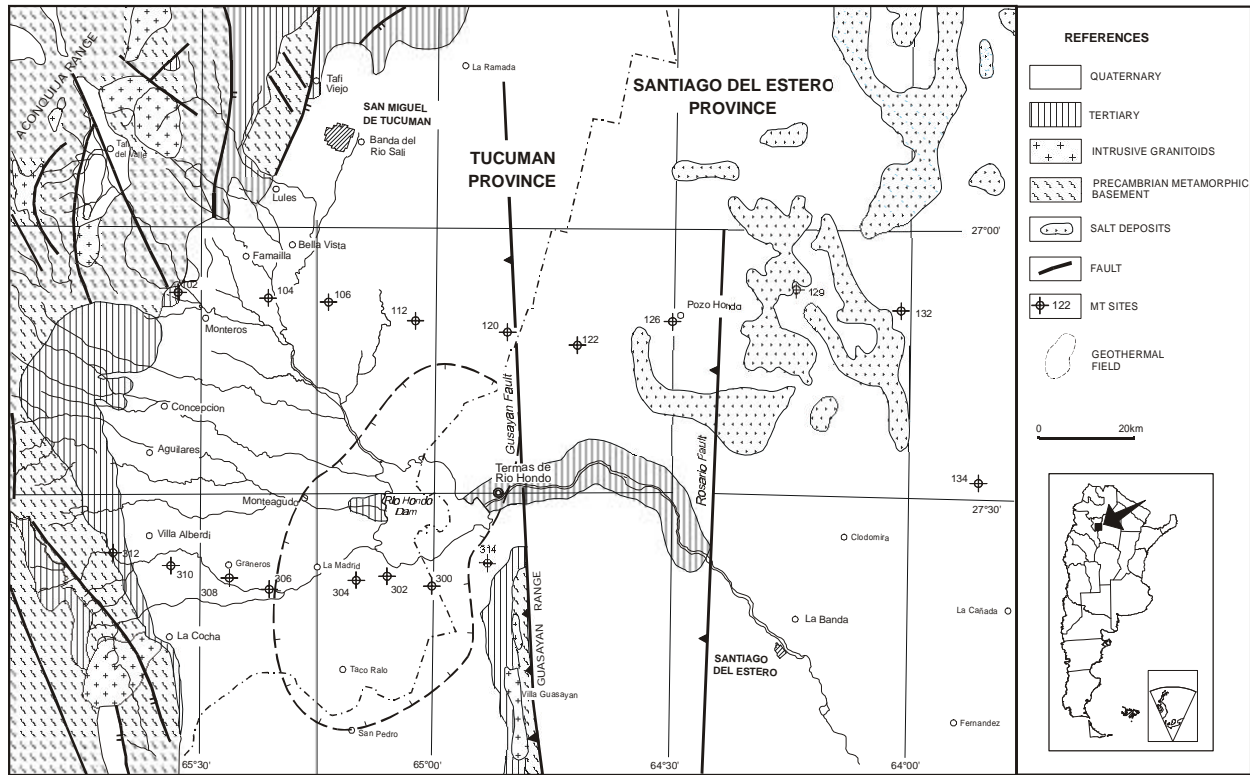
Local geological setting

The Tucumán Plain (TP) is at the northern end of the PR, where the plate dip is steeping northward. In this region both the subducted plate and overlying mantle appear anomalous. In the southern part, the TP is bordered by the Guasayán Range which reaches an altitude of approximately 600 m. On the west, the TP is bordered by the Aconquija Range, which has been elevated more than 5 Km along an east-dipping high angle thrust on its western side. Very little is known in detail about the stratigraphy of the TP basin because, with the exception of a single well in the northeastern TP, no wells have penetrated the Pliocene. Thus deeper stratigraphy must be inferred from outcrops at the border of the basin and from geophysical techniques. In Table 1 we present the stratigraphic scheme and the aquifer features.

Table 1. Stratigraphic scheme and aquifer features.

AGE	LITOLOGY	THICKNESS	AQUIFERS
QUATERNARY	HOLOCENE: Alluvial fans, eolic deposits, dunes, playa and recent deposits. PLEISTOCENE: Loessic and Siltloessic deposits.	150 m	Aquifers have high discharges and excellent qualities for most requirements
		200–400 m	Aquifers have good quality water.
TERTIARY		350–700 m	Aquifers have much higher water quality although some salinity and are artesian...
		2500 m	Aquifers have poor water quality.

Figure 1. Magnetotelluric (MT) sites along two east-west (E-W) traverses in Tucumán Province and extending eastward into Santiago del Estero Province.



Data acquisition and analysis

Data were collected using wideband MT receiver (EMI MT-24) in three bands to nominally cover 250 to 0.001 Hz. Time series were recorded at three digitization rates: 960 Hz (medium (M) band); 60 Hz (low (L) band); and 6.25 Hz (very-low (V) band). The electrical field wires and 3-component magnetic coil sensors were installed in geomagnetic coordinates, which in this region is almost identical to geographic coordinates.

MT impedance tensors and vertical to horizontal magnetic field transfer functions were estimated in the measurement coordinate system preliminary using the robust code (EMTF) of Egbert and Booker (1987). Impedance tensor decomposition (Smith, 1995) were employed to analyze MT data.

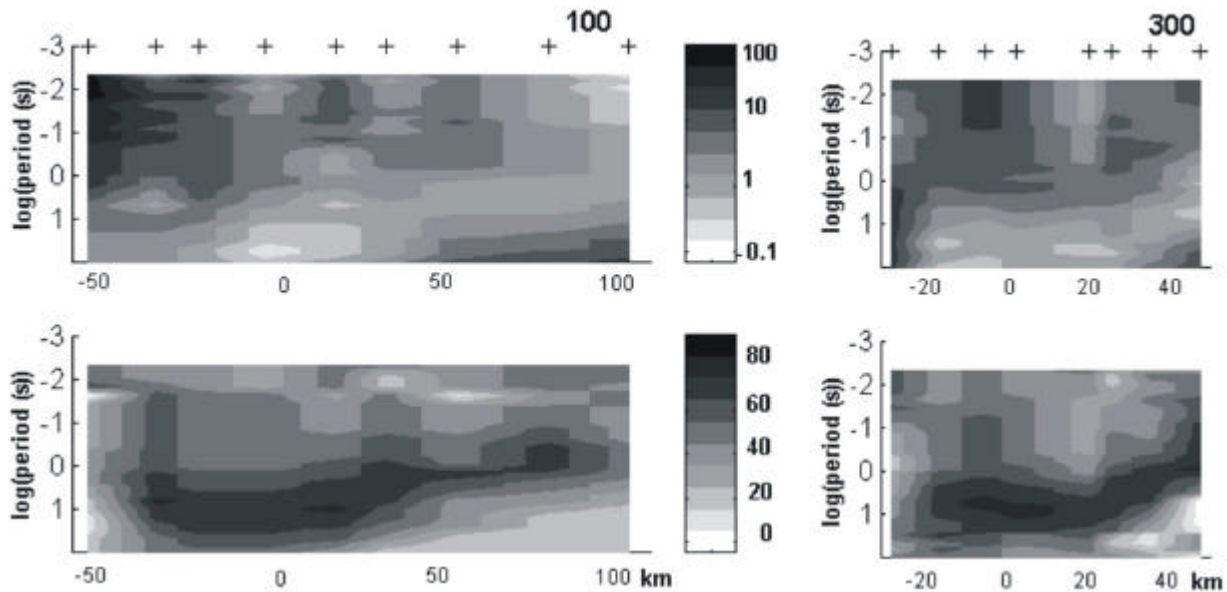
For the 100 line, the coincidence of the apparent resistivity and phase for both polarizations at periods shorter than 1 second suggests locally 1-dimensional (1-D) shallow structure at all sites. Impedance tensor decomposition at 1 second, confirms that there is no preferred strike and that the electric field has, at most, a distortion that is isotropic. As the period increases, at all sites, there is a strike close to 0°.

For the 300 line, in the center of the valley, sites 310

to 306 show 1-D behavior at periods shorter than 1 second and a consistent regional strike of N 20°W above 1 second, which rotates to 0° as the period increases above 50 seconds. Thus these sites show a 1-D surface structure, a shorter period strike dominated by the contact between the sedimentary cover and the ridge to the west and a longer period strike dominated by the Guasayán Range Fault system.

The upper-crustal structure along the 300 line is more complicated than the 100 line. At sites 300 and 314, the impedance tensor decomposition shows that the electric field at these two sites is 100% polarized for periods greater than 50 seconds (i.e. its direction is independent of the source magnetic field). When this happens, normal MT interpretation breaks down. These two sites are within the active geothermal field and the direction of the electric field is sub-parallel to the Guasayán Fault. The structure responsible for this extreme distortion is probably the result of very shallow hydrothermal alteration, whose orientation is controlled by the Guasayán Fault. We did not use periods greater than 50s at these two sites in subsequent 2-D inversions.

Figure 2. Pseudosections for data measured at 100 and 300 lines, for TM mode.



MT 2D Inversion

Since a single strike over the full band-width of our data has to be an approximation, we adopted the criterion that it is best to interpret only the TM mode for data (Fig. 2) along profiles approximately normal to strike. To apply the 2-D algorithm of Smith and Booker (1991) we established a western boundary condition, based on the presence of the resistive Aconquija Range outcrops west out of our most westerly sites, so to constrain the vertical structure we consider that at 100 Km west 102 and 312 the resistivity was 100 Ohm-m in the top 5 Km and 1000 Ohm-m below. The algorithm interpolates the log resistivity between the most western site and this

constrain.

The result is that the very high conductivity of the TP is rapidly terminated in the direction of the Aconquija Range. Two additional constrains were used (at 102 to 120 and at 310 to 300 sites) considering the seismic reflection (Fig. 3) corresponding to velocities of about 1800 m/s and 2600 m/s, at the top and the bottom of the Miocene Formation.

Periods from 0.05 to 100s were used in the inversion. We set a floor to the data error of 10% (3.9 degrees in phase) so with these increased errors, the TM inversions converged easily to a normalized RMS of 1.0.

Figure 3. Resistivity models corresponding to 100 and 300 lines.

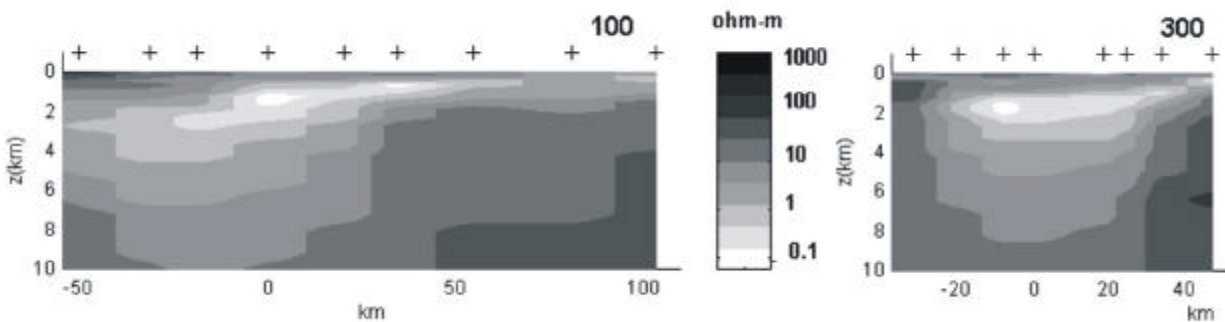
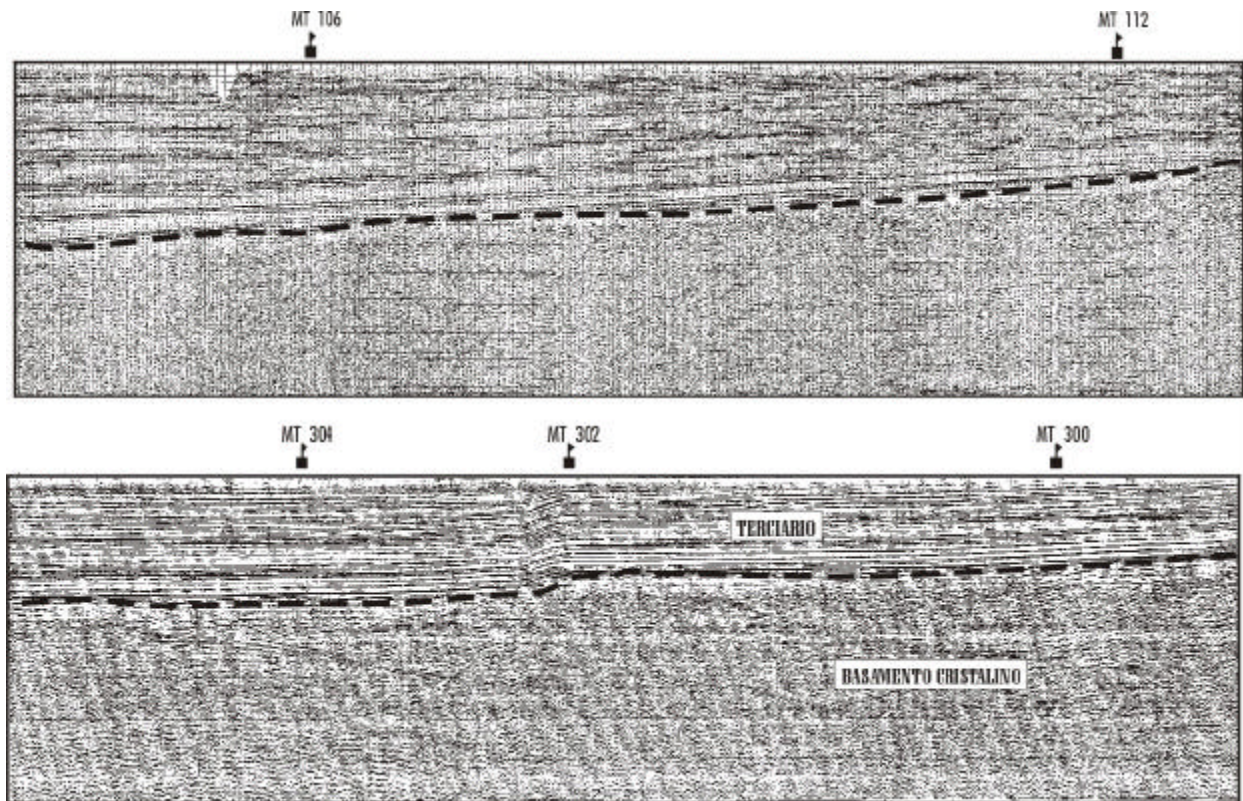


Figure 4. Seismic reflection profiles used to constrain the MT model at coincident sites. The 2600 m/s velocity interface is dashed.



Conclusions

Our result is that the Tucumán Plain (TP) basin sediments can be divided into two main layers. The lower, highly conductive zone can be identified with the highly saline Miocene Calchaquense Unit, which is observed to outcrop as the Guasayán Formation in the Guasayán Range. Overlaying the saline Miocene formations is the Pliocene Las Cañas (Araucanense Unit) with resistivities ranging from 1 to 10 Ohm-m. These will contain water of much better quality. Our model do not shows any strong resistivity contrast in the near-surface that could be used to distinguish the

References

- Cristallini, E., 2000 (personal communication).
 Egbert, G. and Booker, J., 1987. Robust estimation of geomagnetic transfer function estimation, *Geophys. J. R. Astron. Soc.*, 87,173-194.
 Osella, A. M., Pomposiello, M. C., Favetto, A., Sainato, C. and Martinelli P., 1993. Bidimensional Geoelectric Modeling of a Geothermal Anomaly in the Eastern Border of Aconquija Range, *Acta Geod. Geophy. et Montanist*, 28, 329-341.
 Pomposiello, M. C., Mon, R. and Díaz, M. T., 1991. The gravity field of Tucumán Plain and its

contact between the Tertiary and Quaternary (Fig. 4). An important additional step taken to improve our interpretation was to use the seismic reflection lines to constrain model interfaces. We could constrain the geometry of the sharp resistivity contrast between the Pre-Cambrian basement and the overlying sedimentary rocks. This led to a more accurate estimate of the actual formation resistivity of the Miocene and a better determination of the contact between the Pliocene and Miocene given by the geometry of this sharp change in resistivity.

implications in structural geology, *Géodynamique*, 6(1), 3-8.

- Pomposiello, M. C., Osella, A. M., Maidana, A. and Borzotta, E., 1994. MT Studies in the S-E region of Tucumán Plain in the N-W of Argentina, *J. South. Amer. Earth. Sc.*, 7(2), 101-107.
 Smith, J. T. and Booker, J., 1991. Rapid inversion of two- and three-dimensional magnetotelluric data, *J. Geophys. Res.*, 96, 3,905-3,922.
 Smith, J. T., 1995. Understanding telluric distortion matrices, *Geophys. J. Int.* 122, 219-226.



Scattering of Electromagnetic Plane Waves by a Vertical Dike Under a Conductive Overburden: Implications for GPR and TDEM

Lurimar Smera Batista

UNIT/CPGG/UFBA

Edson Emanuel Starteri Sampaio

CPGG/UFBA

Abstract

The expressions for the exact solution of the scattering of a TE mode electromagnetic plane wave in the time domain, by a vertical dike under a conductive horizontal layer, have been established. Integral representations composed of one-sided Fourier transforms describe the scattered electric field components in each one of the five media: air, overburden, dike, and the country rocks on both sides of the dike. The determination of the terms of the series representing the spectral components of the Fourier integrals requires the inversion of a sparse matrix, and the method of successive approaches. The zero-order term of the electric field has been computed on models of vertical dike with overburden, with different geometrical and electrical parameters. The results allow to determine the approximate variation of the TE mode electric field above the overburden, along the direction perpendicular to the strike of the dike. The results demonstrate the efficiency of this forward electromagnetic modeling, and are fundamental for the interpretation of GPR ("Ground Probing Radar") and TDEM geophysical data.

Introduction

The investigation of the scattering of plane waves by a lateral variation of the physical properties of rocks is a fundamental question in applied geophysics. Sommerfeld (1896) and Wiener & Hopf (1931) solved the scattering problem for the interaction between an electromagnetic plane wave and a perfectly conductive half-plane.

Recently several numerical modeling algorithms have been developed to investigate 2D and 3D scattering EM problems, in order to reduce computation costs and to improve efficiency. Some are flexible either because they employ non-uniform sampling intervals or because evaluate the derivatives with different degrees of precision. Others may excite the system with different functions, re-

strict the information at the boundaries, and so on. All these approaches compromise, in a way or other, the precision of the final result.

There are few options of the analytical solution for the problem of 2D EM scattering by an Earth model. Sampaio and Fokkema (1992) established such a solution in the frequency domain for the case of a TE mode electromagnetic plane wave interacting with an outcropping fault in the form of an infinite series. Sampaio and Popov (1997) adapted this solution for the time domain, and computed the field employing the zero-order term of the series. Batista and Sampaio (1999) developed a similar analytical solution for the case of vertical dike under a conductive overburden in the frequency domain.

This paper presents and discusses the adaptation of the work by Batista and Sampaio (1999) for the time domain. Its objective is to provide analytical tools to test the numerical techniques of forward and inverse modeling of 2D TE mode electromagnetic scattering problems in the time domain. It also aims to give means for a better interpretation of: (i) Ground Probe Radar (GPR) data by improving the models described in Seol et al. (2001) and in Leparoux et al. (2001); and (ii) Time Domain Electromagnetic (TDEM) data by improving the models described in Weidelt (1981) and in Song and Lee (1998).

Formulation and solution of the problem

An electromagnetic plane wave propagates in the positive z direction, and impinges normally on the interface between the air and the earth. It is scattered by a geological structure constituted of a vertical dike covered by a plane horizontal layer as shown in Figure 1. The primary components of the electric and the magnetic fields are horizontal everywhere and orthogonal to each other. The problem consists in solving the time domain wave

equation in two dimensions in each medium:

$$(\partial_x^2 + \partial_z^2 - \sigma_n \mu_0 \partial_t - \varepsilon_0 \mu_0 \partial_t^2) e_n(x, z, t) = 0, \quad (1)$$

where $n = 0, 1, 2, 3, 4$; μ_0 is the free-space magnetic permeability; ε_n is the dielectric permittivity of each medium; σ_n is the electrical conductivity of each medium; and $e_n(x, z, t)$ represents the y component of electric field vector in the time domain.

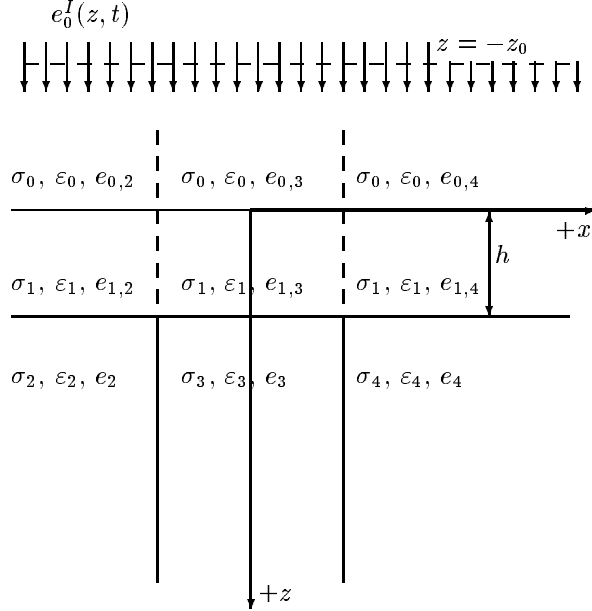


Figure 1: Representation of the geometry of the model, of the incident primary field in the time domain, and of the electrical parameters in each medium.

The solutions of the differential equation (1) in medium 0 ($z < 0$), assume the following forms: for $x < -a$,

$$e_{0,2}(x, z, t) = e_0^I(z, t) + e_{0,2}^R(z, t) + e_{0,2}^S(x, z, t); \quad (2)$$

for $-a < x < a$,

$$e_{0,3}(x, z, t) = e_0^I(z, t) + e_{0,3}^R(z, t) + e_{0,3}^S(x, z, t); \quad (3)$$

for $x > a$,

$$e_{0,4}(x, z, t) = e_0^I(z, t) + e_{0,4}^R(z, t) + e_{0,4}^S(x, z, t). \quad (4)$$

where, $e_0^I(z, t)$ represents the incident electric field; $e_{0,j}^R(z, t)$, $j = 2, 3, 4$, represents the reflected field; and $e_{0,j}^S(x, z, t)$, $j = 2, 3, 4$, represents the secondary scattered field. The subscripts j relate to the halfspace $z > h$, respectively for medium 2, 3 and 4.

The incident field, $e_0^I(z, t)$, occurs only in free-space ($z < 0$), and satisfies the one-dimensional wave equation,

$$(\partial_z^2 - \varepsilon_0 \mu_0 \partial_t^2) e_0^I(z, t) = 0, \quad (5)$$

and it is given by

$$e_0^I(z, t) = e_0(t) * \delta(t - \frac{z}{c}). \quad (6)$$

In (6), $c = (\sqrt{\varepsilon_0 \mu_0})^{-1}$ is the free-space velocity of the electromagnetic wave; and $\delta(v)$ represents the Dirac Delta function.

The reflected field, $e_{0,j}^R(z, t)$, $j = 2, 3, 4$, above the surface of the Earth is computed by the following formula,

$$e_{0,j}^R(z, t) = \frac{1}{\pi} \Re \left(\int_0^\infty E_0(\omega) \frac{r_j - 1}{r_j + 1} e^{i\omega(t + \frac{z}{c})} d\omega \right). \quad (7)$$

In (7), $E_0(\omega)$ represents the amplitude of the incident field; and r_j is the ratio between the characteristic admittance of the medium and the apparent admittance at the surface of the Earth, expressed by,

$$r_j = \frac{k_0[k_1 + k_j \tanh(ik_1 h)]}{k_1[k_j + k_1 \tanh(ik_1 h)]}.$$

The scattered field, $e_{0,j}^S(x, z, t)$, $j = 2, 3, 4$, above the surface of the Earth is computed by the following formula.

$$e_{0,j}^S(x, z, t) = \frac{1}{2\pi} \int_{-\infty}^\infty E_{0,j}^S(x, z, \omega) e^{i\omega t} d\omega. \quad (8)$$

In (8), $E_{0,j}^S(x, z, \omega)$ represents the scattered field in the frequency domain. Substituting the expressions of $E_{0,j}^S$ (Batista & Sampaio, 1999) in (8) and making $E_0(\omega) = 1$, we can express the scattered field in the time domain as:

$$e_{0,2}^S = \frac{1}{2\pi^2} \Re \left(\int_{-\infty}^\infty ik_0 e^{i\omega t} (I_{2,1} + I_{2,2}) d\omega \right); \quad (9)$$

$$e_{0,3}^S = \frac{1}{2\pi^2} \Re \left(\int_{-\infty}^\infty ik_0 e^{i\omega t} (I_{3,1} - I_{3,2}) d\omega \right); \quad (10)$$

$$e_{0,4}^S = \frac{1}{2\pi^2} \Re \left(\int_{-\infty}^\infty ik_0 e^{i\omega t} (-I_{4,1} - I_{4,2}) d\omega \right). \quad (11)$$

In Equations (9), (10) and (11), $I_{n,j}$, for $n = 2, 3, 4$ and $j = 1, 2$, represent integrations of the dummy variable α , expressed as follows:

$$I_{2,1} = b_0 \int_{-\infty}^\infty \frac{e^{-\sqrt{\alpha^2 - (\frac{\omega}{c})^2}(-a-x) + i\alpha z}}{\alpha^2 - (\frac{\omega}{c})^2} d\alpha; \quad (12)$$

$$I_{2,2} = c_0 \int_{-\infty}^{\infty} \frac{e^{-\sqrt{\alpha^2 - (\frac{\omega}{c})^2}(a-x) + i\alpha z}}{\alpha^2 - (\frac{\omega}{c})^2} d\alpha; \quad (13)$$

$$I_{3,1} = b_0 \int_{-\infty}^{\infty} \frac{e^{-\sqrt{\alpha^2 - (\frac{\omega}{c})^2}(a+x) + i\alpha z}}{\alpha^2 - (\frac{\omega}{c})^2} d\alpha; \quad (14)$$

$$I_{3,2} = c_0 \int_{-\infty}^{\infty} \frac{e^{-\sqrt{\alpha^2 - (\frac{\omega}{c})^2}(a-x) + i\alpha z}}{\alpha^2 - (\frac{\omega}{c})^2} d\alpha; \quad (15)$$

$$I_{4,1} = b_0 \int_{-\infty}^{\infty} \frac{e^{-\sqrt{\alpha^2 - (\frac{\omega}{c})^2}(a+x) + i\alpha z}}{\alpha^2 - (\frac{\omega}{c})^2} d\alpha; \quad (16)$$

$$I_{4,2} = c_0 \int_{-\infty}^{\infty} \frac{e^{-\sqrt{\alpha^2 - (\frac{\omega}{c})^2}(-a+x) + i\alpha z}}{\alpha^2 - (\frac{\omega}{c})^2} d\alpha; \quad (17)$$

Those integrals are of the same type, and may be generically represented by,

$$I = \int_{-\infty}^{\infty} \frac{e^{-\sqrt{\alpha^2 - (\frac{\omega}{c})^2}|y| + i\alpha z}}{\alpha^2 - (\frac{\omega}{c})^2} d\alpha, \quad (18)$$

that has the following solution:

$$I = i\pi \int_0^y H_0^2\left(\frac{\omega}{c}\sqrt{\xi^2 + z^2}\right) d\xi - i\pi \frac{c}{\omega} e^{i\omega \frac{z}{c}}, \quad (19)$$

where $H_0^2(v)$ is the Hankel function of the second kind and zero order.

Applying the result of (19) in (12)-(17), and substituting the value of y by the respective linear combinations of x and a , in each integral, performing some simple algebraic operations, one determine the expressions that solve the improper integrals,

$$I_{2,1} = i\pi b_0 \left[\sqrt{\frac{2}{\pi}} e^{\frac{i\pi}{4}} \int_0^{-a-x} \frac{e^{-i\frac{\omega}{c}\sqrt{\xi^2 + z^2}}}{\sqrt{\frac{\omega}{c}\sqrt{\xi^2 + z^2}}} d\xi - \frac{c}{\omega} e^{i\omega \frac{z}{c}} \right]; \quad (20)$$

$$I_{2,2} = i\pi c_0 \left[\sqrt{\frac{2}{\pi}} e^{\frac{i\pi}{4}} \int_0^{a-x} \frac{e^{-i\frac{\omega}{c}\sqrt{\xi^2 + z^2}}}{\sqrt{\frac{\omega}{c}\sqrt{\xi^2 + z^2}}} d\xi - \frac{c}{\omega} e^{i\omega \frac{z}{c}} \right]; \quad (21)$$

$$I_{3,1} = i\pi b_0 \left[-\sqrt{\frac{2}{\pi}} e^{\frac{i\pi}{4}} \int_0^{a+x} \frac{e^{-i\frac{\omega}{c}\sqrt{\xi^2 + z^2}}}{\sqrt{\frac{\omega}{c}\sqrt{\xi^2 + z^2}}} d\xi + \frac{c}{\omega} e^{i\omega \frac{z}{c}} \right]; \quad (22)$$

$$I_{3,2} = i\pi c_0 \left[\sqrt{\frac{2}{\pi}} e^{\frac{i\pi}{4}} \int_0^{a-x} \frac{e^{-i\frac{\omega}{c}\sqrt{\xi^2 + z^2}}}{\sqrt{\frac{\omega}{c}\sqrt{\xi^2 + z^2}}} d\xi - \frac{c}{\omega} e^{i\omega \frac{z}{c}} \right]; \quad (23)$$

$$I_{4,1} = i\pi b_0 \left[-\sqrt{\frac{2}{\pi}} e^{\frac{i\pi}{4}} \int_0^{a+x} \frac{e^{-i\frac{\omega}{c}\sqrt{\xi^2 + z^2}}}{\sqrt{\frac{\omega}{c}\sqrt{\xi^2 + z^2}}} d\xi + \frac{c}{\omega} e^{i\omega \frac{z}{c}} \right]; \quad (24)$$

$$I_{4,2} = i\pi c_0 \left[-\sqrt{\frac{2}{\pi}} e^{\frac{i\pi}{4}} \int_0^{-a+x} \frac{e^{-i\frac{\omega}{c}\sqrt{\xi^2 + z^2}}}{\sqrt{\frac{\omega}{c}\sqrt{\xi^2 + z^2}}} d\xi + \frac{c}{\omega} e^{i\omega \frac{z}{c}} \right]. \quad (25)$$

Substituting (20)-(25) in (9)-(11) and making the necessary algebraic operations, we obtain the expressions for the scattered electric field in the time domain, above the surface of the Earth, $z < 0$.

Numerical Results

In order to show the validity and applicability of the algebraic results, we computed the electric field normalized by the minimum absolute value of the magnetic field, $|h_x(z, t)|$, at $z = -9 m$, of two models of a vertical dike respectively with conductivities $\sigma_3 = 0,01 S/m$ (Figure 2) and $\sigma_3 = 0,1 S/m$ (Figure 3), with a width $2a = 20 m$, immersed in a country rock of conductivity $\sigma_2 = \sigma_4 = 0,05 S/m$, and covered by an overburden with a conductivity $\sigma_1 = 0,001 S/m$ and thickness $h = 30 m$. Figures (2) and (3) show the variation of the scattering of the normalized electric field as a function of time and horizontal distance (x axis). It is a straightforward matter to identify the center of the dike and its contacts with the country rock by a visual inspection. We also observe that the scattering becomes different of zero for values of time larger than $250 ns$, as expected from the vertical distance between the observation point and the top of the dike. We can also notice that the value of the field on the central part is either larger or smaller than the surroundings, respectively for a more resistive or more conductive dike than the country rock.

Conclusion

We established the exact solution for the scattering of an electromagnetic plane wave, in the time domain, by a vertical dike between two quarter-spaces and covered by a horizontal layer. The time domain algebraic expressions have been obtained by an inverse Fourier transformation of the zero-order solution in the frequency domain. The secondary fields have been determined by integration of the Hankel function of second kind and zero or-

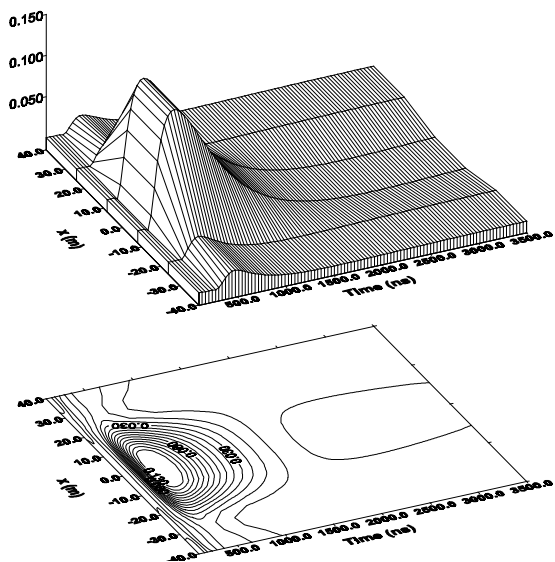


Figure 2: 3D representation and contour curves of the variation of the scattering of the electric field as a function of time and horizontal distance at $z = -9 m$. $\sigma_1 = 0,001 S/m$, $\sigma_2 = \sigma_4 = 0,05 S/m$, $\sigma_3 = 0,01 S/m$, $2a = 20 m$ and $h = 30 m$.

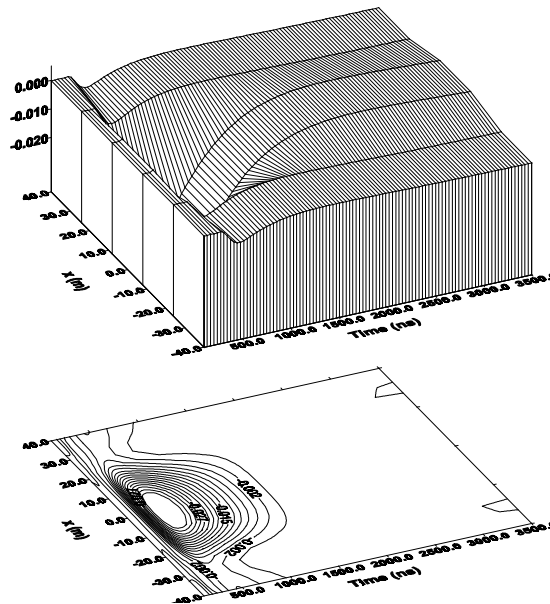


Figure 3: 3D representation and contour curves of the variation of the scattering of the electric field as a function of time and horizontal distance at $z = -9 m$. $\sigma_1 = 0,001 S/m$, $\sigma_2 = \sigma_4 = 0,05 S/m$, $\sigma_3 = 0,1 S/m$, $2a = 20 m$ and $h = 30 m$.

der. The computed data serves to illustrate the behaviour of the secondary field above the surface of the Earth and to demonstrate the efficiency and good approximation of the zero-order expression in the time domain. Those data may therefore be used in the inverse modeling and subsequent interpretation of GPR (Ground Probing Radar) and TDEM geophysical survey data.

References

BATISTA, L. S. & SAMPAIO, E. E. S.. Scattering of Electromagnetic Plane Waves by a Buried Vertical Dike. 6th International Congress of SBGf, 1999.

LEPAROUX, D., GIBERT, D. & CÔTE, P.. Adaptation of Prestack Migration to Multi-Offset Ground-Penetrating Radar (GPR) Data. *Geophys. Prosp.*, 49, 374-386, 2001.

SAMPAIO, E. S. & FOKKEMA, J. T.. Scattering of Monochromatic Acoustic and Electromagnetic Plane Waves By Two Quarter Spaces. *J. Geophys. Res.*, 97(B2), 1953-1963, 1992.

SAMPAIO, E. S. & POPOV, M. M.. Zero-Order

Time Domain Scattering of Electromagnetic Plane Waves by Two Quarter Spaces. *Radio Science*, 32(2), 305-315, 1997.

SEOL, S. J., KIM, J., SONG, Y. & CHUNG, S.. Finding the Strike Direction of Fractures Using GPR. *Geophys. Prosp.*, 49, 300-308, 2001.

SOMMERFELD, A.. *Mathematical Theory of Diffraction*. *Math. Ann.*, 47, 317-374, 1896.

SONG, Y. & LEE, K. H.. A Wide-Band Integral Equation Solution for EM Scattering by Thin Sheets. 68th SEG meeting, New Orleans, USA, Expanded Abstracts, 436-439, 1998.

WEIDELT, P.. Report on Dipole Induction by a Thin Plate in a Conductive Halfspace with an Overburden. Federal Institute of Earth Sciences and Materials, 1981.

WIENER, N. & HOPF, E.. One Classe of Singular Integrals. *Proc. Prussian Acad. Math. Phys. Sec.*, 696-796, 1931.

Acknowledgments

We acknowledge the support from CNPQ.



TEM SURVEY AT SERGIPE-ALAGOAS BASIN

Paulo de Tarso L. Menezes, Eutair R. De Morais, Alan S. Cunha, GEFEX-DGAP/FGEL/UERJ, ptarso@uerj.br

Introduction

Carbonates make up about 20% of the sedimentary rocks record, but they account for more than 50% of the world's proven oil reserves (Palaz & Marfut, 1997). Carbonates differ from siliciclastics in generation, geomorphology, and diagenesis, all of which modify the mineralogy, porosity and permeability so important to reservoir quality.

Recent discoveries of high porosity's layers in deeply seated carbonate sediments have pointed out that deep hydrocarbon carbonate reservoirs are an important Brazilian exploration frontier (Brunh, 1990). Among the most impressive deep reservoirs in Brazil are the fields of Badejo, Pampo e Linguado at Campos Basin (reservoir is located 2500-3100 m depth - Lagoa Feia Formation), and Tubar^ao at Santos Basin (reservoir at 4600-4850 m depth - Guaruj^a Formation).

3D seismic surveys have been carried out and a great number of deep wells have been drilled. Despite the great amount of data, the effort is still insufficient for a detailed evaluation of the hydrocarbon potential of deep carbonate reservoirs. One of the several reasons is that there are more than 30 basins to be explored, covering an area over 5,000,000 km².

At Sergipe-Alagoas Basin, northeast Brazil (Fig. 1), the onshore part there is a great number of carbonates and siliciclastics sediments outcrops. There is also a great collection of boreholes, seismic (2D & 3D), gravity and magnetic data. As consequence, the basin has become a great laboratory for studies of the evolutionary processes of the margin east Brazilian basins

The work presented here is part of a multidisciplinary project named "High resolution stratigraphy applied to geometry and quality of carbonate reservoirs", developed by FGEL/UERJ & PETROBRAS (The Brazilian Oil Company). TEM measurements were performed over an outcropping zone of a carbonate section (Riachuelo Fm.) of Sergipe-Alagoas Basin (Fig. 1). The Riachuelo Formation is correlated to the carbonate reservoirs of Santos and Campos Basin and deep prospects at Espirito Santo/Cumuruxatiba, Barreirinhas and Potiguar Basins (Mendes, 1994).

The objective of the project is to integrate geological and geophysical data (borehole, 2D seismics and EM) to unveil the geometry, stratigraphy and the depositional settings of the carbonate bodies of Sergipe-Alagoas Basin. The final model is expected to be exported to other Brazilian basins.

TEM Survey

We collected 49 SIROTEM-MK3 100 and 50m side single loop stations at four NW striking profiles and in-between. Some of the stations were collected at known oil fields. Figure 1 shows the location of the sites superimposed to a simplified geological map. The sites were preferably collected nearby the outcrops of Riachuelo Formation and boreholes with resistivity logs. The dataset was primarily processed using the software TEMIXXL. Figure 2 shows apparent resistivity pseudosection for two profiles from the northern part of the studied area. Both profile crosses known oil fields.

The objective is to determine de geometry of shallow carbonates that cannot be achieved by seismic interpretation. For example we show in Figure 3 a typical Dip seismic profile of the basin. As can be seen, we only have interpretable data after 0.1s.

1D Inversions

In order to have a more detailed picture of the resistivity distribution of the subsurface 1D Occam's smooth inversion was applied to all dataset. The inversion parameter used were 15 layers and a maximum of 20 iteration. Inversion was stopped with an error lesser than 1%.

The inverted model and fitting for 2 stations of profile P1 is shown in Fig. 4. As can be seen in the given example all sites had a very good fitting, indicating a 1D earth. This is corroborated by the outcrops and by seismics (Fig. 3).

Interpretation and Considerations

In order to use the inverted models to produce a regional picture, we assembled together all 1D Occam's inversion along both profiles. Such procedure allowed us to infer any lateral continuity that may exist among the inverted models. This produces the continuity sections showed in Figure 5.

Both profiles shows very similar features indicating the continuity of the sedimentary units along the studied area. With the TEM dataset it is possible to map 3 main geoelectric units, a resistor on the top (carbonates), followed by a conductor (shale) and by a resistor (carbonate).

It's interesting to note that stations located at known oil fields presents low resistivity zone at depth, for example sites 7 and 9 at profile P1; and sites 16 and 15 at profile P2. Others sites not shown here and located at known oil fields exhibits the same behavior. Several authors correlates

conductivity anomalies to alteration plumes of hydrocarbon (Smith & Rowe, 1997). Taking into account our results, EM technique can be used as an effective prospecting tool at Sergipe-Alagoas Basin.

Future work evolves the correlation of our results with borehole, seismic and potential field data, not shown here because they are still confidential data, but soon will be released. The whole dataset will be integrated in GOCAD platform to generate a final model for the albian carbonate section.

Acknowledgements

We would like to thank MCT-ON for the loaning of the SIROTEM system for data acquisition.

References

- Mendes, J. M. C., 1994. Análise Estratigráfica da Seção Neo-Aptiana/Eocenomaniana (Fm Riachuelo) na área do Alto de Aracaju e adjacências Bacia de Sergipe-Alagoas. UFRGS. Masters Degree Thesis. 166p.
- Mendes, J. C. M., 1998. Sergipe-Alagoas Basin Exploration History. The Search. p 17-22.
- Palaz, I. and Marfurt, K. J., 1997. Carbonate Seismology. SEG Geophysical Developments series, 6. 423p.
- Smith, R. and Rowe, J., 1997. A New Regional Exploration Method for Detecting Hydrocarbon Alteration Plumes: the ALTREX TM Method. Exploration Geophysics, 28: 286-291.

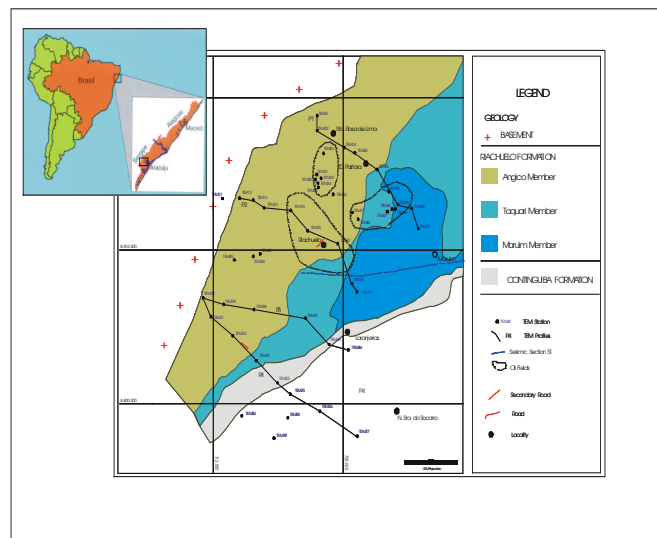


Figure 1 - TEM stations superimposed to the simplified geological map of the studied area.

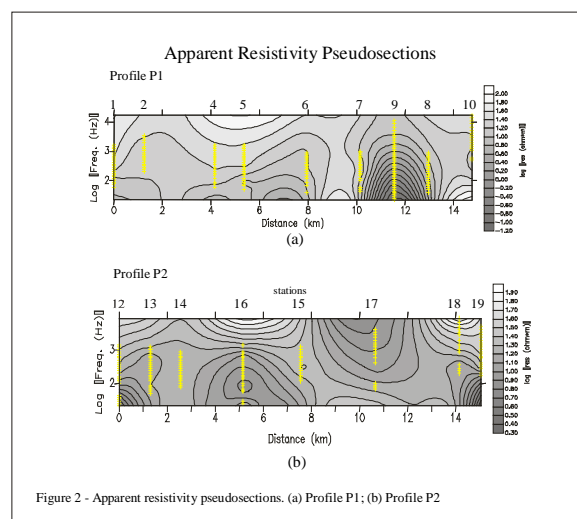


Figure 2 - Apparent resistivity pseudosections. (a) Profile P1; (b) Profile P2

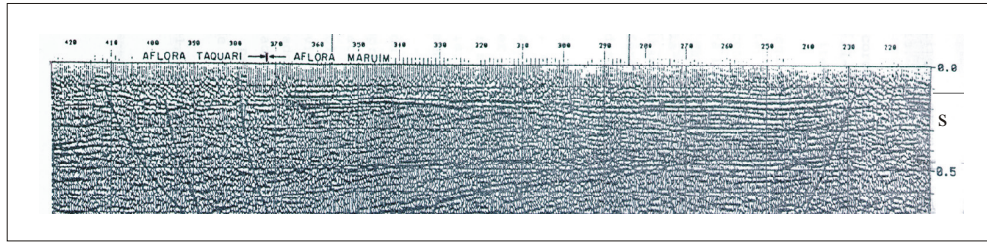


Figure 3 - Seismic Section S1 (see Fig. 1 for localization). No interpretable data until 0.1 s. (Mendes 1994)

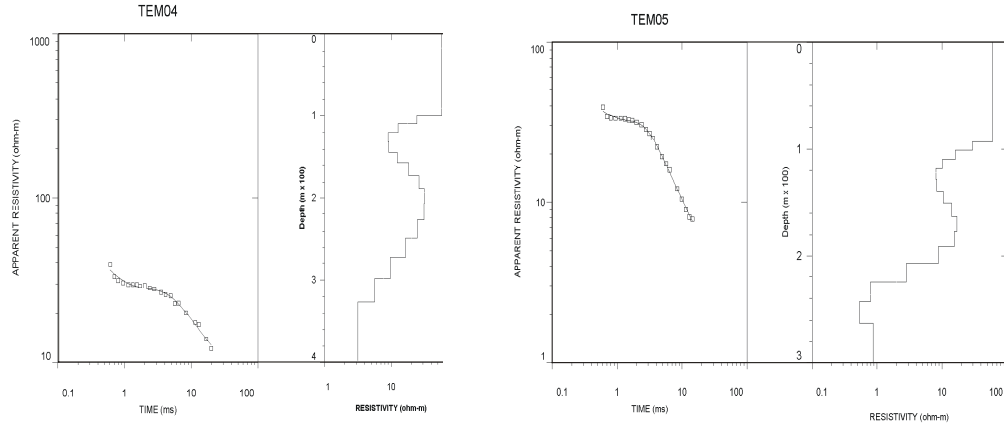


Figure 4 - 1D inverted models and fitting

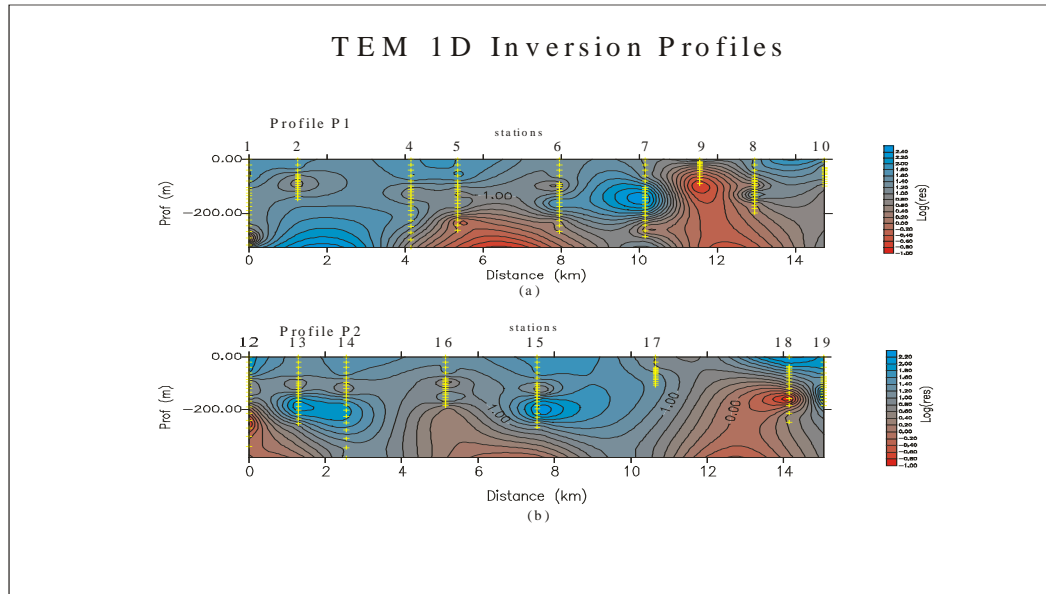


Figure 5 - Continuity section. The 1D inverted models are assembled together to produce these sections. (a) Profile P1; (b) Profile P2.

The Effect of Air in the Numerical Solution of the TE Mode of the Magnetotelluric Method

Michael Heimer; Luiz Rijo, Universidade Federal do Pará, Brazil
 mheimer@receita.fazenda.gov.br; rijo@amazon.com.br

Abstract

We present the numerical solution of the model of an infinite fault for the TE mode using the finite elements method to investigate the effect of the air in the TE solution. We compare our solution for the normalized electric field with one approximated analytic solution, which neglects the effect of the air, and with another exact semi-analytic solution. The latter comparison shows a difference that cannot be explained by numerical errors. Examining the effect of the air on apparent resistivity, we compare three profiles of apparent resistivity obtained with our FE solution with the profiles obtained using the approximated solution. The discrepancy between the apparent resistivities shows to be small, figuring in the range of the instrumental field error.

Introduction

Due to its importance in studying large geological features, the magnetotelluric method has been widely employed since the thirtys. This usefulness yielded the interest in obtaining mathematical descriptions of its models. For the simple 2D models as a fault has been presented several analytic solutions. However, when the geometry of the model becomes more complex, the solution must be numerical. On the other hand, to guarantee the reliability of the numerical solutions, we need to make calibration comparisons with known analytic solutions.

Cagniard (1953) introduced the basic one-dimensional model of plane waves scattering at the air-earth interface. Relying on this model where presented analytic solutions for several bi-dimensional models, which we can classify into transverse-magnetic (TM) mode and transverse-electric (TE) mode models. The case of magnetic polarization (TM mode) happens when the magnetic field is parallel to the axis of the structure. D'Erceville & Kunetz (1962) presented the analytical solution for a fault with a substratum of infinite resistivity and of infinite conductivity. The case of electric polarization (TE mode), where the electric field is parallel to the axis of the structure, is a problem of greater mathematical complexity, because of the propagation of the secondary electric field created by the discontinuity through the air. Weaver (1963) proposed an approximated analytic solution for the model of an infinite fault, neglecting the effect of the air. Sampaio (1983) proposed an exact semi-analytic solution for the same case. Numerical

solutions have been proposed by Hohmann (1971), using integral equations, by Jones & Price (1972), using finite differences and by Rijo (1977) using the finite elements method.

In this work we present the numerical solution of the model of an infinite fault for the TE mode using the finite elements method, to investigate the effect of the air in the TE solution. Comparing our solution for the normalized electric field with the solutions presented by Weaver (op. cit.) and Sampaio (op. cit.) we note, besides the expected difference to the approximated Weaver solution, a difference to the Sampaio solution that cannot be explained by numerical errors. To examine the effect of the air on apparent resistivity, we compared three profiles of apparent resistivity obtained with our FE solution with the profiles obtained using the Weaver solution. In this case, the discrepancy between the solutions is much smaller than the discrepancy of the E_y solutions.

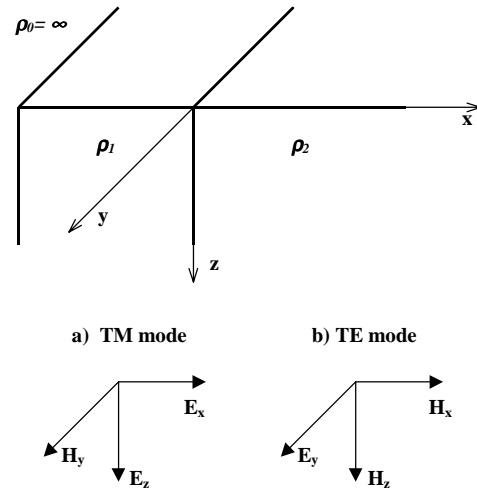


Figure 1 – Model of an infinite fault a) TM mode b) TE mode

FE algorithm calibration with TM mode

The calibrations of our finite elements algorithm were made with the model of a infinite fault in TM mode shown in Figure 1a. We used FE formulation via Galerkin's method to solve the Helmholtz equation

$$\frac{\partial}{\partial x} \left(\frac{1}{\sigma} \frac{\partial H_y}{\partial x} \right) + \frac{\partial}{\partial z} \left(\frac{1}{\sigma} \frac{\partial H_y}{\partial z} \right) + i\omega \mu H_y = 0$$

We applied the FE algorithm to solve the problem using two different approaches: for the total magnetic field and for the secondary magnetic field.

The Effect of Air in the Numerical Solution of MT Method

For comparison we used the horizontal component of the electric field, obtained through the numerical differentiation of the expression $E_x = -\rho \frac{\partial H_y}{\partial z}$, because

it varies over the plane $z=0$ of the fault, being discontinuous at $x=0$ and thus very sensible for all kind of errors. Both approaches led to the same results and the final comparison was made with the analytic solution using the method proposed by D'Erceville & Kunetz (op. cit.), yielding perfect agreement, as shown in Figure 2.

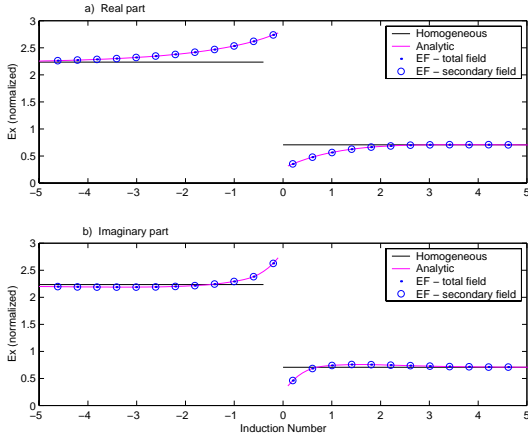


Figure 2 – Normalized electric field over an infinite fault in MT mode a) Real part b) Imaginary part

The TE mode

Both from the analytical and from the numerical point of view the TE mode, shown in Figure 1b, represents a mathematically more complex problem than the TM mode, since the E_y component to be found is no longer constant at the plane $z=0$ like the H_y component in the TM mode. This phenomena we can call the “effect of the air”, because it represents the propagation through the air of the secondary electric field created by the discontinuity. Thus, we can no longer set the boundary with the Neumann condition at $z=0$. It is necessary to include the air in our FE mesh, and to set the boundary condition on a plane $z=h$ above the air/earth interface, with h sufficiently big to guarantee that there are no more effects of the secondary electric field. Again, we used the two FE approaches of total and secondary field, this time to solve the Helmholtz equation:

$$\frac{\partial^2 E_y}{\partial x^2} + \frac{\partial^2 E_y}{\partial z^2} + k^2 H_y = 0$$

The total electric field approach works without sources and its boundary conditions are:

- i) $E_y = 0$ at $z = \infty$
- ii) $E_y = E_0^j \exp(-ik_j z)$ at $x = -\infty$ ($j=1$) and $x = \infty$ ($j=2$) and $z > 0$, where $E_0^j = \omega \mu_j H_0 / k_j$
- iii) $E_y = E_0^j (1 - ik_j z)$ at $x = -\infty$ ($j=1$) and $x = \infty$ ($j=2$) and $z < 0$, where $E_0^j = \omega \mu_j H_0 / k_j$
- iv) $E_y = E_0 - i\omega \mu H_0 h$, where $E_0 = .5 x/x_{max} (E_0^2 - E_0^1) + .5 (E_0^2 - E_0^1)$, x_{max} the value assumed for $x = \infty$ and h the value of z assumed for $z = -\infty$.

The secondary electrical field approach assumes the primary field $E_y^{p,1}$ for the entire terrain and uses the same as source. The boundary conditions are:

- i) $E_y^s = 0$ at $z = \infty$ and at $x = -\infty$.
- ii) $E_y^s = E_y^{p,2} - E_y^{p,1}$ at $x = \infty$.
- iii) $E_y^s = E_0 - E_0^1$ at $z = -\infty$.

The total electric field is obtained summing the primary field to the secondary field obtained by FE.

Again, both approaches led to the same results. An additional care to guarantee the reliability of our solution was to test different kind of meshes, including a fine sparsely equal-spaced mesh.

The apparent resistivity was found computing first numerically the expression $H_x = \frac{1}{i\omega \mu} \frac{\partial E_y}{\partial z}$ and than

$$\rho_a = \frac{1}{\omega \mu} \left| \frac{E_y}{H_x} \right|^2.$$

Results for the normalized electric field

To comprise a wide range of frequencies and metric dimensions we calculated our solution for the normalized electric field, i. e., $E_{y, norm} = E_y / |k| / (\omega \mu)$ and plotted it as a function of the induction number, $\theta = \sqrt{\omega \mu \sigma_2} x$. The resistivity contrast is denoted by $R = \rho_1 / \rho_2 = \sigma_2 / \sigma_1$. We considered three cases, $R = 2$, $R = 10$ and $R = 50$. The real and the imaginary parts of the normalized electric field for this cases are shown in Figures 3 to 8, where we compare our FE solution with the Weaver solution, which neglects the effect of the air, with the Sampaio solution as presented in his work (Sampaio 1985), which is an exact semi-analytic solution of the problem and with the case of an earth as an homogeneous layer of conductivity σ_j . In all cases we observe differences of magnitudes far greater than the monitored numerical errors of the FE method. The tendency of the midpoint as a point of inflection with small inclination of our FE solution seems to follow the Weaver solution rather than the Sampaio solution. Also we observe that the

The Effect of Air in the Numerical Solution of MT Method

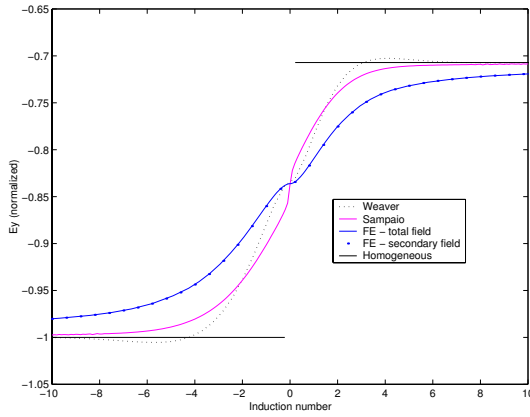


Figure 3 – Real part of the electric field in TE mode for $R = 2$

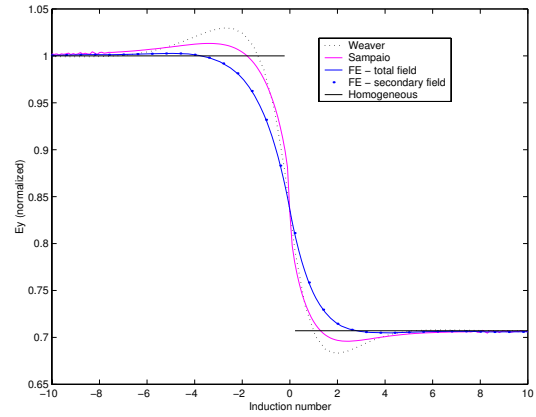


Figure 4 – Imaginary part of the electric field in TE mode for $R = 2$

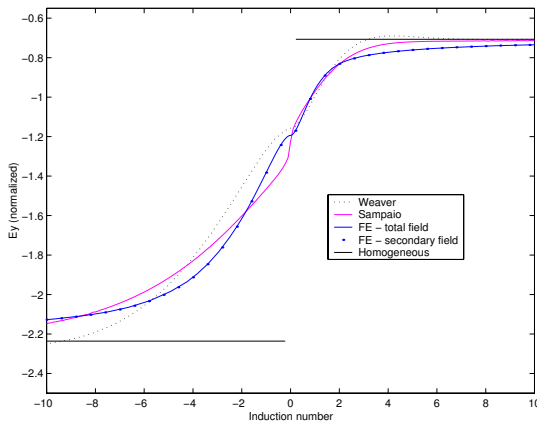


Figure 5 – Real part of the electric field in TE mode for $R = 10$

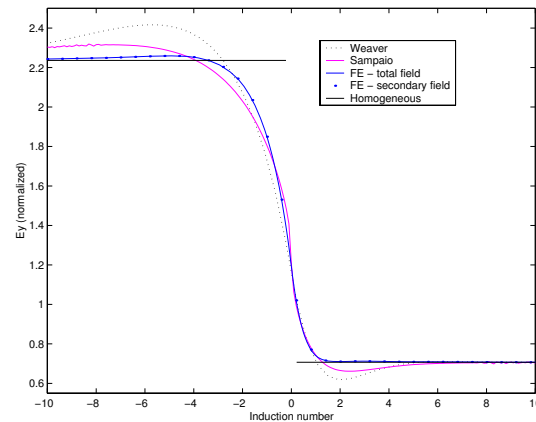


Figure 6 – Imaginary part of electric field in TE mode for $R = 10$

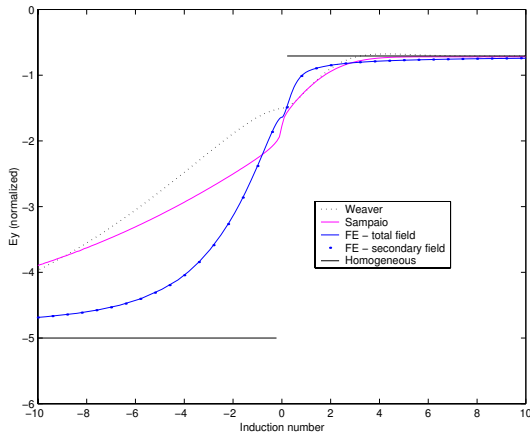


Figure 7 – Real part of electric field in TE mode for $R = 50$

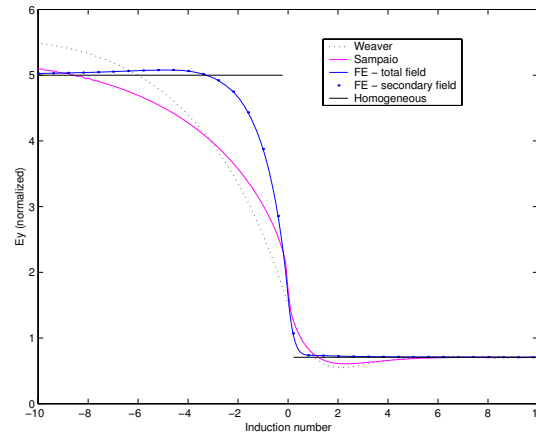


Figure 8 – Imaginary part of electric field in TE mode for $R = 50$

discrepancy between the solutions seems to increase with the increase of R .

Results for Apparent Resistivity

The Figures 9 to 11 show three profiles of apparent resistivity, calculated for the frequency of 100 Hz, using the Weaver solution and our FE solution, again for the resistivity contrasts of 2, 10

and 50. The discrepancy between the solutions is smaller than the discrepancy of the E_y solutions, due to the intrinsic smoothing effect of the apparent resistivity function. The magnitude of the discrepancy is very small for small resistivity contrast and increasing for increasing R . In all cases, the discrepancy is smaller than the instrumental field error.

The Effect of Air in the Numerical Solution of MT Method

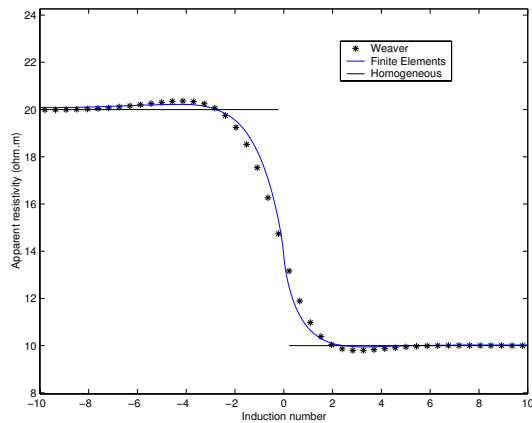


Figure 9 – Apparent resistivity profile for $f=100\text{Hz}$ with $R=2$ in the TE mode

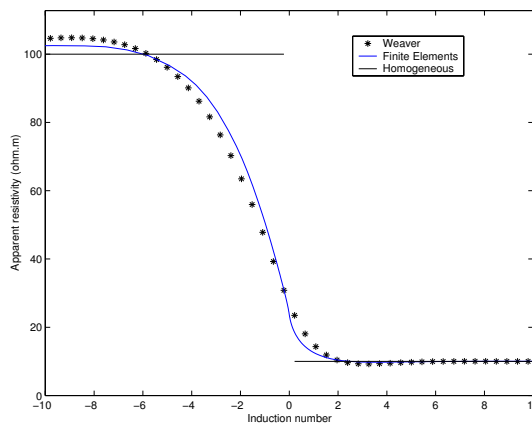


Figure 10 – Apparent resistivity profile for $f=100\text{Hz}$ with $R=10$ in the TE mode

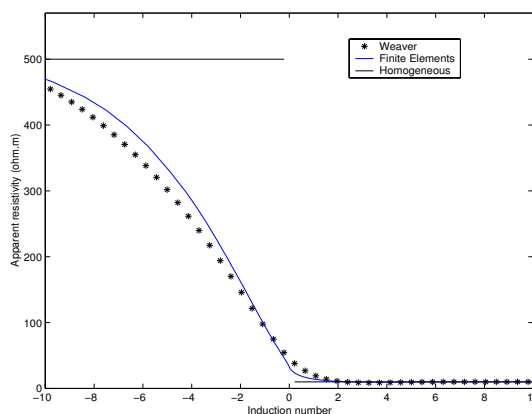


Figure 11 – Apparent resistivity profile for $f=100\text{Hz}$ with $R=50$ in the TE mode

Conclusions

We presented the numerical solution of the model of an infinite fault for the TE mode using the finite elements method. The comparison of our solution for the normalized electric field with the solution presented by Weaver showed an expected difference because of the effect of the air, which was neglected by Weaver. However, the difference between our solution and the semi-analytic solution given by Sampaio cannot be explained by numerical errors.

To examine the effect of the air on apparent resistivity we compared three profiles of apparent resistivity obtained with our FE solution with the profiles obtained using the Weaver solution, obtaining a very small discrepancy between the solutions, smaller than the instrumental field error. This suggests that, in praxis, the Weaver solution is a good approximation for geophysical prospecting.

References

- Cagniard, L. (1953) - Basic theory of the magnetotelluric method of geophysical prospecting, *Geophysics*, 18, 605-635.
- D'Erceville, I. & Kunetz, G. (1962) - The effect of a fault on the Earth's natural electromagnetic field, *Geophysics*, 27(5): 651-665.
- Hohmann, G. (1971) - Electromagnetic scattering by conductors in the Earth near a source of current, *Geophysics*, 36(1): 101-131.
- Jones, F. W. & Price, A. T. (1970) - The perturbations of alternating geomagnetic fields by conductivity anomalies, *Geophysics*, 20, 317-334.
- Rijo, L. (1977) - Modelling of electric and electromagnetic data, PhD Thesis, University of Utah, 240 pp.
- Sampaio, E. E. S. (1985) - Espalhamento de uma onda eletromagnética plana por dois quartos-de-espaço condutores, Trabalho de professor titular, UFBA, 35 pp.
- Weaver, J. (1963) - The electromagnetic field within a discontinuous conductor with reference to geomagnetic micropulsations near a coast line, *Canadian Journal of Physics*, 41(3): 484-495.

Acknowledgments

We would like to thank the Universidade Federal do Pará for logistical support. Also we thank Agência Nacional de Petróleo (ANP) for the financial support given to our Graduate Course at UFPA.

The use of telluric and magnetotelluric methods in graben studies

Fernando A. Monteiro Santos(1), Eugénio P. Almeida(1, 2), António Soares(1), Rita Nolasco(1)

and Luís Mendes Victor(1)

(1)Centro de Geofísica da Universidade de Lisboa, Lisboa, Portugal, email: dfams@fc.ul.pt,

(2)Instituto Politécnico de Tomar

Abstract

In past years telluric measurements have been used on sedimentary basins to explore lateral variation of electrical resistivity. Magnetotellurics is currently used in investigation both, vertical and lateral changes in electrical conductivity of earth subsurface. This paper concerns the application of both methods to the study of a graben in NE Portugal and shows that the complementary of the methods can be used in order to infer information concerning the three-dimensionality of geological structures.

Introduction

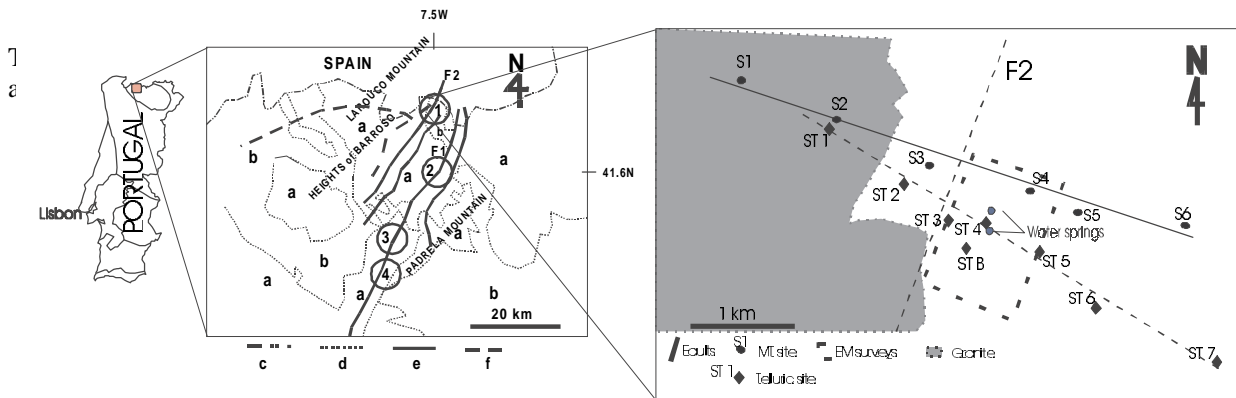


Figure 1 – General overview of NE Portugal geology and location of the study area. F1-Chaves-Verin fault; F2-Vilarelho da Raia fault; a-Granitic formations; b-Metasediments; c-Portugal-Spain boundary; d-geologic limits; e-fault; f-fault (probable). Springs: 1-Vilarelho da Raia; 2-Chaves; 3-Vidago; 4-Pedras Salgadas

waters along the megalineament of Verin-Chaves-Penacova (NE Portugal, Figure 1). Several geophysical and geochemical studies have been carried out in order to characterise the recharge areas, depth and shallow water paths and water residence time (Aires-

Barros et al., 1995, 1998; Monteiro Santos et al. 1995, 1996, 2001; Marques et al., 2000). The results obtained indicated that, although the chemical and isotopic composition of Vilarelho da Raia cold waters is similar to Chaves hot waters, they have different recharge areas. The lower temperature (17°C) and flow rate (2.5 l/min) of the Vilarelho da Raia springs, together with the lower tritium activity, pointed to a longer circulation time from the recharge area to the surface (Marques et al., 2000).

Due to the commercial interest of the Vilarelho da Raia spring, some geophysical experiments were designed to draw the main local geological features. Geophysical investigations included the application of electromagnetic SP telluric and magnetotelluric

structure of the graben in the Vilarelho da Raia area, are presented. The paper shows the complementary aspects of those techniques in geological studies.

The use of telluric and magnetotelluric methods in graben studies

Geological sketch

The Vilarelho da Raia - Chaves region (Figure 1) is part of a major hydrogeological province where the upflow of thermomineral waters are structurally controlled by the fault systems associated with the NNE-SSW megafault extending from Verin (Spain) to Penacova (central Portugal). The geomorphology of that province is dominated by several tectonic depressions. The "Chaves basin" and "Vilarelho da Raia basin" are grabens whose axes are roughly oriented NNE-SSW. They are bounded at the east side by the edge of Padrela Mountain showing an escarpment with a 400 m throw in Chaves region. In the NW part of Vilarelho da Raia area, the geomorphology is controlled by the Larouco Mountain (1500 m a.s.l.) whose edge is oriented NNE-SSW.

The region is located in the Ante-Mesozoic Iberian Massif that consists mainly of Hercynian granites and Palaeozoic metasediments (Portugal Ferreira et al., 1992). The oldest formations correspond to the Schisto-Graywacke Complex (Ante-Ordovician). At Ordovician and Silurian times quartzites and schists were formed, being metamorphosed at the end of Palaeozoic by the Hercynian granitic intrusions. The Vilarelho da Raia and Chaves granites have been classified into the alkaline granites of the 3rd Hercynian phase (310 My). The Silurian metamorphic formations have been recognised in both easternwards and westernwards sides of the Chaves basin. The most recent formations are Miocene-Pleistocene sedimentary series (lacustrine, alluvial, detritic, etc.). These formations show variable thickness along the basins. Alpine Orogeny originated Extensive neotectonic features. These events were responsible for the formation of several low-enthalpy hydrothermal fields.

Magnetotelluric and telluric surveys

Six magnetotelluric (MT) soundings were carried out across the graben in order to characterise the distribution of the electrical resistivity in depth. Data were acquired in the frequency range from 180 to 0.01 Hz. The measurement directions of the horizontal magnetic and electric fields were N26E and N116E, in accordance with the direction of the main tectonics structures at surface.

The data have been processed by a robust method (Chave and Thomson, 1989). Figure 2 shows data acquired at three sites. The scattering in the apparent resistivities due to the static shift was small (less than a decade) and for this reason the static-shift correction was not considered. Therefore, only the

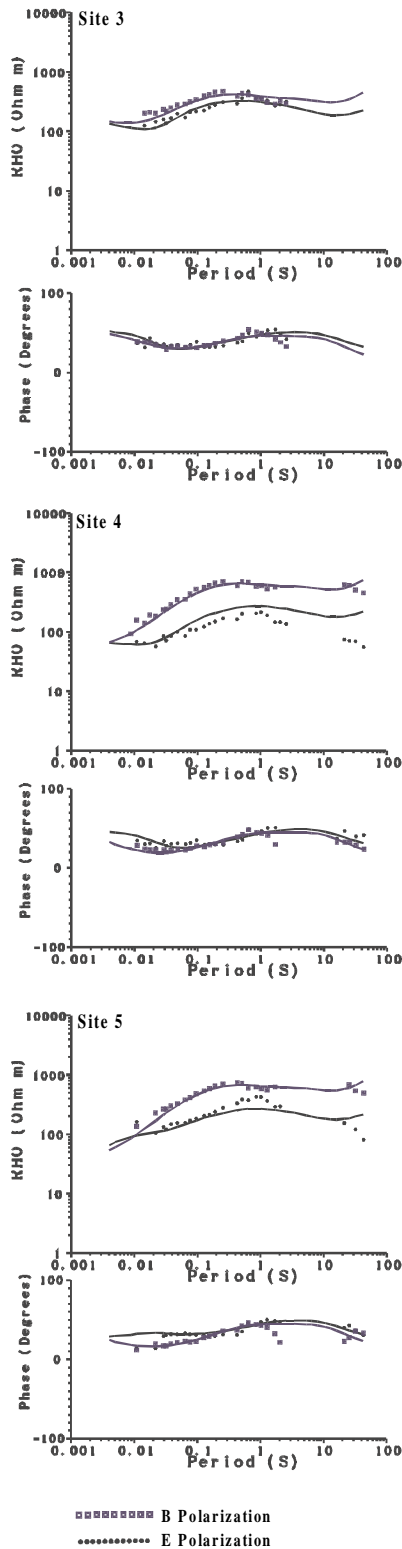


Figure 2 – Magnetotelluric data (symbols) and model response (lines) at three sites.

The use of telluric and magnetotelluric methods in graben studies

uppermost part of the crust (3 km) has been investigated.

The telluric method was intensively used in the study of sedimentary structures several years ago (see e.g. Yungul, 1977). However, the use of the method has decreased in the last years. Although based on the same theory, the magnetotelluric and telluric methods are used to solve different kinds of exploration problems: the telluric method is mainly a lateral exploration tool and the MT is a vertical exploration tool. Practical and theoretical aspects of the telluric method have been studied by several authors (see Yungul, 1977 and references therein). In this method two orthogonal components of the electric field are measured simultaneously at two separated sites: at the base station (B) and at the field station (F). It is assumed that the components of the electric field at the two sites are linearly related:

$$\mathbf{E}^F = \mathbf{T} \mathbf{E}^B \quad (1)$$

The elements of the matrix \mathbf{T} (transfer function) are constants depending only on the direction of the measurements and subsurface structure. The Jacobian \mathbf{J} of the transfer function is the magnitude used in the telluric method. Several methods are described in the literature to calculate \mathbf{J} values. In this study we have used least square techniques to estimate \mathbf{J} .

Figure 1 shows the location of the telluric stations used in this study. Shown in Figure 3 is the telluric anomaly obtained along the profile. The rise in \mathbf{J} at the central part of the profile (sites 4 and 5) is believed to be due to rising basement.

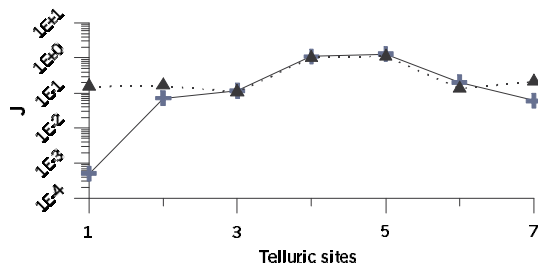


Figure 3 – Telluric data (cross) and model response (triangle).

Two-dimensional interpretation

Two-dimensional inversion of the MT data was undertaken using the program of Mackie et al. (1997). The inversion was carried out on both TE and TM modes jointly. Figure 4 (upper) presents the obtained model. The data fit for all sites is quite good (see Figure 2). The final rms is 5.6. The model displays the general pattern of the sedimentary filling (resis-

tivity ranging from 10 to 250 ohm m), in the area of the profile, with a more conductive (resistivity <100 ohm m) structure beneath sites 4 and 5. The granitic bedrock (1000 ohm m) is also well displayed in the model, rising in the western part of the profile, beneath sites 2 and 3.

The telluric anomaly was modelled assuming a two-dimensional approach with strike perpendicular to the telluric profile. In this case \mathbf{J} is equal to the ratio of the electric field along the profile (TM mode in MT modelling) at field site to that at base site. The value of \mathbf{J} at site 4 is close to the unit, revealing that the geoelectrical structure at this site is similar to that one at B site. Therefore, site 4 was taken as base site in the modelling procedure. Figure 4 (bottom) shows the model obtained by trial-and-error technique. The data fit (Figure 3) is perfectly acceptable. The model displays the basement structure in the zone of the profile. Geological logs carried out in two boreholes made in the vicinity of the water springs (Figure 1) confirm the bedrock rising observed beneath sites 4 and 5.

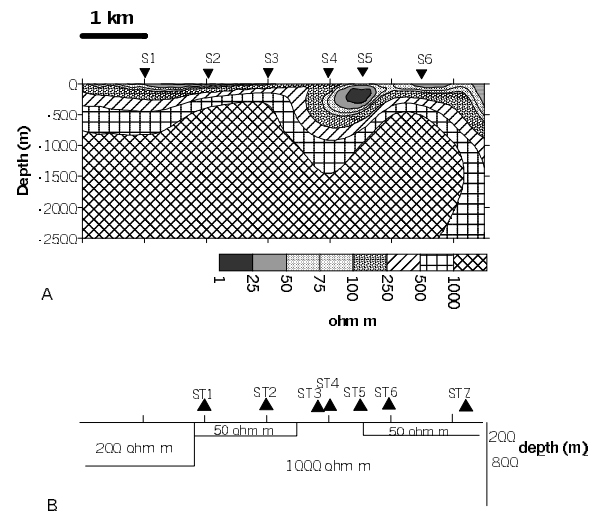


Figure 4 – Magnetotelluric (A) and telluric (B) models obtained by inversion and modelling, respectively.

Conclusions

Two-dimensional inversion of six MT soundings and two-dimensional modelling of seven telluric soundings carried out across the Vilarelho da Raia graben (NE Portugal) allow the characterisation of the electrical behaviour of shallow structures. The sedimentary filling of the basin, with a maximum thickness of 1

The use of telluric and magnetotelluric methods in graben studies

km, was found to be conductive due to the clay and water presence. The faulted bedrock has been revealed as having a strong topography probably originated by vertical movements of blocks during Alpine Orogeny.

Finally, this work shows that the combination of the magnetotelluric and telluric surveys can be useful in the reconnaissance of the three-dimensionality inherited to tectonic graben structures.

References

- Aires-Barros L, Marques JM, Graça RC (1995) Elemental and isotopic geochemistry in the hydrothermal area of Chaves / Vila Pouca de Aguiar (Northern Portugal). *Environmental Geology* 25 4: 232 - 238.
- Aires-Barros L, Marques J M, Graça RC, Matias M J, Weijden C. H. van der, Kreulen R, Eggenkamp HGM (1998) Hot and cold CO₂-rich mineral waters in Chaves geothermal area (northern Portugal). *Geothermics* 27 1: 89 - 107.
- Chave, A.D. and Thomson, D.J., (1989). Some comments on magnetotelluric response function estimation, *J. Geophys. Res.*, 94, 14215-14222.
- Mackie, R., Rieven, S. and Rodi, W., (1997). Users manual and software documentation for two-dimensional inversion of magnetotelluric data.
- Marques J M, Aires-Barros L, Graça R C, (2000). Papel do CO₂ na mineralização das águas associadas a sistemas geohidrológicos dominados pela presença de rochas granitóides. *Proceedings do 5º Congresso da Água*, 25 a 29 de Setembro de 2000, Culturgest, Lisboa. 16 pp.
- Monteiro Santos F A, Dupis A, Andrade Afonso A R, Mendes-Victor L A, (1995). Magnetotelluric observations over the Chaves geothermal field (NE Portugal)-preliminary results. *Physics of the Earth and Planetary Interiors* 91: 203-211.
- Monteiro Santos, F. A., Dupis, A., Andrade Afonso, A. R., Mendes-Victor, L. A., (1996). An audio-magnetotelluric survey over the Chaves geothermal field (NE Portugal). *Geothermics* 25 3: 389 - 406.
- Monteiro Santos, F.A., Almeida, E.P., Castro, R., Nolasco, R. and Mendes Victor, L.A., (2001). A hydrogeological investigation using EM34 and SP surveys. EPS (submitted).
- Portugal Ferreira M., Sousa Oliveira A., Trota A. N., (1992). Chaves geothermal pole. Geological Survey, I and II. Joule I Program, DGXII, CEE. UTAD (Universidade de Trás-os-Montes e Alto Douro) internal report.
- Yungul, S. H., (1977). The telluric methods in the study of sedimentary structures-a survey. *Geoexploration*, 15, 207-238.

Acknowledgments

The authors would like to thank FCT/MCT for supporting this work in scope of the project AquaTransfer (PRAXIS, N 3/3.1/CEG/2664/95).



Two-step inversion scheme for complex magnetotelluric apparent resistivity data

Atahebson B. Santos, Edson E. S. Sampaio*, and Milton J. Porsani, PPPG/UFBA

Summary

Interpretation of magnetotelluric data under the assumption of isotropic and one-dimensional structures is a valuable procedure for exploration and solid earth geophysics investigation. Because its interpretation requires an efficient inverse modeling, we propose and evaluate an inversion code, which consists of two steps. Both steps employ jointly the modulus and the phase of the apparent resistivity function. The first one consists of the use of the asymptotic Bostick-Niblett approach. The second employs the result of the inversion obtained in the first step as a starting model to apply an extension to complex valued data of the linearized inversion with a multiple reweighted least-squares method. We applied the analysis both to synthetic data and to field data from the Paraná Basin in Brazil. The results show that the inversion procedure presents a faster convergence without loss of accuracy, increases the resolving power of the MT technique, and may improve its capability to delineate deep conductors. Therefore a reasonable interpretation of the data employing one-dimensional model can be achieved even in the presence of relatively noisy data, and under conditions that slightly violate the premise of lateral homogeneity.

Introduction

The magnetotelluric method MT is an electromagnetic method of natural sources proposed both by Tikhonov (1950) and Cagniard (1953). MT aims to determine the spatial distribution of the electrical conductivity of the earth, specially to delineate deep conductive targets, based on the measurement of the natural electromagnetic field. As such, its interpretation represents an important application for both deep strata geological mapping and geophysical exploration. Though simple, the adoption of a layered isotropic medium to represent the subsurface is quite often justifiable (Whittall and Oldenburg 1992). Therefore 1D inversion is a common procedure and quite frequently gives useful results for the interpretation of MT data.

In this paper we propose the analysis of MT data, under the assumption of an 1D condition, jointly employing the modulus and the phase, in two steps. The first step consists of the use of the asymptotic Bostick-Niblett approach, following the procedure developed by Ramos and Sampaio (1993). The second step employs the result of the inversion obtained in the first step as a starting model, to apply an extension to complex data of the linearized inversion with a multiple reweighted least-squares (MRLS) method proposed by Porsani et al (2001).

The MRLS method already proved to be effective for the

inversion of real VES data. Here we analyse its effectiveness for the inversion of complex MT synthetic and field data. We also investigate if the joint inversion employing the complex valued data may increase the resolving power of the MT technique and improve its capability to delineate deep conductors. As a case history example, we have successfully applied this two-step inversion technique for the interpretation of MT data from the Paraná Basin, Southern Brazil.

Methodology

The Magnetotelluric Method

From the measurement of the horizontal and mutually orthogonal components of the electric (E_{x1} or E_{y1}) and the magnetic (H_{y1} or H_{x1}) fields at the surface of the earth (top of the first layer) for several values of frequency, we can compute the variation of the electromagnetic impedance on the surface of the earth as a function of frequency employing the following equation:

$$\hat{Z}_{xy1} = \frac{E_{x1}}{H_{y1}}, \quad \text{or} \quad \hat{Z}_{yx1} = -\frac{E_{y1}}{H_{x1}}, \quad (1)$$

where: 1 refers to the first layer, and x, y refer to two mutually orthogonal horizontal directions. For the present analysis of 1D earth we will express the electromagnetic impedance on the top of the n th layer as \hat{Z}_n . On the other hand the intrinsic impedance of the n th layer is given by $Z_n = \frac{\omega \mu_0}{\kappa_n}$, where: $\omega = 2\pi f$, f being the frequency in hertz, μ_0 the magnetic permeability, and n is the wave number of the n th layer. For an earth constituted of N homogeneous and isotropic layers the surface impedances are given by

$$\begin{aligned} \hat{Z}_1 &= Z_1 \frac{\hat{Z}_2 + Z_1 \tanh(i\kappa_1 h_1)}{Z_1 + \hat{Z}_2 \tanh(i\kappa_1 h_1)}, \\ \hat{Z}_n &= Z_n \frac{\hat{Z}_{n+1} + Z_n \tanh(i\kappa_n h_n)}{Z_n + \hat{Z}_{n+1} \tanh(i\kappa_n h_n)}, \quad n = 2, \dots, N-1 \\ \hat{Z}_N &= Z_N \end{aligned} \quad (2)$$

where h_n is the thickness of the n th layer.

Let us define a complex apparent resistivity function of frequency $\rho_a = |\rho_a| e^{i\phi_a}$, such that:

$$|\rho_a| = \frac{1}{\omega \mu_0} |\hat{Z}_1|^2 \quad \text{and} \quad \phi_a = \Delta \phi_1 - \frac{\pi}{2}, \quad (3)$$

where: $\Delta \phi_1$ is the phase difference between the electric and the magnetic fields on the surface; both ρ_a and $\Delta \phi_1$ are given in radians, and ρ_a is given in ohm.m.

Two-step inversion

From the knowledge of the electromagnetic impedance on the surface we can search the distribution of the electrical resistivity of the subsurface employing the concept of an apparent resistivity function. Since this function contains information of both the modulus and the phase it can be employed for a joint inversion of MT data.

The Bostick-Niblett Inversion

Niblett and Sayn-Wittgenstein (1960) and Bostick (1977) independently proposed an asymptotic method for the inversion of 1D MT data. Ramos and Sampaio (1993) analysed both techniques thoroughly and showed that they are equivalent. According to the Bostick-Niblett inversion, given $|\rho_a|$ and ϕ_a as a function of the period $T = 1/f$, we can obtain a distribution of the resistivity ρ with depth D , such that:

$$D \approx 355.88 \sqrt{|\rho_a| T}, \quad \rho_N(D) = |\rho_a| \frac{1 + m(T)}{1 - m(T)}, \quad (4)$$

$$m(T) = \frac{d \log(|\rho_a|)}{d \log(T)}, \quad \rho_B(D) = |\rho_a| \left(\frac{\pi}{2 \phi_a} - 1 \right). \quad (5)$$

In those equations ρ_N and ρ_B are respectively the Niblett and the Bostick distribution of the resistivity with depth and are given in ohm.m, T is given in seconds, D is given in meters. Figure 2 displays the modulus of the apparent resistivity as a function of the period for two orthogonal directions. The logarithmic mean of the apparent resistivity data have been smoothed to produce, via Equation 5, the Bostick distribution curve shown in Figure 4. Subsequently the Bostick derivative distribution shown in Figure 5 has been computed. The derivative curve gives an estimate of the position of the geo-electric boundaries. The result of this inversion yielded 8 geo-electric layers. The eight resistivities and seven thicknesses obtained have been used as a starting model for the subsequent interpretation employing the MRLS method proposed by Porsani et al (2001).

Multiple reweighted least-squares method (MRLS)

Let us write the deviations between the complex observed and the complex computed data in terms of an exponent dependence,

$$f(\mathbf{m}, s, \beta) = [\Delta d(\mathbf{m}, s)]^\beta = [(\rho_c(s) - \rho_c(\mathbf{m}, s))]^\beta. \quad (6)$$

where $\rho_c(s)$ and $\rho_c(\mathbf{m}, s)$ represent the complex observed data and the complex calculated data. We now quasi-linearize $f(\mathbf{m}, s, \beta) \approx \tilde{f}(\mathbf{m}, s, \beta)$ by expanding in a Taylor series about the current model, \mathbf{m}_k , and retaining only the first derivative term. By using vector and matrix notation the resulting equation can be represented as,

$$\mathbf{f}(\mathbf{m}, \mathbf{s}, \beta) \approx \tilde{\mathbf{f}}(\mathbf{m}, \mathbf{s}, \beta) = \mathbf{f}_{\beta k} - \mathbf{W}_{\beta k} \mathbf{G}_k \Delta \mathbf{m}, \quad (7)$$

where \mathbf{G}_k is the sensitivity matrix, $\Delta \mathbf{m} = \mathbf{m} - \mathbf{m}_k$ is the parameter vector correction, $\mathbf{f}_{\beta k} = \mathbf{f}(\mathbf{m}_k, \mathbf{s}, \beta)$ is the

vector of the data deviation whose elements are calculated with equation (6) for $s_i, i = 1, \dots, M$, and $\mathbf{W}_{\beta k}$ is a weighting diagonal matrix whose elements may be computed as,

$${}^k w_{ii} = \beta [\Delta d(\mathbf{m}_k, s_i)]^{\beta-1} \Delta d(\mathbf{m}_k, s_i). \quad (8)$$

We note that $\tilde{\mathbf{f}}(\mathbf{m}, \mathbf{s}, \beta)$ in equation (7) is a linear function of $\Delta \mathbf{m}$, and a solution can be obtained by solving the complex linear system of equation in the LS sense,

$$(\mathbf{W}_{\beta k} \mathbf{G}_k) \Delta \mathbf{m}_k = \mathbf{f}_{\beta k}. \quad (9)$$

For any value of β ($\beta \neq 0$) the LS solution can be obtained and the expression for updating the current model may be written,

$$\mathbf{m}_{k+1} = \mathbf{m}_k + (\mathbf{G}_k^H \mathbf{W}_{\beta k}^H \mathbf{W}_{\beta k} \mathbf{G}_k)^{-1} \mathbf{G}_k^H \mathbf{W}_{\beta k}^H \mathbf{f}_{\beta k}. \quad (10)$$

The LS approach based on equation (10) can be seen as an iterative procedure where the row i of the sensitivity matrix is weighted by the factor ${}^k w_{ii}$ (eq. 8) which is a function of the deviation between the observed resistivity values and the ones computed from the current model \mathbf{m}_k . A similar equation was derived by Scales and Gersztenkorn (1988) for the LS method by using L^p norm. Equation (10) gives the solution of the inverse problem for a specific value of β . The concept of a multiple reweighted least-squares approach can be employed by using a specified range of β values. Employing K different values for β in each iteration and solving equation (10) K times, K different possibilities for updating the current model can be obtained. By evaluating the fitness value for each candidate model we can select as current model the one which presents the best performance. The steps of the MRLS algorithm used in the numerical examples are presented in Porsani et al (2001).

Numerical Results

The synthetic model represents a 5-layer medium with the following parameters: $\rho_1 = 200 \text{ ohm.m}$, $\rho_2 = 20 \text{ ohm.m}$, $\rho_3 = 200 \text{ ohm.m}$, $\rho_4 = 15 \text{ ohm.m}$, $\rho_5 = 1000 \text{ ohm.m}$, $h_1 = 10 \text{ m}$, $h_2 = 200 \text{ m}$, $h_3 = 1000 \text{ m}$ and $h_4 = 4000 \text{ m}$ (Ramos and Sampaio 1993).

The inversion of the synthetic data was done in the logarithmic domain. Figure 1, displays the result of the inversion of the synthetic data employing the resistivity data. Because we know the true model for the synthetic data, we could represent not only the adjustment of the data on each iteration but also the fit between the current and the true model. We employed 50 values of $0.1 < \beta < 6.0$ for the inversion. The fit of both the inverted data and of the parameters is excellent, giving an error of less than 1%. Notice that it was not possible to invert these data employing fixed values of β : either $\beta = 1$, which corresponds to the conventional least squares, or $\beta = 0.5$, which corresponds to the absolute minimum, because a divergence happened in both cases. Figures 6, 7, 8, and

Two-step inversion

9 show the inversion of the real MT data employing, respectively, the values of the modulus, the phase, and the complex resistivity function. Figure 10 shows in a same graph the variation of the resistivity with depth as obtained from the Bostick, the modulus, the phase, and the complex apparent resistivity inversions. The final models resulting from the modulus and the complex apparent resistivity inversion agree in general, and both give close fits to the apparent resistivity (Figures 6 and 8). Though the fit of the phase (Figure 7) was also good, its model is different specially in the shallow features.

Conclusions

The problem of 1D inversion of MT data has been analysed sequentially employing both the asymptotic Bostick-Niblett approach and the linearized inversion with a multiple reweighted least-squares method. We applied the analysis both to synthetic data and to field data from the Paraná Basin in Brazil. The results show that the MT inversion procedure is greatly improved by jointly employing the complex valued data consisting of the modulus and the phase of the apparent resistivity. The procedure gives a faster convergence without loss of accuracy, increases the resolving power of the MT technique, and may improve its capability to delineate deep conductors. This happens because we employ two sequence of data that may have different resolving powers at different depth levels. On the other hand the interpretation employing only the phase data is not good.

Therefore a reasonable interpretation of the data employing 1D model can be achieved even in the presence of relatively noisy data, and under conditions that slightly violate the premise of lateral homogeneity. Also the use of the multiple reweighted least-squares method gives robustness to the inversion making the linearized inversion approach not so dependent on the choice of the initial model. Its use is fully justified, and its application to the inversion of other geophysical problems may also give good results.

Acknowledgements

We thank CNPq for the fellowship, and to Mr. J. L. Porsani for providing the MT data. We acknowledge the fruitful comment of Professor S. Niwas and the revision of Professor B. Ursin.

References

Bostick, F. X., 1977. *A simple almost exact method of MT analysis*. In: *Workshop on Electrical Methods in Geothermal Exploration*. Salt Lake City, U. S. Geological Survey, Appendix, 175-177 il. (Contract: 14-08-0001-G-359).

Cagniard, L., 1953. *Basic theory of the magnetotelluric method of geophysical prospecting*. In: *Magnetotelluric Methods, Geophysics Reprint, 5*, edited by Vozzof, K.

Niblett, E. R. and Sayn-Wittgenstein, C., 1960. *Variation of electrical conductivity with depth by the magnetotelluric method*, *Geophysics*, **25**, 998-1008.

Porsani, M.J., Niwas, S. and Ferreira, N.R. 2001. *Robust inversion of vertical electrical sounding data using a multiple reweighted least-squares method*, *Geophysical Prospecting (inpress)*.

Ramos, R. G. N. and Sampaio, E. E. S., 1993. *Estudo comparativo das técnicas assintóticas mais utilizadas na interpretação de sondagens magnetotélúricas*, *Revista Brasileira de Geociências*, **11**, 65-79.

Sen, M., and Stoffa, P. L., 1995. *Global optimization methods in geophysical inversion*, Elsevier, Amsterdam.

Scales, J. and Gersztenkorn, A., 1988. *Robust methods in inverse theory*, *Inverse Problem*, **4**, 1071-1091.

Tikhonov, A.N., 1950. *On determining electrical characteristics of the deep layers of the earth's crust*. In: *Magnetotelluric Methods, Geophysics Reprint, 5*, edited by Vozzof, K.

Whitall, K.P., e Oldenburg, D.W., 1992. *Inversion of Magnetotelluric Data for a One-Dimensional Conductivity*, *Geophysical Monograph Series, Society of Exploration Geophysicists, Tulsa*.

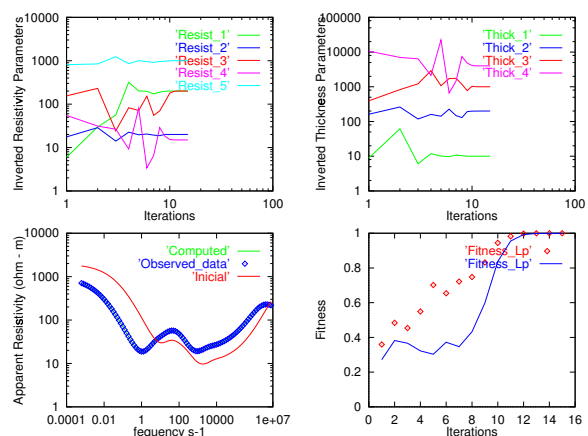


Fig. 1: Result of the inversion of the resistivity data. Above: Convergence of the parameters resistivity and thickness for each iteration. Below: Synthetic data (Observed_data) and the initial (Initial) and inverted (Computed) models are in the left. The fitness between the data (diamonds) and between the models (line) for each iteration are in the right. Initial model: $\rho_1 = 400 \text{ ohm.m}$, $\rho_2 = 10 \text{ ohm.m}$, $\rho_3 = 100 \text{ ohm.m}$, $\rho_4 = 35 \text{ ohm.m}$, $\rho_5 = 2000 \text{ ohm.m}$, $h_1 = 5 \text{ m}$, $h_2 = 100 \text{ m}$, $h_3 = 500 \text{ m}$, and $h_4 = 2000 \text{ m}$.

Two-step inversion

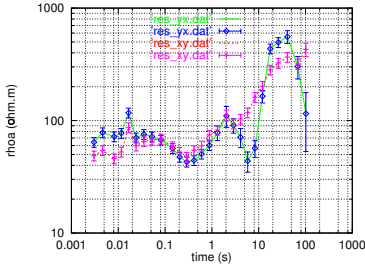


Fig. 2: Modulus of the apparent resistivity as a function of the period for the directions xy (res_xy.dat) and yx (res_yx.dat).

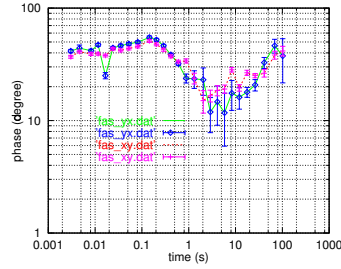


Fig. 3: Phase of the apparent resistivity as a function of the period for the directions xy (fas_xy.dat) and yx (fas_yx.dat).

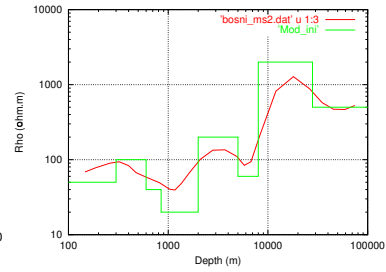


Fig. 4: Bostick distribution of the resistivity with depth (bosni_ms2.dat) and the initial model used for inverting the field data (Mod_ini).

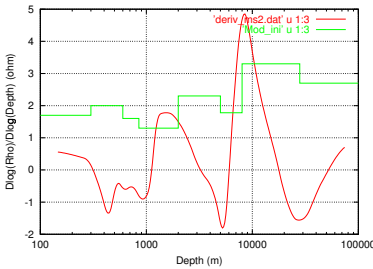


Fig. 5: Derivative of the Bostick distribution of the resistivity data (deriv_ms2.dat) and the initial model used for inverting the field data (Mod_ini).

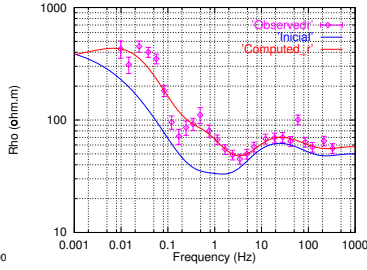


Fig. 6: Result of the inversion of the field apparent resistivity data showing the observed data (Observedr), the initial model (Initial) and the inverted model (Computed_r).

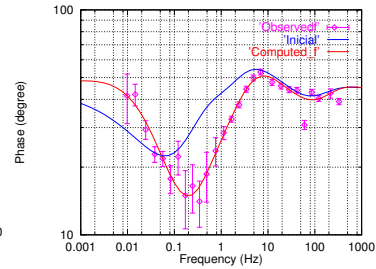


Fig. 7: Result of the inversion of the field phase data showing the observed data (Observedf), the initial model (Initial) and the inverted model (Computed_f).

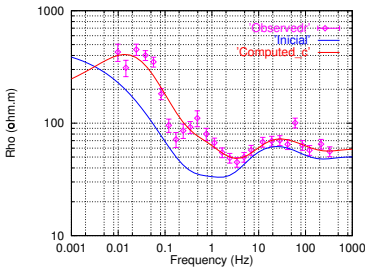


Fig. 8: Fit of the field resistivity data as a result of the inversion of the complex resistivity data, showing the observed data (Observedr), the initial model (Initial) and the inverted model (Computed_c).

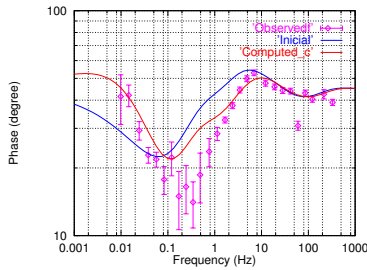


Fig. 9: Fit of the field phase data as a result of the inversion of the complex resistivity data, showing the observed data (Observedf), the initial model (Initial) and the inverted model (Computed_c).

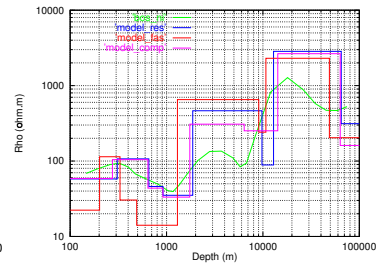


Fig. 10: Comparison between the final resistivity models performing the inversion using the Bostick transform (bos_mi), the field resistivity data (model_res), the field phase data (model_fas) and the complex resistivity function (model_comp).